LBL-8042

Lawrence Berkeley Laboratory

UNIVERSITY OF CALIFORNIA

Materials & Chemical Sciences Division

Some Double Resonance and Multiple Quantum NMR Studies in Solids

D.E. Wemmer
(Ph.D. Thesis)

August 1978

Prepared for the U.S. Department of Energy under Contract DE-AC03-76SF00098

SOME DOUBLE RESONANCE AND MULTIPLE QUANTUM NMR STUDIES IN SOLIDS

Abstract

DAVID EARL WEMMER
Materials and Molecular Research Division
Lawrence Berkeley Laboratory
University of California
Berkeley, California 94720

In the first section of this work we present the theory and experimental applications to analysis of molecular motion of chemical shielding lineshapes obtained with high resolution double resonance NMR techniques. Analysis of ^{13}C powder lineshapes in hexamethylbenzene (HMB) and decamethylferrocene (DMFe) show that these molecules reorient in a jumping manner about the symmetry axis. In DMFe it is shown that jumps of $2\pi/5$ radians occur most often. ^{13}C powder lineshapes in pentamethylbenzene show that the motion present above the crystallographic phase transition at 24°C is a nonuniform rotational motion about the pseudo six-fold axis. Several models for this motion are discussed. Analysis of proton chemical shielding lineshapes of residual protons in heavy ice (D_2O) show that protons are exchanged among the tetrahedral positions of neighboring oxygen atoms, consistent with motion expected from defect migration.

The second section of this work describes the application of Fourier Transform Double Quantum NMR to measurement of chemical shielding of deuterium in powder samples. Studies of partially deuterated benzene and ferrocene give equal shielding anisotropies, $\Delta\sigma = -6.5$ PPM. Theoretical predictions and experimental measurements of dipolar couplings between deuterons using FTDQ NMR are presented. Crystals of

$BaC\ell O_3 \cdot D_2O$, α,β d-2 HMB and α,β,γ d-3 HMB were studied, as were powders of d-2 HMB and anisic acid.

The third section of this work discusses general multiple quantum spectroscopy in dipolar coupled spin systems. Theoretical description is made for creation and detection of coherences between states without quantum number selection rules $\Delta m = \pm 1$. Descriptions of techniques for partial selectivity of order in preparation and detection of multiple quantum coherences are made. The effects on selectivity and resolution of echo pulses during multiple quantum experiments are discussed. Experimental observation of coherences up to order 6 have been made in a sample of benzene dissolved in a liquid crystal. Experimental verifications of order selection and echo generation have been made.

SOME DOUBLE RESONANCE AND MULTIPLE QUANTUM NMR STUDIES IN SOLIDS

Contents

I. BASIC FORMALISM

A. Introduction 1

B. Density Matrix 1

C. Hamiltonians 3

1. Zeeman, rf 4
2. Chemical Shielding 5
3. Qaudrupole Coupling. 6
4. Dipolar Coupling 7

D. Rotations 8

1. Cartesian Basis. 9
2. Spherical Basis. 10
3. Orientation Dependent Tensors. 11

II. EFFECTS OF MOTION

A. Introduction 13

B. Decoupling: Approach to High Resolution 14

1. Single Quantum 15
2. Double Quantum 18

C. Sensitivity Considerations 22

D. Limiting Cases for Powder Lineshapes 25

1. Rigid 25
2. Rapid Motion 27

E. Slow Motions 28

1. Random Rotations 29
2. Symmetry Related Jumps. 31

F. Computational Approach. 36

G. Hexamethylbenzene (HMB) 38

H. Decamethylferrocene (DMFe). 43

I. Ice 48

J. Pentamethylbenzene 54

K. Discussion 57

III. DOUBLE QUANTUM NMR

A. Introduction 59

B. Theory 60

1. Fictitious Spins-1/2 60
2. Hamiltonians 63
3. Density Matrix 70
4. Real Responses 80
5. Polycrystalline Samples 81
6. Dipolar Couplings 85
   a) Hamiltonians 85
   b) Preparation and Detection 95
   c) Powder Lineshapes 96
   d) Echoes 97
7. Broadening Mechanisms 98

C. Experimental 100

1. d-1 Benzene 100
2. Ferrocene 102
3. $BaClO_3 \cdot D_2O$ 103

4. Hexamethylbenzenes d-1, α,β d-2, α,β,γ d-3, d-18 106

a) Powder Spectra - Single Quantum. 107

b) Single Crystals α,β d-2, α,β,γ d-3 111

c) Double Quantum Powder Spectra d-1, d-2 . . . 112

5. Anisic Acid. 115

D. Discussion 116

IV. MULTIQUANTUM NMR IN DIPOLAR SYSTEMS

A. Introduction 118

B. Fictitious Spin-1/2 Formalism 118

C. Comparison for Spin-1. 120

D. Preparation and Detection. 123

E. Echoes 129

F. Off Resonance and Phase Behavior 132

G. Amplitudes, Symmetry and Simplification. 135

H. Experimental, Benzene in EBBA 137

I. Discussion 141

V. THE SPECTROMETER

A. Magnet 143

B. Frequency Generation 143

C. Receiver 144

D. Phase Detector 144

E. Digitizers 145

F. Probes 145

G. Transmitters 147

H. Pulse Programmer 147

I. Computer and Software 148

J. Discussion 149

Appendix A Spherical Form for Tensors 151

Appendix B Optimization of Cross Polarization Time. 154

Appendix C Optimization of Recycle Delay. 156

Appendix D Matrix Solution of Exchange. 157

Appendix E Program Listings 161

Appendix F Fictitious Spin Commutators and Anticommutators. . . 176

Appendix G Trigonometric Functions of Operators 178

Appendix H Synthesis of Deuterated HMB 180

References 181

Figure Captions 188

Figures 204

Acknowledgments

Of course in a short space it is not possible to properly thank all of those who helped in some way with this work, hence it must suffice to list the names of a few and extend my gratitude to all the others I have known in Berkeley. To Alex Pines go special thanks for sharing his insights, ideas and energies without which this work would have been impossible. To the postdocs I worked with and learned so much from; Dave Ruben, Shimon Vega, Alfred Höhener and Shan Hsi, and to the students who were companions, friends and teachers; Tom Shattuck, Jim Murdoch, Steve Sinton, Gary Drobny, Dan Weitekamp, Larry Sterna, Jau Tang, Dick Eckman go special thanks for making "the lab" enjoyable as well as educational. Credit for brilliance in sample preparation must go to Herbert Zimmermann and Sid Wolfe, and thanks for looking after "details" and typing go to Carol Hacker and Kathie Altes. Of course the technical support of all LBL personnel and Chemistry Department personnel are gratefully acknowledged as is financial support from an NSF Energy Traineeship. Last but most of all go thanks to Joanne who put up with it all.

This work was supported by the Division of Chemical Sciences, Office of Basic Energy Sciences, U.S. Department of Energy under contract number DE-AC03-76SF00098.

I. BASIC FORMALISM

A. Introduction

The development of NMR techniques has often been aided by the simplicity of theoretical description of magnetic spin systems. This simplicity arises since there is a finite number of energy levels to be considered and since the energies involved are much smaller than thermal energies under virtually all experimental conditions. In this chapter we briefly present the basic formalism to be used in understanding experiments in the later parts. The Hamiltonian is composed of several parts since for many of the experiments several couplings must be considered. However, in this section we describe terms only in the presence of the Zeeman interaction, and postpone description of effects arising from the simultaneous presence of several couplings until necessary to describe specific experiments. Three general classes of couplings will be treated; spins coupling to external fields (static and radio frequency), spins coupling to surroundings (quadrupolar and chemical shielding), spins coupling to other spins (homonuclear and heteronuclear dipolar couplings), each in turn.

B. Density Matrix

In general the Hamiltonian of a spin system for NMR studies may be written as a sum of several terms:

$$\mathcal{H} = \mathcal{H}_z + \mathcal{H}_{rf} + \mathcal{H}_{cs} + \mathcal{H}_Q + \mathcal{H}_D \qquad \text{(I-1)}$$

The dynamical evolution of the system may be described through the density matrix. In its most general form, the full equilibrium density matrix ρ_E is given by

$$\rho_E = e^{-\beta\mathcal{H}} / \mathrm{Tr}(e^{-\beta\mathcal{H}}) \qquad \text{where} \quad \beta = 1/kT. \tag{I-2}$$

However, if one notes that $kT \gg \|\mathcal{H}\|$, ($\hbar\omega_o/k \simeq 0.01\,K$ for protons in a 42 kG field), then the exponential may be expanded and only the first terms kept to give the high temperature approximation

$$\rho_E \simeq \frac{1 - \beta\mathcal{H}}{\mathrm{Tr}(1)} . \tag{I-3}$$

Since the constant operator 1 will not enter into the calculation of any observables we may alternately use the reduced density matrix

$$\rho_E \simeq \beta\mathcal{H}. \tag{I-4}$$

The expectation value of any operator Q may then be calculated

$$\langle Q \rangle = \mathrm{Tr}(\rho Q). \tag{I-5}$$

The time evolution of the density matrix may be calculated from the Von Neumann equation ($\hbar = 1$):

$$\frac{\partial}{\partial t} \rho(t) = i[\rho(t), \mathcal{H}] \tag{I-6}$$

The formal solution to this equation for a time-independent Hamiltonian is

$$\rho(t) = e^{-i\mathcal{H}t}\ \rho(0)\ e^{i\mathcal{H}t}. \tag{I-7}$$

More general solutions including explicit time dependence in $\mathcal{H}$ and relaxation effects are known[1,2,3] but will be added only as needed. Frequently we will express ρ for a spin I as an expansion in a complete operator basis ($(2I+1)^2$ operators), and calculate coefficients of particular basis operators as a function of time. Explicit examples of this will appear in Chapter III.

C. Hamiltonians

The Hamiltonians for magnetic resonance experiments may be written in terms of the angular momentum operators I_x, I_y, I_z which form a spin vector. The coupling of this spin vector to applied or intrinsic local fields may be described through coupling tensors. Such second rank tensors $\underset{\approx}{A}$ may be described in a Cartesian basis as 3×3 matrices, A_{ij}. The coupling Hamiltonian between two vectors $\underset{\sim}{X}$ and $\underset{\sim}{Y}$ is

$$\mathcal{H} = \underset{\sim}{X} \cdot \underset{\approx}{A} \cdot \underset{\sim}{Y} = \sum_{i,j=1}^{3} X_i A_{ij} Y_j. \tag{I-8}$$

It is generally convenient to express the Hamiltonian in units of frequency (ν) or angular frequency (ω) rather than energy.

1. Zeeman, rf

First we will describe the interaction of the spin with externally applied fields. For a static field this is termed the Zeeman coupling and may be written:

$$\mathcal{H}_z = \underset{\sim}{H}_0 \cdot \underset{\approx}{Z} \cdot \underset{\sim}{I} \tag{I-9}$$

where $\underset{\approx}{Z} = -\gamma_I \underset{\approx}{1}$, $\underset{\approx}{1}$ is the identity matrix and $\underset{\sim}{H}_0 = (0, 0, H_0)$, defining the field to be in the z direction. This can be written in simpler form

$$\mathcal{H}_z = -\gamma_I H_0 I_z = -\omega_0 I_z. \tag{I-10}$$

The spin may also couple to a radio-frequency oscillating magnetic field, which we will term the rf part of the Hamiltonian. Such a coupling is given by

$$\mathcal{H}_{rf} = \underset{\sim}{H}_1 \cdot \underset{\approx}{Z} \cdot \underset{\sim}{I} \tag{I-11}$$

where $H_1 = 2\,(H_x, H_y, 0)\cos\omega t$, assuming we apply the rf field only in the x-y plane. Frequently we will take the rf field to define the direction of the x-axis. In such a case the Hamiltonian may be written more simply as

$$\mathcal{H}_{rf} = -2\gamma_I H_1 \cos\omega t\; I_x. \tag{I-12}$$

For many experiments it is convenient to go into an interaction picture defined by the transformation operator

$$T = e^{-i\omega I_z t}. \tag{I-13}$$

This picture is called the rotating frame, and corresponds to observing the spin from a frame which rotates at angular velocity ω about the z - axis. In this frame

$$\mathcal{H}_z = -\Delta\omega I_z \qquad \Delta\omega = \omega_0 - \omega \tag{I-14}$$

and the rf term becomes time independent

$$\mathcal{H}_{rf} = -\gamma_I H_1 = -\omega_1 I_x. \tag{I-15}$$

The density matrix above (I-4) may also be transformed into the rotating frame,

$$\rho^* = e^{-i\omega I_z t} \rho\, e^{i\omega I_z t} \tag{I-16}$$

and the Hamiltonians in (I-7) are taken in their rotating frame form. Henceforth the density matrix will always be used in this form and the asterisk will be dropped.

2. Chemical Shielding

The Zeeman coupling may be altered somewhat through the screening of the nucleus by the surrounding electrons. This effect is termed chemical shielding and may be described in a manner similar to the Zeeman coupling

$$\mathcal{H}_{cs} = \underset{\sim}{H}_0 \cdot \underset{\approx}{\sigma} \cdot \underset{\sim}{I} \tag{I-17}$$

where $\underset{\approx}{\sigma}$ is the shielding tensor given as

$$\underset{\approx}{\sigma} = \gamma_I \begin{pmatrix} \sigma_{xx} & \sigma_{xy} & \sigma_{xz} \\ \sigma_{yx} & \sigma_{yy} & \sigma_{yz} \\ \sigma_{zx} & \sigma_{zy} & \sigma_{zz} \end{pmatrix}.$$

Since this coupling is much smaller than the Zeeman, we need only consider the secular part, that is the part which commutes with $\mathcal{H}_z$. It is then

$$\mathcal{H}_{cs} = \gamma_I H_0 \sigma_{zz} I_z. \tag{I-18}$$

We may take this tensor to be symmetric (antisymmetric parts can only contribute a second order term[2]). There is then a coordinate system in which $\underset{\approx}{\sigma}$ is diagonal, which we call the principle axis frame. In this frame we will term the diagonal elements σ_{11}, σ_{22} and σ_{33} where $\sigma_{11} \leqslant \sigma_{22} \leqslant \sigma_{33}$. Since these terms are generally very small we will measure them in parts per million (PPM) of the applied field. $\Delta\sigma = \sigma_{33} - 1/2(\sigma_{11} + \sigma_{22})$ is defined to be the anisotropy of the shielding tensor, $\eta = \sigma_{11} - \sigma_{22}$ the asymmetry, and $\sigma_{iso} = 1/3\ \mathrm{Tr}(\underset{\approx}{\sigma}) = 1/3(\sigma_{11} + \sigma_{22} + \sigma_{33})$ the isotropic shift. The angular dependence of anisotropic coupling terms is discussed below, Section ID.

3. Quadrupolar Coupling

While the Zeeman coupling comes from the interaction of the magnetic dipole of the nucleus with the external magnetic field, an additional coupling may exist between the nuclear quadrupole moment and electric field gradients from the surrounding electrons and nuclei. The

Hamiltonian for this interaction is

$$\mathcal{H}_Q = \frac{eQV_{zz}}{4I(2I-1)}\left[3I_z^2 - I(I+1) + \frac{1}{2}\eta_Q(I_+^2 + I_-^2)\right] \qquad \text{(I-19)}$$

where Q is the nuclear quadrupole moment, $\eta_Q = (V_{yy} - V_{xx})/V_{zz}$, $|V_{zz}| \geq |V_{yy}| \geq |V_{xx}|$ are the principle values of the electric field gradient tensor. In the presence of a large magnetic field ($\|\mathcal{H}_z\| >> \|\mathcal{H}_Q\|$, a criterion met for all experiments described herein), we keep only the secular part

$$\mathcal{H}_Q = \frac{eQ\ V_{zz}}{4I(2I-1)}\left[3I_z^2 - I(I+1)\right]. \qquad \text{(I-20)}$$

For a spin with I = 1/2, $\left\langle 3I_z^2 - I(I+1)\right\rangle = 0$, so the quadrupole interaction will only be observed for spins with $I \geq 1$. It is also worth noting that this Hamiltonian is bilinear in I, the full implications of which will be described in Chapter III. The transformation properties of the field gradient tensor are the same as for the shielding tensor. However, Laplace's equation requires that the field gradient tensor be traceless, that is $V_{xx} + V_{yy} + V_{zz} = 0$.

4. Dipolar Coupling

The energy of a spin is also effected by the local fields generated by its neighbors. Such effects may either be through space couplings, termed dipolar or direct couplings, or transmitted through bonds, termed spin-spin or J couplings. Since, in general, for the systems of interest here the former are many times larger than the latter, we will only treat dipolar couplings. These are of two types, between like spins or homonuclear, and between unlike spins or heteronuclear. For either

type of coupling the full coupling Hamiltonian may be written between spins I and S as

$$\mathcal{H}_D = \underset{\sim}{I} \cdot \underset{\approx}{D} \cdot \underset{\sim}{S} \tag{I-21}$$

where $D_{ij} = \frac{\gamma_I \gamma_S}{r_{IS}^3} (\delta_{ij} - 3e_i e_j) \qquad i,j = x, y, z, \quad \delta_{ij}$

is the Kronecker delta function, $e = (e_x, e_y, e_z)$ is a unit vector from spin I to spin S, and r_{IS} is the distance between them. From the definition it is clear that this coupling tensor is symmetric and traceless. As in the case of the quadrupolar Hamiltonian we keep only the secular part of $\mathcal{H}_D$ in the presence of the Zeeman coupling. If the coupling is homonuclear and the I-S internuclear vector is along the field direction

$$\mathcal{H}_D = \frac{-\gamma_I^2}{r_{IS}^3} (3I_z S_z - I \cdot S). \tag{I-22}$$

However, if the dipolar coupling is heteronuclear the last term becomes nonsecular so

$$\mathcal{H}_D = - \frac{\gamma_I \gamma_S}{r_{IS}^3} 2I_z S_z. \tag{I-23}$$

If many spins are present the dipolar Hamiltonian is simply a sum of terms, as in (I-22) or (I-23), over all pairs of spins.

D. Rotations

We have described the Hamiltonians above in a single axis system, with H_o along the z axis. To relate the laboratory frame and the principle axis frames and parameters of each coupling, then we must also

describe the orientation dependence of each coupling tensor. Fortunately this dependence may be described for a general tensor, then applied to each case as needed.

1. Cartesian Basis

The tensors above have been described in Cartesian form. These may be transformed from one frame of reference to another through application of an Euler transformation matrix. The orientation of the new frame with respect to a previous one is defined by a set of Euler angles $\Omega = \alpha, \beta, \gamma$ (using the convention of Rose[4]). Such a transformation is described by a rotation of α about the z axis to give x',y',z', directions followed by a rotation of β about the y' axis to give x", y", z" directions, then finally a rotation of γ about z" to give the final frame z''' , y''', z''' (Figure 1). Mathematically this may be described by a transformation matrix $\underset{\approx}{R}$ applied to the coupling tensor to give the coupling in the new frame,

$$\underset{\approx}{A}^{R} = \underset{\approx}{R}^{+} \underset{\approx}{A} \underset{\approx}{R} \qquad \text{(I-24)}$$

where

$$\underset{\approx}{R} = \begin{pmatrix} \cos\alpha \cos\beta \cos\gamma - \sin\alpha \sin\gamma & \sin\alpha \cos\beta \cos\gamma + \cos\alpha \sin\gamma & -\sin\beta \cos\gamma \\ -\cos\alpha \cos\beta \sin\gamma - \sin\alpha \cos\gamma & -\sin\alpha \cos\beta \sin\gamma + \cos\alpha \cos\gamma & \sin\beta \sin\gamma \\ \cos\alpha \sin\beta & \sin\alpha \sin\beta & \cos\beta \end{pmatrix} \qquad \text{(I-25)}$$

This form is also useful for describing motion about one axis. The average tensor may be calculated by averaging, with an appropriate weighting function, over one of the transformation coordinates. The process

may be repeated to transform to yet another frame, however for two transformations the spherical tensor form below is often more convenient. The most common transformation is from a principle axis frame to the lab frame, explicit examples of which are given in (3) below.

2. Spherical Basis

The orientation dependence of the Hamiltonian may also be described through use of spherical tensors. Spherical tensors are formed for the coupling tensor, A_{μ}^{ℓ}, and for the vector components, $T_m^{(\ell)}$ (see Appendix A for details). These spherical tensors are linear combinations of the Cartesian components which transform as representations of the rotation group. The coordinate transformation Ω is generated by summation of A tensor elements with elements of the Wigner rotation matrix $D(\Omega)$

$$A_m^{R(\ell)} = \sum_{\mu} D_{\mu m}^{(\ell)}(\Omega)\, A_{\mu}^{(\ell)} . \tag{I-26}$$

The full Hamiltonian is then written as a contraction of the A and T tensors

$$\mathcal{H} = \sum_{\ell=0}^{2} \sum_{m=-\ell}^{\ell} (-1)^m \sum_{\mu} D_{\mu m}^{(\ell)}(\Omega)\, A_{\mu}^{(\ell)}\, T_{-m}^{(\ell)} \quad . \tag{I-27}$$

A second transformation Ω' is generated simply by repeating the procedure of (I-26)

$$A_m^{R'(\ell)} = \sum_{m'} D_{m'm}^{(\ell)}(\Omega') A_{m'}^{R(\ell)} = \sum_{m'} \sum_{\mu} D_{m'm}^{(\ell)}(\Omega')\; D_{\mu m'}^{(\ell)}(\Omega) A_{\mu}^{(\ell)} . \tag{I-28}$$

Again the effect of motion may be introduced as an average over one of the transformation coordinates.

3. Orientation Dependent Tensors

We now apply these transformation operations to the tensor couplings described in C above. In each case we transfer the coupling Hamiltonian from its principle axis system to the lab frame defined by the magnetic field direction. The transformations will be given by sets of Euler angles (α, β, γ) subscripted to signify that in general this transformation is different for each coupling. The chemical shielding may thus be written as either

$$\mathcal{H}_{cs} = (\cos^2\alpha_{cs}\sin^2\beta_{cs}\sigma_{11} + \sin^2\alpha_{cs}\sin^2\beta_{cs}\sigma_{22} + \cos^2\beta_{cs}\sigma_{33})\gamma_I H_0 I_z \qquad \text{(I-29)}$$

or in terms of spherical components

$$\mathcal{H}_{cs} = \left\{\frac{1}{3}\sigma_{iso} + \frac{2}{3}\Delta\sigma P_2(\cos\beta_{cs}) + \frac{\eta}{2}\sin^2\beta_{cs}\cos 2\alpha_{cs}\right\}\gamma_I H_0 I_z . \qquad \text{(I-30)}$$

The quadrupole coupling may be written in an exactly analogous fashion, remembering that the tensor is traceless

$$\mathcal{H}_Q = \frac{1}{4}\omega_Q \left\{P_2(\cos\beta_Q) + \eta_Q \sin^2\beta_Q \cos 2\alpha_Q\right\}\left(3I_z^2 - I(I+1)\right) \qquad \text{(I-31)}$$

where $\omega_Q = \dfrac{3e^2qQ}{\hbar 2I(2I-1)}$ $\quad eq = V_{zz}$ $\quad \eta_Q = \dfrac{V_{xx} - V_{yy}}{V_{zz}}$.

The dipolar coupling is also traceless and must be axially symmetric ($\eta = 0$) and may then be written as

$$\mathcal{H}_D = + \frac{\gamma_I \gamma_S \hbar}{r^3} P_2\left(\cos\beta_D\right)\left(I_z S_z - \delta_{IS} \frac{1}{4}(I_+ S_- + I_- S_+)\right) \qquad \text{(I-32)}$$

where $\delta_{IS} = 1$ for homonuclear couplings and $\delta_{IS} = 0$ for heteronuclear couplings.

The angular dependence described in this section is also useful to describe the behavior of the spectrum of a single crystal as it is rotated in a magnetic field.

II. EFFECTS OF MOTION

A. Introduction

In the last chapter we have seen that many of the couplings which determine the NMR spectrum of a solid are anisotropic. Motion of the spins may then cause averaging of various parts of the Hamiltonian, inducing a change in the observed spectrum. Averaging of dipole-dipole couplings, observed as a narrowing of the resonance line, has been used extensively since the early days of NMR to detect motion in a wide variety of solids,[5,6] most containing either protons or fluorine. Several reviews have been written describing such work.[7,8,9] Since many coupled spins are present, the resonance line consists of one broad line with little, if any, structure. Characterization of the motion is achieved through calculation of the linewidth or second moment to be compared with experiment. Although useful information may be obtained in this way, the characterization of the motion is not unique, and requires a knowledge of the crystal structure for calculation of the second moment and linewidth. In addition, while sensitive to the presence of motion, this approach cannot provide any information about the microscopic dynamics of the motion. Linewidth studies are often supplemented with studies of relaxation times T_1, $T_{1\rho}$, and T_{1D}. These relaxation times are more sensitive to the dynamics of the motion than to the geometry and hence are very useful for measurements of correlation times and activation energies. However, again determination of the nature of the motion is achieved through model calculations where often more than one model

is consistent with experimental data. In this chapter we present examples of a new high resolution approach to the study of molecular motion in solids, which gives more information than was previously obtainable with any technique. By studying the details of the chemical shielding lineshape as a function of temperature we obtain information about both the symmetry and dynamics of the motion. Several examples are presented in later sections.

B. Decoupling: Approach to High Resolution

To use the chemical shielding tensor for studies of dynamics we must be able to remove any other couplings which could degrade resolution. By observing only spin 1/2 nuclei we assure that quadrupole couplings do not interfere. Dipolar couplings are removed through use of dilute spin NMR as pioneered by Pines, Gibby and Waugh.[13] We will observe a spin species which occurs at very low concentrations in the sample. In this case the average distance between observed spins is large whence from Eq. I-22 we see that the homonuclear dipolar coupling becomes very small. The spins to be observed may be naturally dilute (as 1.1% ^{13}C in ^{12}C) or may be intentionally diluted in another isotope (1% ^{1}H in ^{2}H). While dilution eliminates homonuclear couplings, heteronuclear dipolar coupling to an abundant spin species (^{1}H or ^{2}H) may still be present. By strongly irradiating these spins near their Larmor frequency the broadening from the heteronuclear couplings may be removed. Such "dipolar coupling" is well known for spin 1/2 nuclei.[11,12,13] The accepted criterion for achieving decoupling is that the strength of the rf field,

in frequency units γH_1, be greater than the width of the abundant spin line or undecoupled dilute spin line, whichever is larger. If the abundant spins have $I=1$, their resonance line may be severely broadened by quadrupole coupling to a width $\sim\omega_Q$, apparently requiring that $\gamma H_1 >> \omega_Q$. Since ω_Q is generally quite large (~ 100 kHz for ^2H) this is very difficult to achieve experimentally. However Meiboom and co-workers[14] realized that in such a quadrupolar system rapid double quantum transitions between the $m = \pm 1$ levels could also provide decoupling since the $m = 0$ level does not affect the observed spins. Although their work was in a liquid crystal system, the technique has been extended to general solids by Pines, Vega and Mehring.[15,16] To compare the criteria for decoupling through single and double quantum transitions we will apply coherent averaging theory[3,15,16] to each, treating the dipolar part of the Hamiltonian as a perturbation.

1. Single Quantum

For coupled spin 1/2 nuclei, the rotating frame Hamiltonian is (S spins observed, I spins decoupled, $I_p = \sum_j I_{jp}; P = x,y,z$).

$$\mathcal{H} = -\Delta\omega I_z - \omega_1 I_x + \mathcal{H}_{IS} \qquad \text{(II-1)}$$

where $\mathcal{H}_{IS}$ is the appropriately tuncated dipolar Hamiltonian

$$\mathcal{H}_{IS} = \sum_j b_j S_z I_{jz} \qquad \text{compare (I - 32)} \qquad \text{(II-2)}$$

and couplings among I spins have been ignored.

To calculate the effect of the first two terms of (II-1) on the third, which is responsible for broadening the S spin resonance, we first tilt the Hamiltonian to be along the effective field direction defined by the combination of I_x and I_z terms. This is done with a tilt operator along the y direction.

$$T_y = e^{i\theta I_y} \tag{II-3}$$

where θ is the angle between the z axis and the direction of the effective field

$$\theta = \tan^{-1} \frac{\omega_1}{\Delta\omega} \qquad \omega_e = \sqrt{\omega_1^2 + \Delta\omega^2}. \tag{II-4}$$

In this frame the Hamiltonian becomes

$$\mathcal{H}^T = -\omega_e I_z + \sum_j b_j S_z (\cos\theta\ I_{jz} + \sin\theta\ I_{jx}). \tag{II-5}$$

The first term then induces a cyclic and periodic time dependence in the second.

$$\mathcal{H}^T_{IS}\ (t) = e^{-i\omega_e I_z t}\ \mathcal{H}^T_{IS}\ e^{+i\omega_e I_z t} \tag{II-6}$$

$$= \sum_j b_j S_z I_{jz}\ \cos\theta + \sum_J b_j S_z\ \sin\theta(\cos\omega_e t\ I_{jx} + \sin\omega_e t\ I_{jy}).$$

To calculate the effect of this over one cycle of time $t_c = \frac{2\pi}{\omega_e}$ we use the average Hamiltonians defined by Waugh[16] (keeping only enough terms to guarantee one nonzero term):

$$\bar{\mathcal{H}} = t_c^{-1} \int_0^{t_c} \tilde{\mathcal{H}}(t)\, dt$$

$$\bar{\mathcal{H}}^{(1)} = (2it_c)^{-1} \int_0^{t_c} dt_2 \int_0^{t_1} dt_1 \left[\tilde{\mathcal{H}}(t_2), \tilde{\mathcal{H}}(t_1)\right] \tag{II-7}$$

$$\bar{\mathcal{H}}^{(2)} = (6t_c)^{-1} \int_0^{t_c} dt_3 \int_0^{t_3} dt_2 \int_0^{t_2} dt_1 \Big([\tilde{\mathcal{H}}(t_3), [\tilde{\mathcal{H}}(t_2), \tilde{\mathcal{H}}(t_1)]] + [[\tilde{\mathcal{H}}(t_3), \tilde{\mathcal{H}}(t_2)], \tilde{\mathcal{H}}(t_1)] \Big).$$

For the case at hand $\tilde{\mathcal{H}}(t) = \mathcal{H}_{IS}^{T}(t)$ giving

$$\bar{\mathcal{H}} = \sum_j b_j \cos\theta \; S_z I_{jz} \tag{II-8}$$

$$\bar{\mathcal{H}}^{(1)} = \sum_j \frac{b_j^2}{\omega_e} \sin\theta \; S_z^2 (\cos\theta I_{jx} - \frac{1}{2} \sin\theta \; I_{jz}) \tag{II-9}$$

$$\bar{\mathcal{H}}^{(2)} = \sum_j \frac{b_j^3}{\omega_e^2} \; S_z^3 (P_2(\cos\theta) I_{jx} - \sin\theta \cos\theta \; I_{jz}). \tag{II-10}$$

The S spin free induction decay is given by

$$G(t) = \mathrm{Tr}\, (S_x e^{-i\mathcal{H}_s t} S_x e^{+i\mathcal{H}_s t}). \tag{II-11}$$

Therefore only terms which do <u>not</u> commute with S_x must be considered. Since $[S_z^2, S_x] = 0$ the $\bar{\mathcal{H}}^{(1)}$ term will have no effect on the S spin resonance. Decoupling is achieved as the remaining terms, $\bar{\mathcal{H}}$ and $\bar{\mathcal{H}}^{(2)}$, become small. For the leading term this means $\cos\theta \sim 0$, and for a fixed value of $\Delta\omega$ that $\omega_1 >> \Delta\omega$. If the I spins are irradiated on resonance ($\Delta\omega = 0, \theta = 90°$) $\bar{\mathcal{H}}^{(2)}$ is the leading nonzero term. This becomes small for $\omega_e = \omega_1 >> D$, where D characterizes the average dipolar coupling and may be written as the square

root of the second moment of the operator part of (II-10),[15]

$$D^3 = \frac{1}{2}\left\{\frac{\mathrm{Tr}\,[\,S_z^3 \sum_j b_j^3 I_{jx}, S_x]^2}{\mathrm{Tr}\; S_x^2}\right\}^{1/2} . \qquad \text{(II-12)}$$

Thus, the rough criterion that rf strength be greater than the width of the line to induce decoupling is valid. However we will now show that for double quantum decoupling a less stringent condition must be met.

2. Double Quantum

To describe decoupling in a spin system of quadrupole coupled nuclei we will use the fictitious spin 1/2 operators of Vega and Pines.[18,19] These operators are very useful for description of spin 1 systems and further use of them will be made in Chapter III to describe coherent effects, and many more details are presented there. Nine fictitious spin operators $I_{p\ell}$ are defined in terms of the spin angular momentum operators I_p as:

$$I_{p1} = \frac{1}{2} I_p$$

$$I_{p2} = \frac{1}{2} (I_q I_r + I_r I_q) \qquad \text{(II-13)}$$

$$I_{p3} = -\frac{1}{2} (I_q^2 - I_r^2) \qquad p,q,r = x,y,z \text{ or cyclic permutation.}$$

with commutation relations:

$$[\,I_{pj}, I_{pk}] = i\, I_{p\ell} \qquad j,k,\ell = 1,2,3 \text{ or cyclic permutation.} \qquad \text{(II-14)}$$

Each set of three operators with given p form a spin - 1/2 subspace which, under certain conditions, may evolve independently of the other subspaces. I_{z1}, I_{z2} and I_{z3} have matrix elements only between the ±1 levels and will be used to describe double quantum effects. The I spin Hamiltonian is, in the rotating frame,

$$\mathcal{H} = -\Delta\omega I_z - \omega_1 I_x + \frac{1}{3}\omega_Q(3I_z^2 - I(I+1)) + \mathcal{H}_{IS}. \qquad \text{(II-15)}$$

This may be rewritten in terms of the fictitious spin operators as:

$$\mathcal{H} = -2\Delta\omega I_{z1} - 2\omega_1 I_{x1} + \frac{2}{3}\omega_Q(I_{x3} - I_{y3}) + \mathcal{H}_{IS} \qquad \text{(II-16)}$$

and again ignoring couplings among I spins

$$\mathcal{H}_{IS} = \sum_j 2b_j\, S_z I_{jz1}. \qquad \text{(II-17)}$$

We now tilt to a new frame in a fashion analogous to (II-3) with the tilt operator

$$T_{x2} = e^{i\phi I_{x2}} \qquad \text{(II-18)}$$

where

$$\phi = \tan^{-1}\frac{2\omega_1}{\omega_Q}. \qquad \text{(II-19)}$$

When $\omega_1 << \omega_Q$, $\phi \sim 0$ and the tilted Hamiltonian may be written:[19]

$$\mathcal{H} = -2\Delta\omega I_{z1} - \frac{\omega_1^2}{\omega_Q} I_{z3} + \frac{2}{3}\omega_Q(I_{x3} - I_{y3}) + \mathcal{H}_{IS}. \qquad \text{(II-20)}$$

Since $I_{x3} - I_{y3}$ commutes with all other terms of the Hamiltonian, it may be ignored. Then the effective part of the Hamiltonian is

$$\mathcal{H} = -2\Delta\omega\, I_{z1} - \frac{\omega_1^2}{\omega_Q} I_{z3} + \mathcal{H}_{IS}. \tag{II-21}$$

At this point the Hamiltonian is exactly analogous to the single quantum Hamiltonian of (II-1), now with all operators in the z, or double quantum fictitious space. We then proceed in exactly the same manner as above. First we tilt so that the z,1 axis is along the effective field direction defined by the combination of terms I_{z1} and I_{z3}, which is accomplished by a tilt with I_{z2}

$$T_{z2} = e^{i\theta I_{z2}} \tag{II-22}$$

with

$$\theta = \tan^{-1}\left(\frac{\omega_1^2}{2\omega_Q\Delta\omega}\right). \tag{II-23}$$

In analogy to (II-5) this gives

$$\mathcal{H}^T = -\omega_e I_{z1} + \sum_j b_j S_z(\cos\theta I_{jz1} + \sin\theta I_{jz3}) \tag{II-24}$$

where

$$\omega_e = \sqrt{\left(2\Delta\omega\right)^2 + \left(\frac{\omega_1^2}{\omega_Q}\right)^2} \tag{II-25}$$

Following (II-6) and (II-7) above we obtain for the average Hamiltonians

$$\bar{\mathcal{H}} = \sum_j b_j \; 2\cos\theta \; S_z I_{jz1} \tag{II-26}$$

$$\bar{\mathcal{H}}^{(1)} = \sum_j \frac{b_j^2}{\omega_e} 4\sin\theta \; S_z^2 (\cos\theta I_{jz3} - \frac{1}{2} \sin\theta I_{jz1}) \tag{II-27}$$

$$\bar{\mathcal{H}}^{(2)} = \sum_j \frac{b_j^3}{\omega_e^2} 8\sin\theta \; S_z^3 (P_2(\cos\theta) I_{jz3} - \sin\theta \cos\theta \, I_{jz1}). \tag{II-28}$$

Again $\bar{\mathcal{H}}^{(1)}$ is ineffective so we want to make $\bar{\mathcal{H}}$ and $\bar{\mathcal{H}}^{(2)}$ small. Then $\cos\theta \sim 0$ requires that for fixed $\Delta\omega$ we have $\omega_1^2 >> 2\Delta\omega\omega_Q$. If the spins are irradiated on resonance ($\Delta\omega = 0, \theta = 90°$) then the leading term is $\bar{\mathcal{H}}^{(2)}$. As for single quantum we then require that $\omega_e >> D$, in this case giving

$$\frac{\omega_1^2}{\omega_Q} >> D \quad \text{or} \quad \omega_1 >> \sqrt{\omega_Q D} \tag{II-29}$$

where D is defined in direct analogy to (II-12). In many cases this criterion is much less severe than the $\omega_1 >> \omega_Q = \Delta\omega$ which would apply for single quantum decoupling. In deuterium-proton systems where ν_Q = 100 kHz and D = 5 kHz are reasonable couplings, the requirement ν_1 >>22kHz can easily be met where ν_1>>100 kHz cannot. However for double quantum decoupling, the adjustment of decoupling frequency is much more critical since it enters as a product with ω_Q, which may be very large. In the above analysis we have left out the effect of couplings among the I spins. For deuterium, and most other quadrupolar nuclei, the homonuclear dipolar couplings are much smaller than the

quadrupole couplings and hence may be ignored without serious effect. For decoupling spin 1/2 nuclei with large gyromagnetic ratios (^{1}H, ^{19}F, ^{31}P) the homonuclear couplings may be larger than the heteronuclear couplings. In this case, of course, the I-I couplings must not be ignored. If the spins to be decoupled occur as strongly coupled groups of n spins, weakly coupled to other spins, their behavior may be similar to a single spin n/2 nucleus, and multiple quantum effects may again become important. Such effects will be discussed further in Chapter IV. As n becomes large the requirement for achieving decoupling is once again that the decoupling field in frequency units be larger than the width of both the I and S spin resonances. In the work presented here double quantum effects are very important in decoupling ^{2}H from ^{1}H, but probably less important in decoupling ^{1}H from ^{13}C. From these arguments we may conclude that decoupling is feasible both for spin 1/2 and spin 1 nuclei to give high resolution chemical shielding powder patterns.

C. Sensitivity Considerations

While dilution is necessary to reduce homonuclear dipolar couplings, it also substantially reduces sensitivity. This loss may be at least partially offset through use of signal averaging and cross polarization enhancement techniques. All experiments described here have been done using pulse-Fourier Transform methods.[20] Through use of high speed computers, many transient responses may be digitized and averaged to improve signal-to-noise ratio before Fourier Transformation to give the spectrum. A description of the spectrometer and experimental setup is presented in Chapter V. While in theory, some of the experiments

(those in Chap. II) described here could be done with conventional CW methods, the high decoupling power usually required makes this approach practically unfeasible. In addition, the techniques of Chapter III and Chapter IV depend on nonlinear responses of the system, and require coherence transfer methods for detection requiring that they be done with the pulsed approach. For experiments where ^{13}C was observed, Proton Enhanced Nuclear Induction Spectroscopy[13] (PENIS) was used. This technique has been described in detail elsewhere,[21,13] hence we will present only the aspects important to the present experiments. Polarization is transferred from the abundant spins (^{1}H) to the dilute spins (^{13}C) by matching Zeeman energy of the two spin systems in the rotating frame.[22] Fluctuations in the dipolar couplings of the abundant spins from the flip-flop part of the dipolar Hamiltonian (second part of (I-32)) cause exchange of energy between the two spin systems. If the abundant spin species was prepared at very low temperature in the rotating frame, as by spin locking, then the dilute spin system will be cooled, yielding a large polarization. Thermodynamic considerations show that for ^{13}C we expect the maximum polarization attainable in this manner to be four times the polarization attained by equilibration in the static magnetic field.[13] When contact is made between the two spin system, it takes some time to reach equilibrium. In many cases the approach to equilibrium may be approximated by an exponential growth of carbon magnetization, with a time constant T_{IS}. Transient oscillations have been noted during cross polarization,[23,24] (and in fact exploited[25]), but are not important for the present analysis. In addition to transfer of magnetization to carbon, the proton system is heated through spin lattice

processes with a time constant $T_{1\rho}$. If $T_{1\rho}$ is the same order as T_{IS} or shorter then the carbon magnetization will never reach its equilibrium value. The magnetization as a function of cross polarization time can be calculated,[2] and is shown in Figure 2. It is clear that for given values of T_{IS} and $T_{1\rho}$ there exists an optimum cross polarization time for maximizing signal to noise. In many rigid solids $T_{1\rho}$ is very long and any cross polarization time longer than T_{IS} will give good results. However, when motion of the spins is present, as for cases of interest here, $T_{1\rho}$ may be very short and the cross polarization time must be adjusted accordingly. Optimum parameters are described in Appendix B. When $T_{1\rho}$ becomes very short the maximum polarization obtainable for ^{13}C becomes smaller, eventually dropping below the equilibrium Zeeman value. Even at this point, however, there may be an advantage of cross polarization over free induction decay experiments. This advantage stems from the fact that the spin lattice relaxation time, T_1, for carbon is generally much longer than for protons. In a free induction decay experiment one must wait a time of the order $T_1(^{13}C)$ before repeating the experiment, while for cross polarization the optimum waiting period is 1.26 $T_1(^1H)$ (see Appendix C). The pulse sequences used for both cross polarization and free induction decay experiments are shown in Figure 3. Through use of signal averaging, and where applicable cross polarization, very good signal to noise may be obtained for even very broad powder spectra. As we will see, good signal to noise is necessary for the lineshape analysis to be performed.

D. Limiting Cases for Powder Lineshapes

1. Rigid

While it is often useful to study samples which are single crystals, making possible systematic variation of the relative orientations of molecular and laboratory axis systems, it is often desirable and sometimes necessary to work on powdered samples. A powder sample will be taken to mean a collection of crystallites of some material prepared such that there is a uniform distribution of crystal axis orientations relative to the laboratory axes. Unlike a glass, which is disordered on a molecular scale, the samples are locally crystalline, with well defined crystal structure. The lineshape for a tensor coupling in a powder sample (we will consider chemical shielding) was derived by Bloembergen and Rowland.[26] For rigid solids the basic lineshape for these couplings depends on the symmetry at the nucleus. If the symmetry is sufficiently high, tetrahedral or octahedral, then a tensor description is really not necessary. The position of the resonance line will have no angular dependence, and may be characterized simply by an isotropic chemical shift σ_i. The line shape for a powder of such molecules will consists of a single sharp line at σ_i. An excellent example of this is the ^{13}C spectrum of a sample of powdered diamonds obtained by Van der Hart.[27] The carbons are located on sites of tetrahedral symmetry and the spectrum is a single sharp line. If the site of the spin has C_n symmetry, where $n \geqslant 3$, then the chemical shift must be equal everywhere in the plane perpendicular to the C_n axis. This is termed axially symmetric with angular dependence (from (I-29)):

$$\sigma_{zz} = \sin^2\beta\ \sigma_\perp + \cos^2\beta\ \sigma_\parallel \qquad \text{(II-30)}$$

where $\sigma_\perp$ and $\sigma_\parallel$ are respectively the chemical shifts perpendicular to and along the C_n axis, and β is the angle between the C_n axis and the applied field, or laboratory z axis. To describe the lineshape for a powder of such molecules, single spin spectra must be added for all possible orientations, with appropriate weights. More formally, for an orientation Ω with spectrum $I(\omega,\Omega)$ a powder gives

$$I(\omega) = \int_\Omega I(\omega,\Omega)\ d\Omega\ . \qquad \text{(II-31)}$$

For an axial shielding tensor this gives

$$\begin{aligned} I(\omega) &\sim (\sigma_\perp - \omega)^{-1/2} \qquad \text{for} \qquad \sigma_\perp \geqslant \omega \geqslant \sigma_\parallel \\ &\sim (\omega - \sigma_\perp)^{-1/2} \qquad \text{for} \qquad \sigma_\parallel \geqslant \omega \geqslant \sigma_\perp\ . \end{aligned} \qquad \text{(II-32)}$$

An example of this type of lineshape is given in Figure 4a, showing the characteristic sharp spike on one side of the spectrum. For a spin in a site with lower symmetry than discussed above, the full angular dependence from (I-29) must be used. The resulting lineshape[26] is

$$\begin{aligned} I(\omega) &\sim \sqrt{\frac{\sigma_{33}-\sigma_{11}}{\omega-\sigma_{11}}} \int_0^{\pi/2} \left\{ 1 - \frac{(\sigma_{22}-\sigma_{11})}{(\sigma_{33}-\sigma_{22})} \frac{(\sigma_{33}-\omega)}{(\omega-\sigma_{11})} \sin^2\gamma \right\}^{-1/2} d\gamma \quad (\sigma_{22} < \omega < \sigma_{33}) \\ I(\omega) &\sim \sqrt{\frac{(\sigma_{33}-\sigma_{11})}{(\sigma_{33}-\omega)} \frac{(\sigma_{33}-\sigma_{22})}{(\sigma_{22}-\sigma_{11})}} \int_0^{\pi/2} \left\{ 1 - \frac{(\omega-\sigma_{11})}{(\sigma_{33}-\omega)} \frac{(\sigma_{33}-\sigma_{22})}{(\sigma_{22}-\sigma_{11})} \sin^2\gamma \right\}^{-1/2} d\gamma \quad (\sigma_{11} < \omega < \sigma_{22})\ . \end{aligned} \qquad \text{(II-33)}$$

These are complete elliptical integrals of the first kind, which are tabulated in Abramowitz and Steegun.[28] An example of this type of lineshape is given in Figure 4b, showing the characteristic sharp spike in central part of the line. It is worth noting that if $\sigma_{11} = \sigma_{22}$ or $\sigma_{22} = \sigma_{33}$ accidentally for a site of low symmetry, an axial tensor as described above will be obtained. In real spectra the lineshapes described above are broadened by residual dipolar couplings, relaxation etc., so that the discontinuities (spikes) are made finite. Even with broadening, however, the relatively sharp edges at $\sigma_{\perp}$ and $\sigma_{\parallel}$ or σ_{11}, σ_{22} and σ_{33} make possible quite accurate determinations of the principle valves of the shielding tensor directly from the powder spectrum. If several chemically different sites are present, the resulting lineshape is simply a sum of the powder patterns described above. In some cases it is possible to determine principle valves of four or five partially overlapping tensors from a single powder spectrum.[30]

2. Rapid Motion

When rapid (the definition of this will be made precise shortly) molecular motions occur, the shielding tensors are averaged to give new tensors, for which site symmetry is replaced by the symmetry of the motion. The extreme limit of this is a liquid where both rotational and translational motions are rapid and isotropic, and only the trace of the shielding tensor may be observed. In plastic crystals molecules also undergo isotropic reorientation, though translational motion is quite restricted. The tumbling motion alone is enough to average the tensor so that only the trace may be observed. An illustrative spectrum for a

molecule in a plastic phase is shown in Figure 5. Many other molecules undergo a more restricted motion in the solid state. Particularly common are molecules which reorient about one axis. If a free rotation occurs about this axis the resulting shielding tensor will be axially symmetric, with the unique direction along the rotation axis. The resulting tensor may be calculated from (I-24), by taking the new z axis along the rotation axis and averaging over the third Euler angle, γ. We thus obtain

$$\sigma_{11}^{R} = \sigma_{22}^{R} = \frac{1}{2}(\cos^2\alpha\cos^2\beta+\sin^2\alpha)\sigma_{11}+\frac{1}{2}(\sin^2\alpha\cos^2\beta+\cos^2\alpha)\sigma_{22}+\frac{1}{2}\sin^2\beta\sigma_{33}$$

$$\sigma_{33}^{R} = \cos^2\alpha\,\sin^2\beta\,\sigma_{11}+\sin^2\alpha\sin\beta\,\sigma_{22}+\cos^2\beta\,\sigma_{33} \qquad \text{(II-34)}$$

showing the expected axial symmetry (Figure 6). If two rotational motions are present, both rapid but one much more than the other, the spectrum may be obtained by sequential application of this single axis calculation, first taking the static tensor to the fastest motion axis system, then transforming to the second motion frame, giving the observed tensor. Such an approach has been used to interpret phosphorous shielding tensors in phospholipid bilayers.[31]

E. Slow Motions

While study of shielding tensors in the static and rapid motion limits can provide information about the motion occurring, it has recently been shown theoretically[32,33,34] and experimentally[33,35] that much more information may be obtained through detailed studies of the powder lineshape in the slow motion regime. Often it is possible (when phase

transitions do not interfere) to vary the motion from static to rapid continuously, by variation of sample temperature.

To relate physically interesting parameters to the experimental lineshapes, models for the motion must be developed. In the present work two models are considered and the lineshapes generated with their assumptions are used to extract meaningful information through comparison with experiment.

1. Random Rotations

We first consider two models which are very similar, rotational Brownian motion and rotational random jumps. Rotational Brownian motion may be described as a random walk through angle, characterized average angle and frequency of jumps. Two cases are of interest, rotational diffusion (Brownian motion) about a fixed axis and general isotropic rotational diffusion. The choice between these for a particular system depends on geometrical constraints from crystal structure and may be determined from the lineshape in the rapid motion (high temperature) limit. Whether rotations occur about a fixed axis or a random axis, we may specify the average time τ_R between jumps. This rotational diffusion is in principle identical to translational Brownian motion, both are stationary Markov processes. This motion contributes to the evolution of the density matrix (from which the lineshape may be calculated) in a simple way:[32]

$$\frac{d\rho(\overline{\Omega})}{dt} = -i\,[\mathcal{H}, \rho(\overline{\Omega})] + \Gamma_{\overline{\Omega}}\,\rho(\overline{\Omega})$$

where (II-35)

$$\Gamma_{\overline{\Omega}} = \frac{1}{\tau_R}\,\nabla^2_{\overline{\Omega}}$$

is the contribution from rotational diffusion and $\overline{\Omega}$ describes the orientation of the molecular axis system. In the high temperature approximation, ignoring saturation, and assuming steady state, (II-35) may be Fourier Transformed to give ($\hat{A}B \equiv [A,B]$)

$$[\omega + \hat{\mathcal{H}}_0 + \hat{\mathcal{H}}_{cs}(\overline{\Omega}) + i\,\Gamma_{\overline{\Omega}}]\,\rho(\overline{\Omega}) = -\,CI_- \qquad \text{(II-36)}$$

where ω is the observation frequency, $\mathcal{H}_0$ is the Zeeman Hamiltonian (I-10) and $\mathcal{H}_{cs}$ is the orientation dependent chemical shift (I-30). The solution of this equation for ρ, as a function of ω may be used to calculate the spectrum

$$I_{\overline{\Omega}}(\omega) = \mathrm{Tr}\,(S_+\,\rho(\overline{\Omega})). \qquad \text{(II-37)}$$

A model of this type, in which all orientations of a molecule are equally probable seems most reasonable in a material lacking local structure, such as a glass, or on a surface.

The rotational random jumps model is in principle very similar to rotational diffusion, but jumps occur through random angles, with all angles equally probable, as an activated process, with a rate constant χ. This model yields lineshapes very much like those for rotational diffusion[32a] and will not be discussed further. This model is sometimes referred to as "hard collision" and is similar to the model used for

some of our calculations, Section II-F.

2. Symmetry Related Jumps

In a crystalline material we expect only a few allowed molecular orientations. Motions which occur might then be restricted to jumps which correspond to symmetry operations for the molecule. We may specify the basic molecular orientation by a set of angles $\overline{\Omega}$. For such an orientation a spin may experience different chemical shifts in each of n symmetry related positions with the same $\overline{\Omega}$. We then distinguish among the symmetry related orientations by a further set of angles, Ω_i ($i = 1,2,\ldots,n$). The spin essentially occupies different sites in the molecule and henceforth we use the term sites to refer to the various symmetry related orientations. The exchange due to jumping is then specified by the rate constants W_{ij} for a spin jumping from site i to site j. The contribution of this motion to the evolution of the density matrix may be calculated with operator Λ_i, defined by

$$\Lambda_i \rho_i(\Omega_i,\overline{\Omega}) = \sum_j W_{ij} \, [\rho(\Omega_j,\overline{\Omega}) - \rho(\Omega_i,\overline{\Omega})] \, , \qquad \text{(II-38)}$$

in a fashion similar to rotational diffusion [32]

$$\frac{\partial \rho(\Omega_i,\overline{\Omega})}{\partial t} = -i \, [\mathcal{H}, \, \rho(\Omega_i,\overline{\Omega})] + \Lambda_i \, \rho(\Omega_i,\overline{\Omega}) . \qquad \text{(II-39)}$$

In fact both rotational diffusion and jumping may simultaneously occur and the effects may be added to give

$$\frac{dp}{dt} \, (\Omega_i,\overline{\Omega}) = -i \, [\mathcal{H},\rho(\Omega_i,\overline{\Omega})] + \Gamma_{\overline{\Omega}} \, \rho(\Omega_i,\overline{\Omega}) + \Lambda_i \, \rho(\Omega_i,\overline{\Omega}) . \qquad \text{(II-40)}$$

In some cases inclusion of both terms is necessary, however for cases of interest here each model will be considered separately.

Now we wish to find the steady state solution to this set of coupled equations (II-39). In the high temperature approximation ignoring saturation effects, we set (II-40) equal to zero, then Fourier transform to give the frequency domain equation: $(\hat{A}B \equiv [A,B])$

$$[\omega + \hat{\mathcal{H}}_0 + \hat{\mathcal{H}}_{cs}\ (\Omega_i,\overline{\Omega}) + i\Lambda_i]\ \rho(\Omega_i,\overline{\Omega}) = -\ CI_- \ . \qquad \text{(II-41)}$$

We now define the magnetization for site i as

$$g_i = \mathrm{Tr}\ (I_+\ \rho(\Omega_i,\overline{\Omega})) = \mathrm{Tr}(I_+\ \rho_i) \qquad \text{(II-42)}$$

where for convenience we have dropped the parametric parameter $\overline{\Omega}$ and subscripted g and ρ to indicate site. We may then derive from (II-41) by taking a trace with I_+, and using (II-38):

$$i(\omega-\omega_i)\ g_i + \sum_j (g_j - g_i)\ W_{ij} = iC_i \qquad \text{(II-43)}$$

where ω_i is the frequency at the ith site and C_i is a constant proportional to the population of the ith site. Since the exchange of magnetization among the different sites is achieved by molecular rotation, the W_{ij} must transform according to the local symmetry at the molecular level, specified by a point group G. Then each W_{ij} may be associated with a specific group element R_α which takes site i into site j. All W_{ij} which belong to symmetry operations in the same class must take on the same value, so we may replace the sum over sites in (II-43) by a sum over classes C of G:

$$\sum_j W_{ij}\ (g_j - g_i) = \sum_c W_c \sum_{\alpha\varepsilon c} (R_\alpha - 1)\ g_i . \qquad \text{(II-44)}$$

To use the symmetry to the fullest extent we now expand g_i in a complete set of basis functions of G:

$$g_i = \sum_{\lambda\mu} a^i_{\lambda\mu}\ g_{\lambda\mu} = \sum_\lambda g_{i\lambda} \qquad \text{(II-45)}$$

where λ labels the irreducible representation and μ indexes the row in a multidimensional representation of G. Group theory tells us that

$$\sum_{\alpha\varepsilon c} R_\alpha\ g_{\lambda\mu} = n_c \frac{\chi^\lambda_c}{\nu_\lambda}\ g_{\lambda\mu}\ , \qquad \text{(II-46)}$$

where n_c is the number of elements in class c, and χ^λ and ν_λ are the character and dimension of the λ representation. Combining (II-44, 45, 46) we find

$$\sum_{ij} W_{ij}\ (g_j - g_i) = -\sum_\lambda W_\lambda \sum_\mu a^i_{\lambda\mu}\ g_{\lambda\mu} = -\sum_\lambda W_\lambda\ g_{i\lambda} \qquad \text{(II-47)}$$

where we have defined the rate for the λ representation:

$$W_\lambda = \sum_c n_c W_c \left(1 - \frac{\chi^\lambda_c}{\nu_\lambda}\right). \qquad \text{(II-48)}$$

If we define $\alpha_i = i(\omega - \omega_i)$ then we may write (II-43) (using (II-47)) as:

$$\alpha_i\ g_i - \sum_\lambda W_\lambda\ g_{i\lambda} = i\ C_i . \qquad \text{(II-49)}$$

Our goal is to calculate the observable NMR spectrum, which is proportional to g_{A1}. Solving (II-49) for g_{A1} is complicated by the fact that the g_i are not in general diagonal in terms of the irreducible representations of G, requiring that we know which of the equations for magnetizations are coupled together. $\alpha_i g_i$ has a symmetry lower than G; in fact its important symmetry elements are the operations of G which leave the frequency of the ith site unchanged. These operations form a subgroup S of G. When we expand g_i in terms of irreducible representations λ of G we need only consider those λ which when taken as irreducible representations of S contain the totally symmetric S representation, since these alone have the correct symmetry to contribute to g_{A1}. Then in (II-45), (II-47) and (II-49) we need only include these "relevant" representations in the sums. Often the restriction to relevant representations simplifies considerably the calculation. If S contains just the identity then no simplification occurs. If, on the other hand, S = G, then the spectrum is totally invariant to the motion, and no parameters are needed (note $W_{A1} = 0$ always from (II-48)).

In the case that there is only one relevant representation, beyond A_1, (II-49) may be solved in a simple way. The expansion (II-45) may be written

$$g_i = g_{iA1} + g_{i\lambda}. \qquad \text{(II-50)}$$

We may then solve for $g_{i\lambda}$ and insert

$$\alpha_i g_i - W_\lambda (g_i - g_{iA1}) = i\, C_i \qquad \text{(II-51)}$$

or

$$g_i = \frac{iC_i - W_\lambda\, g_{iA1}}{\alpha_i - W_\lambda}. \qquad \text{(II-52)}$$

The g_i may be summed to give the total magnetization:

$$g(\omega) = \sum_i g_i = ng_{Al} = \sum_i \frac{iC_i - W_\lambda g_{Al}}{\alpha_i - W_\lambda}, \qquad \text{(II-53)}$$

which may be rearranged to give

$$g(\omega) = \frac{i \sum_i \frac{C_i}{\alpha_i + W_\lambda}}{1 - \frac{W_\lambda}{n} \sum_i \frac{1}{\alpha_i + W_\lambda}} . \qquad \text{(II-54)}$$

The absorption lineshape is just the real part of the complex magnetization $g(\omega) \alpha g_{Al}$, for the particular orientation $\overline{\Omega}$, and symmetry has considerably reduced the work that most be done. Even in the more complex cases where several representations must be considered, group theory has provided a simple way to count and classify the exchange rates which must be considered. This solution is compared with a direct matrix solution in Appendix C.

In the calculations above, the lineshapes were for a particular orientation $\overline{\Omega}$. However the experiments to be compared were performed on powder samples. Thus we must include one further step, the integration of single orientation lineshapes over all possible orientations with appropriate weighting factors:

$$I\ (\omega) = \int_{\overline{\Omega}} I_{\Omega}(\omega)\ d\overline{\Omega} \qquad \text{(II-55)}$$

to give the final powder lineshape.

We will see that lineshapes resulting from rotational diffusion are very different from the jumping model in the slow motion regime, thus allowing us to experimentally distinguish between the two models.

F. Computational Approach

Alexander, Baram and Luz[33] have calculated lineshapes for several cases of interests using (II-40), by expanding $\rho(\Omega_i,\bar{\Omega})$ in a complete set of angular functions. While they achieved considerable simplification when only one time parameter was necessary, their methods have no particular advantages in other cases. The approach we have used for calculation of model lineshapes is based on well known theories of chemical exchange, applied in a straightforward numerical approach. In the jumping model the orientations of the molecule are related by symmetry so the probability of the spin occupying any of the allowed sites must be equal. In matrix form the Bloch equations including chemical exchange (II-43) may be written:[1]

$$\underset{\approx}{A}\,\underset{\sim}{g} = -\,i\omega_1 M_0\,\underset{\sim}{1} \qquad \text{(II-56)}$$

where g_k is the complex magnetization for the $k^{\underline{th}}$ site, $\underset{\approx}{A}$ is the coupling matrix described further below, ω_1 is the r.f. field strength and M_0 the equilibrium magnetization. The diagonal elements of $\underset{\approx}{A}$ contain the information about the different sites:

$$A_{kk} = i\,(\omega - \omega_k) + \frac{1}{T_{2k}} + \frac{1}{\tau_k} \qquad \text{(II-57)}$$

where ω_k is the chemically shifted frequency of the $k^{\underline{th}}$ site (calculated from (I-30) or (I-28) for a particular molecular orientation), T_{2k} is the

spin-spin relaxation time of the $k^{\underline{th}}$ site and $(\tau_k)^{-1} = \sum_j \tau_{jk}^{-1}$. The time τ_{jk} is the inverse rate of jumps from the $j^{\underline{th}}$ to the $k^{\underline{th}}$ site. The off diagonal elements of $\underset{\approx}{A}$ are the couplings among magnetizations from the motion,

$$A_{jk} = - \tau_{jk}^{-1} . \tag{II-58}$$

The lineshape for the exchanging molecule is then given by $g(\omega)$ which is proportional to the imaginary part of the total magnetization, $g(\omega) = \sum_k g_k$. Formally we may solve (II-56) for $\underset{\sim}{g}$:

$$\underset{\sim}{g} = - i\omega_1 M_0 \underset{\approx}{A}^{-1} \underset{\sim}{1} \tag{II-59}$$

then

$$\begin{aligned} g(\omega) = \mathrm{Im}\left(\sum_j g_j\right) &= \mathrm{Im}\left(\sum_j - i\omega_1 M_0 \sum_k A_{jk}^{-1}\right) \\ &= - \omega_1 M_0 \ \mathrm{Re}\left(\sum_{jk} A_{jk}^{-1}\right). \end{aligned} \tag{II-60}$$

It is then the work of the computer to invert the matrix $\underset{\approx}{A}$ for each ω and given input jump parameters τ_{jk}, and average over all possible orientations, to give the final powder lineshape. If only one time constant is necessary to completely describe the motion, that is $\tau_{jk} = \tau_{\ell m}$ for all j, k, ℓ and m, it is possible to analytically invert $\underset{\approx}{A}$ and sum the elements, (Appendix C). The result is

$$g(\omega) = \mathrm{Re}\left(\frac{n\tau\gamma}{n\tau-\gamma}\right) \tag{II-61}$$

where $\gamma = \sum_j 1/A_{jj}$ and $\tau = n\,\tau_{jk}$

and n is the number of sites with distinct chemical shifts which are being exchanged. This removes the matrix inversion step in the calculation and reduces the time necessary for calculation.

The rotational diffusion model may not be calculated exactly with the exchange matrix formation. However we may approximate it rather closely by taking a very large number of discrete sites, spaced with appropriate symmetry for the axial or isotropic case. Exchange is then taken in the hard collision limit, the probability of going from any site to any other is equal. The calculated spectra thus generated are virtually identical to those generated by the expansion methods of Alexander, Baram and Luz.

The programs used for calculation of one time constant (MTHEX) and multiple time constant (SEXCH) calculations are given in Appendix E. A program for generating rigid and extreme narrowing powder patterns (PPGEN) is also given.

G. Hexamethylbenzene (HMB)

The first observation of motion about the sixfold symmetry axis in hexamethylbenzene was made by Andrew,[36] using wide line proton NMR. He observed a decrease in the linewidth from about 7.5 Gauss at 135K to about 3 Gauss at 210K. The second moment from liquid nitrogen temperature up to 135K could be explained only if rapid methyl group rotation were already occurring at liquid nitrogen temperature, so he attributed the further narrowing to rotation about the sixfold axis. The crystal structure of HMB at room temperature had been determined,[37,38] and showed well defined positions for the carbon atoms, ruling out

rotational diffusion. Thus Andrew concluded that the motion must be a "sixfold tunneling on nonuniform rotation of the molecule about the sixfold axis." Further characterization of this motion has been carried out through proton T_1[39] and $T_{1\rho}$[40] measurements as a function of temperature. While such measurements cannot provide information about the symmetry of the motion, they can provide rather accurate determinations of activation energies. This motion has also been detected through its effect on the ^{13}C lineshape.[29] The spectra at room temperature and 123K are shown in Fig. 7. Since the methyl peak obscures the σ_{33} element of the ring carbon tensor, only σ_{11} and σ_{22} may be obtained directly from the spectra, but σ_{33} may be calculated if the isotropic shift is also measured. At 123K for the ring carbons we obtain values σ_{11} = - 98±2 PPM and σ_{22} = - 23±2 PPM relative to an external liquid benzene reference. For an isotropic shift of -4 PPM, σ_{33} = 109±4 PPM, in good agreement with values previously measured.[29] At room temperature we see that the tensor has become axially symmetric, with $\sigma_{\perp}$ = - 59±1 PPM and we calculate $\sigma_{\parallel}$ = 107±3 PPM. Note that $\sigma_{\perp} = \frac{1}{2}(\sigma_{11}+\sigma_{22})$ and $\sigma_{\parallel}=\sigma_{33}$ within experimental error. From (II-34) we conclude that $\beta = 0°$, the rotation occurs about the σ_{33} axis. From early single crystal work[41] σ_{33} for aromatic carbons was found to be perpendicular to the aromatic plane. This was confirmed for HMB in a later single crystal study.[42]

From the arguments presented in Section II-E, using the group $C = D_6$ for the molecule and $S = D_2$ for the chemical shift, we find only two relevant representations A_1 and E_2. This means that only one time constant is necessary to describe the effect of motion on the line shape. While from a theoretical standpoint the specification that E_2 is the

only relevant representation supplied all of the information necessary to calculate the spectrum, we desire a physical understanding of the time constant. Figure 8 shows all rotations which the molecule may undergo, and the rates at which they occur. The chemical shielding tensor has inversion symmetry so that the chemical shifts for pairs of sites across the ring (i.e., 1 and 4) must be the same. Thus for a collection of molecules with the same molecular orientation, the spectrum will consist of three lines, as in the lower part of Fig. 8. Since the chemical shift does not change in a jump from orientation A to D, the spectrum will be invariant to the rate W_{14}, and it need not be included at all. We also note that orientations B and F (similarly C and E) are reached by the same rotation, differing only in sense, hence the rates W_{12} and W_{16} (similarly W_{13} and W_{15}) must be equal. At this point it seems that two rates, W_{12} and W_{13} must be used to describe the motion. However we now note that jumps of the W_{12} type transfer magnetization between lines A and B, B and C, and C and A; and jumps of the W_{13} type transfer magnetization between A and C, B and D(A), and C and E(B). Since the two types of jumps achieve the same exchange of magnetization, they cannot be independently detected, instead their sum $W_{12} + W_{13} = \tau^{-1}$ determines the lineshape.

In both rotational diffusion and jumping models, the rapid motion limit must be an axially symmetric tensor with $\sigma_{\perp} = \frac{1}{2}(\sigma_{11} + \sigma_{22})$ and $\sigma_{\parallel} = \sigma_{33}$. In the slow motion range of time constants $\tau^{-1} \sim |\sigma_{22} - \sigma_{11}|$, with σ's in frequency units, the powder pattern will not be described by a simple shielding tensor. In the rotational diffusion model, the

sharp features of the powder pattern will broaden, and as the rotational frequency increases slowly merge to form the axial tensor. This happens because the spins exchange among a wide range of frequencies, yielding sharp features only when the rate of exchange far exceeds the range of frequencies sampled.

For the jumping model the situation is quite different. As the molecule jumps a spin is exchanged among sites with only three different frequencies. For a few particular orientations of the molecule, two of the three frequencies are very close together. In this case these two lines will coalesce at low jump frequencies moving intensity into two particular regions of the powder pattern. Figure 9 (a) and (c) show two orientations which give rise to degenerate line positions, and one general orientation. Spectra for collections of molecules with orientation (b) and close to orientation (c) are shown in Fig. 10. The rapid averaging for the two lines close together is evident in the right hand spectra, while on the left hand side the spectra get increasingly broad for low jump rates. Figure 11 shows the powder averages for rotational diffusion and jumping models, as a function of jump frequency. Such spectra have also been calculated by Alexander, Baram and Luz[33] using an approximate expansion method. These compare well with our calculations. The extra-features or bumps in the jump model are quite obvious and indicative of this model.

Experimental ^{13}C spectra were obtained for HMB with the spectrometer described in Chapter V. A sample of commercial HMB (Eastman Kodak, used without further purification) was compressed into a pellet of

weight ~200 mg. All spectra were taken using the single contact cross polarization technique, optimizing mixing time empirically at each temperature, over a range of 0.5 to 5 msec. Recycle delays were also empirically adjusted, and ranged from 2 to 5 sec. Several hundred decays were averaged at each temperature before Fourier Transformation to give the final spectra.

The experimental spectra are presented in Fig. 12, along with theoretical spectra for the jump model. The extra features in the spectra at ~ -40 and -80 PPM are quite evident. An expanded spectrum at -135.8°C is shown in Fig. 13, where these features are particularly pronounced. The presence of these features and the overall shape of the powder patterns are consistent only with a jumping model, as expected from the previous NMR and x-ray experiments. The jump frequency at each temperature may be estimated by comparison with theoretical spectra. A plot of the logarithm of approximate jump rate against inverse temperature is presented in Fig. 14. From this, using a linear least squares fit we obtain an activation energy of ~ 5.5 kcal/mole for the jumping, in reasonable agreement with values obtained from relaxation studies.[30,40] Some caution should be exercised in comparing jump rates from this study and those determined from relaxation, since the rate W_{14} is not included in our measurements, but would be included for relaxation measurements, however evidence will be presented in the next section that the rates W_{14} and W_{13} are probably small.

H. Decamethylferrocene (DMFe)

Although DMFe has not been previously studied by either x-ray or NMR techniques, its close relative ferrocene has been extensively studied. For ferrocene the room temperature crystal structure shows well defined carbon atom positions,[43] but NMR shows a strong decrease in proton linewidth in the 55-75K temperature range.[44,45,46] As for HMB this implies that motion occurs as jumps about the C_5 axis of the molecule. However since no information is available about DMFe, our conclusions must be reached solely from the powder lineshape.

^{13}C powder spectra for DMFe at room temperature and -180° C are shown in Fig. 15. At low temperature we find an asymmetric pattern with tensor elements $\sigma_{11} = 1.0 \pm 1$ PPM, $\sigma_{22} = 42.5 \pm 1$ PPM and, calculated from the isotropic shift, $\sigma_{33} = 105.1 \pm 3$ PPM.* At room temperature the tensor becomes axial, with elements $\sigma_{\perp} = 27.3 \pm 1$ PPM and $\sigma_{\parallel} = 94.0 \pm 1$ PPM giving an isotropic shift of 49.5 ± 2 PPM. In HMB the orientation of the shielding principle axis system relative to the molecular frame was determined entirely from symmetry (although assignment of particular tensor elements to specific directions requires single crystal studies). For DMFe the plane of ring carbon atoms is no longer a symmetry plane, as for HMB, due to the iron atom. However, the vertical symmetry plane through the iron and dividing the ring remains defining one principle axis uniquely, perpendicular to this plane, and requiring the other two elements lie in the plane. If we assume that the motion leading to axialization of the shielding tensor is rotation about the C_5 axis, and assign tensor elements

---

*All ^{13}C tensor elements reported in PPM relative to external liquid benzene.

to direction in analogy to HMB, σ_{22} out of the symmetry plane and σ_{33} closest to along the rotation axis, then we may solve for the angle between σ_{33} and the rotation axis. This is done by transforming from principle axis system to rotation axis system as in (II-34). In this case α=0, β = variable, γ = averaged, so that using the observed rigid and averaged tensor values above we obtain

$$\frac{1}{2}\cos^2\beta\,(1.0) + \frac{1}{2}\,(42.5) + \frac{1}{2}\sin^2\beta\,(105.1) = 27.3.$$

We find from this $\beta = \pm 19°$, the angle between the σ_{33} and rotation axes. Although the sign of β may not be determined from (II-34), it seems physically reasonable to have a positive value, the σ_{33} axis shifting to pass closer to the iron atom. This orientation is represented schematically in Fig. 16. It is not surprising that a strong covalent bond, such as that between the metal and ring, should rotate the shielding tensor.

The effect of the metal is also manifested in the dramatic reduction in width of the shielding tensor relative to HMB ($\sigma_{33}-\sigma_{11} = 104$ PPM in DMFe but 207 PPM in HMB), although both have six pi electrons. Previous correlations of isotropic chemical shifts with pi electron densities have been made.[47] On this basis it appears that about half of the pi density resides on the metal. It is expected that a more ionic metallocene would have both a downfield isotropic shift and wider shielding tensor. This has been partially confirmed by measurements of isotropic shifts, and widths of motionally narrowed shielding tensors in ferrocene, ruthenocene and magnesocene. The bonding in ferrocene and ruthenocene is expected to be very similar since they are in the same column of the

periodic table. The chemical shifts measured are 59 PPM and 55 PPM for ferrocene and ruthenocene respectively with anisotropies ($\sigma_{\parallel} - \sigma_{\perp}$) 75 ± 2 PPM and 78 ± 2 PPM. On the other hand magnesocene, expected to be much more ionic has a chemical shift of 20 PPM and anisotropy 132 ± 4 PPM.[48,49] Although part of the difference could be from rotation of the tensor in analogy to DMFe, it is expected that the electron densities plays a more important role.

To analyze the motion of the rings in DMFe, we again follow the arguments in Section II-E, using the group D_5 to describe the molecular symmetry. Whether the rings take on the expected staggered or eclipsed confirmation, and whether motion occurs as overall molecular rotation, or rotation of one ring relative to the other cannot be determined from these studies and will not affect the arguments presented. Among the representations of D_5, A_1, E_1 and E_2 are relevant, so two rates are necessary to completely specify the motion. The allowed jumps for one of the rings are shown in Fig. 17. For a general orientation of the ring we expect a five line spectrum. The orientations B and E (and similarly C and D) are reached from A by the same rotation in different senses, so rates W_{12} and W_{15} must be equal (similarly W_{13} and W_{14} must also be equal). In this case there is no further symmetry to consider, and the rates W_{12} and W_{13} are independent, and both must be specified to calculate the powder lineshape, for the jumping model.

The lineshape for rotation diffusion will be almost identical to those for HMB (Fig. 11), the only difference occurring in the slight downfield movement of σ_{33} (105 PPM) to $\sigma_{\parallel}$ (94 PPM), which does not happen

for HMB. Since the lineshapes are so similar, calculations were not repeated for DMFe.

To specify the two parameters for the jump model we will use the ratio of the two types of jumps W_{12}/W_{13}, and the total jump rate $W_{12} + W_{13}$. It is instructive to first examine two limiting cases, $W_{12}/W_{13} = \infty$ (only jumps of $2\pi/5$ allowed) and $W_{12}/W_{13} = 0$ (only jumps of $4\pi/5$ allowed). As for HMB, there are certain molecular orientations, relative to the field, which give rise to degeneracies in site frequencies. Two of these orientations are shown in Figs. 18 and 19, together with spectra for nearby orientations. The spectra for each orientation are shown for a variety of total jump rates W, for both limiting cases. From these it is clear that lines directly exchanged by the jumps sharpen quickly and remain sharper than those lines which are only indirectly exchanged. Therefore the two types of jumps, $2\pi/5$ and $4\pi/5$, give rise to extra features, or bumps, in different parts of the powder spectrum, the downfield portions of which are also shown in Figs. 18 and 19.

Although the above models are instructive, a model which allows only jumps of $4\pi/5$ seems physically very unreasonable, although jumps of $2\pi/5$ only seems plausible. We will call the $2\pi/5$ jump only model a "soft" collision model. The other physically reasonable case is a "hard" collision model for which $W_{12}/W_{13} = 1$, all types of jumps equally probable. These models really differ only in time scale for occurrence of collisions which exchange enough energy with an "activated" molecule (one with enough rotational energy to overcome the rotational potential barrier) to prevent it from continuing to rotate. In the soft collision model the deactivating collisions are very frequent, while in the hard collision case rotations of $2\pi n/5$ are equally probable, for small interger n (we still assume

the time during rotation is short relative to time between rotations) corresponding to "infrequent" deactivation. The complete powder lineshapes for these two models are shown in Fig. 20. The most striking difference in these spectra is the weakening of the bump near 35 PPM, in the hard collision case. This feature arises from $2\pi/5$ jumps (see Fig. 19) and as they become less probable this feature weakens, to be replaced by a bump not clearly resolved from the peak at σ_{22} (see Fig. 18), as $4\pi/5$ jumps become more probable.

Experimental ^{13}C spectra for DMFe were obtained with the spectrometer described in Chapter V. The sample of DMFe was prepared in Professor G. Whiteside's laboratory at MIT, and was generously given to us. The sample was a yellow powder, estimated to be greater than 98% pure. Above 200 mg of this powder was compressed into a pellet, and was used to obtain all spectra shown here. Spectra were recorded using single contact cross polarization, optimizing mixing time and recycle delay empirically at each temperature. Several hundred decays were averaged before Fourier Transformation to give final spectra.

The experimental spectra are shown in Fig. 21, for a variety of temperatures. The features at approximately 15 and 35 PPM are quite pronounced at low temperatures, as is the shoulder shape at slightly higher temperatures. These features certainly rule out a rotational diffusion model. In Fig. 22 we show an expanded plot of one experimental spectrum with several theoretical plots for varying W_{12}/W_{13} ratios. It is clear that the experimental spectrum corresponds to a fairly large W_{12}/W_{13} ratio (we estimate >10, but the lineshape essentially converges to the

"soft" model for $W_{12}/W_{13} \sim 10$ making improvement of the estimate beyond this point impossible). To our knowledge this is the first time it has been possible to even estimate this type of ratio for reorientation in the solid state.

As for HMB we may estimate the jump frequency from the line-shape. A plot of the log of the estimated jump rate versus inverse temperature is shown in Fig. 23. A linear least squares fit to a straight line gives an activation energy of 3.2 kcal/mole. This is a bit higher than the activation energy measured for rotation in ferrocene, 2.3 kcal/mole,[45] which seems quite reasonable.

Although this is the first case for which a soft collision model has been verified, it seems likely that there is nothing magical in the structure of DMFe, and that similar rotational motion in other solids (including HMB) also occur in a "soft" collision manner. It would certainly be interesting to verify this in a nonmethylated ferrocene or ferrocene analog, for which the symmetry arguments above still apply.

I. Ice

The importance of water in the world around us has prompted study of all its forms. Although simple in chemical composition, and extensively studied there is still much controversy about many aspects of the structure and dynamics of the liquid state, and many aspects of dynamics in the solid state. High resolution proton NMR studies in highly deuterated ice now give us a detailed picture of proton motions.

NMR has played an important role in the study of ice for many years. However most previous work has provided only indirect information

about dynamics, through studies of moments of the proton resonance line,[50] and measurements of relaxation times T_1, $T_{1\rho}$ and T_{1D}.[51] Additional studies have been made of the quadrupole couplings in deuterated[52,53] and oxygen-17[54] enriched ice, which can give useful information about the structure of ice, but due to the large spittings involved can only put upper limits on rates for any motions occurring.

The techniques listed above are all relatively limited in achievable resolution. The first measurement of the chemical shielding tensor for protons in ice did not come until it was realized decoupling of deuterium could be achieved with reasonable r.f. fields (see Section II-C), allowing application of the dilute spin approach.[16] The rigid molecule tensor was found to be axially symmetric with principle values $\sigma_{\parallel} = 15 \pm 2$ PPM and $\sigma_{\perp} = -19 \pm 2$ PPM (relative to external TMS), Fig. 24. There was a shift of 2 ± 1 PPM of the trace of the tensor in the solid relative to the isotropic liquid. This tensor has also been measured subsequently using multiple pulse techniques, with reasonable agreement.[55] However, when motion of the spins is present it is not clear that multiple pulse sequences could provide sufficient narrowing to resolve the fine structure of interest in the present study.

In ice I_h, the ordinary form of ice at low pressure and reasonable temperature, the oxygen atoms occupy an hexagonal lattice, each oxygen having a regular tetrahedron of others surrounding it. The protons lie between oxygens, normally one between each pair of oxygens. It is known from measurements of entropy at low temperature[56] that there is no long range ordering of proton positions. An ordered structure for ice, as described above, does not allow for any motion of spins, except

vibrational motion from phonons. However, many dynamic phenomena, i.e. mechanical and dielectric relaxation and electrical conduction,[57] have been observed even in very pure samples of ice. These have been attributed to defects occurring in the I_h structure. The most widely accepted form for defects which allow molecular rotation are Bjerrum faults. There are two types of these faults, D and L, which correspond to having either two protons (D type) or no protons (L type) between a given pair of oxygens. These are thought to be formed in a slow step (high activation energy) then migrate rapidly (low activation energy) through molecular rotations, as shown in Fig. 25 for a D type fault.

The migration of Bjerrum defects throughout the lattice randomly reorients individual water molecules among the six equivalent positions at a given lattice site, Fig. 26. While the proton chemical shielding tensor is not required by local symmetry to be axially symmetric (as it would be if only the oxygens were considered), to experimental accuracy it is symmetric, so the unique direction certainly lies along the O - H vector. Motion exchanges the tensor symmetry axis between the four corners of a tetrahedron. For the analysis of Section II-E we take the "molecular" group G to be T_d. Then the relevant representations are A_1 and T_2, so we need only one jump rate to describe the spectrum. This is clear physically in that jumps from any orientation to any other differ only in the direction of the axis of rotation. The alternate model, for rotational diffusion, will no longer be restricted to rotation about a fixed axis. Rather it will consist of random rotations about random axes. In either case, because of the high symmetry, the fast motion limit will be a single line.

Although we have lifted the restriction of uniaxiality in the rotation, the lineshapes are similar in character to those previously described. In the rotational diffusion model, the sharp features of the powder pattern broaden and lose shape with increasing jump rate, eventually merging to a single line. In the jumping model we again predict an extra bump in the powder pattern, due to an orientation producing degeneracies in line positions. However, in previous cases, only two of three (HMB) or five (DMFe) lines were degenerate, leading to broadening of all lines for high jump rates. In ice, however, when the field is along one of the C_2 axes, all four lines are degenerate, and fall at the isotropic value (half of the tetrahedral angle is the magic angle). In this case the lines never broaden for any jump rate, resulting in a much sharper "bump", limited in width only by other broadening mechanisms, Fig. 27. The lineshapes for a variety of jump rates for jumping and rotational diffusion models are shown in Fig. 28. As for the other cases discussed, the structure in the "bump" region is quite distinctive for the jump model. The lineshapes for a jumping tetrahedron were also calculated by Speiss,[34] for analysis of motion in solid P_4.[35] Our lineshapes are quite similar to his, although there are small quantitative differences. P_4 has tetrahedral molecular symmetry and was shown to reorient in a jumping manner.

Of the dynamic phenomena observed in ice, dielectric relaxation, electrical conduction and diffusion, only dielectric relaxation is well explained by migration of Bjerrum faults. To explain conduction and diffusion other types of defects have been postulated and we must consider

molecules and Bjerrum defects have also been discussed. Theoretical estimates show that these alone should be a factor of five too slow to explain observed diffusion rates. Their effect would be indistinguishable from those above.

Experimental proton spectra were taken as a function of temperature with the spectrometer described in Chapter V. The sample was Bio-Rad Laboratories D_2O (specified 99.8 mole % pure, H_2O, HOD < 0.25%) with ~0.5% distilled H_2O added. The sample was frozen and sealed under vacuum in a 6mm pyrex tube. Data were taken as free induction decays following a 90° pulse with high power deuterium decoupling ($H_1 \simeq 60G$), and a 1 minute recycle delay. Several hundred decays were averaged before Fourier Transformation to give final spectra.

The experimental spectra for a variety of temperatures are shown in Fig. 29, along with theoretical spectra for the jump model. Although the resolution in the experimental spectra is somewhat limited (probably by residual homonuclear dipolar coupling) the features of the jumping model are certainly present. We may then conclude that the rapid motions of protons in heavy ice, exchange the proton shielding tensor among the corners of a tetrahedron. In light of the previous discussion this is not surprising.

Again we may estimate jump rates by matching experimental and theoretical spectra as a function of temperature. A logarithmic plot of jump rate versus inverse temperature is shown in Fig. 30. A linear least square fit gives an activation energy of 3.5 kcal/mole. This is far less than the 13.4 kcal/mole activation energy measured for dielectric relaxation and the 15 kcal/mole measured for diffusion, in very

their contributions to averaging of the NMR lineshape. Ionic defects have been invoked to explain electrical conduction. Ions are generated in a high activation energy step by transfer of a proton from one water molecule to another, giving one H_3O^+ and one OH^-. These then migrate in successive low activation energy steps by further proton transfers which conserve the number of ions present. We note that all proton motions are jumps along a single O - O vector. Such jumps leave the shielding tensors of all protons unchanged, and hence do not contribute to the averaging of the NMR lineshape. Shielding tensors for the ions themselves will be different than for water, but they exist in such low concentrations that they may be ignored completely. Both Bjerrum and ionic defects are the result of proton mispositioning and cannot explain mass transport or diffusion. Diffusion coefficient measurements have shown that oxygen and hydrogen diffuse through crystals of ice at approximately the same rate. This suggests that defects in the oxygen lattice are interstitial water molecules, and molecular vacancies. Migration of interstitial molecules does not provide a mechanism for reorientational relaxation (dielectric) in the bulk, since a molecule jumping into an interstitial space leaves a record of its orientation in the positions of protons which surrounded it. Another molecule entering this site must take the same orientation or create a Bjerrum defect. However if diffusing molecules exchange rapidly between interstitial and lattice sites then individual molecules may change their orientation and hence contribute to the averaging of the NMR lineshape, in the same fashion discussed for Bjerrum defects. Composite defects consisting of "bound" interstitial

pure ice samples.[57] However, since these have been measured for pure samples, they should represent the energy of formation for the defect giving rise to particular dynamic effects. Our sample was not carefully purified (and water is notorious for being difficult to purify), hence the barrier we measure may be for migration of intrinsic defects in our sample, rather than for their creation. This barrier is thought to be $\sim$ 5 kcal/mole.[58] In addition, the comparison with dielectric relaxation and diffusion data is complicated since both contribute to the motional narrowing of chemical shielding. Further studies using this approach on carefully purified and doped samples may be very useful in separating activation energies for the creation and migration of various defects in heavy ice. Similar studies might be useful in other proton containing solids, for example metal hydrides.

J. Pentamethylbenzene (PMB)

We have seen that a great deal of information about the dynamics of molecular motion may be obtained by study of the powder lineshape as a function of temperature. These lineshapes are particularly informative in the slow motion regime. However there are some cases where motion sets in at a phase transition, going directly from a rigid solid to the motionally narrowed limit. Pentamethylbenzene provides an example of this type of behavior. While the information that may then be obtained through powder lineshape studies is limited, when coupled with other techniques it may be possible to fully characterize the motion.

Crystallographic phase transitions in PMB were first observed by calorimetric methods.[91] NMR measurements of proton T_1 and linewidths[92] showed that above the transition at 24° C some molecular motion in addition to methyl rotation occurs. The crystal structure of PMB is not known, so that accurate second moment calculations could not be done. From geometrical constraints it was presumed that motion was about the axis perpendicular to the molecular plane and hence was similar to that of hexamethylbenzene.

The sample used for present studies was commercial PMB (Aldrich > 98% purity) used as was. Approximately 200 mg was compressed into a 6 mm diameter pellet, and spectra were taken with the spectrometer described in Chapter V, using cross polarization techniques. Temperature was maintained to ± 0.5° C.

Figure 30a shows the carbon spectra for PMB above and below the phase transition at 24° C. The spectra are superpositions of spectra from tensors for the four types of ring carbon, plus the methyls at the high field edge. At the lower temperature the width of the spectra are exactly what one would expect in analogy to those for the closely related compounds, durene and hexamethylbenzene.[42] Above the transition the tensors are partially averaged, to the values found by Waugh *et al.*, in their study of shielding tensors in PMB. It is immediately clear that the motion is not as simple as in HMB since the tensors are not axially symmetric in the high temperature phase. No further narrowing of the powder pattern occurs up to the melting point at 54° C.

The remaining asymmetry in the high temperature phase must be interpreted as a biasing of motion in some way. There are two distinct models which will fit the NMR data and hence cannot be distinguished by our experiments alone. The first is a rocking motion by the molecule or jumping between two orientations not related by symmetry. If we assume that all time is spent at the endpoints of the rocking or jumping motion (I-29) may be averaged to calculate the new tensor. The angular dependence of the σ_{11} and σ_{22} elements for such a planar motion is simple, $\sigma = \sigma_{11} \cos^2\alpha + \sigma_{22} \sin^2\alpha$, and the averaged σ_{11} value for two positions separated by angle 2α is $\bar{\sigma}_{11} = \frac{1}{2} (\sigma_{11} \cos^2\alpha + \sigma_{22} \sin^2\alpha + \sigma_{11} \cos^2(-\alpha) + \sigma_{22} \sin^2(-\alpha))$. Since σ_{11}, σ_{22} and $\bar{\sigma}_{11}$ are known from the combination of high and low temperature phases this is easily solved to give $\alpha = 22^\circ$, corresponding to jumps between positions separated by 44°. If the molecule is allowed to spend time between the endpoints of its oscillations, then the potential function must be specified to calculate the shielding tensor. If one assumes a square well potential for example, then we may calculate the average tensor element

$$\bar{\sigma}_{11} = \int_{-\alpha}^{\alpha} \sigma_{11} \cos^2 + \sigma_{22} \sin^2\alpha \; d\alpha / \int_{-\alpha}^{\alpha} d\alpha \, .$$

The integrals are easy to evaluate analytically and may be solved to give $\alpha = 39^\circ$ corresponding to oscillations through an angle of 78°. Potential functions with central minima would predict oscillations through a larger angle.

An alternate model for the motion is jumps between symmetry related positions, as for HMB but with unequal populations (equivalently energies) for the different possible orientations. In this case the model is underdetermined, that is, there are an infinite number of different populations which give rise to the proper averaged tensor. However, if we assume that lattice sites have C_2 symmetry, and that the two orientations for which the molecular C_2 axis is not along the crystal C_2 axis have equal populations, then there is only one independent parameter in the problem. The chemical shift of the three different possible sites are easily calculated. Since we know $P_1 + 2P_2 = 1$, $\bar{\sigma} = P_1 \sigma_1 + P_2 \sigma_2 + P_2 \sigma_3$ may be solved for any orientation ($\bar{\sigma}$, σ_1, σ_2 and σ_3 all are known) to give $P_1 = 0.812$, $P_2 = 0.094$.

In either model the "missing" methyl group is undoubtedly crucial in changing the motion from simple six-fold jumping as was observed in HMB. While it is not possible to distinguish between the models above with NMR alone, these studies provide information which is complementary to that which may be obtained by x-ray crystallograpic techniques. When x-ray studies are done on the high temperature phase, the combined information may make complete characterization of the motion possible.

K. Discussion

The studies presented in this Chapter demonstrate that high resolution NMR techniques applied to ordered phases can provide an extremely sensitive probe of molecular motions. While they are applicable to single crystals (see theoretical spectra in Sections G and H), they are equally applicable to powder samples. This is particularly important

in extension of studies of noncrystalline samples, i.e., glasses, polymers and molecules adsorbed on surfaces, where single crystals are impossible to obtain. The sensitivity of NMR lineshapes to the microscopic dynamics of reorientation processes is unique, and has allowed us to get a clearer picture of the correlation function for molecular rotation. From these studies it is clear that the symmetry of the potential function imposed upon a molecule by its neighbors controls the nature of the reorientation process, and from high temperature x-ray data it is clear that the shape of the potential is maintained even when jumps occur very often.

III. DOUBLE QUANTUM NMR

A. Introduction

Most of the recent advances in solid state NMR have come through the development of techniques for obtaining high resolution spectra in complex systems. In the previous chapter we have discussed one approach to high resolution in some systems and have demonstrated the type of information made available through such studies. In this chapter we will discuss the application of a new technique, Fourier Transform Double Quantum NMR,[18,19] to measurements of chemical shielding in powders of quadrupolar coupled nuclei and to measurement of dipolar couplings in both single crystals and powders in the presence of quadrupole couplings. Figure 31 represents schematically the reasons why a new type of spectroscopy was necessary. Quite simply, the quadrupole coupling is so much larger than chemical shifts or dipolar couplings, that in a powder it is quite impossible to see the smaller couplings. In favorable cases single crystals may be studied to yield both the quadrupole coupling and chemical shifts or dipolar couplings, but even in single crystals FTDQ NMR may be used to reduce linewidths.

For the studies presented here we will restrict ourselves to observation of deuterium, for which quadrupole couplings are fairly small ($\sim 10^5$ Hz) relative to the Zeeman coupling (2.8×10^7 Hz), but large compared to chemical shifts ($\sim 6 \times 10^2$ Hz) and dipolar couplings ($\sim 10^3$ Hz), although in principle this restriction is not necessary.

The initial motiviation for FTDQ NMR came from the observation that the quadrupole coupling shifts the $m = +1$ and -1 levels by the same amount, in the same direction, Fig. 32. Thus the two photon absorption comes at a frequency ω_0, independent of the quadrupole coupling constant. Such two photon absorptions have been discussed for C.W. NMR,[59] as have general multiple quantum absorptions,[60] but do not provide a method for high resolution spectroscopy in solids since heteronuclear dipolar broadening and power broadening cannot be avoided. These problems have been overcome through application of pulsed NMR methods, very similar in many respects to those described in Chapter II. Selective dilution is used to reduce homonuclear dipolar couplings among deuterons, while high power decoupling may be applied to remove heteronuclear dipolar couplings without severe sample heating. In order to describe the experimental approach completely, the next section will present the formalism developed for general multiquantum NMR. Experimental measurements of chemical shielding in powders will be discussed in Section C, along with the measurement of deuterium - deuterium dipolar couplings, using FTDQ NMR for both single crystals and powders.

B. Theory

1. Fictitious Spins - 1/2

In NMR of spin 1/2 nuclei, the rotating frame vector representation of magnetization has played an important role in understanding and developing pulsed NMR experiments. However recent experiments[16,18,61] have shown that such a three dimensional vector is not sufficient to describe the dynamics of some systems, in particular spins with $I > \frac{1}{2}$ in

the presence of an electric field gradient. In this section we will describe an operator formalism with which such experiments may be described.

The general approach to description of pulsed NMR experiments was mentioned in Chapter 1. For a system of I spins in a magnetic field, the state of the system is described by the density matrix ρ, with dimension $(2I+1) \times (2I+1)$. This matrix may be expanded in a set of $N = (2I+1)^2-1$ traceless, linearly independent Hermitian operators, A_n, plus the identity operator

$$\rho(t) = \sum_{n=1}^{N} a_n(t)\, A_n + a_o \underset{\approx}{1} \quad . \qquad \text{(III-1)}$$

The coefficient a_n may be calculated from initial conditions and the equation of motion (I-6). If we start with the system in thermal equilibrium, in the high temperature approximation we may write

$$\rho_0 = \frac{1}{2I+1}\left(1 + \frac{\omega_o}{kT} I_z\right) \quad . \qquad \text{(III-2)}$$

If the Hamiltonian contains only interactions linear in spin variables, Zeeman, chemical shift and r.f. irradiation, the closed cyclic permutation relations of I_x, I_y and I_z allow us to restrict the sum in (III-1) to only the angular momentum operators I_x, I_y and I_z:

$$\rho = \sum_{p=x,y,z} a_p(t) I_p + a_o 1 \quad . \qquad \text{(III-3)}$$

It is then the three coefficients a_x, a_y, and a_z which are the vector description of the state. However when the Hamiltonian contains

interactions which are bilinear in spin variables, quadrupole, dipole and scalar or spin-spin, the description of ρ must contain more operators than just I_x, I_y and I_z. In the expansion of ρ (III-1), any complete set of operators A_n may be used. However with judicious choice, some valuable aspects of a vector representation may be preserved when bilinear couplings are present. The first set of operators chosen[19] were found to be particularly useful in description of pure nuclear quadrupole resonance experiments,[62] but as will be shown are also very useful for NMR. This set was chosen because of convenient commutation relations between the individual operators. For reasons of convenience and symmetry, nine operators were defined rather than the required eight. In terms of I_x, I_y and I_z these operators are given by

$$\begin{aligned}
I_{x1} &= \frac{1}{2} I_x & I_{y1} &= \frac{1}{2} I_y & I_{z1} &= \frac{1}{2} I_z \\
I_{x2} &= \frac{1}{2} (I_y I_z + I_z I_y) & I_{y2} &= \frac{1}{2} (I_z I_x + I_x I_z) & I_{z2} &= \frac{1}{2} (I_x I_y + I_y I_x) \\
I_{x3} &= \frac{1}{2} (I_z^2 - I_y^2) & I_{y3} &= \frac{1}{2} (I_x^2 - I_z^2) & I_{z3} &= \frac{1}{2} (I_y^2 - I_x^2) \quad .
\end{aligned} \tag{III-4}$$

The definition of the extra operators causes the linear dependence $I_{x3} + I_{y3} + I_{z3} = 0$. Each set of operators I_{p1}, I_{p2}, and I_{p3} have the same commutation relations as the Cartesian angular momentum operators,

$$[I_{p1}, I_{p2}] = i\, I_{p3} \tag{III-5}$$

or cyclic permutation of 1,2,3. These commutation relations are also sufficient to give simple rotation behavior,

$$e^{-i\theta I_{p1}}\, I_{p2}\, e^{i\theta I_{p1}} = I_{p2} \cos\theta + I_{p3} \sin\theta \quad . \tag{III-6}$$

Since these operators behave exactly as those for a spin 1/2, these have been called fictitious spin-1/2 operators, in analogy to Feynmann[63] and Abragam,[1] and with each set of operators I_{p1}, I_{p2} and I_{p3} we can associate a state vector in a three dimensional Cartesian space. The complete state of the system is the specified by three vectors in three spaces. Although such a description seems complex at first sight we will see that for many experiments of interest only one space will have a nonzero vector and its evolution will be restricted to that single space. Further commutation relations and rotations which will prove useful for later computations are presented in Table I. A complete table of commutators and anticommutators may be found in Appendix F. If these operators are represented in matrix form in the eigenbasis of I_z^2, Table II, their form is related to the spin-1/2 Pauli matrices.

2. Hamiltonians

To calculate the expected results of experiments it will now be convenient to express the Hamiltonian, as well as the density matrix, in terms of the operators defined above. For the present we will include off resonance (chemical shift), r.f. field and quadrupole terms, adding dipolar couplings later. From Chapter I we write the Hamiltonian:

$$\mathcal{H} = -\omega_0 I_z - 2\omega_1 I_x \cos\omega t + \frac{1}{3}\omega_Q[3I_z^2 - I(I+1)] . \quad \text{(III-7)}$$

As done previously this may be transformed to the frame rotating at ω, the irradiation frequency:

$$\mathcal{H}^* = -\Delta\omega I_z - \omega_1 I_x + \frac{1}{3}\omega_Q[3I_z^2 - I(I+1)] \quad \text{(III-8)}$$

Table I

COMMUTATORS

$$[I_{pi}, I_{pj}] = iI_{p,k} \qquad [I_{p2}, I_{q2}] = \frac{-i}{2} I_{r1}$$

$$[I_{p1}, I_{q2}] = \frac{-i}{2} I_{r2} \qquad [I_{p1}, I_{q3} - I_{r3}] = 0$$

$$[I_{p2}, I_{q1}] = \frac{-i}{2} I_{r2}$$

ROTATIONS

$$\exp(-i\theta I_{pi})\ I_{pj}\ \exp(i\theta I_{pi}) = \cos\theta\ I_{pj} + \sin\theta\ I_{pk}$$

$$\exp(-i\theta I_{p1})\ I_{q1}\ \exp(i\theta I_{p1}) = \cos\frac{\theta}{2}\ I_{q1} + \sin\frac{\theta}{2}\ I_{r1}$$

$$\exp(-i\theta I_{p1})\ I_{q2}\ \exp(i\theta I_{p1}) = \cos\frac{\theta}{2}\ I_{q2} - \sin\frac{\theta}{2}\ I_{r2}$$

$$\exp(-i\theta I_{p2})\ I_{q1}\ \exp(i\theta I_{p2}) = \cos\frac{\theta}{2}\ I_{q1} - \sin\frac{\theta}{2}\ I_{r2}$$

$$\exp(-i\theta I_{p2})\ I_{q2}\ \exp(i\theta I_{p2}) = \cos\frac{\theta}{2}\ I_{q2} - \sin\frac{\theta}{2}\ I_{r1}$$

where $p, q, r = x, y, z$ or cyclic permutation

and $i, j, k = 1, 2, 3$ or cyclic permutation.

$$I_{x,1} = \frac{1}{2} I_x \qquad \frac{1}{2}\begin{pmatrix} 0 & 0 & 0 \\ 0 & 0 & 1 \\ 0 & 1 & 0 \end{pmatrix}$$

$$I_{x,2} = \frac{1}{2}(I_y I_z + I_z I_y) \qquad \frac{1}{2}\begin{pmatrix} 0 & 0 & 0 \\ 0 & 0 & -i \\ 0 & i & 0 \end{pmatrix}$$

$$I_{x,3} = -\frac{1}{2}(I_y^2 - I_z^2) \qquad \frac{1}{2}\begin{pmatrix} 0 & 0 & 0 \\ 0 & 1 & 0 \\ 0 & 0 & -1 \end{pmatrix}$$

$$I_{y,1} = \frac{1}{2} I_y \qquad \frac{1}{2}\begin{pmatrix} 0 & 0 & 1 \\ 0 & 0 & 0 \\ 1 & 0 & 0 \end{pmatrix}$$

$$I_{y,2} = \frac{1}{2}(I_z I_x + I_x I_z) \qquad \frac{1}{2}\begin{pmatrix} 0 & 0 & i \\ 0 & 0 & 0 \\ -i & 0 & 0 \end{pmatrix}$$

$$I_{y,3} = -\frac{1}{2}(I_z^2 - I_x^2) \qquad \frac{1}{2}\begin{pmatrix} -1 & 0 & 0 \\ 0 & 0 & 0 \\ 0 & 0 & 1 \end{pmatrix}$$

$$I_{z,1} = \frac{1}{2} I_z \qquad \frac{1}{2}\begin{pmatrix} 0 & i & 0 \\ -i & 0 & 0 \\ 0 & 0 & 0 \end{pmatrix}$$

$$I_{z,2} = \frac{1}{2}(I_x I_y + I_y I_x) \qquad \frac{1}{2}\begin{pmatrix} 0 & 1 & 0 \\ 1 & 0 & 0 \\ 0 & 0 & 0 \end{pmatrix}$$

$$I_{z,3} = -\frac{1}{2}(I_x^2 - I_y^2) \qquad \frac{1}{2}\begin{pmatrix} 1 & 0 & 0 \\ 0 & -1 & 0 \\ 0 & 0 & 0 \end{pmatrix}$$

$$\boxed{[I_{p,j}, I_{p,k}] = i I_{p,\ell}}$$

$p = x, y, z$

$j, k, \ell = 1, 2, 3$ or cyclic permutation

XBL 7611-9877a

Table II

where $\Delta\omega \equiv \omega_0 - \omega$. Since all further calculations will be in the rotating frame we drop the asterisk henceforth. Using the operators defined above this may be written:

$$\mathcal{H} = -2\Delta\omega I_{z1} - 2\omega_1 I_{x1} + \frac{2}{3}\omega_Q(I_{x3} - I_{y3}). \qquad \text{(III-3)}$$

For a variety of values of $\Delta\omega$, ω and ω_Q we will see that the behavior under this Hamiltonian is quite simple. Since these have been derived in considerable detail elsewhere[19,64] we will only discuss the form and experimental implications of the Hamiltonian, in these cases. To simplify the calculations of density matrix evolution, the Hamiltonians will be written wherever possible as a sum of terms, all of which commute.

To do this we will try to write the Hamiltonian in terms of the diagonal operators I_{x3}, I_{y3} and I_{z3}. This is accomplished by rotating the Hamiltonian into a new "tilted" frame, so that the vector representation of the Hamiltonian has components only along the I_{p3} axes. The tilt operators are defined as $U_{pi}(\phi) = \exp(i\phi I_{pi})$ meaning a rotation of angle ϕ about the p,i (p = x,y,z and i = 1,2,3) axis. These are applied to operators X as $U^{+}_{pi}(\phi)\ X\ U_{pi}(\phi)$.

Case 1.

$\Delta\omega = 0$, $\omega_1 = 0$; no irradiation, with rotating frame at frequency ω_0 on resonance, no tilt necessary.

$$\begin{aligned}\mathcal{H} &= +\frac{2}{3}\omega_Q(I_{x3} - I_{y3}) \\ &= \omega_Q I_{x3} - \frac{1}{3}\omega_Q(I_{y3} - I_{z3}) \qquad \text{(III-10)} \\ &= -\omega_Q I_{y3} - \frac{1}{3}\omega_Q(I_{z3} - I_{x3}).\end{aligned}$$

These three forms are equivalent and hence may be freely interchanged. Under this Hamiltonian an initial density matrix $\rho(0) = I_x$ evolves very simply:

$$\rho(t) = 2e^{-i\mathcal{H}t}\, I_{x1}\, e^{i\mathcal{H}t} = 2(I_{x1}\cos\omega_Q t + I_{x2}\sin\omega_Q t). \qquad \text{(III-11)}$$

We see that the evolution is restricted to the fictitious I_x space.

Case 2

$\Delta\omega \neq 0$; $\omega_1 = 0$; no irradiation with rotating frame off resonance.

$$\mathcal{H} = -\,2\Delta\omega I_{z1} + \frac{2}{3}\omega_Q(I_{x3} - I_{y3}). \qquad \text{(III-12)}$$

To rewrite this as a sum of commuting operators we apply a tilt of $U_{z2}(\pi/2) = e^{i\pi/2\, I_{z2}}$,

$$\mathcal{H}^T = 2\Delta\omega\, I_{z3} + \frac{2}{3}\omega_Q\,(I_{x3} - I_{y3}). \qquad \text{(III-13)}$$

Case 3

$\Delta\omega = 0$, $\omega_1 \neq 0$; irradiation on resonance.

$$\mathcal{H} = -\,2\omega_1 I_{x1} + \omega_Q I_{x3} - \frac{1}{3}\omega_Q(I_{y3} - I_{z3}). \qquad \text{(III-14)}$$

Again to write as the sum of commuting parts we tilt with $U_{x2}(\theta) = e^{i\theta I_{x2}}$ where $\theta = \tan^{-1}(2\omega_1/\omega_Q)$,

$$\mathcal{H}^T = \omega_e I_{x3} - \omega_Q(I_{y3} - I_{z3}) \qquad \text{(III-15)}$$

$$= -\frac{1}{2}(\omega_e - \omega_Q) I_{z3} + [\,\frac{2}{3}\omega_Q + \frac{1}{2}(\omega_e - \omega_Q)]\,(I_{x3} - I_{y3})$$

where we define an effective frequency

$$\omega_e = (4\omega_1^2 + \omega_Q^2)^{1/2} . \qquad \text{(III-16)}$$

If $\omega_1 << \omega_Q$ then (III-15) approximately goes to the the simpler form

$$\mathcal{H}^T = -\left(\frac{\omega_1^2}{\omega_Q}\right) I_{z3} + \frac{2}{3}\omega_Q(I_{x3} - I_{y3}) . \qquad \text{(III-17)}$$

Case 4

$\Delta\omega \neq 0$, $\omega_1 \neq 0$; general off resonance irradiation. In this case all terms in the Hamiltonian must be considered, and in general there is no simple transformation to generate the Hamiltonian as a sum of commuting terms. Solutions for this case may be calculated numerically by computer. However for important cases for which $\omega_1 << \omega_Q$, approximate analytical forms may be generated.

Case 4a

$\Delta\omega \sim \omega_Q$, $\omega_1 << \omega_Q$; irradiation near the low quadrupole satellite. Writing $\Delta\omega = \omega_Q + \delta\omega$

$$\mathcal{H} = -2(\omega_Q+\delta\omega) I_{z1} + \frac{2}{3}\omega_Q(I_{x3}-I_{y3}) + 2\omega_1 I_{x1} . \qquad \text{(III-18)}$$

Tilting this with $U_{z2}(\pi/2)$,

$$\begin{aligned} \mathcal{H}^T &= 2(\omega_Q+\delta\omega) I_{z3} + \frac{2}{3}\omega_Q(I_{x3}-I_{y3}) - \sqrt{2}\omega_1 (I_{x2}-I_{y2}) \\ &= -\delta\omega I_{x3} - \left(\frac{4}{3}\omega_Q + \delta\omega\right)(I_{y3}-I_{z3}) - \sqrt{2}\omega_1(I_{x1} - I_{y2}) . \end{aligned} \qquad \text{(III-19)}$$

Using the approximation $\omega_1 << \omega_Q$ the last term $\sqrt{2}\,\omega_1 I_{y2}$ may be neglected giving

$$\mathcal{H}^T = -\delta\omega\, I_{x3} - \sqrt{2}\,\omega_1\, I_{x1} - (\tfrac{4}{3}\,\omega_Q + \delta\omega)(I_{y3} - I_{z3}). \qquad \text{(III-20)}$$

Since the last term is commutative with the others it may be disregarded in most cases and the behavior of the system will be like that of an ordinary spin-1/2 system, off resonance by $\delta\omega$ and with a modified γ.

Case 4b

$\Delta\omega \sim -\omega_Q$, $\omega_1 << \omega_Q$; irradiation near the upper quadrupole satellite. By a procedure exactly analogous to case 4a, with $\Delta\omega = -\omega_Q + \delta\omega$ we obtain

$$\mathcal{H}^T = -\delta\omega I_{y3} + \sqrt{2}\,\omega_1\, I_{y2} - (\tfrac{4}{3}\omega_Q - \delta\omega)(I_{z3} - I_{x3}). \qquad \text{(III-21)}$$

The form and behavior are exactly analogous to Case 4a.

Case 4c

$\Delta\omega \sim 0$, $\omega_1 << \omega_Q$; irradiation near the center of the spectrum. This is where we expect the interesting double quantum effects to occur. We let $\Delta\omega = \delta\omega$,

$$\mathcal{H} = -2\delta\omega\, I_{z1} - 2\omega_1 I_{x1} + \tfrac{2}{3}\,\omega_Q\,(I_{x3} - I_{y3}). \qquad \text{(III-22)}$$

To get this to the desired form we tilt with $U_{x2}(\theta) = e^{i\theta I_{x2}}$ where $\theta \equiv \tan^{-1}(2\omega_1/\omega_Q)$ giving

$$\mathcal{H}^T = -2\delta\omega\,(\cos\tfrac{\theta}{2}\, I_{z1} + \sin\tfrac{\theta}{2}\, I_{y2}) + \omega_e I_{x3} - \tfrac{1}{3}\,\omega_Q(I_{y3} - I_{z3}). \qquad \text{(III-23)}$$

Since $2\delta\omega\omega_1 << \omega_Q^2$ the $\sin\frac{\theta}{2}$ term may be ignored giving

$$\mathcal{H}^T = -2\delta\omega I_{z1} - \frac{1}{2}(\omega_e - \omega_Q) I_{z3} + \frac{2}{3}\omega_Q (I_{x3} - I_{y3}) \qquad \text{(III-24)}$$

and $\omega_e - \omega_Q$ may be further approximated by ω_1^2/ω_Q. Again the third term commutes with the others, so that the behavior is exactly like a spin-1/2.

3. Density Matrix

Up to this point we have found Hamiltonians in a simple form, but in a tilted space. It is important to remember that for calculations of density matrix evolution, we must also tilt the density matrix, with the same operator used to tilt the Hamiltonian. This results in the following tilted operators for observables: Case 4a. $\Delta\omega = \omega_Q + \delta\omega$, The tilt operator is $U_{z2}(\frac{\pi}{2})$ giving

$$I_x^T = \sqrt{2}\,(I_{x1} - I_{y2}) \quad \text{and} \quad I_y^T = \sqrt{2}\,(I_{y1} + I_{x2}). \qquad \text{(III-25)}$$

Case 4b

$\Delta\omega = \delta\omega$, $\delta\omega$ and $\omega_1 << \omega_Q$

The tilt operator is $U_{x2}(\theta)$, $\tan\theta = 2\omega_1/\omega_Q$ giving

$$I_x^T = 2(\omega s\theta\, I_{x1} - \sin\theta\, I_{x3}) \quad \text{and} \quad I_y^T = 2(\cos\frac{\theta}{2}\, I_{y1} - \sin\frac{\theta}{2}\, I_{z2}). \qquad \text{(III-26)}$$

Case 4c

$\Delta\omega = -\omega_Q + \delta\omega$, $\delta\omega$ and $\omega << \omega_Q$

The tilt operator is $U_{z2}(\frac{\pi}{2})$ giving

$$I_x^T = \sqrt{2}\,(I_{x1} - I_{y2}) \quad \text{and} \quad I_y^T = \sqrt{2}\,(I_{y1} + I_{x2}). \qquad \text{(III-27)}$$

Any other operators needed in the density matrix calculations may be tilted in the same manner.

Now that Hamiltonians have been defined for the cases of practical interest here, we may proceed with theoretical calculations of experiments. These calculations break up logically into three parts, preparation of a desired density matrix, its evolution under some particular Hamiltonian, and then detection of some signal representative of the state of the system. In some instances this is then a special form of two dimensional NMR.[65] We will write the density matrix expanded in terms of the fictitious operators

$$\rho(t) = \sum_{i=1}^{3} \sum_{p=x,y,z} a_{pi}(t) I_{pi} \qquad \text{(III-28)}$$

where

$$\rho(t) = e^{-i\mathcal{H}t}\, \rho(0)\, e^{i\mathcal{H}t}. \qquad \text{(III-29)}$$

At thermal equilibrium the initial density matrix is

$$\rho_0 = bI_z \quad \text{with} \quad b = \frac{\omega_0}{kT}. \qquad \text{(III-30)}$$

This initial density matrix must also be tilted when tilted Hamiltonians are used in the calculation.

For irradiation near one satellite, Case 4a (or 4b) the tilt operator was $U_{z2}(\frac{\pi}{2})$. In this frame the initial density matrix is

$$\rho_0^T = -2bI_{z3} = bI_{x3} + b(I_{y3} - I_{z3}) \qquad \text{(III-31)}$$

and applying (III-29), and $\mathcal{H}^T$ (III-20) with $\delta\omega = 0$;

$$\rho^T(t) = b\ (I_{x3}\ \cos\sqrt{2}\ \omega_1 t + I_{z2} \sin\sqrt{2}\ \omega_1 t) + b(I_{y3} - I_{z3}). \qquad \text{(III-32)}$$

The first term is from rotation about x1 in the fictitious x space. The second term comes from the quadrupole coupling; it does not yield a signal, and thus may be ignored for the present, although it is crucial for cross polarization experiments.[64] After a pulse we may calculate the signals which may be observed, $\langle I_x(t)\rangle$ and $\langle I_y(t)\rangle$ from (I-5). We define signals in the x and y directions at time t

$$\begin{aligned} S_x(t) &= \gamma \left\langle I_x(t)\right\rangle = \gamma \mathrm{Tr}(\rho(t)\ I_x) = \gamma \mathrm{Tr}(\rho^T(t)\ I_x^T) \\ S_y(t) &= \gamma \left\langle I_y(t)\right\rangle = \gamma \mathrm{Tr}(\rho(t)\ I_y) = \gamma \mathrm{Tr}(\rho^T(t)\ I_y^T). \end{aligned} \qquad \text{(III-32)}$$

Using the tilted forms for $\rho(t)$, I_x and I_y we find for t = pulse width:

$$\begin{aligned} S_x(t) &= 0 \\ S_y(t) &= \sqrt{2}\ b\gamma\ \sin\sqrt{2}\ \omega_1 t\ \mathrm{Tr}(I_x{}^2) = \frac{1}{2\sqrt{2}}\ S_0\ \sin\sqrt{2}\ \omega_1 t \\ S_0 &\equiv 4Nb\gamma\ \frac{1}{2(2I+1)} = \frac{2}{3}\ N\gamma b \end{aligned} \qquad \text{(III-33)}$$

where N is the number of spins in the sample. For this rotation in the x-space, the magnetogyric ratio is effectively $\sqrt{2}\ \gamma$. Dropping the I_{y2} term in the tilted Hamiltonian eliminates any response from the distant quadrupole satellite. Exactly analogous equations may also be derived for the upper satellite.

When the off resonance term is included in the above calculation

$$\mathcal{H}^T = -\ \delta\omega\ I_{x3} - \sqrt{2}\ \omega_1\ I_{x1} \qquad \text{(III-34)}$$

and the signals are

$$S_x(t) = \frac{1}{2\sqrt{2}} S_0 \sin\phi \cos\phi (1 - \cos\omega_s t)$$

$$S_y(t) = \frac{1}{2\sqrt{2}} S_0 \cos\phi \sin\omega_s t \qquad \text{(III-35)}$$

where

$$\omega_s = (\delta\omega^2 + 2\omega_1^2)^{1/2} \quad \text{and } \phi = \tan^{-1} \frac{\delta\omega}{\sqrt{2}\,\omega_1} .$$

Thus a small off resonance term only induces a slight mixing of the y signal into x.

For irradiation near the center of the spectrum, Case 4c, we proceed in an analogous fashion. The tilt operator used was $U_{x2}(\theta)$, giving a tilted initial density matrix

$$\rho^T(0) = 2b \left(\cos\frac{\theta}{2} I_{z1} + \sin\frac{\theta}{2} I_{y2}\right). \qquad \text{(III-36)}$$

Applying (III-29) with $\mathcal{H}^T$ (III-24)

$$\rho^T(t) = 2b \cos\frac{\theta}{2} [I_{z1}\cos\tfrac{1}{2}(\omega_e-\omega_Q)t - I_{z2} \sin\tfrac{1}{2}(\omega_e-\omega_Q)t]$$
$$+ 2b \sin\frac{\theta}{2} [I_{y2}\cos\tfrac{1}{2}(\omega_e-\omega_Q)t + I_{y1} \sin\tfrac{1}{2}(\omega_e-\omega_Q)t]. \qquad \text{(III-37)}$$

For $\omega_1 << \omega_Q$ this may be simplified to

$$\rho^T(t) = 2b \left(I_{z1} \cos\frac{\omega_1^2}{\omega_Q} t - I_{z2} \sin\frac{\omega_1^2}{\omega_Q} t \right). \qquad \text{(III-38)}$$

The second term in (III-38) is of great importance to us. The operator I_{z2} has matrix elements only between $|+\rangle$ and $|-\rangle$ levels (see Table II) and hence represents in the density matrix a coherence between these levels,

which are coupled together directly only by a double quantum transition. In this case the behavior is again that of a fictitious spin-1/2 (the z space), and where the state rotates about the effective field I_{z3} with an effective magnetogyric ration $\frac{\omega_1}{\omega_Q}\gamma$, behavior previously observed by Hatanaka et al.[61] The signals after the pulse may be calculated using the tilted I_x and I_y operators.

$$I_x^T = 2(\cos\theta\ I_{x1} - \sin\theta\ I_{x3})$$
$$I_y^T = 2(\cos\frac{\theta}{2}\ I_{y1} - \sin\frac{\theta}{2}\ I_{z2}). \qquad \text{(III-39)}$$

Then

$$S_x(t) = 0$$
$$S_y(t) = \frac{1}{2}\gamma\ S_0\ \sin\theta\ [\sin\frac{1}{2}(\omega_e-\omega_Q)t + \sin\frac{1}{2}(\omega_e-\omega_Q)t] \approx 0 \qquad \text{(III-40)}$$

where $S_y(t) = 0$ since $\sin\theta \approx 0$. After such a weak pulse in the center of the quadrupole split spectrum we predict no signal, i.e., the double quantum state has no ordinary magnetization associated with it. We will call a weak pulse of this sort a double quantum pulse. As for usual r.f. pulses we may adjust the length to give a $\frac{\pi}{2}$ rotation simply by adjusting $t = \pi\ \omega_Q/2\omega_1^2$.

The most general case, where ω_1, ω_Q and $\Delta\omega$ maybe of the same size cannot be easily solved analytically. When such cases are of interest, a computer must be used to follow the complex motions of the state vectors.

Once some particular state of the system has been prepared, usually by application of r.f. pulses, we wish to calculate its evolution under the Hamiltonian without any r.f. irradiation,

$$\mathcal{H} = -2\Delta\omega\ I_{z1} + \frac{2}{3}\omega_Q(I_{x3} - I_{y3}). \qquad \text{(III-40)}$$

This is again done by calculating (III-29) where $\rho(0)$ is now the non-equilibrium density matrix prepared by some r.f. pulse or pulses, though it may still be specified by

$$\rho(0) = \sum_i \sum_p a_{pi}\ (0)\ I_{pi} \qquad \text{(III-41)}$$

We will ignore relaxation effects in our calculations, although it may be added phenomenologically as a damping with time of any coherence, with time constant T_2. If we assume that $a_{p3}\ (0) = 0$ for all p, then the coefficients of operators in (III-28) for any time may be easily calculated and are shown in Table III. In the particular case $\Delta\omega = 0$ the behavior is simpler and

$$\begin{aligned} a_{x1}(t) &= a_{x1}(0)\ \cos\omega_Q t - a_{x2}(0)\ \sin\omega_Q t \\ a_{x2}(t) &= a_{x1}(0)\ \sin\omega_Q t + a_{x2}(0)\ \cos\omega_Q t \\ a_{y1}(t) &= a_{y1}(0)\ \cos\omega_Q t + a_{y2}(0)\ \sin\omega_Q t \\ a_{y2}(t) &= -a_{y1}(0)\ \sin\omega_Q t + a_{y2}(0)\ \cos\omega_Q t. \end{aligned} \qquad \text{(III-42)}$$

Comparison of (III-42) and Table III makes clear that under the quadrupole coupling alone the x and y spaces evolve independently, but when a resonance offset is present these spaces are mixed. As was predicted from the energy levels in Fig. 32, the double quantum z space evolves only with resonance offset, completely independent of quadrupole coupling.

Table III

$$a_{x1}(t) = \frac{1}{2}[a_{x1}(0)+a_{y2}(0)]\cos(\omega_Q-\Delta\omega)t - \frac{1}{2}[a_{x2}(0)+a_{y1}(0)]\sin(\omega_Q-\Delta\omega)t$$

$$- \frac{1}{2}[a_{y1}(0)-a_{x2}(0)]\sin(-\omega_Q-\Delta\omega)t - \frac{1}{2}[a_{y2}(0)-a_{x1}(0)]\cos(-\omega_Q-\Delta\omega)t$$

$$a_{x2}(t) = \frac{1}{2}[a_{x2}(0)+a_{y1}(0)]\cos(\omega_Q-\Delta\omega)t + \frac{1}{2}[a_{x1}(0)+a_{y2}(0)]\sin(\omega_Q-\Delta\omega)t$$

$$- \frac{1}{2}[a_{y1}(0)-a_{x2}(0)]\cos(-\omega_Q-\Delta\omega)t + \frac{1}{2}[a_{y2}(0)-a_{x1}(0)]\sin(-\omega_Q-\Delta\omega)t$$

$$a_{y1}(t) = \frac{1}{2}[a_{y1}(0)-a_{x2}(0)]\cos(-\omega_Q-\Delta\omega)t - \frac{1}{2}[a_{y2}(0)-a_{x1}(0)]\sin(-\omega_Q-\Delta\omega)t$$

$$+ \frac{1}{2}[a_{x1}(0)+a_{y2}(0)]\sin(\omega_Q-\Delta\omega)t + \frac{1}{2}[a_{x2}(0)+a_{y1}(0)]\cos(\omega_Q-\Delta\omega)t$$

$$a_{y2}(t) = \frac{1}{2}[a_{y2}(0)-a_{x1}(0)]\cos(-\omega_Q-\Delta\omega)t + \frac{1}{2}[a_{y1}(0)-a_{x2}(0)]\sin(-\omega_Q-\Delta\omega)t$$

$$+ \frac{1}{2}[a_{x1}(0)+a_{y2}(0)]\cos(\omega_Q-\Delta\omega)t - \frac{1}{2}[a_{x2}(0)+a_{y1}(0)]\sin(\omega_Q-\Delta\omega)t$$

$$a_{z1}(t) = a_{z1}(0)$$

$$a_{z2}(t) = a_{z2}(0)\cos 2\Delta\omega t$$

$$a_{x3}(t) = a_{z2}(0)\sin 2\Delta\omega t$$

$$a_{x3}(t) = a_{y3}(t) = 0.$$

Using the results of Table III the signals observed may be calculated.

$$S_x(t) = \gamma \, Tr(\rho(t) \, I_x) = a_{x1}(t)\psi(t)$$
$$S_y(t) = \gamma \, Tr(\rho(t) \, I_y) = a_{y1}(t)\psi(t) \qquad \text{(III-43)}$$

where $\psi(t)$ takes care of normalization and any damping terms. We may also define a double quantum coherence, through not directly observable,

$$Q(t) = a_{z2}(t) \; \psi(t) \qquad \text{(III-44)}$$

whose decay, monitored in a fashion described below, gives a high resolution NMR spectrum, the basis of Fourier Transform Double Quantum NMR.

The calculation above of preparation and evolution of particular states gives us all the information of interest, from a theoretical viewpoint. However, in any experiment all information about the system must derive from measurement of the observables, S_x and S_y. If we irradiate near one of the quadrupole satellites, then an observable signal is obtained (III-35), its evolution may be directly observed and followed, Table III, and Fourier Transformation of this signal allows measurement of ω_Q, $\Delta\omega$ and $\psi(t)$. The intent of this chapter is to gain further high resolution information from the double quantum decay Q(t), (III-44). Since this coherence evolves without detectable signal, after preparing it and letting it evolve for time τ, we must transfer the coherence into an observable. This may be achieved by application of a strong r.f. pulse, $\omega_1 >> \omega_Q$, and $\omega_1 >> \Delta\omega$. In this case the only important term in the Hamiltonian is the r.f.,

$$\mathcal{H} = - 2\omega_1 I_{x1} \qquad \text{(III-45)}$$

which will induce only single quantum transitions. The effect of this

Hamiltonian on any initial density matrix is easily calculated. Table IV lists the effect of a strong pulse on different initial density matrices. From the table it is easily seen that a pulse such that $\omega_1 t = \pi/2$ rotates a density matrix I_{z2} into I_{y2}, which evolves under the r.f. free Hamiltonian (III-40) to give a signal. Figure 33 shows the pulse sequence used for FTDQ NMR. Starting with an equilibrium density matrix $\rho_i = I_{z1}$, a double quantum pulse $\omega_1^2 / \omega_Q t_{p1} = \pi/2$ is applied to give

$$\rho\ (t_{p1}) = I_{z2}\,. \qquad \text{(III-46)}$$

This evolves for a time τ, Table III, to give

$$\rho(t_{p1} + \tau) = -\ I_{z2}\ \cos 2\Delta\omega\tau + I_{z3}\ \sin 2\Delta\omega\tau. \qquad \text{(III-47)}$$

A strong (single quantum) pulse $\omega_1 t_{p2} = \pi/2$ is applied to probe the coherence giving

$$\rho(t_{p1} + \tau + t_{p2}) = I_{y2}\ \cos 2\Delta\omega\tau + \frac{1}{2}\,[\,I_{x3} - (I_{y3} - I_{z3})]. \qquad \text{(III-48)}$$

This then evolves for a time t during which signal is observed,

$$\begin{aligned} S_x(t) &= S_0\ \cos 2\Delta\omega\tau\ \ \sin\omega_Q t\ \sin\Delta\omega t \\ S_y(t) &= S_0\ \cos 2\Delta\omega\tau\ \ \sin\omega_Q t\ \cos\Delta\omega t. \end{aligned} \qquad \text{(III-49)}$$

It is sometimes convenient to Fourier Transform the observed signal $S_x + iS_y$, and plot the peak intensities against τ to give the double quantum free induction decay. A second Fourier Transform yields the double quantum spectrum, free of quadrupole couplings. In another approach $S_x(0)$ and $S_y(0)$ are used to generate the double quantum free induction decay.

Table IV

ρ_i (before pulse)	ρ_f (after P pulse)
I_{p1}	I_{p1}
I_{p2}	$I_{p2} \cos 2\omega_1 t - I_{p3} \sin 2\omega_1 t$
I_{p3}	$I_{p3} \cos 2\omega_1 t + I_{p2} \sin 2\omega_1 t$
I_{q1}	$I_{q1} \cos\omega_1 t - I_{r1} \sin\omega_1 t$
I_{q2}	$I_{q2} \cos\omega_1 t + I_{r2} \sin\omega_1 t$
I_{q3}	$-\frac{1}{2}(I_{p3} \cos 2\omega_1 t + I_{p2} \sin 2\omega_1 t) + \frac{1}{2}(I_{q3}-I_{r3})$
I_{r1}	$I_{r1} \cos\omega_1 t + I_{q1} \sin\omega_1 t$
I_{r2}	$I_{r2} \cos\omega_1 t - I_{q2} \sin\omega_1 t$
I_{r3}	$-\frac{1}{2}(I_{p3} \cos 2\omega_1 t + I_{p2} \sin 2\omega_1 t) - \frac{1}{2}(I_{q3} - I_{r3})$

p, q, r = x, y, z or y, z, x

4. Real Responses

In the previous section we have derived the response of a spin 1 system to ideal pulses. However when doing experiments real pulses are used which often differ considerably from ideality. For double quantum pulses we assumed $\omega_1 << \omega_Q$, so that r.f. effects on the single quantum transitions could be ignored. For a real pulse of reasonable strength, a significant amplitude for the single quantum coefficient may be generated in addition to double quantum, Fig. 34 and Fig. 35. The response to an arbitrary pulse can be calculated, and the constraints that a_{z2} be maximized and that there is no observable signal after the pulse leads to two requirements[19,64]

$$t_{p1} = \frac{2m-1}{\omega_Q}\pi \qquad \text{(III-50)}$$

$$k,\ m = 1,2\ldots\ k \geqslant m$$

$$\omega_1 = \frac{1}{2}\left[\left(\frac{2k}{2m-1}\right)^2 - 1\right]^{1/2} \omega_Q. \qquad \text{(III-51)}$$

A pulse meeting these requirements for any k,m will create a density matrix of I_{z2}. Even if these requirements are not fulfilled some I_{z2} may be created and observed, but analysis is more complex.

For the probing single quantum pulse we assumed that $\omega_1 >> \omega_Q$, a requirement often difficult to meet in practice. The result after an arbitrary pulse may be calculated also[19,64] giving signal

$$S_y(t) = S_0\ a_y \cos 2\Delta\omega\tau\ \sin(\omega_Q t + \phi) \qquad \text{(III-52)}$$

where

$$a_y = (a_{y1}(T)^2 + a_{y2}(T)^2)^{1/2}$$
$$\phi = \tan^{-1}(a_{y1}(T)/a_{y2}(T)) \qquad \text{(III-53)}$$
$$T = t_{p1} + \tau + t_{p2} .$$

The effect of ω_Q on a_y and ϕ are shown in Fig. 36. While this effect introduces a scaling of efficiency in a particular experiment, as long as ω_1 and ω_Q are constant through an experiment it causes no problems.

5. Polycrystalline Samples

In all of the analysis of double quantum calculations just performed it was implicitly assumed that there was only one value of ω_Q to be considered, and for a single crystal sample this may be true (more often there are a small number of ω_Q values, each of which may be treated separately). However in a powder sample the values of ω_Q range from $-\frac{3}{4}eQV_{zz}$ to $+\frac{3}{4}eQV_{zz}$ continuously (see (I-20)). Since the effects of pulses are dependent on the size of ω_Q, this greatly complicates analysis. Since many approximations will break down for at least some ω_Q values, the responses to pulses henceforth will be predicted exactly by computer. It will be valuable to see the efficiency of each pulse as a function of ω_Q, since each value of ω_Q will correspond to some specific chemical shift. This means that the chemical shift (or dipolar) powder pattern must be multiplied by a transfer function representing the efficiency with which double quantum coherence for each ω_Q was prepared and probed by the pulses applied. The first step in an experiment, the preparation of double quantum coherence is shown in Fig. 37. For each experiment the

pulse amplitude, ω_1, and length may be optimized to give the best possible response for the range of ω_Q values involved, through use of computer simulations. Figure 38 then shows the overall transfer function for preparation and detection of a_{z2} immediately after the probe pulse. While there is some loss in sensitivity compared to ideality the response is fairly uniform over a wide range of ω_Q values. For $\omega_Q = 0$ (no quadrupole coupling) double quantum coherence cannot be prepared and for any pulse sequence the transfer function must drop to zero there. In a real experiment, however, signal cannot be detected immediately after a pulse due to a finite recovery time from the pulse overload for electronic components in the spectrometer. This delays measurement of signal for ~ 30 μsec after the last pulse. Since the density matrix still evolves during this time, the transfer function is changed to that in Fig. 39. Since this changes sign many times any broadening will average the response to zero. To alleviate this problem a quadrupole echo may be used. Such echoes are well known in quadrupolar systems,[1] and the expected response is easily calculated with the fictitious spin formalism. An initial state $\rho_i = I_{z1}$ is subjected to two single quantum ($\omega_1 >> \omega_Q$, $\Delta\omega$) $\pi/2$ pulses spaced by a time τ, the first pulse being in the x direction, the second in the y. Then from Tables III and IV

$$a_{y1}(t_{p1}) = 1 \quad \text{and} \quad a_{y1}(2\tau) = \cos^2\Delta\omega\tau\ \psi(2\tau) \qquad \text{(III-54)}$$

$$a_{x1}(2\tau) = \cos\Delta\omega\tau\ \sin\Delta\omega\tau\ \psi(2\tau).$$

If $\Delta\omega = 0$ or τ is kept short then the refocusing by the second pulse is very good. Figure 40 shows the exact response to a pair of strong pulses, and we see that there is better than 80% refocusing even for values of ω_Q

not much less than ω_1, and the echo amplitude is a good measure of I_{z1} before the pulses. We may then combine these echo pulses with a pair of weak pulses. The first weak pulse creates I_{z2} coherence, it evolves for a variable time, then the second pulse "stores" the magnitude of double quantum coherence along I_{z1} which is probed by the echoing pair after a time T_2, which allows single quantum coherence to decay. Figure 41 shows the overall transfer function for such a pulse sequence. While the response is far from the ideal straight line at unit efficiency, such a pulse sequence should give a measurable intensity even at large ω_Q, and hence the corresponding chemical shielding (or dipolar) powder pattern should have its proper width. If we assume that the quadrupole and chemical shielding tensors are both axial, with their symmetry axes in the same direction we can easily calculate the shape of the unbroadened powder pattern from the transfer function, Fig. 42.

The response to two strong pulses suggests an alternate method for preparation of double quantum coherence. If two strong pulses are applied as above for generating an echo, but both are of x phase, then with proper timing the density matrix may be made proportional to I_{z2}. Before the first pulse $\rho_i = I_{z1}$. Application of a $\pi/2$ x pulse yields

$$\rho(t_{p1}) = I_{y1}. \qquad \text{(III-55)}$$

Free evolution for a time τ gives (Table III)

$$\begin{aligned} a_{x1}(\tau) &= \sin(\Delta\omega\tau)\ \cos(\omega_Q\tau) \\ a_{x2}(\tau) &= \sin(\Delta\omega\tau)\ \sin(\omega_Q\tau) \\ a_{y1}(\tau) &= \cos(\Delta\omega\tau)\ \cos(\omega_Q\tau) \\ a_{y2}(\tau) &= \cos(\Delta\omega\tau)\ \sin(\omega_Q\tau). \end{aligned} \qquad \text{(III-56)}$$

If $\omega_Q >> \Delta\omega$ then we may choose τ so that $\omega_Q\tau = \pi/2$ and $\Delta\omega\tau \approx 0$ so that $a_{y2} \approx 1$. The second $\pi/2$ x-pulse then rotates a_{y2} into a_{z2}, Table IV. For a polycrystalline sample then the transfer function will be approximately $\sin\omega_Q\tau$, the coefficient of I_{y2}. Since this transfer function may be changed by varying τ, a Fourier series approximation to a square wave may be generated. Figure 43 shows the first three transfer functions that would be summed with appropriate weighting to give the total transfer function also shown. Although sensitivity is lost in such an experiment, in principle an arbitrarily good transfer function may be generated. Figure 44 shows the actual result of a three term square wave approximation, with imperfect pulses, by computer simulation.

For many powder samples obtaining good signal to noise ratio can be a problem. If the four pulse sequence of Fig. 41 is used then the signal is sampled at only one point. Since separate experiments must be performed for each value of τ, experiments become very long if much averaging must be done at each τ. This may be reduced somewhat by noticing that <u>at</u> the echo point the density matrix is I_{y1}, exactly the same as after the strong x pulse. Hence if at a time τ after the echo another y pulse is applied a second echo should occur. In fact this may be repeated several times before off resonance and broadening damp the echo amplitude. Figure 45 shows the response to a simple echo sequence, the third echo response and the average of four sequential echoes. By coadding the signals from each echo the signal to noise ratio at each τ may be increased considerably. Of course this average echo transfer function must be multiplied by that for the preparation sequence to give the overall efficiency for the experiment.

6. Dipolar Couplings

a) Hamiltonians

Up to this point we have ignored the possibility of dipolar couplings among deuterons. If a sample contains small groups of spins close together, relatively separated from other groups the resonance line may show structure from the dipolar couplings. Since dipolar couplings contain information about orientations and distances (I-32), their measurement may provide useful information. This was realized long ago by Pake, who used fine structure in proton resonance lines for analysis of the structure of water in hydrated crystals.[66] However applications of this approach are limited to simple systems. Measurements of heteronuclear dipolar couplings have been made using variations of dilute spin NMR in powders[67,68,69] and single crystals.[70,71,72,73] In some cases multiple pulse sequences were used to suppress couplings among abundant spins, however most of these techniques are applicable only to small systems. A few measurements have been made of homonuclear couplings between ^{13}C[69,74,75] for determinations of distances and relative orientations of chemical shielding and dipolar coupling tensors. Working with naturally dilute spins has the advantage that two specific sites may be enriched in the observed spin so that their relative positions may be determined without excessive interference from other sites. Deuterium labelling allows the possibility of determining hydrogen positions in a similar manner. This is very attractive since hydrogens are particularly difficult to find in x-ray structure determinations. However, unlike the other systems mentioned which were studied by NMR, deuterium has quadrupole couplings which broaden both single crystal and powder lines, often

to the point that dipolar couplings are unobservable. Since FTDQ NMR removes quadrupole couplings from the spectrum its use should make such studies feasible.

The Hamiltonian for two spins I and S which have quadrupole couplings and are dipolar coupled to each other is

$$\mathcal{H} = -\omega_0 I_z - \omega_0 S_z + \frac{1}{3}\omega_{QI}\,[3I_z^2 - I(I+1)] + \frac{1}{3}\omega_{QS}\,[3S_z^2 - S(S+1)] - d_{IS}\,(2I_zS_z - I_xS_x - I_yS_y), \tag{III-57}$$

where

$$d_{IS} = \frac{\gamma^2\hbar}{r^3}\,P_2(\cos\beta_{IS})$$

contains all of the structural information, and assuming that differences in chemical shift are small compared to both dipolar and quadrupolar terms, we drop them completely. This Hamiltonian may easily be rewritten in the fictitious spin operator formalism to give:

$$\mathcal{H} = -2\Delta\omega I_{z1} - 2\Delta\omega S_{z1} + \frac{2}{3}\omega_{QI}\,[I_{x3} - I_{y3}] + \frac{2}{3}\omega_{QS}\,[S_{x3} - S_{y3}] - d_{IS}\,[2I_{z1}S_{z1} - I_{x1}S_{x1} - I_{y1}S_{y1}]. \tag{III-58}$$

In Chapter I we discussed the truncation of the dipolar and quadrupolar terms in the Hamiltonian by the much larger Zeeman coupling. In the present case since the quadrupole coupling is generally much larger than the dipolar coupling we must truncate the dipolar coupling with respect to the quadrupolar coupling. Two limiting cases arise which we will consider: equivalent deuterons, $\omega_{QI} - \omega_{QS} = 0$ and nonequivalent deuterons $|\omega_{QI} - \omega_{QS}| >> 4d_{IS}$. To calculate the secular contribution of the dipolar term in the Hamiltonian we first find the time dependence in it induced

by the quadrupole term. In the equivalent case we find

$$\mathcal{H}_D(t) = e^{-i\mathcal{H}_Q t} \mathcal{H}_D e^{i\mathcal{H}_Q t} \tag{III-59}$$

$$= 4d_{IS} [2I_{z1}S_{z1} - (\cos\omega_Q t\ I_{x1} + \sin\omega_Q t\ I_{x2})(\cos\omega_Q t\ S_{x1} + \sin\omega_Q t\ S_{x2}) \tag{III-60}$$

$$- (\cos\omega_Q t\ I_{y1} - \sin\omega_Q t\ I_{y2})(\cos\omega_Q t\ S_{y1} - \sin\omega_Q t\ S_{y2})]$$

where $\omega_Q = \omega_{QI} = \omega_{QS}$. If we then average over one cycle of $\omega_Q t$ to extract the time average part we find

$$\mathcal{H}_D' = 4d_{IS} [2I_{z1}S_{z1} - \frac{1}{2} (I_{x1}S_{x1} + I_{x2}S_{x2} + I_{y1}S_{y1} + I_{y2}S_{y2})] . \tag{III-61}$$

In the nonequivalent case an analogous procedure gives:

$$\mathcal{H}_D(t) = 4d_{IS}[2I_{z1}S_{z1} - (\cos\omega_{QI} t\ I_{x1} + \sin\omega_{QI} t\ I_{x2})(\cos\omega_{QS} t\ S_{x1} + \sin\omega_{QS} t\ S_{x2})$$

$$- (\cos\omega_{QI} t\ I_{y1} - \sin\omega_{QI} t\ I_{y2})(\cos\omega_{QS} t\ S_{y1} - \sin\omega_{QS} t\ S_{y2})] . \tag{III-62}$$

The time average is then just

$$\mathcal{H}_D' = 4d_{IS} (2I_{z1}S_{z1}) . \tag{III-63}$$

These are the expected results and are exactly analogous to the quenching of flip-flop terms in the dipolar Hamiltonian for heteronuclear couplings as opposed to homonuclear, in which they are pseudo secular. In the most general case $|\omega_{QI} - \omega_{QS}| \approx 4d_{IS}$ all terms must be kept.

We wish to compare the single quantum and double quantum spectra expected for these systems. The single quantum transitions may be calculated from the Fourier Transform of $\langle I_x(t) + i\, I_y(t)\rangle$ through calculation

of (using $\mathcal{H}$ of (III-58) with appropriately truncated $\mathcal{H}_D$)

$$\left\langle I_x(t)\right\rangle = \mathrm{Tr}(e^{-i\mathcal{H}t}\ 2I_{x1}\ e^{i\mathcal{H}t}\ 2I_{x1})$$
$$\left\langle I_y(t)\right\rangle = \mathrm{Tr}(e^{-i\mathcal{H}t}\ 2I_{x1}\ e^{i\mathcal{H}t}\ 2I_{y1}). \qquad \text{(III-64)}$$

It is often easier to calculate the transition frequencies and moments as done in conventional cw absorption experiments. To do this we first find the eigenfunctions, then calculate the matrix elements of $I_x + S_x$. This is quite easily done for two deuterons since only the dipolar flip-flop term is nonsecular in the eigenbasis of I_z. Tables V and VI list the eigenfunctions, energies and allowed single quantum transitions for two equivalent and nonequivalent deuterons, respectively. These eigenfunctions and energies may of course be calculated for the general case,[96] however such generality is not necessary here.

The double quantum spectrum may be calculated in an analogous fashion, from the evolution of I_{z2} and S_{z2}. If the two deuterons are equivalent then the detected signals from I_{z2} and S_{z2} are inseparable and we calculate the evolution of the sum. For two inequivalent deuterons the single quantum signals are separated by the difference in quadrupole couplings and hence I_{z2} and S_{z2} may be detected separately. This separation is important in analysis of signals in more complex systems.[76] Assuming that the double quantum coherence can be prepared and detected (to be discussed shortly), the evolution we wish to calculate is:

$$Q(t) = \mathrm{Tr}(e^{-i\mathcal{H}t}\ (I_{z2} + S_{z2})\ e^{i\mathcal{H}t}(I_{z2}+S_{z2})) \qquad \text{(III-65)}$$

Table V

Eigenfunctions, energies and transitions for two equivalent deuterons, dipolar coupled ($\Delta\omega_Q = 0$).

	Eigenfunction $\|I\ S\rangle$	Energy (frequency units)
1)	$\|11\rangle$	$-2\omega_0 + \frac{2}{3}\omega_Q + 2d$
2)	$1/\sqrt{2}\ (\|10\rangle + \|01\rangle)$	$-\omega_0 - \frac{1}{3}\omega_Q - d$
3)	$1/\sqrt{2}\ (\|10\rangle - \|01\rangle)$	$-\omega_0 - \frac{1}{3}\omega_Q + d$
4)	$\|0\ 0\rangle$	$-\frac{4}{3}\omega_Q$
5)	$1/\sqrt{2}\ (\|1{-1}\rangle + \|{-1}1\rangle)$	$\frac{2}{3}\omega_Q - 2d$
6)	$1/\sqrt{2}\ (\|1{-1}\rangle - \|{-1}1\rangle)$	$\frac{2}{3}\omega_Q - 2d$
7)	$1/\sqrt{2}\ (\|0{-1}\rangle + \|{-1}0\rangle)$	$\omega_0 - \frac{1}{3}\omega_Q - d$
8)	$1/\sqrt{2}\ (\|0{-1}\rangle - \|{-1}0\rangle)$	$\omega_0 - \frac{1}{3}\omega_Q + d$
9)	$\|{-1}{-1}\rangle$	$-2\omega_0 + \frac{2}{3}\omega_Q + d$

	Transition Frequencies	Intensity
7) → 9)	$\omega_0 + \omega_Q + 3d$	2
1) → 2)	$\omega_0 - \omega_Q - 3d$	2
2) → 4)	$\omega_0 - \omega_Q + d$	2
2) → 5)	$\omega_0 + \omega_Q - d$	1
3) → 6)	$\omega_0 + \omega_Q - 3d$	1
5) → 7)	$\omega_0 - \omega_Q + d$	1
6) → 8)	$\omega_0 - \omega_Q + 3d$	1
4) → 7)	$\omega_0 + \omega_Q - d$	2

Table VI

Eigenfunctions, energies and transitions for two inequivalent deuterons dipolar coupled ($\Delta\omega_Q >> D$).

	Eigenfunction $\|I\ S\rangle$	Energy (frequency units)
1)	$\|1\ 1\rangle$	$-2\omega_0 + \frac{1}{3}\omega_{QI} + \frac{1}{3}\omega_{QS} + 2d$
2)	$\|1\ 0\rangle$	$-\omega_0 + \frac{1}{3}\omega_{QI} - \frac{2}{3}\omega_{QS}$
3)	$\|1\ -1\rangle$	$\frac{1}{3}\omega_{QI} + \frac{1}{3}\omega_{QS} - 2d$
4)	$\|0\ 1\rangle$	$-\omega_0 - \frac{2}{3}\omega_{QI} + \frac{1}{3}\omega_{QS}$
5)	$\|0\ 0\rangle$	$-\frac{2}{3}\omega_{QI} + \frac{2}{3}\omega_{QS}$
6)	$\|0\ -1\rangle$	$\omega_0 - \frac{2}{3}\omega_{QI} + \frac{1}{3}\omega_{QS}$
7)	$\|-1\ 1\rangle$	$\frac{1}{3}\omega_{QI} + \frac{1}{3}\omega_{QS} - 2d$
8)	$\|-1\ 0\rangle$	$\omega_0 + \frac{1}{3}\omega_{QI} - \frac{2}{3}\omega_{QS}$
9)	$\|-1\ -1\rangle$	$2\omega_0 + \frac{1}{3}\omega_{QI} + \frac{1}{3}\omega_{QS} + 2d$

	Transition frequencies	Intensity
1) → 2)	$\omega_0 - \omega_{QS} - 2d$	1
2) → 3)	$\omega_0 + \omega_{QS} - 2d$	1
4) → 5)	$\omega_0 - \omega_{QS}$	1
5) → 6)	$\omega_0 + \omega_{QS}$	1
7) → 8)	$\omega_0 - \omega_{QS} + 2d$	1
8) → 9)	$\omega_0 + \omega_{QS} + 2d$	1
1) → 4)	$\omega_0 - \omega_{QI} - 2d$	1
2) → 5)	$\omega_0 - \omega_{QI}$	1
3) → 6)	$\omega_0 - \omega_{QI} + 2d$	1
4) → 7)	$\omega_0 + \omega_{QI} - 2d$	1
5) → 8)	$\omega_0 + \omega_{QI}$	1
6) → 9)	$\omega_0 + \omega_{QI} + 2d$	1

For equivalent deuterons

$$\mathcal{H} = -2\Delta\omega(I_{z1}+S_{z1}) + \frac{2}{3}\omega_Q(I_{x3}-I_{y3}+S_{x3}-S_{y3}) - 4d_{IS}\left[2I_{z1}S_{z1} - \frac{1}{2}(I_{x1}S_{x1}+I_{x2}S_{x2}) - \frac{1}{2}(I_{y1}S_{y1}+I_{y2}S_{y2})\right] \tag{III-66}$$

which we will write for convenience

$$\mathcal{H} = \mathcal{H}_z + \mathcal{H}_Q + \mathcal{H}_{Dz} + \mathcal{H}_{Dx} + \mathcal{H}_{Dy}. \tag{III-67}$$

To simplify the calculation of (III-65) we now note that many parts of the Hamiltonian commute with each other and with $I_{z2} + S_{z2}$. For the Hamiltonian

$$[\mathcal{H}_z, \mathcal{H}_Q] = [\mathcal{H}_z, \mathcal{H}_D'] = [\mathcal{H}_Q, \mathcal{H}_D'] = 0$$

and

$$[\mathcal{H}_{Dz}, \mathcal{H}_{Dx}] = [\mathcal{H}_{Dz}, \mathcal{H}_{Dy}] = [\mathcal{H}_{Dx}, \mathcal{H}_{Dy}] = 0, \tag{III-68}$$

may be derived from tables of commutators and anticommutators, Appendix F. This allows us to break up the exponential in (III-65) into separate exponentials for each part of the Hamiltonian. In addition,

$$[\mathcal{H}_Q, I_{z2}+S_{z2}] = [\mathcal{H}_{Dx}, I_{z2}+S_{z2}] = [\mathcal{H}_{Dy}, I_{z2}+S_{z2}] = 0 \tag{III-69}$$

so that the terms $\mathcal{H}_Q$, $\mathcal{H}_{Dx}$ and $\mathcal{H}_{Dy}$ may be dropped completely leaving

$$Q(t) = \mathrm{Tr}\left[e^{[+i2\Delta\omega(I_{z1}+S_{z1})+i8d_{IS}I_{z1}S_{z1}]t}(I_{z2}+S_{z2}) \times e^{[-i2\Delta\omega(I_{z1}+S_{z1})-i8d_{IS}I_{z1}S_{z1}]t}(I_{z2}+S_{z2})\right]. \tag{III-70}$$

The traces over I_{z2} and S_{z2} parts are identical and may be calculated separately, and $I_{z2}S_{z2}$ terms vanish. Then the I_{z2} portion gives

$$Q(t) = \mathrm{Tr}\left[e^{-i(-8dS_{z1})I_{z1}} \; e^{-i(-2\Delta\omega)I_{z1}} \; I_{z2} \; e^{i(-2\Delta\omega)I_{z1}} \; e^{i(-8dS_{z1})I_{z1}} I_{z2} \right]$$

$$= \mathrm{Tr}\left[e^{-i(-8dS_{z1})I_{z1}} \; (\cos 2\Delta\omega t \; I_{z2} - \sin 2\Delta\omega t \; I_{z3}) \; e^{i(-8dS_{z1})I_{z1}} I_{z2} \right]$$

$$= \mathrm{Tr}\Big[\cos 2\Delta\omega t \{\cos(8dS_{z1}t) \; I_{z2} - \sin(8dS_{z1}t) \; I_{z3}\} \; I_{z2} \qquad \text{(III-71)}$$

$$- \sin 2\Delta\omega t \{\cos(8dS_{z1}t) \; I_{z3} - \sin(8dS_{z1}t) I_{z2}\} \; I_{z2} \Big].$$

The fictitious spin operators have been defined so that they are orthogonal, hence terms like $\mathrm{Tr}(I_{z2}I_{z3})$ must vanish. The trigonometric functions of the operator may be expanded as shown in Appendix G. Applying these reduces (III-71) to:

$$Q(t) = \mathrm{Tr}\Big[\cos 2\Delta\omega t \; \{1 - (2S_{z1})^2 + (2S_{z1})^2 \cos 4dt\} \; I_{z2}^2$$

$$+ \sin 2\Delta\omega t \; \{2S_{z1} \sin 4dt\} \; I_{z2}^2 \Big]. \qquad \text{(III-72)}$$

Straight forward evaluation of traces gives

$$Q(t) \; \alpha \; \cos 2\Delta\omega t \; + \; \cos(2\Delta\omega + 4d)t \; + \; \cos(2\Delta\omega - 4d)t. \qquad \text{(III-73)}$$

The Fourier transform of this gives three lines of equal intensity at frequencies $2\Delta\omega-4d$, $2\Delta\omega$, $2\Delta\omega+4d$. This is a local field spectrum, i.e., the dipolar flip-flop terms do not contribute to the spectrum. For two inequivalent deuterons the $\mathcal{H}_{Dx}$ and $\mathcal{H}_{Dy}$ terms are not in the secular Hamiltonian, but all other arguments above hold, so the double quantum spectrum for inequivalent deuterons is the same as that for equivalent ones. These are shown in Fig. 46 together with the single quantum spectra.

While the calculation above is simple to perform for two deuterons, it may be very difficult for general arrangments of several spins. In such cases it may be easier to calculate the double quantum spectrum by the method analogous to that used for the single quantum spectra above, using $(I_+^2) + (S_+^2)$ rather than $I_+ + S_+$. The equivalence may be seen by calculating Q(t) in the Hamiltonian eigenbasis $|i\rangle$ and $|j\rangle$.

$$Q(t) = \mathrm{Tr}\,(e^{-i\mathcal{H}t}\, I_{z2}\, e^{i\mathcal{H}t}\, I_{z2}). \tag{III-74}$$

$$Q(t) = \sum_i \sum_j \langle i|e^{-i\mathcal{H}t}|i\rangle\langle i|I_{z2}|j\rangle\langle j|e^{i\mathcal{H}t}|j\rangle\langle j|I_{z2}|i\rangle. \tag{III-75}$$

$$Q(t) = \sum_i \sum_j e^{i(E_j-E_i)t}\, |\langle i|I_{z2}|j\rangle|^2. \tag{III-76}$$

We now note that

$$I_{z2} = \frac{1}{2}(I_xI_y + I_yI_x) = I_+I_+ - I_-I_-. \tag{III-77}$$

Since I_{z2} and I_+^2, I_-^2 have matrix elements between the same eigenstates, the absorption spectrum calculated from I_+^2 will be the same as that calculated from the Fourier Transform of the evolution of I_{z2}. In cases where the single quantum resonances are separated by differences in quadrupole coupling, the double quantum spectrum of each spin may be obtained separately by double Fourier Transformation in the region of each spin's single quantum lines, tremendously simplifying the analysis of complex systems.

The analysis of a three spin system follows exactly that for two spins. For three equivalent deuterons (a deuterated methyl group is a good example) the Hamiltonian, with all terms appropriately truncated for spins I, J and S, is:

$$\mathcal{H} = -2\Delta\omega\,(I_{z1} + J_{z1} + S_{z1}) + \frac{2}{3}\omega_Q\,(I_{x3} - I_{y3} + J_{x3} - J_{y3} + S_{x3} - S_{y3}) \tag{III-78}$$

$$+ 4d\,[\mathcal{H}_{Dz}^{IS} + \mathcal{H}_{Dx}^{IS} + \mathcal{H}_{Dy}^{IS}] + 4d\,[\mathcal{H}_{Dz}^{IJ} + \mathcal{H}_{Dx}^{IJ} + \mathcal{H}_{Dy}^{IJ}]$$

$$+ 4d\,[\mathcal{H}_{Dz}^{JS} + \mathcal{H}_{Dx}^{JS} + \mathcal{H}_{Dy}^{JS}]$$

where (III-66) and (III-67) define the dipolar terms.

The single quantum structure is a bit more complex than for two deuterons but is still easily calculated.[76] To calculate the double quantum structure we will again make use of commutation relations. As for two deuterons, $\mathcal{H}_z$ and $\mathcal{H}_Q$ commute with each other and with the dipolar Hamiltonian. If we call the z dipolar terms $\mathcal{H}_{Dz}$ and the x and y dipolar terms $\mathcal{H}_{Dxy}$, then as for two spins we may easily show that $[\mathcal{H}_{Dz}, \mathcal{H}_{Dxy}] = 0$ and $[\mathcal{H}_{Dxy}, I_{z2} + S_{z2} + J_{z2}] = 0$. Since $[\mathcal{H}_Q, I_{z2} + S_{z2} + J_{z2}] = 0$ the double quantum evolution then reduces to

$$Q(t) = \mathrm{Tr}\left[e^{-it[-2\Delta\omega(I_{z1}+S_{z1}+J_{z1})-8d\,I_{z1}S_{z1}-8d\,I_{z1}J_{z1}-8dS_{z1}J_{z1}]} I_{z2}\, e^{it[-2\Delta\omega(I_{z1}+S_{z1}+J_{z1})-8d\,I_{z1}S_{z1}-8d\,I_{z1}J_{z1}-8d\,S_{z1}J_{z1}]} I_{z2} \right]. \tag{III-79}$$

Since this is again a local field effective Hamiltonian we need not repeat the calculation (III-71) but predict a five line spectrum centered at $2\Delta\omega$, with lines of intensity 1:2:3:2:1 spaced by 4d. This is shown in Fig. 47 together with the single quantum spectrum.

The analysis of more complex systems, for example three deuterons with different quadrupole and dipole couplings, becomes very difficult in the manner used above. In such cases the z and xy parts of the dipolar Hamiltonian will not commute, so a simple local field spectrum is

not expected. The calculation of the transitions of I_+^2 is quite straightforward with a computer or by hand.[76]

b) Preparation and Detection

In the above analysis we have assumed that we could create and detect a density matrix proportional to I_{z2}, exactly as we had done when no dipolar couplings were present. This may be justified for the case assumed, $\omega_Q >> d$, if during weak pulses $\omega_1^2/\omega_Q >> d$ is also satisfied. In this case the dipolar Hamiltonian is a minor perturbation upon the evolution of the system and for reasonably short pulses its effect can be ignored. We will see in the next chapter that if the dipolar Hamiltonian is sufficiently strong, relative to other terms in the full Hamiltonian, that it may also induce multiple quantum transitions. For example in the two deuteron case just discussed double quantum transitions of the type I_+S_+ could be induced, as well as triple and quadrupole quantum transitions which are not allowed in a purely quadrupolar system. Figure 48 shows the possible transitions of all orders for a system of two equivalent deuterons. When $\omega_1 > \omega_Q$ (small quadrupole values) is not met we have already seen that double quantum coherence cannot be prepared efficiently, and here the dipolar part of the Hamiltonian may have a significant effect relative to the other terms. In a powder the double quantum preparation pulse is optimized for the regions of maximum intensity, which generally have large ω_Q values. In this case the pulses are rather short and we do not expect the dipolar Hamiltonian to have significant effect during this short time. During the probing pulses in any of the double quantum sequences we strive to have $\omega_1 >> \omega_Q$, hence the dipolar terms may certainly be ignored.

If the analysis of double quantum coherence is performed with the double Fourier Transform technique (often preferable so that just one spin is observed) then the amplitude of all dipolar lines corresponding to the spin of interest must be included to faithfully represent the total double quantum operator. In some cases it is of interest to observe single quantum lines which correspond to one particular double quantum transition,[77] for example the double quantum transition in the asymmetric manifold of Fig. 48 may be isolated by observing transitions 3) → 6) and 6) → 8) of Table V.

c) Powder Lineshape

As discussed above, the preparation and detection of double quantum transitions in a powder with dipolar coupling presents no new problems. For two deuterons we have seen that each orientation gives a three line spectrum. If we assume that the spins have no anisotropic chemical shift, then this is exactly analogous to the quadrupole coupled spectrum of a spin 3/2. Since the dipolar coupling has axial symmetry, depending only on the relative orientation of the internuclear vector and the field, a powder of paired spins-1 will give the same spectrum as a powder of spins 3/2 with an axial field gradient tensor.[1] This is identical to the pattern of pairs of spins-1/2 of Pake[66] with an additional sharp line in the center.

If the spins have anisotropic chemical shifts as well as dipolar coupling, the powder pattern becomes quite complex. It can be calculated analytically easily only if the shielding tensor has axial symmetry and its symmetry axis is aligned with the dipolar axis. Other

cases may be calculated with use of a computer.

If three equivalent spins are dipolar coupled, then the powder pattern will be like two overlapping spin-1 quadrupole patterns, one twice the width and half the intensity of the other, plus a line in the center. This is already quite a complex powder pattern, and requires quite good resolution experimentally to observe. While powder patterns for other arrangements of spins are easily generated, they will be very complex and hence require exceptional resolution to observe experimentally.

d) Echoes

Since it is rather unusual to find spins without any chemical shielding anisotropy, it would be nice to have a method for removing it, without eliminating the dipolar structure of interest, to simplify dipolar powder patterns. It is possible to achieve this through use of an echo of the Hahn type,[78] since the chemical shift is linear in I_z while the dipolar coupling is bilinear. It is well known that a π pulse following a $\pi/2$ pulse causes refocusing of chemical shifts (and of course off resonance and magnetic field inhomogeneity terms which have the identical form) while it does not change scalar or dipolar couplings. A mathematical analysis of this phenomenon and a discussion of its limitations is postponed until the next chapter. From the above argument we expect a single quantum π pulse in the center of the double quantum evolution period to remove all evolution from off resonance, shielding anisotropy and magnetic field inhomogeneity terms while leaving dipolar and scalar contributions to the evolution unchanged. Such echoes would also be of use for removal of magnetic field inhomogeneity contributions

to the linewidth in studies of relaxation in single crystals or liquid crystals.

7. Broadening Mechanisms

In deuterium NMR there are several broadening mechanisms in addition to those for high resolution NMR of spin-1/2 nuclei in solids. In usual dilute spin NMR the only sources of broadening (excluding motion as studied in the first chapter) are magnetic field inhomogeneity and dipole-dipole couplings among the observed nuclei, or other magnetic nuclei which are not decoupled. Both of these may be minimized by the spectroscopist, the first by shimming the magnetic field to high homogeneity and the second by diluting the magnetic nuclei in a host of non-magnetic ones (^{13}C in ^{12}C).

Of course these also apply to deuterium NMR, but in addition one must consider other sources of broadening. In single crystal samples, defects in the lattice structure cause different parts of the crystal to have slightly different orientation with respect to the magnetic field. Since the large quadrupole couplings change rapidly with orientation, a small defect may cause linewidth large enough to obscure chemical shifts or dipolar couplings of interest. Since double quantum NMR removes the effect of quadrupole couplings, crystal imperfections will no longer be important. Similar broadening is observed in liquid crystal samples due to imperfect alignment of the molecules with the field, and has been successfully removed with double quantum NMR.[76]

The quadrupole coupling as presented in Chapter I was calculated to first order. In fact if the energy is calculated to second order a correction term is necessary.[1] For an axial field gradient tensor this correction for the m magnetic quantum number level is

$$E_m^{(2)} = - m \hbar \frac{\omega_{QM}^2}{12\omega_0} \left(\frac{3}{2} \cos^2\theta \sin^2\theta + \sin^4\theta\right). \qquad \text{(III-80)}$$

where $\omega_{QM} = 3e^2qQ/2\hbar$ is the maximum quadrupole splitting. This correction term moves the ±1 levels in <u>opposite</u> directions by an equal amount. This preserves the center of gravity of the single quantum spectrum, so that chemical shifts determined by single quantum single crystal rotations will be unaffected. However this does shift the double quantum transition position and hence will complicate analysis of double quantum measurements, in single crystals and powders. In a single crystal the quadrupole tensor orientation and magnitude may be known and the position of the double quantum line may be corrected to determine accurately the chemical shift. In a powder, however, many different orientations contribute to the same chemical shift, so it is not simple to correct the powder pattern lineshape. If the relative orientation of the quadrupole and chemical shielding tensors is known, then a correction for the anisotropy may be estimated. For $\omega_{QM} = 3\times10^5$ Hz and $\omega_0 = 2.8\times10^7$ Hz (appropriate for many rigid solids in a field of 42 kG), the second order shift contributes ~100 Hz (3.5 PPM) to the width. While not a severe problem, one must be aware of this for studies of small chemical shifts. Motional averaging, of course, reduces the second order shift as well as the first order.

The last broadening we consider is lifetime broadening due to very short spin lattice relaxation times. The large quadrupole coupling of deuterium provides a very efficient relaxation mechanism when motion occurs with a frequency near the Larmor frequency of deuterium. If T_1 is reduced to 10 msec (much shorter T_1's have been observed) then this will contribute ~ 1 PPM to the homogenous linewidth of both single and double quantum transitions. This cannot be eliminated except by changing the sample temperature to move the frequency of motion away from the Larmor frequency, lengthening the relaxation time.

C. Experimental

1. d-1 Benzene

The first measurement of deuterium chemical shielding anisotropy in a powder was made on a sample of d-1 benzene. Chemical shielding in benzene is of considerable interest both theoretically and practically as the simplest compound which can exhibit ring current induced chemical shifts.[79] At the temperature of the experiments (-40°C) it is well known that benzene rotates about its sixfold axis[1,80] in a manner exactly analogous to hexamethylbenzene. Therefore we expect the quadrupole coupling tensor and chemical shielding tensor to be axial with the unique axis out of the plane of the ring. The chemical shift in the unique direction should be downfield from the perpendicular direction, due to the ring current.

The sample used was 10% d-1 benzene (Merck, 98% d-1) doped into ordinary benzene, sealed under vacuum in a 6 mm diameter pyrex tube. This dilution was used to reduce deuterium-deuterium dipolar couplings and

hence their contribution to the homogeneous linewidth. The liquid was frozen quickly to produce a polycrystalline sample, then maintained at -40±3 C. The single quantum spectrum showed a quadrupole powder pattern of almost axial symmetry, giving a value for eQV_{zz} = 96 kHz. The values for nonrotating benzene have been previously measured[81] as eQV_{zz} = 181 kHz, η = 0.041. If we assign ν_{33} (using the convention that ν_{11}, ν_{22} and ν_{33} represent the three discontinuities in a powder spectrum and $|\nu_{33}| \geq |\nu_{22}| \geq |\nu_{11}|$) to be along the C-D bond and ν_{22} to be out of the plane of the ring we would predict eQV_{zz} = 94 kHz, quite reasonable agreement. T_1 for the deuterium was estimated to be 10 msec and hence relaxation could contribute significantly to the homogeneous linewidth.

Figure 49 summarizes pulse sequences used in FTDQ NMR. For the present sample pulse sequence B was used with P_1 y phase, 20 kHz amplitude and 25 μsec length, P_2 x phase, 50 kHz amplitude and 3 μsec length, and P_3 x phase, 50 kHz amplitude and 4.5 μsec length. The double quantum evolution time τ was incremented in units of 100 μsec, and τ' was fixed at 100 μsec. High power proton decoupling was applied throughout preparation and detection periods. The experiment was performed 500 Hz off resonance from the liquid line position. Figure 50 shows the double quantum free induction decay obtained by taking the echo amplitude for each τ value. The Fourier Transform of this is shown in Figure 51. From this powder pattern we have determined $\Delta\sigma$ = - 6.5±1 PPM ($\Delta\sigma = \sigma_{\parallel} - \sigma_{\perp}$). The homogeneous contribution to the linewidth is ~ 3PPM and is probably a combination of residual dipolar, relaxation and second order quadrupole contributions. The $\sigma_{\parallel}$ element is as we expected downfield from $\sigma_{\perp}$. Recently this anisotropy has been measured using multiple pulse

techniques,[82] and a value of $\Delta\sigma$ in good agreement with ours was obtained. Figure 52 shows the theoretical prediction for the powder lineshape, including transfer functions for all pulses, convoluted with Gaussians of varying widths. The agreement of C with experiment is good, although at this degree of broadening all fine details are lost.

2. Ferrocene

To verify the reliability of FTDQ results we wished to compare shielding anisotropy for a compound which had been carefully studied with multiple pulse techniques. Ferrocene was a convenient choice since it is easily made, is a solid at room temperature and has been carefully studied with multiple pulse NMR.[3] It is very similar to benzene in many ways including motion and we expect it to have similar shielding characteristics.

The sample of 5% randomly deuterated ferrocene was prepared using the method of Fritz and Schaefer,[83] exchanging with deuterophosphoric acid in dioxane. The isotopic label was assumed to be randomly distributed and was quantified by mass spectral analysis. Approximately 200 mg of finely ground labelled ferrocene, compressed into a 6 mm diameter pellet, was used for the present experiments, done at room temperature 20±3°C.

The single quantum spectrum Fig. 53, shows an axial quadrupole powder pattern with eQV_{zz} = 96.81±0.01 kHz and $\eta < 0.002$. This is as expected very similar to the values for benzene.

Pulse sequence D of Figure 49 was used for the double quantum measurements. P_1 and P_2 were 20 kHz amplitude and 25 μsec length, of arbitrary phase. P_3 and P_4 were x and y phase respectively ~ 75 kHz

amplitude and 3.5 μsec width. τ was varied in units of 50 μsec and T_2 and τ' were fixed at 1 msec and 40 μsec respectively. High power proton decoupling was applied during all times except T_2. Figure 54 shows the double quantum free induction decay generated by taking the amplitude of the echo at each τ value. The Fourier Transform of this is shown in Figure 55. The asymmetric line observed is consistent with an axial powder pattern with $\Delta\sigma = -6.5\pm1$ PPM as for benzene. The homogeneous linewidth is somewhat greater than for benzene and is probably due to deuterium dipolar couplings. The deuterium concentration of 5% is considerably higher than in the benzene sample. T_1 was estimated to be longer than 50 msec and hence should contribute to the broadening. The agreement of our value for $\Delta\sigma$ with that of Haeberlen,[3] $\Delta\sigma = -6.5\pm0.1$ PPM from single crystal multiple pulse studies, is gratifying. The single crystal value has been determined on a spherical crystal with corrections for bulk susceptibility anisotropy, and hence is far more accurate than our estimate. In a powder sample our resolution appears somewhat better than is achieved by multiple pulse methods.[3] FTDQ measurement at higher dilution should yield even better resolution.

3. $BaClO_3 \cdot D_2O$

Hydrated salt crystals provide a convenient source of paired deuterons in which to study dipolar couplings. Deuterated barium chlorate monohydrate has been previously studied using cw NMR.[84] These studies showed that at room temperature the water molecules make jumps of 180° about their C_2 axes. Similar behavior has been observed in other hydrated crystals.[85,86] This motion assures that the deuterons in any

water molecule will have the same quadrupole couplings, and the same chemical shift. Chiba[84] observed that the short deuteron-deuteron distance of 1.6 Å led to resolved dipolar structure in the single quantum spectrum, in spite of rather large linewidths. Since there is only one type of water, crystallographically, the single quantum spectrum is a single pair of quadrupole satellites consisting of dipolar multiplets, and provides a convenient system for comparison of single and double quantum dipolar structure.

The sample was a single crystal of barium chlorate monohydrate grown by slow evaporation of nearly saturated D_2O solutions. Commercial $BaClO_3 \cdot H_2O$ was dissolved in 98% D_2O (Biorad Laboratories) then evaporated to dryness. This procedure was repeated, and the resulting powder was again dissolved in D_2O. This solution was allowed to evaporate in a closed box over a period of approximately two weeks. When crystals of sufficient size (5 mm × 3 mm × 1 mm) had grown they were removed from the solution. The crystals were clear and had well developed faces. They were mounted on the end of a Kel-F plastic rod which was then mounted in a goniometer, so that the crystal could be rotated about an axis perpendicular to the magnetic field. The orientation of the crystal was not determined, rotations were performed only to adjust the quadrupole and dipole couplings to convenient size.

A single quantum spectrum of the crystal in the orientation studied is shown in Figure 56, obtained without proton decoupling. The splitting between the satellites is 138.3 kHz. The dipolar structure shown in the expansion is a center pattern of three lines (one incompletely resolved) as expected from two dipole coupled deuterons (Fig. 46),

for which ω_Q and d have opposite signs. In addition there are two weak outer lines which come from HOD molecules. The H-D coupling is three times the D-D coupling, as expected. The H impurity is a result of exchange of water in the air with the D_2O solution. Crystals grown more slowly showed an even higher concentration of H. That these extra lines are from HOD molecules and not crystal imperfections was confirmed by comparison of proton coupled and decoupled spectra. From this spectrum we determine d = 350 Hz.

Double quantum measurements were made employing pulse sequence A of Figure 49. The first pulse was arbitrary phase, 55 kHz amplitude and 9 μsec length. The second pulse was 80 kHz amplitude and 3 μsec length. τ was incremented in units of 25 μsec. Figure 57 shows Fourier Transforms of proton coupled and decoupled double quantum decays. In the proton coupled spectrum the HOD lines are not observed, and the spectrum is the predicted symmetric 1:1:1 triplet. When the protons are decoupled the HOD lines are collapsed and contribute to the center line. The splitting between lines is 1340 Hz giving a value of d = 335 Hz, in good agreement with the single quantum values. There is apparently a small difference in width among the three lines which is not understood. T_1 was measured on this crystal in an orientation with small quadrupole coupling and was found to be ~ 2 msec. This implies a contribution of 160 Hz to the homogeneous linewidth. The linewidths in the spectra of Figure 57 are approximately 750 Hz, and are probably determined by unresolved dipolar couplings to distant water molecules. It is clear from the spectra that the simplification of dipolar structure in the double quantum experiment leads to a practical improvement of resolution, and a somewhat more

accurate determination of the dipolar coupling.

4. Hexamethylbenzenes, d-1, α,β d-2, α,β,γ d-3, d-18

In the development of new techniques (to help define conditions for their optimal application) it often valuable to study a related series of compounds. To this end a series of partially deuterated hexamethylbenzene samples was studied. The molecular motion of this compound at room temperature reduces the quadrupole coupling, greatly reducing the requirements for ideal single quantum pulses. The molecular motion also greatly reduces the chemical shielding anisotropy, so that simple dipolar structure could be observed in powders. The simple crystal structure and reasonable relaxation time make it practical to study single crystals as well.

The partially deuterated hexamethylbenzenes were synthesized from pentamethylbenzene and paraformaldehyde by the procedure described in Appendix H. They were characterized by high resolution NMR and mass spectroscopy. d-18 Hexamethylbenzene (98% deuterated) was purchased from Merck and used without further purification. Diluted samples were prepared by melting together desired weights of labelled and unlabelled material. Single crystals were grown by slow evaporation of saturated carbon tetrachloride solutions, yielding platelike crystals rather than the usual needles. These crystals were fragile but could be glued to goniometer mounts without difficulty. The crystals were clear and had well developed faces.

a) Powder Spectra - Single Quantum

Since there is a great deal of molecular motion in HMB, the quadrupole coupling is greatly reduced from the large values for rigid methylene deuterons (eQV_{zz} = 174 kHz in cyclohexane[81] and 166 kHz in glycine[87]), and hence it is easy to obtain very good spectra for these compounds. Figures 58, 59 and 60 show the single quantum spectra of neat d-1, α,β d-2 and α,β,γ d-3 HMB samples. The results are summarized in Table VII. These are rather startling in several respects. To begin, we know that at room temperature HMB undergoes rapid rotation about its sixfold axis. This would lead us to expect that η would be zero, as observed for ferrocene, which also undergoes rapid uniaxial rotation. From the crystal structure of HMB[37,38] (space group $P2_1$, one molecule per unit cell) we know that molecules are stacked in planes with each molecule tilted 5° out of the plane. Thus a particular methyl group may have two environments, lying in the plane (1/3 of its possible orientations) or slightly out of plane (2/3 of its orientations). The nonzero asymmetry parameter could come about in two ways. First, that the deuterated methyl spends less time in one type of site than the other, or second, that while in one type of site it has a different quadrupole coupling constant from the other. The first possibility is ruled out by natural abundance ^{13}C measurements on the d-1 HMB sample. A biased rotation of this sort would cause the ring carbon tensor to be nonaxial with the same asymmetry parameter as the deuteron. Figure 61 shows carbon spectra for undeuterated HMB and d-1 HMB, with a theoretical spectrum for the biased rotation case. From these we conclude that the source of asymmetry must be different quadrupole coupling tensors for different sites.

Table VII

COMPOUND	eQV_{zz}	η
d-1 HMB	18.95 kHz	0.096±0.002
α,β d-2 HMB	20.9 kHz	0.08 ±0.01
α β γ d-3 HMB	22.2 kHz	0.07 ±0.01
d-18 HMB	22.0 kHz	0.07 ±0.02

The increase in magnitude of the quadrupole coupling in going from d-1 to d-2 to d-3 is also rather surprising. This could come either from a change in the static electric field gradient upon successive deuterations, or from a change in the vibrational and rotational averaging. Since the field gradient is greatly averaged by motion the change in static field gradient would have to be quite large to explain the change observed. However the averaging which occurs from methyl group rotation is very sensitive to the C-C-D bond angle. A static change of ~1.2° in this angle upon going from d-1 to d-2, and 0.8° upon going from d-2 to d-3 would explain the observed spectral changes. Such a static argument is certainly not a complete description; dynamic averaging should be considered. It does, however, make a change in averaging seem a reasonable explanation. Measurements on a number of other deuterated aromatic methyl groups have been made. The quadrupole coupling constants, eQV_{zz}, for toluene, p-xylene and o-xylene are all 52 kHz.[88] Methyl rotation generates an average quadrupole tensor, with the V_{zz} direction along the rotation axis. The directions of V_{xx} and V_{yy} must be perpendicular to this, but cannot be determined further. The sixfold rotation in HMB will average V_{zz} with a value between V_{xx} and V_{yy}. The coupling along the sixfold rotation axis will become the new V_{zz} value. From the data of o-xylene[88] (η = 0.094), we would predict HMB to have an averaged V_{zz} between 17.6 and 21.3 kHz. However in the HMB samples the values range from 14.2 (d-1) to 16.7 (d-3). The reason for this discrepancy is not understood.

It is apparent from the powder spectra that the dipolar linewidth has increased in going from d-1 to d-3 HMB. For high resolution studies we must limit this contribution to the homogeneous linewidth if we are to accurately measure other couplings. The quadrupolar echo provides a convenient way to directly observe the broadening by these couplings. We have seen that at the echo point all evolution due to the quadrupole coupling has been removed, (III-54). The spectrometer resonance frequency may be adjusted so that $\Delta\omega = 0$, so that the damping function $\psi(t)$ may be observed. The damping will come from two sources, dipolar couplings and chemical shift anisotropy. Their contributions may be separated by dilution, since dipolar couplings are concentration dependent but shielding anisotropy is not. Figure 62 shows the echo amplitude vs. time for several HMB samples with different deuterium concentrations. The decay time for the echo amplitude steadily increases with decreasing concentration. Even in this motionally averaged solid there is a significant change upon dilution from d-1 (5.5% total deuterium concentration) to 10% d-1 (0.5% d) at which point chemical shielding probably dominates the linewidth. A very similar approach has been used for measurement of the intermolecular contribution to dipolar linewidths in systems with strongly coupled pairs of spins - 1/2,[89] (these pairs of spins behave very much like a spin-1[90]). Figure 63 shows the expected modulation of echo amplitude when the same experiment is performed off resonance. Equation (III-54) may be rewritten as:

$$a_{x1}(2\tau) = \frac{1}{2}\sin 2\Delta\omega\tau$$
$$a_{y1}(2\tau) = \frac{1}{2}(1 + \cos 2\Delta\omega\tau) \qquad \text{(III-81)}$$

This is exactly the behavior one would expect of a signal evolving without quadrupole couplings with an added on-resonance component. This might be used to measure shielding anisotropy in very dilute systems (if shielding and dipolar terms are of comparable size the evolution under echo sequences may be very complex, see Chapter IV).

b) Single Crystals α,β d-2, α,β,γ d-3

The dipolar couplings within a methyl group are much larger than the linewidth determined by intermolecular couplings and, as for D_2O in hydrates, then yield resolved dipolar structure. The d-2 and d-3 HMB crystals were goniometer mounted so that they could be rotated to give nearly the maximum possible quadrupole splitting. Figure 64 shows the single quantum spectrum of the d-2 HMB crystal. The resolution is considerably better than in the D_2O spectrum and we are not bothered by extra proton split lines. The quadrupole coupling ν_Q = 29.9 kHz, the dipolar coupling d = 104 Hz, and the linewidth is ~ 160 Hz. The double quantum spectrum shown in Figure 65 was obtained with the two pulse sequence, A of Figure 49, with P_1 arbitrary phase, 12.6 kHz amplitude and 33 μsec length. Again it is the expected 1:1:1 triplet, with splittings of 430 Hz giving d = 107 Hz in good agreement with single quantum. The linewidth of the center double quantum line is 250 Hz, somewhat greater than the single quantum value. The increase in linewidth is an indication that field homogeneity may be important in determining the linewidth in this sample. The difference in linewidths among the double quantum lines is not understood.

Figure 66 shows the single quantum spectrum of the d-3 HMB crystal. Again considerable structure is resolved, yielding values ν_Q = 16.0 kHz and d ≈ 119 Hz. The double quantum spectrum in Figure 67 was generated with the same pulse sequence used for the d-2 crystal. The structure, as predicted, is a symmetric five line pattern with intensities 1:2:3:2:1. The dipolar splitting obtained from this is 115 Hz, and is probably more accurate than the single quantum value. The higher deuterium concentration (17%) has broadened the lines considerably, and more accurate dipolar couplings could be obtained in a diluted sample, especially with the simple local field structure in the double quantum spectrum.

c) Double Quantum Powder Spectra d-1, d-2

While the single crystals of HMB showed structure from the dipolar couplings in the single quantum spectrum, the powder spectra do not. Then to gain any information about dipolar couplings in a powder we must use the Double Quantum approach, exactly as used in chemical shielding studies.

The chemical shielding anisotropy in HMB is expected to be rather small. If the shielding tensor in a rigid methyl group were axial and aligned along the C-D bond with $\Delta\sigma$ = - 6 PPM (in analogy with the protons C-H in malonic acid[3]), the molecular motion should reduce $\Delta\sigma$ by about the same amount as the quadrupole coupling (as we have seen, a factor of about 10) so that $\Delta\sigma$ observed should be less than 1 PPM. However there may be a component of shielding from a ring current in analogy to benzene, which would not be averaged by the methyl or ring rotation.

It is difficult to estimate the magnitude of such shielding, but from the data of benzene it seems quite possible that it could be 1-2 PPM.

A sample of 20% d-1 HMB was compressed into a 6 mm × 1 cm pellet. The double quantum spectrum of this sample taken with pulse sequence D of Figure 49 is shown in Figure 68. Pulses P_1 and P_2 were each 30 kHz amplitude and 48 μsec respectively. Pulses P_3 and P_4 were x and y phase, 80 kHz amplitude and 3 μsec long. The double quantum free induction decay was generated by taking the amplitude of the echo for τ values incremented in 200 μsec units. The spectrum is a single, almost symmetric line of width ~ 200 Hz. The lack of resolved structure indicates that the broadening is at least comparable in size to the shielding anisotropy, perhaps larger. T_1 was measured to be ~ 70 μsec, indicating that lifetime is not contributing significantly to the linewidth. The observed linewidth must then come from homonuclear dipolar couplings, other T_2 relaxation processes, and magnetic field inhomogeneity. From this spectrum it is not possible to accurately determine the shielding anisotropy.

Double quantum spectra were also taken for samples of 100% d-2 and 10% d-2 HMB, prepared in the same way as the d-1 sample, using the same pulse sequence as described above except sampling double quantum coherence in 100 μsec units. These are shown in Figure 69. In the 100% d-2 HMB sample dipolar structure is present, but poorly resolved. The distance between the shoulders is 435 Hz yielding a dipolar coupling d = 109 Hz. The spectrum obtained by diluting the d-2 HMB to 10% shows a considerable improvement in resolution, due to reduction of intermolecular dipolar couplings. The splitting between peaks is ~ 425 Hz giving

d = 106 Hz, in good agreement with the value expected, from the single crystal results.

As for chemical shielding, theoretical lineshapes are the ideal shapes multiplied by the transfer function for the pulse sequence used to generate and probe double quantum coherence. The transfer function for the sequence used for these experiments is shown in Figure 70. For small small quadrupole couplings the efficiency is not very good in preparation, but the echoing pulses have greater than 95% efficiency over the entire range for HMB. The theoretical spectra generated with this transfer function (assuming no shielding anisotropy) are shown in Figure 71, with Gaussian broadening of several values. The broadened lineshapes agree very well with the experimental for both 100% and 10% samples. Good agreement could not be obtained with theoretical spectra not including the transfer function. The agreement of the single crystal and powder values for d and the fact that the center line in the powder spectrum is centered between the other peaks and is quite symmetric argues against any large contribution from chemical shielding anisotropy in this spectrum.

The broadening used to simulate the 100% sample's spectrum was ~ 220 Hz, very similar to that observed in the crystal of the same material. For the diluted powder the broadening was reduced to 140 Hz. This demonstrates the importance of working in dilute spin systems if very high resolution is to be obtained.

5. Anisic Acid

In all of the powders studied to this point, the quadrupole, and hence all other couplings, have been averaged by motion. Anisic acid (p-methoxybenzoic acid) deuterated at the acid position provides a system with no motion. As one would expect the quadrupole coupling is quite large and hence the requirements for good single quantum pulses are proportionately increased. However such pulses are still quite within the capabilities of spectrometers with modest r.f. power amplifiers.

The sample was prepared by dissolving commercial anisic acid (Aldrich) in 98% D_2O, evaporating solvent and repeating. Finally, trapped D_2O in the crystals was removed by sublimation at reduced pressure. The resulting powder was compressed into a 6 mm × 1 cm cylinder, and used without other treatment.

The single quantum spectrum of anisic acid, Figure 72, was obtained by Fourier Transforming half a quadrupolar echo, generated by using 100 kHz, 2.25 μsec pulses separated by 30 μsec. The transfer function for this sequence has already been presented in Figure 45, and distortions are quite evident in the spectrum. From this we obtain eQV_{zz} = 169.0±1.0 kHz and η = 0.132±0.004. These values are somewhat larger than those previously measured in carboxylic acids.[64,86] Although the carboxyl region is quite rigid, rotating methyl groups quite near the deuterons[93] provide a relaxation mechanism so that T_1 is only a few seconds.

The double quantum spectrum was taken using the four pulse sequence, D of Figure 49, with $P_1 = P_2$ 37 kHz and 13.5 μsec long, T_2 and τ' fixed at 1 msec and 40 μsec respectively. P_3 and P_4 were 80 kHz and 30 μsec. τ was incremented in units of 50 μsec and 50 points were taken

in the double quantum FID. The free induction decay obtained from the echo amplitude and its Fourier Transform are shown in Figure 73. The spectrum shows considerable structure, however analysis is quite difficult because of the simultaneous presence of chemical shielding and dipolar couplings. Anisic acid, as most carboxylic acids, crystallizes as dimers, bringing pairs of deuterons quite close together. From the crystal structure data[93] we can estimate the distance between deuterons in the dimer at 2.3 Å, which indicates a maximum dipolar splitting of ~ 930 Hz. Chemical shielding has been studied in a number of simple acids,[3] from which an estimate of 25 PPM seems reasonable for $\Delta\sigma$, or in the double quantum spectrum ~ 1400 Hz. The chemical shielding tensor axis is probably aligned along the O-D bond and the dipolar tensor axis will make an angle of about 72° to this, so we expect complex structure. With the somewhat limited resolution in the present spectrum no detailed analysis was attempted. The deuterium concentration is probably too high to obtain very good resolution, and studies of the chemical shielding could be performed on a 10% deuterated sample, for which dipolar couplings would not be a problem.

D. Discussion

In this chapter we have discussed the principles of FTDQ NMR in single crystal and powder samples. The spectroscopy in single crystals is quite simple both in principle and in practice. Powder samples pose some problems due to the presence of a wide range of quadrupole couplings, and perfect double quantum powder patterns cannot be obtained. However, the distortions incurred in powders are predictable and do not generally degrade

the information content of spectra. The influence of dipolar couplings on double quantum spectra is also quite simple and is simply predictable. The experimental feasibility of these techniques has been demonstrated by measurements of chemical shielding in powders and dipolar couplings in both single crystals and powders.

These techniques provide an important supplement to multiple pulse NMR for determination of couplings of interest in simple systems. In addition they provide the opportunity for labeling studies. One or a small number of sites in a large molecular system may be deuterated, and thus selectively observed when multiple pulse spectra would be far too complicated for analysis, due to presence of many different proton types. Chemical shielding can provide information about the electronic environment of the spin and double labeling can give dipolar couplings to provide structural information. This expands greatly the number of systems which may be gainfully studied with NMR of hydrogen isotopes.

IV. MULTI QUANTUM NMR IN DIPOLAR SYSTEMS

A. Introduction

In the last chapter we have investigated the use of quadrupole couplings in generating double quantum coherences. To observe such a nonlinear effect it was necessary to have a Hamiltonian which had terms bilinear in the spin operators, such as quadrupole coupling. Ernst, et al., have used scalar couplings, also bilinear, to induce multiple quantum transitions in liquids.[65] In this chapter we investigate the use of dipolar couplings among spins $\frac{1}{2}$ for generating multiple quantum coherences. We will see that in large spin systems the high order multiple quantum spectra are simple, and should be easier to interpret than the single quantum spectra.

The principles of multiple quantum spectroscopy in dipolar coupled systems are the same as discussed in the last chapter. However the operators introduced for calculations in the quadrupolar system are not well suited for larger systems, so a new set will be used. As the number of spins becomes large the calculations get quite complex, and hence feasible to do exactly only with a computer. However, we will see that many aspects of the experiments can be predicted using arguments of symmetry and statistics alone.

B. Fictitious Spin - $\frac{1}{2}$ Formalism

The operator basis defined in the last chapter was used initially for calculations in pure nuclear quadrupole resonance, making use of the eigenfunctions of I_z^2. In dipolar or scalar coupled systems

there is no natural extension of this basis set. Vega[90] and Ernst[94] have independently proposed a new formalism, an extension of Abragam's fictitious spin - $\frac{1}{2}$, which can be used in description of any spin system, since it is defined in terms of the eigenfunctions of the Hamiltonian. As in the last chapter calculations are performed by writing the Hamiltonian and density matrix in terms of these operators, then taking advantage of their simple commutation relations to predict evolution.

In any spin system with n eigenfunctions which are labeled simply by number $|i\rangle$ i = 1,2, ... n, we define three operators for each pair of states $|i\rangle$ and $|j\rangle$ (or for each generalized transition $|i\rangle \rightarrow |j\rangle$) analogous to the spin $\frac{1}{2}$ Pauli matricies:

$$\langle i|I_x^{ij}|j\rangle = \langle j|I_x^{ij}|i\rangle = \frac{1}{2}$$

$$\langle i|I_y^{ij}|j\rangle = -\langle j|I_y^{ij}|i\rangle = -\frac{i}{2}$$

$$\langle i|I_z^{ij}|i\rangle = -\langle j|I_z^{ij}|j\rangle = \frac{1}{2}$$

$$\langle k|I_\alpha^{ij}|\ell\rangle = 0 \quad \text{for all } k,\ell \neq i,j \qquad \text{(IV-1)}$$

This set has linear dependence among the z operators

$$I_z^{ij} + I_z^{jh} + I_z^{ki} = 0 \quad . \qquad \text{(IV-2)}$$

These operators have been defined so that they have commutation relations analogous to spin - $\frac{1}{2}$ for a single transition:

$$[I_p^{ij}, I_q^{ij}] = i\, I_r^{ij} \qquad p,q,r = x,y,z \text{ or cyclic permutation} \qquad \text{(IV-3)}$$

We must also have commutators for connected transitions

$$[I_x^{ik}, I_x^{jk}] = [I_y^{ik}, I_y^{jk}] = \frac{i}{2} I_y^{ij}$$

$$[I_x^{ik}, I_y^{jk}] = \frac{i}{2} I_x^{ij}$$

$$[I_x^{ik}, I_z^{jk}] = -\frac{i}{2} I_y^{ik}$$

$$[I_y^{ik}, I_z^{jk}] = \frac{i}{2} I_x^{ik}$$

$$[I_z^{ik}, I_z^{jk}] = 0 \qquad \text{(IV-4)}$$

Operators for transitions without a level in common commute. Because of the commutation relations (IV-3) we may again call this a fictitious spin - $\frac{1}{2}$ formalism. The I_x^{ij} and I_y^{ij} operators represent a coherence between levels i and j, regardless of the difference in quantum number between the levels, which we will call n quantum coherence where n is the difference in magnetic quantum number between i and j.

C. Comparison for Spin-1

Of course these operators, as a complete basis set, may also be used for description of a spin-1 system. For a spin-I we may write the observables as a sum of fictitious operators

$$F_\alpha = \sum_{ij} \sqrt{C^{ij}}\, I_\alpha^{ij} \qquad \alpha = x,y$$

$$F_z = \sum_{ij} C^{ij}\, I_z^{ij} \qquad \text{(IV-5)}$$

where $C^{ij} = I(I+1) - M_i M_j$. For comparison, we may write the fictitious

operators of Chapter III in terms of I_α^{ij}, where i and j are eigenstates 1,2,3 of the Hamiltonian with quadrupole coupling and without r.f.:

$$I_{x1} = \frac{1}{\sqrt{2}}(I_x^{12} + I_x^{13})$$

$$I_{x2} = \frac{1}{\sqrt{2}}(I_y^{12} - I_y^{13}) \qquad I_{z1} = I_z^{13}$$

$$I_{x3} = \frac{1}{2}(I_x^{12} + I_z^{12} - I_z^{23}) \qquad I_{z2} = I_y^{13}$$

$$I_{y1} = \frac{1}{2}(I_y^{12} + I_y^{23}) \qquad I_{z3} = -I_x^{13}$$

$$I_{y2} = \frac{1}{\sqrt{2}}(I_x^{12} - I_x^{23})$$

$$I_{y3} = \frac{1}{2}(I_x^{13} - I_z^{12} + I_z^{23}) \qquad \text{(IV-6)}$$

While the operators $I_{p,q}$ have matrix elements between more than two of the states 1, 2 and 3, both are complete basis sets and hence may be interchanged by a formal change of basis set. Of course the operators $I_{p,q}$ and I_α^{ij} will have physically different meanings.

The Hamiltonian for the spin-1 system in the rotating frame,

$$\mathcal{H} = -\Delta\omega I_z + \frac{1}{3}\omega_Q\,(3I_z^2 - I(I+1)) \quad , \qquad \text{(IV-7)}$$

may then be rewritten

$$\mathcal{H} = -\Delta\omega(I_z^{12} + I_z^{23} + I_z^{13}) + \frac{2}{3}\omega_Q\,(I_z^{12} - I_z^{23}) \qquad \text{(IV-8)}$$

To calculate the effect of radiation near one sattelite, as done in Chapter III B.2., we let $\Delta\omega = -\omega_Q + \delta\omega$ and include r.f. to give

$$\mathcal{H} = (-\omega_Q + \delta\omega)(I_z^{12} + I_z^{23} + I_z^{13}) + \frac{2}{3}\,\omega_Q(I_z^{12} - I_z^{23}) + 2\omega_1(I_x^{12} + I_x^{23}) \tag{IV-9}$$

As we ignored the I_{y2} term in the r.f. part previously, we now ignore $2\,\omega_1\,I_x^{23}$, since the energy differences of levels connected with off diagonal elements are much larger than ω_1. The Hamiltonian may then be rewritten as:

$$\mathcal{H} = \delta\omega\; I_z^{12} + \sqrt{2}\,\omega_1\; I_x^{12} - (\frac{4}{3}\,\omega_Q - \delta\omega)(I_z^{23} + I_z^{13}) \tag{IV-10}$$

This may be tilted to give an effective Hamiltonian along the z axis, with $U_{12}(y) = \exp(-i\theta\; I_y^{12})$ and $\theta = \arctan \sqrt{2}\,\omega_1/\delta\omega$:

$$\mathcal{H}_T = \omega_e\; I_z^{12} - (\frac{4}{3}\,\omega_Q - \delta\omega)(I_z^{23} + I_z^{13}) \tag{IV-11}$$

with

$$\omega_e = (2\,\omega_1{}^2 + \delta\omega^2)^{1/2} \quad .$$

The equilibrium density matrix may be written with the new operators:

$$\rho(0) = b(I_z^{12} + I_z^{23} + I_z^{13}) \tag{IV-12}$$

Tilting this with the operator used above

$$\rho_T(0) = b[(\cos\theta\; I_z^{12} - \sin\theta\; I_x^{12}) + (I_z^{23} + I_z^{13})] \tag{IV-13}$$

For a pulse of time t applied to $\rho(0)$ we find

$$\rho(t) = b[(\cos^2\theta + \sin^2\theta \cos\omega_e t)I_z^{12} + \frac{1}{2}(1-\cos\omega_e t)\sin\theta\ I_x^{12}$$

$$- \sin\omega_e t \sin\theta\ I_x^{12} + (I_z^{23} + I_z^{13})] \qquad \text{(IV-14)}$$

Of course with $\theta = 90°$ this produces the same evolution as calculated in Chapter III. The methods of calculating double quantum processes follows exactly that already described,[90,94] and will not be repeated here.

In general the density matrix may be written as

$$\rho(t) = a_o + \sum_{\alpha=x,y,z} [a_\alpha^{12}(t)\ I_\alpha^{12} + a_\alpha^{23}(t)\ I_\alpha^{23} + a_\alpha^{13}(t)\ I_\alpha^{13}] \qquad \text{(IV-15)}$$

With these operators the evolution is quite simple, and applying the commutation relations (IV-4) we find

$$a_x^{ij}(t) = a_x^{ij}(0) \cos\omega_{ij} t - a_y^{ij}(0) \sin\omega_{ij} t$$

$$a_y^{ij}(t) = a_x^{ij}(0) \sin\omega_{ij} t + a_y^{ij}(0) \cos\omega_{ij} t$$

$$a_z^{ij}(t) = a_z^{ij}(0) \text{ with } \omega_{ij} = \omega_i - \omega_j = \langle i|\mathcal{H}|i\rangle - \langle j|\mathcal{H}|j\rangle$$

(IV-16)

All evolution of ij operators is restricted to the ij space and occurs as a rotation about the z axis! This is very convenient and simple for calculation of evolution.

D. Preparation and Detection

As for the last chapter it is clear that the multiple quantum

coherences evolve without observable signals, so we again must break up the experiment into three parts: preparation, evolution and detection. This is shown schematically in Figure 74a. The preparation (P) and detection (D) operations are combinations of pulses and delays which we will specify shortly. We start in thermal equilibrium with density matrix $\rho(0) = b\, I_z$ and detect the amplitude of I_z at the end of the experiment. Then for an evolution time t_e we find

$$\langle I_z(t_e)\rangle = \mathrm{Tr}[D\, e^{-i\mathcal{H}t_e}\, P\, I_z P^+\, e^{i\mathcal{H}t_e}\, D^+\, I_z] \qquad \text{(IV-17)}$$

If we evaluate this in terms of the eigenfunctions of $\mathcal{H}$, the Hamiltonian for free evolution $(\mathcal{H}_z + \mathcal{H}_{cs} + \mathcal{H}_D)$

$$\langle I_z(t_e)\rangle = \sum_i \sum_j \langle i|D^+\, I_z D|j\rangle\, e^{-i\omega_j t_e}\, \langle j|P\, I_z P^+|i\rangle\, e^{+i\omega_i t_e}$$

$$= \sum_i \sum_j \langle i|D^+\, I_z D|j\rangle\langle j|P\, I_z P^+|i\rangle\, e^{-i\omega_{ji} t_e} \qquad \text{(IV-18)}$$

The multiquantum evolution is given by the oscillation of ω_{ji}, the energy difference between any two levels of the system. It is the matrix elements of $D^+ I_z D$ and $P I_z P^+$ which determine the amplitudes of the various multiquantum lines.

The approach we have applied to preparation and detection is similar to that of Chapter III B.5. and also to the approach of Ernst, et al.[65] Two strong (single quantum) pulses are applied spaced by a time τ, represented schematically in Figure 74b. We note that some selectivity may be achieved through careful choice of pulse phases and

experimental conditions, as will be discussed shortly.

To calculate the effect of the preparation and detection operators we write them out explicitly:

$$P = e^{i\theta I_p} e^{i\mathcal{H}_p \tau_p} e^{i\theta I_q} \qquad \text{(IV-19)}$$

where $\theta = \omega_1 t_p$, p and q specify the phase of the r.f. pulses and $\mathcal{H}_p$ is the Hamiltonian during the preparation period. The detection sequence has the same form. This may be simplified considerably in several cases of practical interest, which we examine below.

<u>Case 1</u>. $p = -x$, $q = x$, $\theta = \pi/2$ and $\mathcal{H}_p = \mathcal{H}_D$ the secular dipolar Hamiltonian. In this case we may write:

$$P = e^{i\mathcal{H}_{D_{xx}} \tau_p} \qquad \mathcal{H}_{D_{xx}} = e^{-i\frac{\pi}{2} I_x} \mathcal{H}_D e^{+i\frac{\pi}{2} I_x} \qquad \text{(IV-20)}$$

$\mathcal{H}_{D_{xx}}$ may be interpreted as the dipolar Hamiltonian after a rotation of $\pi/2$ about the x-axis. The effect of this rotation is most conveniently calculated using the dipolar Hamiltonian in its spherical form (see Appendix)

$$\mathcal{H}_D = \sum_{i<j} \sum_{q=-2}^{2} (-1)^q A^{ij}_{2,-q} T^{ij}_{2,q}$$

with

$$A^{ij}_{20} = -d\, C^{ij}_{20} \qquad d = \frac{\sqrt{6}\,\gamma^2 \hbar}{r^3_{ij}}$$

$$A^{ij}_{2\pm1} = \pm d\, C^{ij}_{2\pm1}$$

$$A^{ij}_{2\pm2} = -d\, C^{ij}_{2\pm2} \qquad C_{kq} = \left[\frac{4\pi}{2k+1}\right]^{1/2} Y_{kq}$$

$$T^{ij}_{20} = \frac{1}{\sqrt{6}} (3\ I_{zi}I_{zj} - I_i \cdot I_j)$$

$$T^{ij}_{2\pm1} = \mp(I_{zi}I_{\pm j} + I_{\pm i}I_{zj})$$

$$T^{ij}_{2\pm2} = \frac{1}{2}\ I_{\pm i}I_{\pm j} \qquad \text{(IV-21)}$$

The zeroth and first rank parts vanish because the tensor is traceless and symmetric. The effect of rotation may now be calculated with the Wigner rotation matrix. The secular part of (IV-27) is just

$$\bar{\mathcal{H}}_D = A^{ij}_{20}\ T^{ij}_{20} = \frac{\gamma^2\hbar}{r_{ij}^3} P_2(\cos\theta)(3I_{zi}I_{zj} - I_i \cdot I_j) \qquad \text{(IV-22)}$$

as noted in Chapter I. To rotate this we calculate

$$T'_{20} = \sum_{p=-2}^{2} T_{2p} D^2_{p0}(\alpha\beta\gamma) \qquad \text{(IV-23)}$$

where $\alpha = -\pi/2$, $\beta = \pi/2$ and $\gamma = \pi/2$ for the rotation of (IV-21). Evaluating this we find

$$T'_{20} = \frac{1}{2\sqrt{6}} (3I_{zi}I_{zj} - I_i \cdot I_j) - \frac{1}{2}\sqrt{\frac{3}{8}} (I_{+i}I_{+j} + I_{-i}I_{-j}) \qquad \text{(IV-24)}$$

We note that these terms have matrix elements with $\Delta m = 0, \pm 2$, and that these parts commute. Thus the operator $\exp(i\mathcal{H}_{D_{xx}} \tau_p)$ will only induce coherences between levels separated by an even number of quanta, what we term even quantum transitions, when operating on the initial density matrix I_z.

Case 2. $p = x$, $q = y$, $\theta = \pi/2$ and $\mathcal{H}_p = \mathcal{H}_D$.

This may be calculated in a fashion very similar to Case 1 if we insert a "virtual" pulse which has no real effect but simplifies computation. Immediately after the first x pulse the density matrix is I_y and we insert a pulse $e^{-i\frac{\pi}{2}I_y}$, which has no effect. However for the calculation we now have

$$P = e^{-i\mathcal{H}_{D_{yy}}\tau_p} e^{i\frac{\pi}{2}I_x} \quad ; \quad \mathcal{H}_{D_{yy}} = e^{-i\frac{\pi}{2}I_y} \mathcal{H}_D e^{i\frac{\pi}{2}I_y} \qquad \text{(IV-25)}$$

Of course $\mathcal{H}_{D_{yy}}$ has exactly the same properties as $\mathcal{H}_{D_{xx}}$ but now operates on I_y $(= -\frac{i}{2}(I_+ - I_-))$ instead of I_z and hence only odd quantum transitions will be observed.

Case 3. $p = -x$, $q = x$, $\theta = \pi/2$, $\mathcal{H}_p = -\Delta\omega I_z + \mathcal{H}_D$.

We note that the two parts of $\mathcal{H}_p$ commute. As above we may simply predict the effect of this preparation sequence, by inserting an identity operator:

$$P = e^{i\frac{\pi}{2}I_x} e^{i(-\Delta\omega I_z + \mathcal{H}_D)\tau_p} e^{-i\frac{\pi}{2}I_x}$$

$$= e^{i\frac{\pi}{2}I_x} e^{i\mathcal{H}_D\tau_p} e^{-i\frac{\pi}{2}I_x} e^{i\frac{\pi}{2}I_x} e^{-i\Delta\omega I_z\tau_p} e^{-i\frac{\pi}{2}I_x}$$

$$= e^{i\mathcal{H}_{D_{xx}}\tau_p} e^{-i\Delta\omega I_y\tau_p} \qquad \text{(IV-26)}$$

The order of transitions observed depend on the matrix elements

$$\langle i|P\ I_z\ P^+|j\rangle = \langle i|e^{i\mathcal{H}_{D_{xx}}\tau_p}\ e^{-i\Delta\omega I_y\tau_p}\ I_z\ e^{i\Delta\omega I_y\tau_p}\ e^{-i\mathcal{H}_{D_{xx}}\tau_p}|j\rangle$$

$$= \cos\Delta\omega\tau_p\ \langle i|e^{i\mathcal{H}_{D_{xx}}\tau_p}\ I_z\ e^{-i\mathcal{H}_{D_{xx}}\tau_p}\ |j\rangle$$

$$- \sin\Delta\omega\tau_p\ \langle i|e^{+i\mathcal{H}_{D_{xx}}\tau_p}\ I_x\ e^{-i\mathcal{H}_{D_{xx}}\tau_p}\ |j\rangle \quad . \qquad \text{(IV-27)}$$

It is clear that this is simply a weighted mixture of Case 1 and Case 2 above, and that for an arbitrary $\Delta\omega\tau_p$ <u>both</u> odd and even quantum transitions will be induced. We note that a spread of $\Delta\omega$ values for a sample, due to magnetic field inhomogeneity, makes use of $\Delta\omega\tau_p$ for selecting odd or even quantum transitions unattractive.

The principles of the detection period are identical to those presented above. However we note that since we are, on paper, detecting I_z, but real observables are I_x and I_y, we may omit p_y in the experiments rather than putting in a fifth pulse to probe the amplitude of I_z. For example the detection sequence

$$P_x(\tfrac{\pi}{2})\ \tau_d\ P_{-x}(\tfrac{\pi}{2})\ \text{detect}\ \langle I_z\rangle$$

would detect even quantum transitions, and is equivalent to

$$P_x(\tfrac{\pi}{2})\ \tau_d\ P_{-x}(\tfrac{\pi}{2})\ P_x(\tfrac{\pi}{2})\ \text{detect}\ \langle I_y\rangle = P_x(\tfrac{\pi}{2})\ \tau_d\ \text{detect}\ \langle I_y\rangle$$

since, of course, the -x,x sequence is an identity operator and may be dropped. Similarly

$$P_x(\tfrac{\pi}{2})\ \tau_d\ P_y(\tfrac{\pi}{2})\ \text{detect}\ \langle I_z\rangle$$

will detect odd quantum transitions, but may be replaced by

$$P_x(\tfrac{\pi}{2})\ \tau_d\ P_y(\tfrac{\pi}{2})\ P_y(\tfrac{\pi}{2})\ \text{detect}\ \langle I_x\rangle = P_x(\tfrac{\pi}{2})\ \tau_d\ \text{detect}\ \langle I_x\rangle \quad .$$

An off resonance term in the Hamiltonian will mix even and odd orders in detection just as it did in preparation.

It is also worth noting that if $\mathcal{H}_D$ is rotated through some angle other than $\pi/2$ (IV-20) the resulting T'_{20} will have $\Delta m = \pm 1$ terms in addition to $\Delta m = 0, \pm 2$, so that for all pulse sequences both even and odd orders would be observed. We will see shortly that some detection schemes can avoid this problem.

To this point we have only discussed strong pulse preparation sequences. Weak pulses, with ω_1 values somewhat less than average dipolar couplings, should also generate multiple quantum coherences, in analogy to the deuterium weak pulse preparation. In deuterium systems, where only the r.f. term and a quadrupole term had to be considered, we could obtain an explicit, if only approximate, form for the operator generating double quantum coherence. In systems of many coupled spins there is no simple single operator which drives multiple quantum transitions, so the combined effect of the r.f. and dipolar Hamiltonian would have to be calculated by computer. However with long weak pulses we intuitively feel that many orders of coherences would be generated. The same pulse could be used for detection, just as we use the same two pulse sequence for preparation and detection.

E. Echos

Echos of the Hahn type[78] can be of considerable use in multiple

quantum experiments of dipolar coupled systems. There are two types of echos which we will examine: single quantum and multiple quantum. These are very similar in principle, and some aspects of single quantum echos have been discussed in Chapter III. The simplest case possible is that all spins have the same chemical shift. Then the Hamiltonian for free evolution may be written:

$$\mathcal{H} = -\Delta\omega I_z + \sum_{i<j} d_{ij}\, P_2(\cos\theta)(3I_{zi}I_{zj} - I_i \cdot I_j) \qquad \text{(IV-28)}$$

where $\Delta\omega$ includes off resonance, chemical shift and magnetic field inhomogeneity contributions. It is important to note that in this case $[I_z, \mathcal{H}_D] = 0$. The ordinary single quantum evolution after a $\pi/2$ pulse is given by:

$$S_x(t) = \mathrm{Tr}[e^{-i\mathcal{H}t}\, I_x\, e^{i\mathcal{H}t}\, I_x] \qquad \text{(IV-29)}$$

If we now put a π y-pulse halfway through the evolution period, to create an echo we find:

$$S_x(t) = \mathrm{Tr}[e^{-i\mathcal{H}\frac{t}{2}}\, e^{-i\pi I_y}\, e^{-i\mathcal{H}\frac{t}{2}}\, I_x\, e^{i\mathcal{H}\frac{t}{2}}\, e^{i\pi I_y}\, e^{i\mathcal{H}\frac{t}{2}}\, I_x]$$

Inserting some identity operators this becomes

$$S_x(t) = \mathrm{Tr}[e^{-i\mathcal{H}\frac{t}{2}}\, e^{-i\mathcal{H}^R\frac{t}{2}}\, (-I_x)\, e^{i\mathcal{H}^R\frac{t}{2}}\, e^{i\mathcal{H}\frac{t}{2}}\, I_x] \qquad \text{(IV-30)}$$

where

$$\mathcal{H}^R = +\Delta\omega I_z + \sum_{i<j} d_{ij}\, P_2(\cos\theta)(3I_{zi}I_{zj} - I_i \cdot I_j) \quad .$$

Since the two parts of the Hamiltonian commute, the evolution from off resonance portions cancel, but the bilinear dipolar term remains unchanged, giving

$$S_x(t) = - \mathrm{Tr}\ [e^{-i\mathcal{H}_D t}\ I_x\ e^{i\mathcal{H}_D t}\ I_x] \qquad \text{(IV-31)}$$

as though the experiment had been performed exactly on resonance in a very homogeneous magnetic field. This is useful for preparation of even and odd multiple quantum transitions when combined with appropriate phase pulses as shown in Figure 74 e and g, since $\Delta\omega\tau_p = 0$ effectively for all spins in the sample, to a very high accuracy. This approach is also useful for obtaining very high resolution spectra in inhomogeneous magnets.

If an echo pulse is put into the center of the multiple quantum evolution period, exactly the same principles apply. The effect is particularly easy to calculate if a π pulse of x phase is used with $\pi/2$ x pulses in the preparation and detection periods. The preparation and detection operators consist of only x pulses and bilinear spin terms both of which are invariant to an x π pulse. Then we may write

$$S(t) = \mathrm{Tr}[De^{i\mathcal{H}\frac{t}{2}}\ e^{i\pi I_x}\ e^{i\mathcal{H}\frac{t}{2}}\ PI_zP^+\ e^{i\mathcal{H}\frac{t}{2}}\ e^{i\pi I_x}\ e^{i\mathcal{H}\frac{t}{2}}\ D^+\ I_z]$$

$$= \mathrm{Tr}[De^{i\mathcal{H}^R\frac{t}{2}}\ e^{i\mathcal{H}\frac{t}{2}}\ PI_zP^+\ e^{i\mathcal{H}\frac{t}{2}}\ e^{i\mathcal{H}^R\frac{t}{2}}\ D^+\ (-I_z)] \qquad \text{(IV-32)}$$

where $\mathcal{H}$ and $\mathcal{H}^R$ are defined as above (IV-28) and (IV-30). Again all off resonance, chemical shift and field inhomogeneity terms cancel, so the evolution is solely dipolar. A y π-pulse has the same effect but is a bit

messier to calculate, and inverts the sign of signal.

To this point we have been quite restrictive by specifying that all chemical shifts must be identical. If they are not, the Hamiltonian is

$$\mathcal{H} = \sum_i \Delta\omega I_{zi} + \sum_{i<j} d^{ij} P_x(\cos\theta)(3I_{zi}I_{zj} - I_i \cdot I_j) \qquad \text{(IV-33)}$$

The chemical shift and dipolar parts of the Hamiltonian no longer commute and the evolution under a single echo pulse sequence is complicated. This is very similar to the problems of T_2 measurement in liquids with coupled spins. These have been analyzed in detail elsewhere.[95,96] We note that under an echo train, if spaced sufficiently close together, the chemical shifts will average to zero. In a scalar coupled spin system, all information about the couplings then vanishes. However in a dipolar coupled system, all dipolar couplings should remain, with all chemical shifts removed. A train of echos may be applied in either single quantum or multiple quantum experiments.

F. Off Resonance and Phase Behavior

The evolution of multiple quantum coherences under an off resonance Hamiltonian is of practical importance for separation of various orders of transitions. We have already formally written out the evolution of the density matrix for multiple quantum operators (IV-16), but we wish to examine evolution of multiple quantum operators under simple rotations

$$e^{i\theta I_z} I_x^{ij} e^{-i\theta I_z} \qquad \text{(IV-34)}$$

To find the coefficients of I_x^{ij} and I_y^{ij} we calculate

$$C_x^{ij} = \mathrm{Tr}[e^{i\theta I_z} I_x^{ij} e^{-i\theta I_z} I_x^{ij}] \quad . \qquad \text{(IV-35)}$$

Using the definitions of multiple quantum operators we evaluate this in the eigenbasis of the Hamiltonian:

$$C_x^{ij} = \frac{1}{4}(e^{i\theta m_i} e^{-i\theta m_j} + e^{-i\theta m_i} e^{i\theta m_j})$$

$$= \frac{1}{4}(e^{i\theta(m_i-m_j)} + e^{-i\theta(m_i-m_j)}) = \frac{1}{2}\cos[(m_i-m_j)\theta] \qquad \text{(IV-36)}$$

where $m_i = \langle i|I_z|i\rangle$, the magnetic quantum number of the $i^{\underline{th}}$ state. We may similarly calculate C_y^{ij} by replacing the second I_x^{ij} by I_y^{ij}, giving

$$C_y^{ij} = \frac{1}{2}\sin[(m_i-m_j)\theta] \qquad \text{(IV-37)}$$

We see that the rotation angle (or rate if θ is time dependent) is multiplied by the number of quanta between the $i^{\underline{th}}$ and $j^{\underline{th}}$ levels. Thus if we have a resonance offset of $\Delta\omega$ in the single quantum spectrum, it will be $n\Delta\omega$ in the n quantum spectrum. This provides a simple way of distinguishing the various orders of transition. We note that an echo during the multiple quantum evolution will remove all resonance offset effects and we must use some other method to distinguish the various orders of transitions. Similarly, if the linewidth due to magnetic field inhomogeneity is $\delta\omega$ in the single quantum spectrum, then

it will be $n\delta\omega$ for the n quantum spectrum. For high order transitions such broadening becomes quite severe unless the magnet is very good or echo techniques are applied. It is interesting to note that the line-width of a zero quantum transition (between levels of the same magnetic quantum number) should be independent of magnetic field homogeneity, its width determined by T_2. This effect has also been noted by Ernst, et al.[65]

This rotational behavior also provides a method for separation of transitions of various orders. If instead of the $x\ \tau_p - x\ \tau_e\ x\ \tau_d$ pulse sequence described above (Figure 71c), we change the phase of the preparation pulses, keeping them 180° apart, but leave the detection sequence fixed, an extra order dependent phase factor is added. A pulse in the ϕ direction given by

$$I_\phi = I_x \cos\phi + I_y \sin\phi \qquad \text{(IV-38)}$$

may also be written as

$$I_\phi = e^{-i\phi I_z}\ I_x\ e^{i\phi I_z} \qquad \text{(IV-39)}$$

Rotating the pulses is equivalent to rotating the entire preparation sequence, so that the evolution (IV-17) may be rewritten

$$\langle I_z(t_e)\rangle = \mathrm{Tr}[D e^{-i\mathcal{H}t_e}\ e^{-i\phi I_z}\ P I_z P^+\ e^{i\phi I_z}\ D^+\ I_z] \qquad \text{(IV-40)}$$

Evaluation of this as (IV-18) gives

$$\langle I_z(t_e)\rangle = \sum_i \sum_j \langle i|D^+ I_z D|j\rangle\langle j|P I_z P^+|i\rangle\ e^{-i\omega_{ji} t_e}\ e^{i\phi(m_j - m_i)} \qquad \text{(IV-41)}$$

exactly the previous result except for the order dependent phase shift term. If a number of experiments are performed with different phases, linear combinations of them may be taken to generate spectra of specific orders, in effect a Fourier analysis over phase. If the highest order possible is N then N+1 different phase experiments must be performed to separate all orders. This method of order separation has also been discussed by Ernst[97] et al. Considerable selectivity may be achieved through a few experiments properly chosen. If the preparation is done on resonance or with an echo we have seen that only even transitions will be observed. If two such experiments are done with preparation sequences 90° apart (i.e., $x\ \tau_p\ -x$ and $-x\ \tau_p\ x$) the sum of the resulting spectra will show only 0,4,8 ... quantum spectra and the difference only 2,6,10 ... Such selection works whether the evolution period has an echo or not and provides an alternate method for separation of multiple quantum orders to the $n\Delta\omega$ dependence discussed above.

G. Amplitudes, Symmetry and Simplification

In principle, for a given experiment, (IV-18) allows us to calculate the amplitudes ($\langle i|D^+I_zD|j\rangle$ and $\langle j|PI_zP^+|i\rangle$) as well as frequencies (ω_{ji}) of lines in the multiquantum spectra. To calculate the amplitudes, one must already know all parameters in the dipolar Hamiltonian. However, in most cases the determination of these parameters is the object of the experiment. In addition the operators D^+I_zD and PI_zP^+ are complex and difficult to handle. In many cases it will be sufficient to determine line positions (frequencies) and ignore the amplitude. Since the dipolar Hamiltonian is driving the multiple quantum transitions, we expect that

a preparation period $\tau_p \sim (\overline{d^{ij}})^{-1}$ ($\overline{d^{ij}}$ is some sort of average dipolar coupling in frequency units) should be sufficient to generate many multiple quantum coherences. If we average over some range of τ_p values, we expect all multiple quantum lines to have non-zero amplitudes for some τ_p value, so that the average should be a complete spectrum with some average amplitudes. Phases will be essentially random in these spectra so the average must be of magnitude spectra.

In all of the analysis above we have assumed no symmetry in the set of eigenfunctions of $\mathcal{H}$. This is often not the case, and use of symmetry may simplify things considerably. In particular, the preparation and detection operators have A symmetry so that they induce transitions only among wavefunctions of the same symmetry. Such symmetry factoring reduces the number of possible transitions greatly as well as simplifying calculations.

We have stated that one reason for doing multiple quantum spectroscopy is to obtain spectral simplification in high quantum transitions. In an N spin system (with no symmetry) there are 2^N eigenfunctions. There are then approximately $\binom{N}{m}2^{N-m}$ m-quantum transitions, using simple counting arguments. Thus of course there is one N quantum transition (all spins go from β to α) and 2N transitions of order N-1. This is a tremendous reduction over the $N2^{N-1}$ single quantum transitions. The assignment of lines should be much simpler, and the smaller number of lines makes resolution requirements less stringent. The multiple quantum spectra are also much simpler in cases of high symmetry, as we will see.

H. Experimental, Benzene in EBBA

In order to obtain tractable spectra in dipolar coupled systems, the number of coupled spins must be kept relatively small. As we have discussed in previous chapters this may be achieved in solids through dilution. However, small molecules dissolved in liquid crystals provide a convenient system to test various aspects of multiquantum NMR. Liquid crystal solvents provide an anisotropic medium and when aligned in an external magnetic field cause small molecules dissolved in them to have a preferential orientation with respect to the field. Since these molecules no longer reorient isotropically, as in an ordinary liquid, the intramolecular dipolar couplings no longer average to zero. However there is still very rapid translational diffusion so that intermolecular couplings are averaged to zero and well resolved spectra are observed from the dissolved molecules. This has been known for quite some time and analysis of the dipolar structure has become a popular method for determination of structure and conformation of the dissolved molecules.[98] The number of spins on the liquid crystal molecules themselves is so large that no structure from them is resolved, though they contribute large uneven baselines to the spectra.

For the present experiments benzene was chosen since it is simple, of fairly high symmetry and has a reasonable number of spins. Approximately 15% (by mole) benzene was dissolved in EBBA (p-ethoxy-benzylidine n-butylaniline) so that the solution was nematic at room temperature (20°C), and sealed in a 6 mm glass tube after freezing and pumping. This sample was used for all experiments described. All experiments were performed on the spectrometer described in Chapter V.

Benzene oriented in a liquid crystal has been studied many times before.[99] The D_{6h} symmetry of the molecule breaks the wavefunctions up into 6 classes A, B, $2E_1$ and $2E_2$. The energy levels are shown schematically in Figure 75. With hexagonal symmetry assumed (convenient, not necessary) the spectrum is entirely determined by one dipolar coupling, and three spin-spin couplings, assuming no anisotropic component of spin-spin coupling. From the single quantum spectra, Figure 76, these may be determined $2d_{12}$ = -778.2 Hz, J_{12} = 8.0 Hz, J_{13} = 2.0 Hz, J_{14} = 0.5 Hz; in good agreement with previously determined values (d_{12} scales with order parameter and may not be directly compared). The linewidths in the ordinary single quantum spectrum, top Figure 76, are completely determined by magnetic field homogeniety at ∿ 120 Hz. The spectrum obtained using the echo sequence, Figure 74h, shows much better resolution, and was used for determination of the parameters above. The echos were generated at multiples of 300 μsec. Although 2048 echos were used (∿ 600 msec maximum), the amplitude was still substantial for the longest times and the linewidth observed, ∿ 4 Hz, was limited by truncation of the free induction decay. The ultimate linewidth in these experiments will be limited only by T_2.

Multiple quantum experiments measurements using pulse sequence c of Figure 74 were made for a variety of $\tau_p = \tau_d$ values. These were performed with a resonance offset of 5.97 kHz and hence were not selective in orders of transitions. Spectra were taken for 11 τ values between 9.6 msec and 10.7 msec spaced by 0.1 msec. The spectra were qualitatively similar, but had great variations of intensity in individual m-quantum lines. Due to the complex selection rules for multiple quantum transitions,

the phases of lines in the spectrum vary with τ_p. For this reason all plots and averages were performed on magnitude (or power) spectra. Figure 77 shows the average of the multiple quantum spectra. The theoretical spectra, also shown in Figure 77, we generated using the parameters determined in the single quantum echo experiment, with the assumption that each possible line in any order would appear with equal intensity. Each order was broadened by the appropriate amount for magnetic field inhomogeneity in that order. It is immediately clear that virtually all possible lines appear in the multiple quantum spectrum, though the intensities are not equal. Also, the resonance offset and linewidth are multiplied by the order as expected. With further averaging over preparation and detection periods, more equal intensities for all lines should be observed. In all of these experiments just the amplitude of the signal at the end of the detection sequence was used. If use is made of all signal after the detection sequence, through some type of two dimensional analysis, substantial improvements in signal to noise ratio should be achievable. In such an analysis coherence transfer echos as discussed by Ernst,[100] may enhance signal from high quantum transitions.

The selection experiments described in Section F were also tested on benzene in EBBA. Using $\tau_p = \tau_d = 10$ msec in pulse sequence e Figure 74, with x, -x and x 90° pulses and y 180° pulses, the off resonance, even quantum only spectrum in Figure 78(B) was obtained. The same experiment was performed with y, -y and x 90° pulses and gave the same magnitude spectrum. However when the sum and difference of the phase sensitive multiple quantum free induction decays were taken and Fourier

transformed the spectra of 78 (C) and 78 (D) were obtained, showing the increased selectivity, 0 and 4 quantum only, and 2 and 6 quantum only. The very small intensities in other orders are due to imperfections in pulse phases and amplitudes.

The 0 and 4 quantum selection experiment was also repeated with a much slower sampling rate, to determine the linewidth of the 0-quantum lines. The resulting decay and spectrum are shown in Figure 79. It is clear from the decay that the linewidth of 4 Hz for the zero quantum lines (no echo in the evolution period) was limited by truncation of the FID and the true linewidth is much less.

Since multiple quantum echos remove the evolution from off resonance, they were combined with the phase selection experiments described above, to generate very sharp line spectra without losing the separation of the various multiple quantum orders. Pulse sequence f of Figure 74 was used with $\Delta\omega$ carefully adjusted to zero so that only even order transitions would be observed, and $\tau_p = \tau_d = 10$ msec. Figure 80 shows the spectrum resulting from a single such experiment, containing lines from all even orders. Taking the sum and difference of experiments with both preparation pulses phase shifted by $90°$ gave the spectra shown in Figures 81 and 82.

The separation of orders is quite good. The resolution is clearly greatly improved over that in the previous multiple quantum experiment, Figure 77. In addition the linewidth is the same for all orders, $\sim$ 3 Hz, and was, as for the single quantum, limited by truncation of the free induction decay. These experiments were performed for only one particular τ_p value and hence many possible multiple quantum lines

are not observed. Averaging of a number of τ_p values, as done for the echoless spectrum, would remedy this. Some small single quantum lines were observed, probably because of magnetic field inhomogeneity (some parts of the sample are slightly off resonance even when the average $\Delta\omega$ is zero) and pulse imperfections. The rejection of odd orders could be improved by using an echo in the preparation and detection periods as well as in evolution.

I. Discussion

We have demonstrated that multiple quantum coherences, generated through the dipolar coupling, may be observed even for high orders. The dependences of the multiple quantum orders upon off resonance and phase shifts allow separation of the various orders. Echos may be used to improve linewidths in both single and multiple quantum experiments.

These techniques should prove most valuable in more complex systems. As the number of spins increases the single quantum spectrum rapidly becomes very complex, to the point that lines are no longer separated. In such cases the number of lines in the high order multiple quantum spectra should be much smaller, and hence well resolved and interpretable. Such experiments may prove to be easier and more informative than labeling studies, particularly in liquid crystal and perhaps lipid systems. These techniques are also applicable to solid samples in which relatively isolated groups of spins exist. As such they should be complementary to existing deuterium double quantum, various dilute spin and separated local field techniques for determining relative positions of spins in solids. Studies of relaxation of the various multiquantum

coherences may also provide additional dynamic information.

V. THE SPECTROMETER

The spectrometer used for all of the experiments described in the previous chapters was designed primarily for solid state work, but is quite conventional in many respects. It was homebuilt but includes many commercial components.

A. Magnet

The magnet is a persistent superconducting solenoid made by Bruker Instruments, operating at 42.5 kG. Its dewar has a 3.5 inch diameter room temperature bore and can be easily shimmed, with x, y and z superconducting coils, to less than 1 PPM over a 1 cm^3 region. The operating frequencies for nuclei discussed here are:

^1H	185.02 MHz
^{13}C	46.522 MHz
^2H	28.403 MHz

The field is extremely stable so that no field/frequency lock is necessary.

B. Frequency Generation

A block schematic of the spectrometer's radio frequency section is shown in Figure 83.

The proton frequency is based upon the output of a General Radio Model 1042 frequency synthesizer (0.1 - 160 MHz), at 142.5 MHz. This is doubled to give a local oscillator (ℓ.o.) frequency of 285 MHz, then mixed with the 100 MHz intermediate frequency (i.f.) and filtered to give 185 MHz.

The i.f. is generated by multiplying the G. R. synthesizer's 10 MHz reference by 10. The continuous 185 MHz is passed through commercial quadrature hybrids and switches to give two (or four at times) 90° out of phase channels. The amplitude of the switched r.f. is adjusted in 1dB units with an attenuator and is switched again to insure good isolation. The final switched output goes to the high power transmitters.

The low frequency is generated simultaneously for double resonance, and is based upon the output of a Hewlett-Packard Model 3320A synthesizer. This is doubled for carbon and used directly for deuterium. Switching and quadrature generation is done at the nuclear frequency as for proton. It is mixed with a 30 MHz i.f. to give an ℓ.o. frequency for use in the receiver. The 30 MHz i.f. is generated by tripling the 10 MHz reference from the G. R. synthesizer.

C. Receivers

The proton and low frequency receivers operate in a very similar manner. The first stage is a low noise preamplifier with approximately 25 dB of gain. The signal from this is mixed with the ℓ.o and filtered to give an i.f. signal. This signal is amplified with a variable gain i.f. strip amplifier (up to 70 dB gain). This signal then goes to the phase detector. The overall recovery time from complete saturation (during pulses) is about 20 μsec.

D. Phase Detector

This spectrometer employs dual phase detectors. The i.f. signal from the receiver is passed through a power splitter. The i.f.

reference is passed through a variable delay time, to adjust the relative phase of signal and detector. It is then split by a quadrature hybrid, and each phase is mixed with the signal to give quadrature audio frequency signals, which pass through a variable low pass filter and then are digitized. The signal to noise improvement by having dual detectors is valuable and being able to determine signs of frequency offsets is convenient.

E. Digitizers

In solid state NMR lines may be very broad, and hence it is necessary to have fast sample and holds and analog-digital converters. This spectrometer uses Datel Model SHM2 S/H s with ~ 10 nsec windows, and Datel Model ADCE10B A/D s, 10 bits and 1.25 μsec conversion time. The digitized signal is passed to a NOVA 820 computer, with an overall maximum rate of 333 kHz for complex points. This is sufficiently fast for all work described here, even deuterium quadrupole powder patterns.

F. Probes

The double resonance probes used for this work have crossed coil configurations, and were home built. The lower frequency coil was a solenoid 6 mm in diameter, placed inside an 8 mm outer diameter glass tube. The proton coil was of the Helmholtz type, consisting of two turns on each side, each ~ 1 cm in diameter. These were mounted on the outside of the glass tube. These coils were part of a tuned circuit consisting of homemade series tuning capacitors and parallel commercial silver mica matching capacitors. With 200 watts of r.f. power, rotating fields of

10 G for protons, 60 G for carbon and greater than 100 G for deuterium could be generated. The coils were orthogonal to minimize receiver pick-up of decoupling frequency and the isolation was 30-40 dB. Additional isolation was provided by a low pass or bandpass filter to block the decoupler frequency. The receiver was protected from r.f. pulses at the observed frequency by placing diodes to ground at one quarter wavelength from the probe junction. Series diodes were used to block transmitter noise during observation. The overall probe configuration is shown schematically in Figure 84.

For single resorance experiments on protons (multiple quantum) the Helmholtz coils were replaced with a 6 mm solenoid. This gave a factor of four improvement in signal and r.f. field due to the better filling factor and higher Q of a solenoid.

The coils, mounted above the plastic disk holding the capacitors, are covered with a glass dewar to provide thermal isolation. The temperature is measured with a thermocouple placed near the sample. Temperature control is provided in two stages, by passing heated or cooled gas into the probe dewar through vacuum jacketed tubes. N_2 gas is heated by a resistive heater at the end of the probe. Crude control is provided by the gas flow rate and power delivered to the heater. Cold gas is generated by boiling liquid N_2 from a 50ℓ dewar with a resistive heater. Flow rate is controlled by variation of heater power. Fine control for both heating and cooling is provided by a feedback system. The output of a thermocouple indicator is digitally compared with a settable desired temperature. If the observed temperature is less than the desired a small auxiliary heater in the transfer line into the probe is turned on.

Set and observed temperature are compared several times per second, providing temperature control of ± 0.2°C over a range −190 to + 150°C.

G. Transmitters

Transmitters (high power final stage amplifiers) at all frequencies were class C, tuned tube type. For carbon and deuterium they were Millen design using 3E829 tubes. The proton transmitter was a cavity tuned output type based on a 220 MHz design for radio amateurs,[101] using a 4CX250B tube. All were run with 2.5 kV plate, 130 V bias and 250 - 500 V screen voltage. All are capable of generating 200 watts of pulsed r.f. power. They are driven by commercial solid state amplifiers at ~ 10 watts. Adjustment of r.f. field strength was made by changing screen voltage.

H. Pulse Programmer

The timing of all r.f. pulses and data acquisition is controlled by a pulse programmer. In order to put out the variety of pulse sequences described in this work with very accurate timing, a very flexible programmer was designed and built. The pulse program consists of 16 words of 36 bits which are interpreted in hardware to generate delays and open gates. Twelve bits specify gate outputs for controlling r.f. switches, triggering of the data system, etc. Twelve bits are used to specify a delay, as a number from 0 to $2^{10}-1$ and a multiplier of 250 nsec, μsec, msec or sec. The delays are digitally counted from an internal 4 MHz clock. Each program word may also be flagged as the beginning or end of a loop. There are four loops which may be specified, each with a counter

so that all words between the beginning and end of the loop are executed from 1- 10000 times before continuing beyond the loop. The programmer may also transfer timing control to any one of four external devices for synchronization with other spectrometer functions.

The pulse programmer can operate as a stand-alone device, with pulse programs directly loaded from front panel switches. Delays and loops are also settable with front panel controls. However the programmer is also interfaced to the system's computer (Section V-I), which can control all operations of the programmer, including loading of previously defined pulse programs, setting loop values and starting or stopping execution of the program. This system provides remarkable flexibility in application and is capable of executing very complex pulse sequencies. The computer control allows execution of repetitive experiments, such as T_1 measurement and collection of multiple quantum free induction decays, automatically, greatly improving efficiency over a strictly operator controlled system.

I. Computer and Software

This spectrometer uses a NOVA 820 computer as an on line data processing unit. The computer is interfaced to a CRT terminal for use as a console device, a 5 Mbyte dual disc for program and data storage, a CRT x-y display for data observation, or digital plotter, and the A/D converters for data acquisition.

A large program for operation of the spectrometer was written in a series of overlays residing on the disc so that only a small part is resident in the memory at a time. This allows room for 4k complex data

points in the 16 k word memory in addition to the program. Commands for usual manipulations of free induction decays, performing Fourier Transformation, phase corrections etc., are subroutines in this program. In addition there are routines for manipulation of two dimensional arrays of data, necessary for some double quantum and multiple quantum experiments. A powerful supercommand structure, termed macrocommands, has also been included. These macros are definable sequences of any commands in the operating program. Execution of the macro causes sequential execution of the commands defining it, cyclically, any number of times desired. Up to 100 macros may be defined, and they may be nested (one macro calling another) in any way desired. Such commands provide a rapid and efficient way of collecting and processing data, particularly in two dimensional experiments.

J. Discussion

In many respects the spectrometer described here is typical of pulse-Fourier Transform NMR equipment. There are a few distinguishing features which allow it to perform a wide variety of experiments in ordered phases. The relatively high field and good homogeneity provide good sensitivity and resolution. In dilute spin NMR sensitivity is often a problem which high fields and signal averaging together can overcome. The final r.f. stages of the spectrometer must be capable of generating high power pulses, to cover a wide spectral range and insure complete decoupling. The probes must be designed to withstand the high power (and hence high voltage) pulses and yet retain high sensitivity. A very versatile pulse programmer is necessary for generation of complex pulse

sequences with controllable delays. The data acquisition must be fast enough to faithfully digitize over the wide spectral width found in solids. A computer for data manipulation and storage is necessary. The software should be quite general, with modifications easily made for adaptation to new experiments.

Appendix A Spherical Form For Tensors

Rose gives for multiplication of two tensors:

$$T^{\ell}_{m}(A_1,A_2) = \sum_{m_1} C(\ell_1\ell_2\ell,m_1,m-m_1)\ T^{\ell_1}_{m_1}(A_1)\ T^{\ell_2}_{m-m_1}(A_2)$$

where $C(\ell_1\ell_2\ell,m_1,m-m_1)$ are Clebsch-Gordon coefficients.

Multiplication of two first rank tensors gives us:

zero rank:

$$T^0_0(1,2) = 1/\sqrt{3}\ [T^1_{-1}(1)T^1_1(2) - T^1_0(1)T^1_0(2) + T^1_1(1)T^1_{-1}(2)]$$

first rank:

$$T^1_{-1}(1,2) = -1/\sqrt{2}\ [T^1_{-1}(1)T^1_0(2) - T^1_0(1)T^1_{-1}(2)]$$

$$T^1_0(1,2) = -1/\sqrt{2}\ [T^1_{-1}(1)T^1_1(2) - T^1_1(1)\ T^1_{-1}(2)]$$

$$T^1_1(1,2) = -1/\sqrt{2}\ [T^1_0(1)T^1_1(2) - T^1_1(1)T^1_0(2)]$$

second rank:

$$T^2_{-2}(1,2) = T^1_{-1}T^1_{-1}(2)$$

$$T^2_{-1}(1,2) = 1/\sqrt{2}\ [T^1_{-1}(1)T^1_0(2) + T^1_0(1)T^1_{-1}(2)]$$

$$T^2_0(1,2) = 1/\sqrt{6}\ [T^1_{-1}(1)T^1_1(2) + 2\ T^1_0(1)T^1_0(2) + T^1_1(1)T^1_{-1}(2)]$$

$$T^2_1(1,2) = 1/\sqrt{2}\ [T^1_0(1)T^1_1(2) + T^1_1(1)\ T^1_0(2)]$$

$$T^2_2(1,2) = T^1_1(1)T^1_1(2)$$

Given a cartesian vector $\underset{\sim}{B} = (B_x, B_y, B_z)$ we can form linear combinations which transform as first order spherical harmonics, giving a spherical vector

$$B_{-1} = B_x - iB_y$$

$$B_0 = B_z$$

$$B_{+1} = B_x + iB_y \quad .$$

If we multiply this spherical vector by itself we find (from previous page)

$$T_0^0(1,2) = -1/\sqrt{3}\ [B_x(1)B_x(2) + B_y(1)B_y(2) + B_z(1)B_z(2)]$$

$$T_{-1}^1(1,2) = -1/\sqrt{2}\ [(B_x(1)B_z(2) - B_z(1)B_x(2) - i(B_y(1)B_z(2) - B_z(1)B_y(2))]$$

$$T_0^1(1,2) = i/\sqrt{2}\ [B_x(1)B_y(2) - B_y(1)B_x(2)]$$

$$T_1^1(1,2) = -1/2\ [B_x(1)B_z(2) - B_z(1)B_x(2) + i(B_y(1)B_z(2) - B_z(1)B_y(2))]$$

$$T_{-2}^2(1,2) = 1/2\ [B_x(1)B_x(2) - B_y(1)B_y(2) - i(B_x(1)B_y(2) + B_y(1)B_x(2))]$$

$$T_{-1}^2(1,2) = 1/2\ [B_x(1)B_z(2) - B_z(1)B_x(2) - i(B_y(1)B_z(2) + B_z(1)B_y(2))]$$

$$T_0^2(1,2) = 1/\sqrt{6}\ [2B_z(1)B_z(2) - B_x(1)B_x(2) - B_y(1)B_y(2)]$$

$$T_1^2(1,2) = 1/2\ [-(B_x(1)B_z(2) + B_z(1)B_x(2)) - i(B_y(1)B_z(2) + B_z(1)B_y(2))]$$

$$T_2^2(1,2) = 1/2\ [B_x(1)B_x(2) - B_y(1)B_y(2) + i(B_x(1)B_y(2) + B_y(1)B_x(2))]$$

This gives us the combinations which transform according to the various spherical harmonics.

Now putting in $\mathcal{H} = (0,0,\mathcal{H}_z)$ and $I = (I_x, I_y, I_z)$

$$T^0_0 = -1/\sqrt{3}\ \mathcal{H}_z I_z \qquad T^2_{-2} = 0$$

$$T^1_{-1} = 1/2\ \mathcal{H}_z I_- \qquad T^2_{-1} = 1/\sqrt{2}\ \mathcal{H}_z I_-$$

$$T^1_0 = 0 \qquad T^2_0 = 2/\sqrt{6}\ \mathcal{H}_z I_z$$

$$T^1_1 = 1/2\ \mathcal{H}_z I_+ \qquad T^2_1 = 1/\sqrt{2}\ \mathcal{H}_z I_+$$

$$T^2_2 = 0$$

And for shielding tensor, diagonal in p.a. system

$$A^0_0 = -1/\sqrt{3}\ (\sigma_{11}+\sigma_{22}+\sigma_{33}) \qquad A^2_2 = 1/2\ (\sigma_{11}-\sigma_{22})$$

$$A^1_{-1} = 0 \qquad A^2_{-1} = 0$$

$$A^1_0 = 0 \qquad A^2_0 = 1/\sqrt{6}\ (2\sigma_{33}-\sigma_{11}-\sigma_{22})$$

$$A^1_1 = 0 \qquad A^2_1 = 0$$

$$A^2_2 = 1/2\ (\sigma_{11}-\sigma_{22})$$

$$\mathcal{H} = A^0_0 T^0_0 + A^2_0 T^2_0$$

$$= [\tfrac{1}{3}(\sigma_{11}+\sigma_{22}+\sigma_{33}) + \tfrac{1}{3}(2\sigma_{33}-\sigma_{11}-\sigma_{22})]\ {}_z I_z = \sigma_{33} H_z I_z$$

Appendix B Optimization of Cross Polarization Time

To a good approximation, for the single contact cross polarization experiments used for this work, heating of the proton (I spin) reservoir by contact with dilute spins (S spins) is small compared to heating by the lattice, occuring with time constant $T_{1\rho}$. In this approximation the inverse temperatures of the two systems follow differential equations:

$$\frac{d\beta_S(t)}{dt} = -\frac{1}{T_{IS}}\,(\beta_S(t)-\beta_I(t))$$

$$\frac{d\beta_I(t)}{dt} = -\frac{1}{T_{1\rho}}\,\beta_I(t)$$

with initial conditions $\beta_S(0) = 0$ and $\beta_I(0) = \beta_{IO}$. The solutions are easily found to be

$$\beta_S(t) = \frac{\beta_{IO}}{(1-\frac{T_{IS}}{T_{1\rho}})}\,(e^{-t/T_{1\rho}} - e^{-t/T_{IS}})$$

$$\beta_I(t) = \beta_{IO}\,e^{-t/T_{1\rho}}$$

We wish to maximize $\beta_S(t)$, and hence the S polarization. $\beta_S(t)$ reaches its maximum at time

$$t_m = \frac{T_{1\rho}\,T_{IS}}{T_{1\rho}-T_{IS}}\,\ln(\frac{T_{1\rho}}{T_{IS}}) \qquad \text{for} \qquad T_{1\rho} \neq T_{IS}$$

or

$$t_m = T_{IS} = T_{1\rho} \qquad \text{for} \qquad T_{1\rho} = T_{IS}$$

t_m is then the optimum contact time for the cross polarization. Since it is very time consuming to measure $T_{1\rho}$ and T_{IS}, most often the adjustment of cross polarization time will be made empirically. However it is worth noting that for short $T_{1\rho}$ (on the order of usual T_{IS} values $\sim$ 200 μsec) the mixing time must be much less than the usual few milliseconds.

Appendix C Optimization of Recycle Delay

We wish to optimize signal to noise in a "saturating" experiment, for a fixed total aquisition time T. The spin lattice relaxation time for relevant spins = T_1, and recycle delay (to be optimized) = τ.

The magnetization at time τ after saturation is

$$M(t) = M_0(1-e^{-\tau/T_1}) \quad .$$

The number of experiments that can be done in time T is

$$N = T/\tau \quad .$$

The signal to noise goes up linearly with signal (magnetization) and as square root of number of experiments averaged

$$S/N(T,\tau) = M_0(1-e^{-\tau/T_1})(T/\tau)^{1/2}$$

To maximize in τ

$$\left(\frac{\partial\ S/N(T,\tau)}{\partial\tau}\right)_{T,T_1} = 0 = \frac{1}{2\tau} + \frac{1}{T_1} - \frac{e^{-\tau/T_1}}{2\tau}$$

requiring that $e^{-\tau/T_1} = 1 + \frac{2\tau}{T_1}$. The zero found numerically is at

$$\tau = 1.2564\ T_1$$

and represents the optimum recycle delay for maximization of S/N. This is, however, a rather weak maximum, so values near it are almost as good.

Appendix D Matrix Solution for Exchange

This appendix describes an analytical inversion for the exchange matrix $\underset{\approx}{A}$ to derive the lineshape for spins undergoing hard collision exchange. We wish to calculate

$$I(\omega) = \mathrm{Re}\{\underset{\sim}{P}\cdot\underset{\approx}{A}^{-1}\cdot\underset{\sim}{I}\}$$

where $\underset{\sim}{P}$ is a population vector, $\underset{\approx}{A}$ is the exchange matrix and $\underset{\sim}{I}$ is the unit vector. For an exchange problem with n sites, where probabilities for going from any site to any other are equal, the rate of jumps between any two sites will be $1/(n-1)\tau$ where τ is the average lifetime of a state. If we assume that the T_2 values for all sites are equal then the exchange matrix is defined by:[1]

$$A_{jj} = i(\omega_j-\omega) + \frac{1}{T_2} + \frac{1}{\tau}$$

$$A_{jk} = -\frac{1}{(n-1)\tau} \qquad j \neq k$$

The inversion of $\underset{\approx}{A}$ may be done simply if it can be written in the form

$$\underset{\approx}{A} = \underset{\approx}{B} + \underset{\sim}{u}\underset{\sim}{v}$$

where $\underset{\approx}{B}$ is easily inverted. In the case at hand we can make $\underset{\approx}{B}$ diagonal, and hence trivially invertable by taking

$$\underset{\sim}{u} = \underset{\sim}{I}_{cn} \qquad \underset{\sim}{v} = \frac{-1}{(n-1)\tau}\ \underset{\sim}{I}_{rn}$$

where $\underset{\sim}{I}_{cn}$ and $\underset{\sim}{I}_{rn}$ are respectively n dimensional column and row identity

vectors. Then

$$\underset{\sim}{u}\underset{\sim}{v} = \frac{-1}{(n-1)\tau} \underset{\sim}{I}_{cn} \underset{\sim}{I}_{rn}$$

where $\underset{\sim}{I}_{cn} \underset{\sim}{I}_{rn}$ has ones everywhere. This leaves

$$B_{jj} = i(\omega_j - \omega) + \frac{1}{T_2} + \frac{n}{(n-1)\tau}$$

$$B_{jk} = 0 \qquad j \neq k \qquad .$$

We define $\gamma_j = B_{jj}^{-1}$ which are the diagonal elements of $\underset{\approx}{B}^{-1}$ which has all off diagonal elements zero. With $\underset{\approx}{A}$ written this way

$$\underset{\approx}{A}^{-1} = \underset{\approx}{B}^{-1} - \lambda \underset{\sim}{y}\underset{\sim}{z}$$

where

$$\underset{\sim}{y} = \underset{\approx}{B}^{-1} \underset{\sim}{u} \quad , \quad \underset{\sim}{z} = \underset{\sim}{v} \underset{\approx}{B}^{-1} \quad \text{and } \lambda = \frac{1}{1+\underset{\sim}{z}\underset{\sim}{u}} \quad .$$

In the case at hand,

$$y_j = \gamma_j \qquad\qquad z_j = \frac{-1}{(n-1)\tau} \gamma_j$$

$$\lambda = (1 - \frac{1}{(n-1)\tau} (\gamma_1 + \gamma_2 + \ldots + \gamma_n))^{-1}$$

and

$$\underset{\sim}{y}\underset{\sim}{z}_{jk} = \frac{-1}{(n-1)\tau} \gamma_j \gamma_k \qquad .$$

Then

$$A_{jk}^{-1} = \delta_{jk}\gamma_j + \frac{\lambda}{(n-1)\tau} \gamma_j \gamma_k \qquad .$$

The final result we desire is $\sum_j \underset{\sim}{P} \cdot \underset{\sim}{A}^{-1}$

We define

$$\zeta = P_1\gamma_1 + P_2\gamma_2 + \ldots + P_n\gamma_n$$

$$\Gamma = \gamma_1 + \gamma_2 + \ldots + \gamma_n \quad .$$

Now

$$\sum_j \underset{\sim}{P} \cdot \underset{\approx}{A}^{-1} = \frac{(n-1)\tau\ \zeta}{(n-1)\tau - \Gamma}$$

and

$$I(\omega) \propto \mathrm{Re}\ \{\frac{(n-1)\tau\ \zeta}{(n-1)\tau - \Gamma}\} \quad .$$

This result is equivalent to that derived in the text (II-54), arrived at from a very different approach.

To see this we compare II-54

$$g(\omega) = \frac{i \sum_i \frac{c_i}{\alpha_i + \omega_i}}{1 - \frac{\omega_\lambda}{n} \sum_{-i-} \frac{1}{\alpha_i + \omega_\lambda}}$$

where the symbols have their previously defined meanings and c_i is proportional to the population of the $i^{\underline{th}}$ state. In the matrix solution we have eliminated jumps of 2π whereas they have been included in the solution of Chapter II. To compare the solutions then we replace n-1 of the Appendix solution by n. Then

$$\frac{1}{\alpha_i+\omega_\lambda} = \lambda_i \quad , \quad \sum_i \frac{1}{\alpha_i+\omega_\lambda} = \Gamma$$

and $\sum_i \frac{c_i}{\alpha_i+\omega_\lambda} = k\zeta$ with k a proportionality constant. We may then write

$$g(\omega) = \frac{nk'\zeta}{n\tau_\lambda-\Gamma} \quad ,$$

the same as the matrix solution.

Appendix E Listings of Programs MTHEX, SEXCH, PPGEN

```
PAUSE
C       OBTAINS LINESHAPE FOR HARD COLLISION EXCHANGE OF SEVERAL
C       SITES WITH DIFFERENT CHEMICAL SHIELDING AND
C       DIFFERENT POLULATIONS
C
        INTEGER BLANK,STAR,PLOT(100)
        REAL EULER(3,10),LPPM,LOMG,JFREQ,INTEN(200),OMG(10),LARGE
        REAL SIG11(10),SIG22(10),SIG33(10),SIGISO(10),OMGISO(10)
        REAL OMG11(10),OMG22(10),OMG33(10),ETAH(10),POPV(10)
        COMPLEX GAMMA,ZETA
C
C       OPEN FILE FOR LATER PLOTTING
        CALL FGTFS (ISLOT,IERR)
        IF (IERR .EQ. 0) GO TO 2
        WRITE (10,1) IERR
1       FORMAT (1X,'ERROR CODE =', 0I3)
        GO TO 100
2       CALL FOPFL ('CDC:DA',ISLOT,IERR)
        IF (IERR .EQ. 0) GO TO 7
        WRITE (10,1) IERR
        GO TO 100
C
C       INITIALIZE
7       BLANK=' '
        STAR='*'
        IPMAX=40
        PI=4.0*ATAN(1.0)
C
C       OBTAIN INVARIANT PARAMETERS
10      WRITE (10,11)
11      FORMAT(1X,'ENTER SPECTROMETER FREQ IN MHZ: ')
        READ (11) XNU0
        IF (XNU0 .LE. 0) GO TO 100
        OMG0=2.0*PI*XNU0
        WRITE (10,12)
12      FORMAT(1X,'ENTER NUMBER OF SITES: ')
        READ (11) NSITE
        DO 16 J=1,NSITE
        WRITE (10,13) J
13      FORMAT (1X,'ENTER SIG11,SIG22,SIG33 FOR SITE ',I3,' IN PPM: ')
        READ (11) SIG11(J),SIG22(J),SIG33(J)
        SIGISO(J)=(SIG11(J)+SIG22(J)+SIG33(J))/3.0
        OMGISO(J)=SIGISO(J)*OMG0
        OMG11(J)=(SIG11(J)-SIGISO(J))*OMG0
        OMG22(J)=(SIG22(J)-SIGISO(J))*OMG0
        OMG33(J)=(SIG33(J)-SIGISO(J))*OMG0
        ETAH(J)=(OMG11(J)-OMG22(J))/2.0
        WRITE (10,14) J
14      FORMAT(1X,'ENTER EULER ANGLES FOR NUCLEUS',I3,' IN DEGREES: ')
        READ (11) (EULER(I,J),I=1,3)
        DO 15 I=1,3
        EULER(I,J)=EULER(I,J)*PI/180.0
15      CONTINUE
16      CONTINUE
        WRITE (10,165)
165     FORMAT(1X,'ENTER POPULATION VECTOR: ')
        READ (11) (POPV(I),I=1,NSITE)
        WRITE (10,17)
17      FORMAT(1X,'ENTER LOW AND HIGH POLAR ANGLES IN DEGREES: ')
        READ (11) PMIN,PMAX
        PMIN=COS(PMIN*PI/180.0)
```

```
      PMAX=COS(PMAX*PI/180.0)
      WRITE (10,18)
18    FORMAT(1X,'ENTER NUMBER OF POLAR ANGLES: ')
      READ (11) NPOLAR
      DPOLAR=(PMAX-PMIN)/NPOLAR
      WRITE (10,19)
19    FORMAT(1X,'ENTER LOW AND HIGH AZIMUTHAL ANGLES IN DEGREES: ')
      READ (11) AMIN,AMAX
      AMIN=AMIN*PI/180.0
      AMAX=AMAX*PI/180.0
      WRITE (10,20)
20    FORMAT(1X,'ENTER NUMBER OF AZIMUTHAL ANGLES: ')
      READ (11) NAZIM
      DAZIM=(AMAX-AMIN)/NAZIM
      WRITE (10,21)
21    FORMAT(1X,'ENTER LOW AND HIGH PLOT LIMITS IN PPM: ')
      READ (11) LPPM,HPPM
      LOMG=LPPM*OMG0
      HOMG=HPPM*OMG0
      WRITE (10,22)
22    FORMAT(1X,'ENTER NUMBER OF FREQUENCY POINTS: ')
      READ (11) NOMG
      DPPM=(HPPM-LPPM)/(NOMG-1)
      DOMG=(HOMG-LOMG)/(NOMG-1)
C
C     OBTAIN VARYING PARAMETERS
25    WRITE (10,26)
26    FORMAT(1X,'ENTER JUMP FREQUENCY IN HZ: ')
      READ (11) JFREQ
      IF (JFREQ .LE. 0.0) GO TO 10
      TAU=1.0/JFREQ
      TAUN=(NSITE-1.0)*TAU
      WRITE (10,27)
27    FORMAT(1X,'ENTER T2 IN SEC: ')
      READ (11) T2
      RPART=NSITE*JFREQ/(NSITE-1.0)+1.0/T2
C
C     INITIALIZE INTENSITIES
      DO 31 I=1,NOMG
      INTEN(I)=0.0
31    CONTINUE
C
C     LOOP OVER ORIENTATIONS
      DO 38 IPOLAR=1,NPOLAR
      CTH=PMIN+IPOLAR*DPOLAR
      CSQTH=CTH*CTH
      SSQTH=1.0-CSQTH
      STH=SQRT(SSQTH)
      P2CTH=1.5*CSQTH-0.5
      DO 37 IAZIM=1,NAZIM
      AZIM=AMIN+IAZIM*DAZIM
C
C     OBTAIN SITE FREQUENCIES
      DO 32 J=1,NSITE
      ALPHA=EULER(1,J)
      BETA=EULER(2,J)
      GAM=EULER(3,J)
      PHI=AZIM+GAM
      CB=COS(BETA)
      CSQB=CB*CB
```

```
      SSQB=1.0-CSQB
      SB=SQRT(SSQB)
      P2CB=1.5*CSQB-0.5
      CBH=COS(BETA/2)
      CSQBH=CBH*CBH
      SSQBH=1.0-CSQBH
      C4BH=CSQBH*CSQBH
      S4BH=SSQBH*SSQBH
      OMG(J)=OMGISO(J)+(P2CTH*P2CB+0.75*SSQTH*SSQB*COS(2.0*PHI)-
     1 3.0*STH*CTH*SB*CB*COS(PHI))*OMG33(J)+
     2 (SSQTH*C4BH*COS(2.0*(PHI+ALPHA))+SSQTH*S4BH*COS(2.0*(PHI-ALPHA))+
     3 STH*CTH*SB*((CB+1.0)*COS(PHI+2.0*ALPHA)+
     4 (CB-1.0)*COS(PHI-2.0*ALPHA))+P2CTH*SSQB*COS(2.0*ALPHA))*ETAH(J)
32    CONTINUE
C
C     LOOP OVER OMEGA
      DO 36 IOMG=1,NOMG
      OMEGA=LOMG+(IOMG-1)*DOMG
C     GET GAMMA,ZETA
      GAMMA=0.0
      ZETA=0.0
      DO 35 I=1,NSITE
      GAMMA=GAMMA+CMPLX(1.0,0.0)/CMPLX(RPART,OMEGA-OMG(I))
      ZETA=ZETA+CMPLX(POPV(I),0.0)/CMPLX(RPART,OMEGA-OMG(I))
35    CONTINUE
C     GET INTENSITY
      INTEN(IOMG)=INTEN(IOMG)+REAL(CMPLX(TAUN,0.0)*ZETA/
     1 (CMPLX(TAUN,0.0)-GAMMA))
36    CONTINUE
37    CONTINUE
38    CONTINUE
C
C     NORMALIZE INTENSITIES
      LARGE=0.0
      DO 41 I=1,NOMG
      IF (INTEN(I) .GT. LARGE) LARGE=INTEN(I)
41    CONTINUE
      DO 42 I=1,NOMG
      INTEN(I)=INTEN(I)/LARGE
42    CONTINUE
C
      PAUSE
C     PLOT
      DO 53 I=1,NOMG
      PPM=LPPM+(I-1)*DPPM
      PPM=PPM+SIGN(0.5E-01,PPM)
      DO 51 J=1,IPMAX
      PLOT(J)=BLANK
51    CONTINUE
      IPLOT=IPMAX*INTEN(I)
      IF (IPLOT .LT. IPMAX) IPLOT=IPLOT+1
      PLOT(IPLOT)=STAR
      WRITE (10,52) PPM,INTEN(I),(PLOT(J),J=1,IPMAX)
52    FORMAT(1X,'FREQ=',F7.1,' INTEN=',F7.4,' I',100A1)
53    CONTINUE
C
C
C     OUTPUT DATA INTO FILE FOR PLOT
C
      WRITE (ISLOT,71) (INTEN(I),I=1,NOMG)
```

```
71      FORMAT(F7.4)
C
        GO TO 25
C
100     CALL FRSFL
        CALL FENUS(0)
        END
```

```
C       OBTAINS LINESHAPE FOR SOFT COLLISION EXCHANGE
C
        INTEGER BLANK,STAR,PLOT(100)
        REAL EULER(3,10),LPPM,LOMG,JFREQ,INTEN(200),OMG(10),LARGE
        REAL RREL(10,10),R(100)
        COMPLEX A(100),DET
        INTEGER LWORK(10),MWORK(10)
C
C       OPEN FILE FOR LATER PLOTTING
        CALL FGTFS (ISLOT,IERR)
        IF (IERR .EQ. 0) GO TO 2
        WRITE (10,1) IERR
1       FORMAT (1X,'ERROR CODE =', OI3)
        GO TO 100
2       CALL FOPFL ('CDC:DA',ISLOT,IERR)
        IF (IERR .EQ. 0) GO TO 7
        WRITE (10,1) IERR
        GO TO 100
C
C       INITIALIZE
7       BLANK=' '
        STAR='*'
        IPMAX=50
        PI=4.0*ATAN(1.0)
C
C       OBTAIN INVARIANT PARAMETERS
10      WRITE (10,11)
11      FORMAT(1X,'ENTER SPECTROMETER FREQ IN MHZ: ')
        READ (11) XNU0
        IF (XNU0 .LE. 0) GO TO 100
        OMG0=2.0*PI*XNU0
        WRITE (10,12)
12      FORMAT(1X,'ENTER SIG11, SIG22, SIG33 IN PPM: ')
        READ (11) SIG11,SIG22,SIG33
        SIGISO=(SIG11+SIG22+SIG33)/3.0
        OMGISO=SIGISO*OMG0
        OMG11=(SIG11-SIGISO)*OMG0
        OMG22=(SIG22-SIGISO)*OMG0
        OMG33=(SIG33-SIGISO)*OMG0
        ETAH=(OMG11-OMG22)/2.0
        WRITE (10,13)
13      FORMAT(1X,'ENTER NUMBER OF SITES: ')
        READ (11) NSITE
        NSSQ=NSITE*NSITE
        DO 16 J=1,NSITE
        WRITE (10,14) J
14      FORMAT(1X,'ENTER EULER ANGLES FOR NUCLEUS',I3,' IN DEGREES: ')
        READ (11) (EULER(I,J),I=1,3)
        DO 15 I=1,3
        EULER(I,J)=EULER(I,J)*PI/180.0
15      CONTINUE
16      CONTINUE
        WRITE (10,17)
17      FORMAT(1X,'ENTER LOW AND HIGH POLAR ANGLES IN DEGREES: ')
        READ (11) PMIN,PMAX
        PMIN=COS(PMIN*PI/180.0)
        PMAX=COS(PMAX*PI/180.0)
        WRITE (10,18)
18      FORMAT(1X,'ENTER NUMBER OF POLAR ANGLES: ')
        READ (11) NPOLAR
```

```
      DPOLAR=(PMAX-PMIN)/NPOLAR
      WRITE (10,19)
19    FORMAT(1X,'ENTER LOW AND HIGH AZIMUTHAL ANGLES IN DEGREES: ')
      READ (11) AMIN,AMAX
      AMIN=AMIN*PI/180.0
      AMAX=AMAX*PI/180.0
      WRITE (10,20)
20    FORMAT(1X,'ENTER NUMBER POF AZIMUTHAL ANGLES: ')
      READ (11) NAZIM
      DAZIM=(AMAX-AMIN)/NAZIM
      WRITE (10,21)
21    FORMAT(1X,'ENTER LOW AND HIGH PLOT LIMITS IN PPM: ')
      READ (11) LPPM,HPPM
      LOMG=LPPM*OMG0
      HOMG=HPPM*OMG0
      WRITE (10,22)
22    FORMAT(1X,'ENTER NUMBER OF FREQUENCY POINTS: ')
      READ (11) NOMG
      DPPM=(HPPM-LPPM)/(NOMG-1)
      DOMG=(HOMG-LOMG)/(NOMG-1)
      WRITE (10,23)
23    FORMAT(1X,'ENTER RELATIVE RELAXATON MATRIX: ')
      READ (11) ((RREL(I,J),J=1,NSITE),I=1,NSITE)
C
C     OBTAIN VARYING PARAMETERS
25    WRITE (10,26)
26    FORMAT(1X,'ENTER JUMP FREQUENCY IN HZ: ')
      READ (11) JFREQ
      IF (JFREQ .LE. 0.0) GO TO 10
      TAU=1.0/JFREQ
      WRITE (10,27)
27    FORMAT(1X,'ENTER T2 IN SEC: ')
      READ (11) T2
C
C     DO THE WORK
      DO 29 I=1,NSITE
      DO 28 J=1,NSITE
      INDX=(J-1)*NSITE+I
      R(INDX)=RREL(I,J)/TAU
      IF (I .EQ. J) R(INDX)=R(INDX)+1.0/T2
28    CONTINUE
29    CONTINUE
C
C     INITIALIZE INTENSITIES
      DO 31 I=1,NOMG
      INTEN(I)=0.0
31    CONTINUE
C
C     LOOP OVER ORIENTATIONS
      DO 38 IPOLAR=1,NPOLAR
      CTH=PMIN+IPOLAR*DPOLAR
      CSQTH=CTH*CTH
      SSQTH=1.0-CSQTH
      STH=SQRT(SSQTH)
      P2CTH=1.5*CSQTH-0.5
      DO 37 IAZIM=1,NAZIM
      AZIM=AMIN+IAZIM*DAZIM
C
C     OBTAIN SITE FREQUENCIES
      DO 32 J=1,NSITE
```

```
      ALPHA=EULER(1,J)
      BETA=EULER(2,J)
      GAM=EULER(3,J)
      PHI=AZIM+GAM
      CB=COS(BETA)
      CSQB=CB*CB
      SSQB=1.0-CSQB
      SB=SQRT(SSQB)
      P2CB=1.5*CSQB-0.5
      CBH=COS(BETA/2)
      CSQBH=CBH*CBH
      SSQBH=1.0-CSQBH
      C4BH=CSQBH*CSQBH
      S4BH=SSQBH*SSQBH
      OMG(J)=OMGISO+(P2CTH*P2CB+0.75*SSQTH*SSQB*COS(2.0*PHI)-
     1 3.0*STH*CTH*SB*CB*COS(PHI))*OMG33+
     2 (SSQTH*C4BH*COS(2.0*(PHI+ALPHA))+SSQTH*S4BH*COS(2.0*(PHI-ALPHA))+
     3 STH*CTH*SB*((CB+1.0)*COS(PHI+2.0*ALPHA)+
     4 (CB-1.0)*COS(PHI-2.0*ALPHA))+P2CTH*SSQB*COS(2.0*ALPHA))*ETAH
32    CONTINUE
C
C     LOOP OVER OMEGA
      DO 36 IOMG=1,NOMG
      OMEGA=LOMG+(IOMG-1)*DOMG
C     GET A MATRIX
      DO 34 I=1,NSITE
      DO 33 J=1,NSITE
      INDX=(J-1)*NSITE+I
      AR=R(INDX)
      AI=0.0
      IF (I .EQ. J) AI=OMEGA-OMG(I)
      A(INDX)=CMPLX(AR,AI)
33    CONTINUE
34    CONTINUE
C     GET INTENSITY
      CALL CMINV(A,NSITE,DET,LWORK,MWORK)
      SUM=0.0
      DO 35 I=1,NSSQ
      SUM=SUM+REAL(A(I))
35    CONTINUE
      INTEN(IOMG)=INTEN(IOMG)+SUM
36    CONTINUE
37    CONTINUE
38    CONTINUE
C
C     NORMALIZE INTENSITIES
      LARGE=0.0
      DO 41 I=1,NOMG
      IF (INTEN(I) .GT. LARGE) LARGE=INTEN(I)
41    CONTINUE
      DO 42 I=1,NOMG
      INTEN(I)=INTEN(I)/LARGE
42    CONTINUE
C
      PAUSE
C     PLOT
      DO 53 I=1,NOMG
      PPM=LPPM+(I-1)*DPPM
      PPM=PPM+SIGN(0.5E-01,PPM)
      DO 51 J=1,IPMAX
```

```
      PLOT(J)=BLANK
51    CONTINUE
      IPLOT=IPMAX*INTEN(I)
      IF (IPLOT .LT. IPMAX) IPLOT=IPLOT+1
      PLOT(IPLOT)=STAR
      WRITE (10,52) PPM,INTEN(I),(PLOT(J),J=1,IPMAX)
52    FORMAT(1X,'FREQ=',F7.1,' INTEN=',F7.4,' I',100A1)
53    CONTINUE
C
C
C     OUTPUT DATA INTO FILE FOR PLOT
C
      WRITE (ISLOT,71) (INTEN(I),I=1,NOMG)
71    FORMAT(F7.4)
C
      GO TO 25
C
100   CALL FRSFL
      CALL FENUS(0)
      END
```

```
      SUBROUTINE CMINV(A,N,D,L,M)
C
C     INVERTS A MATRIX
C
      DIMENSION A(1),L(1),M(1)
      COMPLEX A,D,BIGA,HOLD
C
      D=1.0
      NK=-N
      DO 80 K=1,N
      NK=NK+N
      L(K)=K
      M(K)=K
      KK=NK+K
      BIGA=A(KK)
      DO 20 J=K,N
      IZ=N*(J-1)
      DO 20 I=K,N
      IJ=IZ+I
      IF(CABS(BIGA)-CABS(A(IJ))) 15,20,20
15    BIGA=A(IJ)
      L(K)=I
      M(K)=J
20    CONTINUE
C
      J=L(K)
      IF(J-K) 35,35,25
25    KI=K-N
      DO 30 I=1,N
      KI=KI+N
      HOLD=-A(KI)
      JI=KI-K+J
      A(KI)=A(JI)
30    A(JI)=HOLD
C
35    I=M(K)
      IF(I-K) 45,45,38
38    JP=N*(I-1)
      DO 40 J=1,N
      JK=NK+J
      JI=JP+J
      HOLD=-A(JK)
      A(JK)=A(JI)
40    A(JI)=HOLD
C
45    IF (CABS(BIGA) .NE. 0.0) GO TO 48
      D=0.0
      RETURN
48    DO 55 I=1,N
      IF(I-K) 50,55,50
50    IK=NK+I
      A(IK)=A(IK)/(-BIGA)
55    CONTINUE
C
      DO 65 I=1,N
      IK=NK+I
      HOLD=A(IK)
      IJ=I-N
      DO 65 J=1,N
      IJ=IJ+N
```

```
      IF(I-K) 60,65,60
60    IF(J-K) 62,65,62
62    KJ=IJ-I+K
      A(IJ)=HOLD*A(KJ) + A(IJ)
65    CONTINUE
C
      KJ=K-N
      DO 75 J=1,N
      KJ=KJ+N
      IF(J-K) 70,75,70
70    A(KJ)=A(KJ)/BIGA
75    CONTINUE
C
      D=D*BIGA
C
      A(KK)=1.0/BIGA
80    CONTINUE
C
      K=N
100   K=K-1
      IF(K) 150,150,105
105   I=L(K)
      IF(I-K) 120,120,108
108   JQ=N*(K-1)
      JR=N*(I-1)
      DO 110 J=1,N
      JK=JQ+J
      HOLD=A(JK)
      JI=JR+J
      A(JK)=-A(JI)
110   A(JI)=HOLD
120   J=M(K)
      IF(J-K) 100,100,125
125   KI=K-N
      DO 130 I=1,N
      KI=KI+N
      HOLD=A(KI)
      JI=KI-K+J
      A(KI)=-A(JI)
130   A(JI)=HOLD
      GO TO 100
150   RETURN
      END
```

```
C       PROGRAM TO CALCULATE POWDER PATTERNS FOR
C       GENERAL TENSORS IN RIGID SOLIDS
        PARAMETER NPT=4096
C
        INTEGER ANS,SMALL,ISIG1(25),ISIG2(25),ISIG3(25),AMP(2048),RES,SM(25) E
        REAL RINT(25),TINT(1024),FINT(1024)
        DIMENSION SIG1(25),SIG2(25),SIG3(25)
C
        NBLK=2*NPT/256
C
C       OPEN OUTPUT FILE
        CALL OPEN(1,'DP0F:RESERVED:SCRATCH',3,IERR)
        IF (IERR.EQ.1) GO TO 10
        WRITE (10,101) IERR
101     FORMAT(1X,'ERROR CODE =',I3)
        GO TO 100
C
C       GET PARAMETERS
10      WRITE (10,11)
11      FORMAT (1X,'ENTER NUMBER OF DIFFERENT TENSORS: ',Z)
        READ (11) NPP
        WRITE (10,12)
12      FORMAT (1X,'ARE TENSORS IN PPM OR PTS: ',Z)
        READ (11,13) ANS
13      FORMAT (A2)
        IF (ANS .EQ. 'PT') GO TO 19
        WRITE (10,14)
14      FORMAT (1X,'ENTER NUMBER OF PPM/PT ON SCALE: ',Z)
        READ (11) CONV
        WRITE (10,15)
15      FORMAT (1X,'ENTER POINT POSITION OF REFERENCE COMPOUND: ',Z)
        READ (11) REFPT
        DO 18 I=1,NPP
151     WRITE (10,16) I
16      FORMAT (1X,'ENTER INTENSITY AND DIAGONAL ELEMENTS OF TENSOR ', I3,'
        READ (11) RINT(I),SIG1(I),SIG2(I),SIG3(I)
        IF ((SIG1(I) .LE. SIG2(I)) .AND. (SIG2(I) .LE. SIG3(I))) GO TO 1
        WRITE (10,161)
161     FORMAT (1X,'CHECK SIZE AND ORDER OF TENSOR ELEMENTS. ')
        GO TO 151
17      ISIG1(I)=SIG1(I)/CONV+REFPT
        ISIG2(I)=SIG2(I)/CONV+REFPT
        ISIG3(I)=SIG3(I)/CONV+REFPT
18      CONTINUE
        GO TO 27
19      DO 20 I=1,NPP
        WRITE (10,16) I
        READ (11) RINT(I),ISIG1(I),ISIG2(I),ISIG3(I)
20      CONTINUE
27      WRITE (10,21)
21      FORMAT (1X,'DO YOU WANT INDEPENDENT SMOOTHING?',Z)
        READ (11,13) RES
        IF (RES .EQ. 'NO') GO TO 24
        DO 23 I=1,NPP
        WRITE (10,22) I
22      FORMAT (1X,'ENTER SMOOTHING FACTOR FOR TENSOR ',I3,':',Z)
        READ (11) SM (I)
23      CONTINUE
C
C       DETERMINE WIDTH, SHIFT LEFT
24      LARGE=ISIG3(1)
        SMALL=ISIG1(1)
        DO 25 I=1,NPP
```

```
      IF (ISIG1(I) .LT. SMALL) SMALL=ISIG1(I)
25    CONTINUE
      DO 26 I=1,NPP
      ISIG1(I)=ISIG1(I)-SMALL+21
      ISIG2(I)=ISIG2(I)-SMALL+21
      ISIG3(I)=ISIG3(I)-SMALL+21
26    CONTINUE
C     INITIALIZE INTENSITY
      DO 28 I=1,1024
      FINT(I)=0.0
28    CONTINUE
C
C     ASSIGN CONSTANTS FOR CALCULATION OF COMPLETE ELLIPTICAL
C     INTEGRALS OF THE FIRST KIND
      A0=1.3862944
      A1=0.1119723
      A2=0.0725296
      B0=0.50
      B1=0.1212478
      B2=0.0288729
C
C     CALCULATE POWDER PATTERNS
      DO 80 I=1,NPP
      DO 29 J=1,1024
      TINT(J)=0.0
29    CONTINUE
      IF (ISIG1(I) .NE. ISIG2(I) .AND. ISIG2(I) .NE. ISIG3(I)) GO TO 50
C
C     DO AXIAL PATTERN
      IF (ISIG2(I) .EQ. ISIG3(I)) GO TO 40
      SUM=0.0
      IS=ISIG1(I)
      IB=ISIG3(I)
      DO 30 J=IS,IB
      TINT(J)=1.0/SQRT(J+1.0-IS)
      SUM=SUM+TINT(J)
30    CONTINUE
      IF (RES .EQ. 'NO') GO TO 35
      SMO=SM(I)
      IF (SMO .EQ. 0) GO TO 35
      TEMP1=0.0
      TEMP2=0.0
      DO 34 LP=1,SMO
      DO 33 K=2,1023
      TEMP1=TINT(K)
      TINT(K)=(TEMP2+2*TINT(K)+TINT(K+1)+1.0E-30)/4
      TEMP2=TEMP1
33    CONTINUE
34    CONTINUE
35    DO 36 J=1,1024
      TINT(J)=RINT(I)*TINT(J)/SUM
      FINT(J)=FINT(J)+TINT(J)
36    CONTINUE
      GO TO 80
40    SUM=0.0
      IS=ISIG1(I)
      IB=ISIG3(I)
      DO 41 J=IS,IB
      TINT(J)=1.0/SQRT(IB+1.0-J)
      SUM=SUM+TINT(J)
41    CONTINUE
      IF (RES .EQ. 'NO') GO TO 45
      SMO=SM(I)
      IF (SMO .EQ. 0) GO TO 45
```

```
      DO 44 LP=1,SMO
      DO 43 K=2,1023
      TEMP1=TINT(K)
      TINT(K)=(TEMP2+2*TINT(K)+TINT(K+1)+1.0E-30)/4
      TEMP2=TEMP1
43    CONTINUE
44    CONTINUE
45    DO 46 J=1,1024
      TINT(J)=RINT(I)*TINT(J)/SUM
      FINT(J)=FINT(J)+TINT(J)
46    CONTINUE
      GO TO 80
C
C     DO NONAXIAL PATTERN
50    SUM=0.0
      IS=ISIG1(I)
      IB=ISIG2(I)
      IT=ISIG3(I)
      DIF1=IT-IS
      DIF2=IT-IB
      DIF3=IB-IS
      IBM1=IB-1
      DO 55 K=IS,IBM1
      PM=SQRT(DIF1*DIF2/((IT-K)*DIF3))
      PAR=(K-IS)*DIF2/((IT-K)*DIF3)
      V=1.0-PAR
      EINT=A0+A1*V+A2*V**2+(B0+B1*V+B2*V**2)*ALOG(1.0/V)
      TINT(K)=PM*EINT
      SUM=SUM+TINT(K)
55    CONTINUE
      IBP1=IB+1
      DO 60 K=IBP1,IT
      PM=SQRT(DIF1/(K-IS))
      PAR=DIF3*(IT-K)/(DIF2*(K-IS))
      V=1.0-PAR
      EINT=A0+A1*V+A2*V**2+(B0+B1*V+B2*V**2)*ALOG(1.0/V)
      TINT(K)=PM*EINT
      SUM=SUM+TINT(K)
60    CONTINUE
      ISGN=1
      IF (TINT(IB-1) .LT. TINT(IB+1)) ISGN=-1.0
      TINT(IB)=6*TINT(IB-ISGN)-5*TINT(IB-ISGN*2)
      SUM=SUM+TINT(IB)
      IF (RES .EQ. 'NO') GO TO 63
      SMO=SM(I)
      IF (SMO  EQ. 0) GO TO 63
      TEMP1=0.0
      TEMP2=0.0
      DO 62 LP=1,SMO
      DO 61 K=2,1023
      TEMP1=TINT(K)
      TINT(K)=(TEMP2+2*TINT(K)+TINT(K+1)+1.0E-30)/4
      TEMP2=TEMP1
61    CONTINUE
62    CONTINUE
63    DO 64 J=1,1024
      TINT(J)=RINT(I)*TINT(J)/SUM
      FINT(J)=FINT(J)+TINT(J)
64    CONTINUE
80    CONTINUE
      BIG=0.0
      DO 81 I=1,1024
      IF (FINT(I) .GT. BIG) BIG=FINT(I)
81    CONTINUE
```

```
32      CONTINUE
C
C       PUT DATA INTO OUTPUT FORMAT
        DO 90 M=1,1024
        AMP(2*M-1)=FINT(M)*32767.0/BIG
90      CONTINUE
C       OUTPUT DATA
        CALL WRBLK (1,0,AMP,NBLK,IERR)
        IF (IERR1 .NE.0) GO TO 100
        SMALL=SMALL-21
        WRITE (10,91) SMALL
91      FORMAT (1X,'SHIFT -',I4,'  POINTS FOR CORRECT POSITION')
C
100     CALL RESET
        END
R
```

COMMUTATORS

A	I_{x1}	I_{x2}	I_{x3}	I_{y1}	I_{y2}	I_{y3}	I_{z1}	I_{z2}	I_{z3}
I_{x1}	0	I_{x3}	$-I_{x2}$	$\frac{1}{2} I_{z1}$	$-\frac{1}{2} I_{z2}$	$\frac{1}{2} I_{x2}$	$-\frac{1}{2} I_{y1}$	$\frac{1}{2} I_{y2}$	$\frac{1}{2} I_{x2}$
I_{x2}		0	I_{x1}	$-\frac{1}{2} I_{z2}$	$-\frac{1}{2} I_{z1}$	$-\frac{1}{2} I_{x1}$	$\frac{1}{2} I_{y2}$	$\frac{1}{2} I_{y1}$	$-\frac{1}{2} I_{x1}$
I_{x3}			0	$-\frac{1}{2} I_{y2}$	$\frac{1}{2} I_{y1}$	0	$-\frac{1}{2} I_{z2}$	$\frac{1}{2} I_{z1}$	0
I_{y1}				0	I_{y3}	$- I_{y2}$	$\frac{1}{2} I_{x1}$	$-\frac{1}{2} I_{x2}$	$\frac{1}{2} I_{y2}$
I_{y2}					0	I_{y1}	$-\frac{1}{2} I_{x2}$	$-\frac{1}{2} I_{x1}$	$-\frac{1}{2} I_{y1}$
I_{y3}						0	$-\frac{1}{2} I_{z2}$	$\frac{1}{2} I_{z1}$	0
S_{z1}							0	I_{z3}	$- I_{z2}$
S_{z2}								0	I_{z1}
S_{z3}									0

$[B,A] = -[A,B]$

Appendix F

ANTICOMMUTATORS

A

	S_{x1}	S_{x2}	S_{x3}	S_{y1}	S_{y2}	S_{y3}	S_{z1}	S_{z1}	S_{z3}
S_{x1}	$\frac{1}{3}(1+S_{y3}-S_{z3})$	0	0	$\frac{1}{2}S_{z2}$	$\frac{1}{2}S_{z1}$	$\frac{1}{2}S_{x1}$	$\frac{1}{2}S_{y2}$	$\frac{1}{2}S_{y1}$	$-\frac{1}{2}S_{x1}$
S_{x2}	0	$\frac{1}{3}(1+S_{y3}-S_{z3})$	0	$\frac{1}{2}S_{z1}$	$-\frac{1}{2}S_{z2}$	$\frac{1}{2}S_{x2}$	$\frac{1}{2}S_{y1}$	$-\frac{1}{2}S_{y2}$	$-\frac{1}{2}S_{x2}$
S_{x3}	0	0	$\frac{1}{3}(1+S_{y3}-S_{z3})$	$-\frac{1}{2}S_{y1}$	$-\frac{1}{2}S_{y2}$	$\frac{1}{3}(-\frac{1}{2}+S_{x3}-S_{y3})$	$\frac{1}{2}S_{z1}$	$\frac{1}{2}S_{z2}$	$\frac{1}{3}(-\frac{1}{2}S_{z3}-S_{x3})$
S_{y1}				$\frac{1}{3}(1+S_{z3}-S_{x3})$	0	0	$\frac{1}{2}S_{x2}$	$\frac{1}{2}S_{x1}$	$\frac{1}{2}S_{y1}$
S_{y2}					$\frac{1}{3}(1+S_{z3}-S_{x3}$	0	$\frac{1}{2}S_{x1}$	$-\frac{1}{2}S_{x2}$	$\frac{1}{2}S_{y2}$
S_{y3}						$\frac{1}{3}(1+S_{z3}-S_{x3}$	$-\frac{1}{2}S_{z1}$	$-\frac{1}{2}S_{z2}$	$\frac{1}{3}(-\frac{1}{2}+S_{y3}-S_{z3})$
S_{z1}							$\frac{1}{3}(1+S_{x3}-S_{y3})$	0	0
S_{z2}							0	$\frac{1}{3}(1+S_{x3}-S_{y3}$	0
S_{z3}							0	0	$\frac{1}{3}(1+S_{x3}-S_{y3}$

$[A,B]_A = [B,A]_A$

1 = unit matrix.

Appendix G Trigonometric Functions of Operators

In the course of human events it sometimes becomes necessary to evaluate trigonometric functions of operators. To do this we make use of the power series expansion of the function

$$\cos x = 1 - \frac{x^2}{2!} + \frac{x^4}{4!} - \frac{x^6}{6!} + \ldots$$

$$\sin x = x - \frac{x^3}{3!} + \frac{x^5}{5!} - \frac{x^7}{7!} + \ldots$$

For the fictitious spin $\frac{1}{2}$ operators we must then evaluate the various powers of operators. It is particularly easy to see from the matrix representation of these operators, Table II, that

$$(2\ I_{p,n})^{2m+1} = 2\ I_{p,n} \qquad (2\ I_{p,n})^{2m} = (2\ I_{p,n})^2$$

for $p = x,y,z, n = 1,2,3$ and all $m \geq 1$. These identities make it possible to factor the operator out of the series to give

$$\cos(\omega I_{p,n} t) = \cos(\frac{\omega}{2}\ 2I_{p,n} t) = 1 - (2I_{p,n})^2 + (2I_{p,n})^2 \cos(\frac{\omega}{2}t)$$

and

$$\sin(\omega I_{p,n} t) = \sin(\frac{\omega}{2}\ 2I_{p,n} t) = 2I_{p,n} \sin(\frac{\omega}{2}t)$$

Of course this also allows us to express an exponential operator in terms of nonexponential ones

$$e^{i\omega I_{p,n} t} = \cos(\omega I_{p,n} t) + i \sin(\omega I_{p,n} t)$$

$$= 1 - (2I_{p,n})^2 + (2I_{p,n})^2 \cos(\frac{\omega}{2}t) + i\ 2I_{p,n} \sin(\frac{\omega}{2}t)$$

It is sometimes convenient to use the identity

$$(2I_{p,n})^2 = \frac{2}{3}(1 + I_{q,3} - I_{r,3})$$

where p,q,r = x,y,z or cyclic permutation for n = 1,2,3.

Appendix H

Synthesis of various deuterated hexamethyl benzenes was performed by Herbert Zimmermann. They were prepared by reaction of pentamethylbenzene (Aldrich) with paraformaldehyde and sodium bromide in acetic acid.

For d-1 HMB 37g of PMB, 19.5g paraformaldehyde and 72g NaBr were dissolved in 140 ml glacial acetic acid at 80°C, and 65.5 ml conc. H_2SO_4 and 65 ml glacial acetic acid were dripped in over 4 hours, with good stirring. The mixture was heated at 90°C for 7 hours, then was put into 2 liters of ice water. After standing overnight it was filtered and well dried under vacuum. The pentamethyl benzylbromide was purified by vacuum distillation. 15 grams of pentamethyl benzylbromide was then dissolved in dry diethylether and was added over 30 minutes to a suspension of 5.2g $LiAlD_4$ (Stohler) in dry diethylether. This mixture was stirred 5 hours. Water then 15% H_2SO_4 was carefully added the ether phase removed and the water phase extracted with other and the combination dried over K_2CO_3/ Na_2SO_4 overnight. Then evaporated to dryness. Crude product of 10.8g was recrystalized from ethanol.

For d_2 HMB 98% deuterated paraformaldehyde and $LiAlH_4$ were used with same procedure.

For d_3 HMB 98% deuterated paraformaldehyde and $LiAlD_4$ were used in the same procedure.

REFERENCES

1. A. Abragam, The Principles of Nuclear Magnetism (Oxford University Press, London, 1961).
2. M. Mehring, Vol. 11, NMR Basic Principles and Progress (Springer Verlag, Heidelberg, 1976).
3. U. Haeberlen, Advances in Magnetic Resonance, supplement (Academic Press, New York, 1976).
4. M. Rose, Elementary Theory of Angular Momentum (John Wiley & Sons, New York, 1957).
5. H.S. Gutowsky and G.E. Pake, J. Chem. Phys. 18, 162 (1950).
6. E.R. Andrew, J. Chem. Phys., 18, 607 (1950).
7. E.R. Andrew, J. Chem. Phys. Solids, 18, 9 (1961).
8. J.G. Powles, J. Chem. Phys. Solids, 18, 17 (1961).
9. E.R. Andrew and P.S. Allen, J. Chim. Phys., 63, 85 (1966).
10. U. Haeberlen and J.S. Waugh, Phys. Rev., 175, 453 (1968).
11. L.R. Sarles and R.M. Cotts, Phys. Rev., 111, 853 (1958).
12. M. Mehring, A. Pines, W.-K. Rhim and J.S. Waugh, J. Chem. Phys., 54, 3239 (1971).
13. A Pines, M.G. Gibby and J.S. Waugh, J. Chem. Phys. 59, 569 (1973).
14. R.C. Hewitt, S. Meiboom and J.C. Snyder, J. Chem. Phys., 58, 5089 (1973) and L.C. Snyder and S. Meiboom, J. Chem. Phys., 58, 5096 (1973).
15. A. Pines, S. Vega and M. Mehring, Phys. Rev., 18, 112 (1978).
16. A Pines, D.J. Ruben, S. Vega and M. Mehring, Phys. Rev. Lett., 36, 110 (1976).

17. U. Haeberlen and J.S. Waugh, Phys. Rev., 175, 453 (1968).

18. S. Vega, T.W. Shattuck and A. Pines, Phys. Rev. Lett., 37, 43 (1976).

19. S. Vega and A. Pines, J. Chem. Phys., 66, 5624 (1977).

20. T.C. Farrar and E.D. Becker, Pulse and Fourier Transform NMR (Academic Press, New York, 1971).

21. S.R. Hartmann and E.L. Hahn, Phys. Rev., 128, 2042 (1962).

22. A general description of rotating frame thermodynamics in A.G. Redfield, Phys. Rev., 98, 1787 (1955).

23. D.A. McArthur, E.L. Hahn and R.E. Walstedt, Phys. Rev., 188, 609 (1969).

24. L. Müller, A. Kumar, T. Baumann and R.R. Ernst, Phys. Rev. Lett., 32, 1402 (1974).

25. R.K. Hester, V.R. Cross, J.L. Ackerman and J.S. Waugh, J. Chem. Phys. 63, 3606 (1975).

26. N. Bloembergen and T.J. Rowland, Acta. Metallurgica 1, 731 (1955).

27. D.L. Van der Hart, in Preprints of the 1976 Coal Chemistry Workshop, Stanford Research Institute, 1976.

28. Abramowitz and Steegun, Handbook of Mathematical Functions (Dover, New York, 1965).

29. A. Pines, M.G. Gibby and J.S. Waugh, Chem. Phys. Lett., 15, 373 (1972).

30. A. Höhener, Chem. Phys. Lett, 53, 97 (1978).

31. S. Kohler, Ph.D. Thesis, University of California, 1976.

32. S. Alexander, A. Baram and Z. Luz, Molec. Phys. 27, 441 (1974).

32a. H. Sillescu, J. Chem. Phys. 54, 2110 (1971).

33. A. Baram, Z. Luz and S. Alexander, J. Chem. Phys., 64, 4321 (1976).

34. H.W. Spiess, Chem. Phys., 6, 217 (1974).

35. H.W. Spiess, R. Grosescu and U. Haeberlen, Chem. Phys., 6, 226 (1974).

36. E.R. Andrew, J. Chem. Phys., 18, 607 (1950).

37. K. Lonsdale, Proc. Roy. Soc., A123, 494 (1929).

38. L.O. Brockway and J.M. Robertson, J. Chem. Soc., 1324 (1939).

39. P.S. Allen and A. Cowking, J. Chem. Phys., 47, 4286 (1967).

40. H.W. Bernard, J.E. Tanner and J.G. Aston, J. Chem. Phys. 50, 5016 (1969).

41. S. Pausak, A. Pines and J.S. Waugh, J. Chem. Phys., 59, 591 (1973).

42. S. Pausak, J. Tegenfeldt and J.S. Waugh, J. Chem. Phys., 61, 1338 (1974).

43. J.D. Donitz, L.E. Orgal and A. Rich, Acta Cryst. 9, 373 (1956).

44. C.H. Holm and J.A. Ibers, J. Chem. Phys. 30, 885 (1959).

45. L.N. Mulay and A. Attalla, J. Amer. Chem. Soc. 85, 702 (1963).

46. M.K. Makova, E.V. Leonova, Yu. S. Karimov and N.S. Kochetkova, J. Organomet. Chem., 55, 185 (1973).

47. H. Spiesecke and W.G. Schneider, Tetrahedron Lett., 14, 468 (1961).

48. D. Wemmer and A. Pines, Lawrence Berkeley Laboratory, Materials and Molecular Research Division Annual Report, 1976, LBL-6016.

49. P.C. Lauterbur and R.B. King, J. Amer. Chem. Soc., 87, 3266 (1965).

50. D.E. Barnaal and I.J. Lowe, J. Chem. Phys., 46, 4800 (1967).

51. D.E. Barnaal and I.J. Lowe, J. Chem. Phys., 48, 4614 (1968).

52. J.A. Jackson and S.W. Rabideau, J. Chem. Phys., 41, 4008 (1964).

53. P. Waldstein, S.W. Rabideau and J.A. Jackson, J. Chem. Phys. 41, 3407 (1964).

54. P. Waldstein and S.W. Rabideau, J. Chem. Phys, 47, 5338 (1968).

55. L.M. Ryan, R.C. Wilson and B.C. Gerstein, to be published.

56. W.F. Giauque and J.W. Stout, J. Amer. Chem. Soc., 58, 1144 (1936).

57. L. Onsage and L.K. Runnels, J. Chem. Phys., 50, 1089 (1969).

58. A. von Hippel, J. Chem. Phys. 54, 145 (1971).

59. H. Wennerström, N.O. Persson and B. Lindman, J. Mag. Res., 13, 348 (1974).

60. S. Yatsiv, Phys. Rev., 113, 1522 (1959).

61. H. Hatanaka, T. Terao and T. Hashi, J. Phys. Soc. Japan, 39, 835 (1975), T. Hatanaka and T. Hashi, J. Phys. Soc. Japan, 39, 1139 (1975).

62. S. Vega, J. Chem. Phys., 63, 3769 (1975).

63. R.P. Feynman, F.L. Vernon and R.W. Hellwarth, J. Appl. Phys., 28, 49 (1957).

64. T.W. Shattuck, Ph.D. Thesis, University of California, Berkeley, 1976.

65. W.P. Aue, E. Bartholdi and R.R. Ernst, J. Chem. Phys., 64, 2229, (1976).

66. G.E. Pake, J. Chem. Phys., 16, 327 (1948).

67. R.K. Hester, V.R. Cross, J.L. Ackerman and J.S. Waugh, J. Chem. Phys., 63, 3606 (1975).

68. M.E. Stoll, A.J. Vega and R.W. Vaughn, J. Chem. Phys., 65, 4093 (1976).

69. S. Kaplan, Ph.D. Thesis, Massachusetts Institute of Technology 1976.

70. R.K. Hester, J.L. Ackerman, B.L. Neff and J.S. Waugh, Phys. Rev. Lett., 36, 1081 (1976).

71. R.E. Stark, R.A. Haberkorn and R.G. Griffin, J. Chem. Phys., 68, 1996 (1978).

72. M.E. Stoll, R.W. Vaughn, R.B. Sailant and T. Cole, J. Chem. Phys., 61, 2896 (1974).

73. R.G. Griffin, A. Pines and J.S. Waugh, J. Chem. Phys. 63, 3676 (1975).

74. H. van Willigen, R.G. Griffin and R.A. Haberkorn, J. Chem. Phys., 67, 5855 (1977).

75. D.L. Van der Hart, J. Mag. Res., 24, 467 (1976).

76. S. Hsi, H. Zimmerman and Z. Luz and references therein, J. Chem. Phys., in press.

77. R. Poupko, R.L. Vold and R.R. Vold, to be published.

78. E.L. Hahn, Phys. Rev. 80, 580 (1950).

79. A. Carrington and A.D. McLachlan, Introduction to Magnetic Resonance (Harper and Row, N.Y., 1967).

80. C.P. Slichter, Principles of Magnetic Resonance (Harper and Row, N.Y., 1963).

81. R.G. Barnes and J.W. Bloom, J. Chem. Phys. 57, 3082 (1972).

82. B.C. Gerstein, private communication.

83. H.P. Fritz and L. Shaefer, Chem. Ber., 97, 1829 (1964).

84. T. Chiba, J. Chem. Phys., 39, 947 (1963).

85. S. Ketudat and U. Pound, J. Chem. Phys., 26, 708 (1957).

86. T. Chiba, J. Chem. Phys. 41, 1352 (1964).

87. R.G. Barnes and J.W. Bloom, Molec. Phys., 25, 493 (1973).

88. R.G. Barnes, W.C. Harper and D.R. Torgeson, J. Chem. Phys., 62, (1975).

89. N. Boder, Y.K. Levine and R.T. Squires, Chem. Phys. Lett., 28, 523 (1974).

90. S. Vega, J. Chem. Phys., in press.

91. H.M. Hoffman, G.S. Parks, and M. Barmore, J. Am. Chem. Soc., 53, 3880 (1931); J.D. Ferry and S.B. Thomas, J. Phys. Chem., 37, 253 (1933).

92. P.S. Allen and A. Cowking, J. Chem. Phys., 49, 789 (1968).

93. R.F. Bryan, J. Chem. Soc. (B) 1967, 1311.

94. A. Wokaun and R.R. Ernst, to be published.

95. R. Freeman and H.D.W. Hill in Dynamic NMR Spectroscopy (eds. L.M. Jackman and F.A. Cotton, Academic Press, N.Y., 1975).

96. R.L. Vold and R.R. Vold, Progress in NMR Spectroscopy, 17, 000 (1978).

97. A. Wokaun and R.R. Ernst, to be published.

98. J.W. Emsley and J.C. Lindon, NMR Spectroscopy Using Liquid Crystal Solvents (Pergamon Press, 1975).

99. A. Saupe, Z. Naturforsch., 20a, 572 (1965).

100. A.P. Maudsley, A. Wokaun and R.R. Ernst, Chem. Phys. Lett., 55, 9 (1978).

101. Radio Amatures Handbook, (American Radio Relay League, Newington, Conn. 1976).

FIGURE CAPTIONS

Figure 1. The sequential rotations, through Euler angles α, β, γ, used for transformations of tensors from one axis system to another. The frame x, y, z is the initial axis system and x''', y''', z''' is the final. The single and double prime systems are intermediate.

Figure 2. The behavior of various magnetizations during a cross polarization experiment. Curve a is the decay of proton magnetization due to spin lattice relaxation in the rotating frame, $T_{1\rho}$ = 10 units. Curve b is the growth of carbon magnetization with time constant T_{IS} = 15 units which would be observed if proton relaxation were not present. Curve c is the actual growth of carbon magnetization including effects of proton relaxation.

Figure 3. Schematic pulse sequences for (a) free induction decay and (b) cross polarization experiments with proton decoupling.

Figure 4. Powder patterns for anisotropic chemical shielding, (a) in the case of axial symmetry and (b) for the general case.

Figure 5. ^{13}C spectrum of adamantane in the plastic phase, showing lines averaged by isotropic reorientation. This spectrum is the result of a single shot, single contact (4 msec) cross polarization experiment.

Figure 6. Chemical shielding powder patterns for nonrotating and rotating molecules. The case shown is for flourine in a model fluoromethyl group with the σ_{33} element along the C-F bond and σ_{11} in the CCF plane for the rigid molecule. Rapid rotation of the methyl yields the axially symmetric pattern.

Figure 7. ^{13}C powder spectra for hexamethylbenzene in the high and low temperature limits. The wide peaks are from the ring carbons and the sharp peaks, which have been truncated, are from the methyl carbons.

Figure 8. Possible jumps for a molecule of HMB in a sixfold symmetric site. In a general orientations there are three different chemical shifts for these sites, represented by lines A, B and C. The rate of jumps from orientation i to j are given by the rate constant W_{ij}.

Figure 9. (a) and (c) are orientations of the HMB molecule with respect to the magnetic field which give rise to degeneracies of line positions. In (a) 1 and 3 are degenerate and in (c) 1 and 2 are degenerate. (b) is an orientation for which the positions of 1, 2 and 3 are nondegenerate.

Figure 10. Spectra for exchanging HMB molecules in orientation (b) of Figure 9 and near orientation (c) of Figure 9. The exchange causes rapid coalescence of the two lines close together in the right hand spectra.

Figure 11. The low field part of theoretical powder lineshapes for exchanging HMB, the left side spectra for the rotational random jump model and the right side for sixfold jumps. Numbers above spectra are total jump rates in Hz.

Figure 12. The low field part of experimental and theoretical spectra of HMB. On the left are experimental ^{13}C spectra for a number of temperatures noted above the spectra. The right side shows again the theoretical spectra for sixfold jump model. The extra features present

in the jump model are clearly present in the experimental spectra.

Figure 13. Experimental ^{13}C spectrum of HMB at -135.8°C. The extra features at -80 PPM and -40 PPM are particularly prominant in this spectrum. The truncated peak at the high field side is from the methyl carbons.

Figure 14. A plot of the log of estimated jump rate against 1/T for HMB. From this we determine an activation energy of 5.5 kcal/mole for ring jumps.

Figure 15. Theoretical and experimental spectra for ^{13}C in DMFe in the rigid and rapid motion limits. The high field lines in the experimental spectra are from the methyl carbons. Unlike HMB, the σ_{33} element of DMFe moves downfield when motion occurs.

Figure 16. Schematic representation of the shielding tensor orientation in DMFe. The angle between σ_{33} and the Z axis (rotation axis) is about 20°. Methyl carbons are not shown and the relative orientation of the rings cannot be determined, staggered conformation is assumed for illustration only.

Figure 17. The possible jumps for the rings of DMFe in a fivefold potential. For general orientations all five sites have different chemical shifts, schematically represented in the lower portion.

Figure 18. Theoretical spectra for DMFe in the two limits $W_{12}/W_{13} = \infty$ and $W_{12}/W_{13} = 0$. Spectra are shown for the single orientation $\alpha = 0°$ $\beta = 0°$ $\gamma = 2°$ at a number of total jump rates for each limit, and for a powder average at 600 Hz total jump rate (at top). Note that

jumps of $2\pi/5$ ($W_{12}/W_{13} = \infty$) exchange magnetization directly between lines 3 and 4 and these lines remain somewhat sharper than others for slow exchange rates. Jumps of $4\pi/5$ ($W_{12}/W_{13} = 0$), on the other hand, exchange magnetization between lines 2 and 5 so that a different region remains sharp. The contribution of these "sharp" regions to the powder lineshapes can be seen as "bumps" at the top.

Figure 19. As Figure 18, but for the orientation $\alpha = 0^{o}$, $\beta = 0^{o}$, $\gamma = 16^{o}$. Now $2\pi/5$ jumps exchange magnetization directly between lines 2 and 3, and $4\pi/5$ jumps directly exchange lines 1 and 4. The "sharp" regions contribute to other "bumps" in the powder spectra. It is rapid averaging in molecules with orientations near these ($\alpha = 0^{o}$ $\beta = 0^{o}$ $\gamma = 0^{o}$ and $\alpha = 0$ $\beta = 0$ $\gamma = 18^{o}$) that give rise to the "bumps" in the powder spectra.

Figure 20. Theoretical powder spectra for the two cases $W_{12}/W_{13} = \infty$ and $W_{12}/W_{13} = 1$ for several total jump rates, with appropriate shielding parameters for ring carbons of DMFe. The "bumps" are quite evident in both sets, though the feature near 35 PPM is weaker in the hard collision ($W_{12}/W_{13} = 1$) case.

Figure 21. Experimental ^{13}C spectra of DMFe at a number of temperatures. The "bumps" in the slow exchange region and axialization at higher jump rates are quite evident. The upfield peaks, which are truncated, are from the methyl carbons.

Figure 22. The experimental spectrum of DMFe at $-172.5^{o}C$ is compared with theoretical spectra for a number of jump ratios W_{12}/W_{13}, for a total jump rate of 600 Hz. The experimental spectrum is in agreement

with a large W_{12}/W_{13} ratio.

Figure 23. A plot of the log of estimated jump rate against 1/T for DMFe. From this we determine an activation energy of 3.2 kcal/mole for ring jumps.

Figure 24. Deuterium coupled and decoupled spectra of residual protons in heavy ice (D_2O), at $-90^{\circ}C$. H concentration was $\sim$0.5% and the decoupling field was $\sim$60 G. From this we obtain $\sigma_{\parallel}$ = 15 PPM and $\sigma_{\perp}$ = -19 PPM.

Figure 25. Symbolic representation of the migration of a D-type Bjerrum defect through the ice lattice. Oxygen atoms occupy the tetrahedral positions and hydrogens are represented by black dots. This migration exchanges water molecules among the six tetrahedral orientations, of Figure 26.

Figure 26. The six equivalent orientations for a water molecule in a tetrahedral environment. Water molecules are exchanged among these orientations by defect migration in ice.

Figure 27. Exchanging lineshapes for water in a tetrahedral environment, showing the dependence of "sharpness" of the isotropic spike on T_2. Total jump rate in both cases is 5000 Hz, with T_2 = 0.001 sec (top) and T_2 = 0.01 sec (bottom).

Figure 28. Theoretical powder spectra for protons in heavy ice undergoing exchange. On the left are lineshapes for the symmetry related jump model and on the right for hard collision random jumps, each at a variety of total jump rates. T_2 was 0.001 sec in

both cases.

Figure 29. Experimental lineshapes for protons in heavy ice at several temperatures, to be compared with the symmetry related jump model on the right. The extra bump of the symmetry related jump model is quite evident in these spectra.

Figure 30. A plot of the logarithm of estimated jump rate vs. 1/T for heavy ice. From this we determine an activation energy of 3.5 kcal per mole for the reorientational motion.

Figure 30a. ^{13}C powder spectra of pentamethylbenzene above (28°C) and below (20°C) the crystallographic transition (24°C). The narrowing above the transition is an indication of restricted motion (marks show approximate σ_{11} and σ_{22} below the transition).

Figure 31. Schematic representation of quadrupolar (top) and chemical shielding (bottom) powder patterns in a solid. Quadrupole couplings are generally about 100 times larger than chemical shifts.

Figure 32. Energy levels for a spin-1 with and without quadrupole couplings. With a quadrupole coupling the $+1 \rightarrow 0$ and $0 \rightarrow -1$ transitions are no longer degenerate (bottom). However the +1 and -1 levels shift equal amounts in the same direction, making possible high resolution FTDQ NMR.

Figure 33. Schematic pulse sequence for FTDQ NMR showing preparation pulse, evolution, and probing pulse. The evolution during τ is independent of the quadrupole coupling.

Figure 34. Comparison of exact computed response (solid curve) and

approximate response (dashed curve) of initial density matrix I_{z1} to a double quantum pulse as a function of time. Although the response is not ideal, the density matrix desired, $a_{z2} \simeq -1.0$, may be prepared through proper selection of pulse length.

Figure 35. Coefficient of single quantum coherence for the pulse of Figure 34. It is desirable to have single quantum response minimized as well as double quantum response maximized in FTDQ NMR.

Figure 36. The distribution of coherence in the y-space after a single pulse on initial density matrix I_{z2}, as a function of ω_Q (marked in kHz along curve). The ideal response for a δ-$\pi/2$ pulse is $a_{y2} = -1$.

Figure 37. Efficiency of preparation of double quantum choerence for initial density matrix I_{z1}, for a single weak pulse, as a function of ν_Q. The change of sign at $\nu_Q = 0$ is not important. The solid curve is the exact calculated response and the dashed curve is the approximate $\cos(\omega_1{}^2/\omega_Q t)$.

Figure 38. Overall efficiency of preparation and detection of double quantum coherence for pulse sequence shown if: detection is immediately after probing pulse (top), or detection is delayed for 30 μsec by spectrometer dead time (bottom).

Figure 39. (bottom part of 38)

Figure 40. Response of initial density matrix I_{z1} to a pair of strong pulses (quadrupolar echo sequence) as a function of ν_Q. This sequence may be used to avoid distortion due to dead time as shown in Figure 38, 39.

Figure 41. Response functions for pulse sequences with two weak pulses. The response in (b) is practically as good as (a) since small amplitude oscillations will be obscured by broadening. The sequence shown in (b) is best suited for experimental application in powder samples since it overcomes the problem of spectrometer dead time.

Figure 42. Response functions for two pulse sequences as a function of ν_Q, multiplied by the intensity function for an axial quadrupole powder pattern (upper curves). These predict the lineshape for chemical shielding if the quadrupolar and shielding tensors are axial, with unique axes aligned.

Figure 43. Ideal response functions for two strong pulse preparation of double quantum coherence, as a function of ν_Q, for three delays between pulses, (a) $\nu_Q\tau = \pi$, (b) $\nu_Q\tau = 3\pi$, (c) $\nu_Q\tau = 5\pi$ where ν_Q is the maximum quadrupole splitting. At the bottom is the sum of these three with appropriate weights for a Fourier approximation to a square wave.

Figure 44. Calculated response function for realistic parameters, with pulse widths and delays adjusted to give the best possible response. The response functions shown are for a maximum quadrupole splitting (separation between sattelites) of 260 kHz, r.f. pulses with ν_1 = 100 kHz and $\Delta\nu = 0$. Shown are responses to the following sequences: (a) 1.75 μsec pulse, 2.25 μsec delay and 2.50 μsec pulse, (b) 1.75 μsec pulse, 10.00 μsec delay and 2.50 μsec pulse, (c) 1.75 μsec pulse, 17.75 μsec delay and 2.50 μsec pulse. At the bottom is the appropriately weighted sum of these showing the very small

deviation from ideal response. A ninety degree pulse on resonance would be 2.50 μsec and the delays $\nu_Q\tau$ of π, 3π and 5π rotations for the maximum splitting are 3.85 μsec, 11.54 μsec and 19.23 μsec respectively.

Figure 45. Response functions for first and third echos in a multiple quadrupole echo sequence as a function of ν_Q. Also shown is the average of response function for the first four echos, showing that averaging of several echos does not degrade response. Pulses were 100 kHz in amplitude and 2.25 μsec in length, and τ was 30 μsec.

Figure 46. Stick spectra for two equivalent and inequivalent deuterons which are dipolar coupled. At top and bottom are single quantum spectra and in the center is the double quantum spectrum, which is the same for equivalent and inequivalent cases, and shows no quadrupole splitting.

Figure 47. Single and double quantum stick spectra for three equivalent deuterons which are dipolar coupled. The double quantum spectrum has no quadrupole splitting.

Figure 48. Energy levels for two equivalent deuterons which are dipolar coupled. Arrows represent all possible transitions. Solid arrows are allowed single quantum transitions and single spin double quantum transitions which would be observed in FTDQ NMR experiments. Dashed lines are zero, two, three and four quantum transitions which could be induced by the dipolar coupling (Ch. IV). The two sets of levels are symemtric (left) and antisymmetric (right) with respect to

exchange of the spins.

Figure 49. Pulse sequences for FTDQ NMR. Experiments on single crystals commonly use A, while D is most often used for powder samples. Data are collected as a function of variable time τ.

Figure 50. Double Quantum free induction decay for d-1 benzene doped 10% into normal benzene, taken at $-40^{o}C$. Points are spaced by 100 μsec.

Figure 51. Fourier Transform of decay in Figure 50 showing chemical shielding anisotropy for the aromatic deuterons. $\Delta\sigma = -6.5$ PPM. The position of liquid benzene is shown.

Figure 52. Theoretical powder patterns for the d-1 benzene experiment, generated by a computer for the pulse sequence used.

Figure 53. Single quantum deuterium spectrum of 5% deuterated ferrocene showing axially symmetric quadrupole powder pattern with $eqV_{zz} = 96.8$ kHz $\eta \simeq 0$.

Figure 54. Double quantum free induction decay for 5% deuterated ferrocene, taken with pulse sequence D of Figure 49. Points are spaced by 50 μsec.

Figure 55. Fourier Transform of the decay in Figure 54. From the width we estimate the chemical shielding anisotropy to be -6.5 PPM, as for benzene. The position of the line was not measured relative to a reference, and the scale has been reduced a factor of two to compensate for double quantum scaling.

Figure 56. Single quantum spectra for a crystal of $BaClO_3 \cdot D_2O$ in an arbitrary orientation. The inserts show the resolved dipolar splitting between deuterons (inner lines), and the extra lines for HOD impurities (outer lines). In this orientation the separation between sattlites is 138.3 kHz.

Figure 57. Proton decoupled (left) and coupled (right) double quantum spectra of $BaClO_3 \cdot D_2O$, taken for the orientation of Figure 56. These spectra were taken with pulse sequence A of Figure 49, with double quantum decays of 50 points spaced by 25 μsec.

Figure 58. Single quantum powder spectrum of d-1 hexamethylbenzene, showing the nonaxial quadrupole coupling tensor. From this we obtain eqV_{zz} = 18.95 kHz and η = 0.096.

Figure 59. Single quantum powder spectrum of α,β d-2 hexamethylbenzene, as Figure 58. eqV_{zz} = 20.9 kHz η = 0.08.

Figure 60. Single quantum powder spectrum of α, β, γ d-3 hexamethylbenzene, as Figure 58. eqV_{zz} = 22.2 kHz η = 0.07.

Figure 61. Carbon spectra for ordinary HMB (bottom) and d-1 HMB (center) showing axial symmetry from rapid rotation about the sixfold axis. The theoretical spectrum (top) shows the lineshape expected if the carbon tensor had the same asymmetry as the deuterium ($\eta \simeq 0.10$). Slight broadening from deuterium is evident for d-1 HMB, but there is no evidence for a nonzero asymmetry parameter.

Figure 62. On-resonance decay of echo amplitude with time between pulses for some deuterated hexamethylbenzene samples. The rate of

decay is clearly associated with deuterium concentration, and hence the strength of deuterium-deuterium dipolar couplings. All curves were obtained while decoupling protons.

Figure 63. Oscillation of echo amplitude with time for d-1 HMB, 500 Hz off resonance. These oscillations clearly demonstrate the behavior predicted by (III-81). The decay of the constant term (top) comes only from T_2 while the oscillations are damped by chemical shielding anisotropy as well.

Figure 64. Single quantum spectrum of a single crystal of d-2 HMB showing quadrupolar and dipolar structure. The quadrupole splitting was nearly the maximum possible for d-2 HMB.

Figure 65. Theoretical (bottom) and experimental double quantum spectra for the d-2 HMB crystal shown in Figure 64. The spectrum was taken with pulse sequence A of Figure 49 for 100 points spaced by 50 μsec.

Figure 66. Single quantum spectrum for a single crystal of d-3 HMB, showing quadrupolar and dipolar structure. As for the d-2 HMB crystal, this crystal was oriented to give nearly the maximum possible dipolar and quadrupolar splittings.

Figure 67. Theoretical (left) and experimental (right) double quantum spectra for d-3 HMB. The spectrum was taken using pulse sequence A of Figure 49 for 100 points spaced by 50 μsec.

Figure 68. Experimental double quantum spectrum of 20% d-1 HMB in ordinary HMB. The linewidth is ∿100 Hz or 3.5 PPM. This spectrum was

obtained using pulse sequence D of Figure 49, for 50 points spaced by 200 μsec.

Figure 69. Experimental double quantum powder spectra for d-2 HMB (top) and d-2 HMB 10% in normal HMB (bottom). The dipolar powder patterns are clearly evident in both. The pulse sequence was the same as for Figure 68.

Figure 70. Response function for the pulse sequence used in Figures 68 and 69. Although response is quite poor near $\nu_Q = 0$, it is quite good near the peaks of the powder pattern, the most intense regions of the spectrum.

Figure 71. Theoretical double quantum powder spectra (compare Figure 69) for dipolar coupled pairs of deuterons, with no shielding anisotropy, generated using the experimental parameters for HMB, including weighting by the transfer function, Figure 71. The width of the Gaussian broadening used is noted to the right.

Figure 72. Experimental single quantum deuterium spectrum of d-1 p-methoxybenzoic acid (anisic acid) obtained by Fourier Transforming the second half of a quadrupolar echo. From this spectrum we obtain $eqV_{zz} = 169.0 \pm 1.0$ kHz and $\eta = 0.132 \pm 0.003$. The high intensity at the center and oscillations in amplitude arise from pulse imperfections. Pulses were ∿80 kHz in amplitude and the time between x and y pulses was 40 μsec.

Figure 73. Double quantum FID (bottom) and spectrum (top) of deuterons in d-1 anisic acid. The structure comes from a combination of dipolar

coupling and chemical shielding anisotropy. FID was taken with pulse sequence D of Figure 49, 50 points with a spacing of 50 μsec.

Figure 74. Pulse sequences used in FT Multiple Quantum NMR. The parts of the experiments are labeled at top, (a) and (b), P, preparation, E, evolution, and D, detection. Other pulse sequences for particular experiments are below: (c) and (d) nonselective multiple quantum, (e) selection of even or odd quantum, (f) nonselective with multiple quantum echo for resolution enhancement, (g) even or odd selective with m.q. echo for resolution enhancement, (h) single quantum echo for resolution enhancement.

Figure 75. Energy levels for oriented benzene. These are labeled with total magnetic quantum number (left) and symmetry (top). All transitions, single quantum and multiple quantum, occur within a single symmetry.

Figure 76. Experimental (top and center) and theoretical (bottom) single quantum spectra of protons in oriented benzene. The top spectrum is the Fourier Transform of an ordinary FID, showing lines broadened by inhomogeniety of H_0. The linewidth is ∿100 Hz. The center spectrum was obtained by Fourier Transform of a single quantum echo FID, Figure 73 (h), showing greatly improved resolution. The lidewidth is ∿3 Hz.

Figure 77. Experimental (top) and theoretical multiple quantum spectra for oriented benzene. The pulse sequence and theoretical parameters used are discussed in the text.

Figure 78. Order selective spectra of oriented benzene. At the top, A, is the nonselective spectrum of Figure 76. B is the even quantum only spectrum obtained with pulse sequence (e) of Figure 73. C and D,show respectively, 0 and 4 quantum selection and 2 and 6 quantum selection obtained by adding and subtracting multiple quantum FIDs with preparation pulses phase shifted by 90° but the same phase detection pulses.

Figure 79. Zero quantum FID and spectrum showing extremely sharp lines, limited in width for the present case by truncation of the FID.

Figure 80. Even quantum selective multiple quantum spectrum with an echo in the evolution period. The full spectral width is one $\Delta\omega$ in Figure 75. The linewidths in this spectrum are $\sim$3 Hz, independent of order. The spectrum is completely symmetric since only a single phase FID was transformed.

Figure 81. 2 and 6 quantum selection in a multiple quantum spectrum obtained with an echo during the evolution period. Just the upper half of the symmetric spectrum is shown. Linewidth was limited by truncation of the multiple quantum FID.

Figure 82. 0 and 4 quantum selection in a multiple quantum spectrum obtained with an echo during the evolution period, as Figure 80. The degree of separation of orders can be seen by observing that the strongest line in this spectrum has less than 3% of this intensity in the 2 and 6 quantum spectrum. Degeneracies in line positions occur

for various orders so that some lines (as that near 2500 Hz) appear in several selective spectra.

Figure 83. Block schematic of the spectrometer used for the experiments described here. Various components are further described in the text.

Figure 84. Detailed schematic of the transmitter and probe configuration.

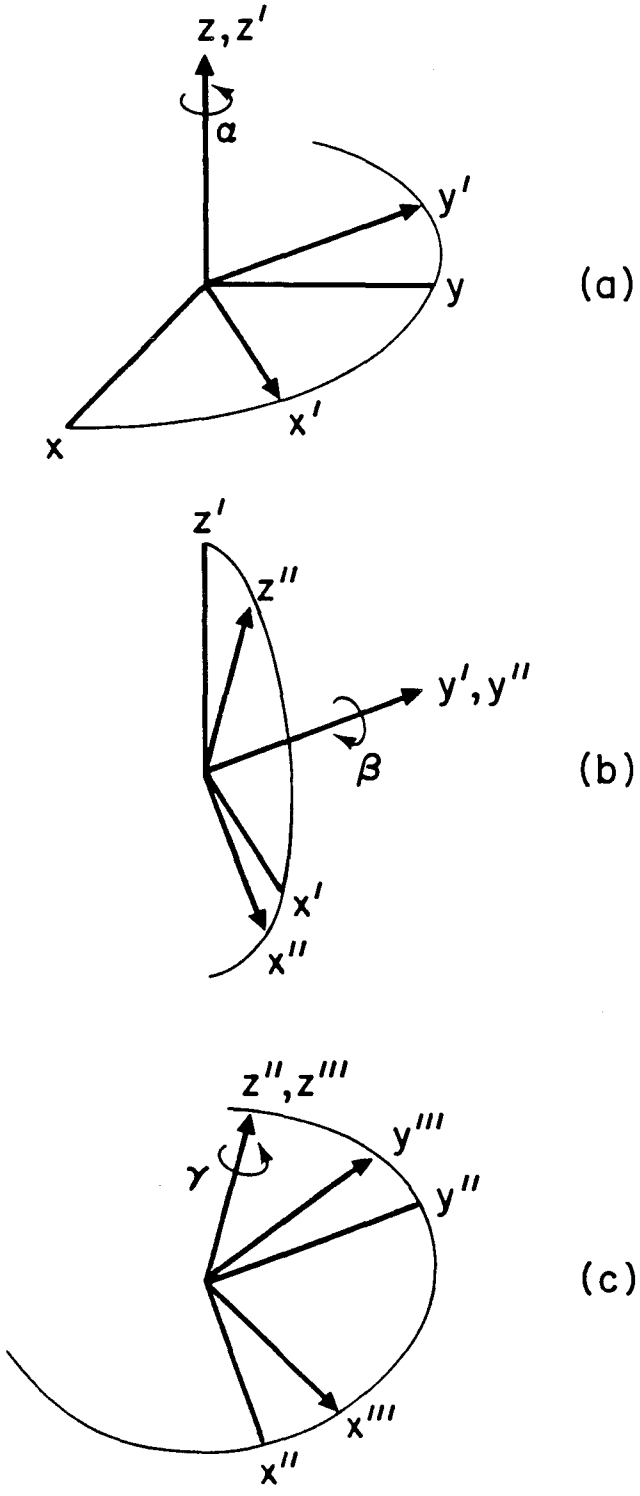

XBL 787-9787

Figure 1

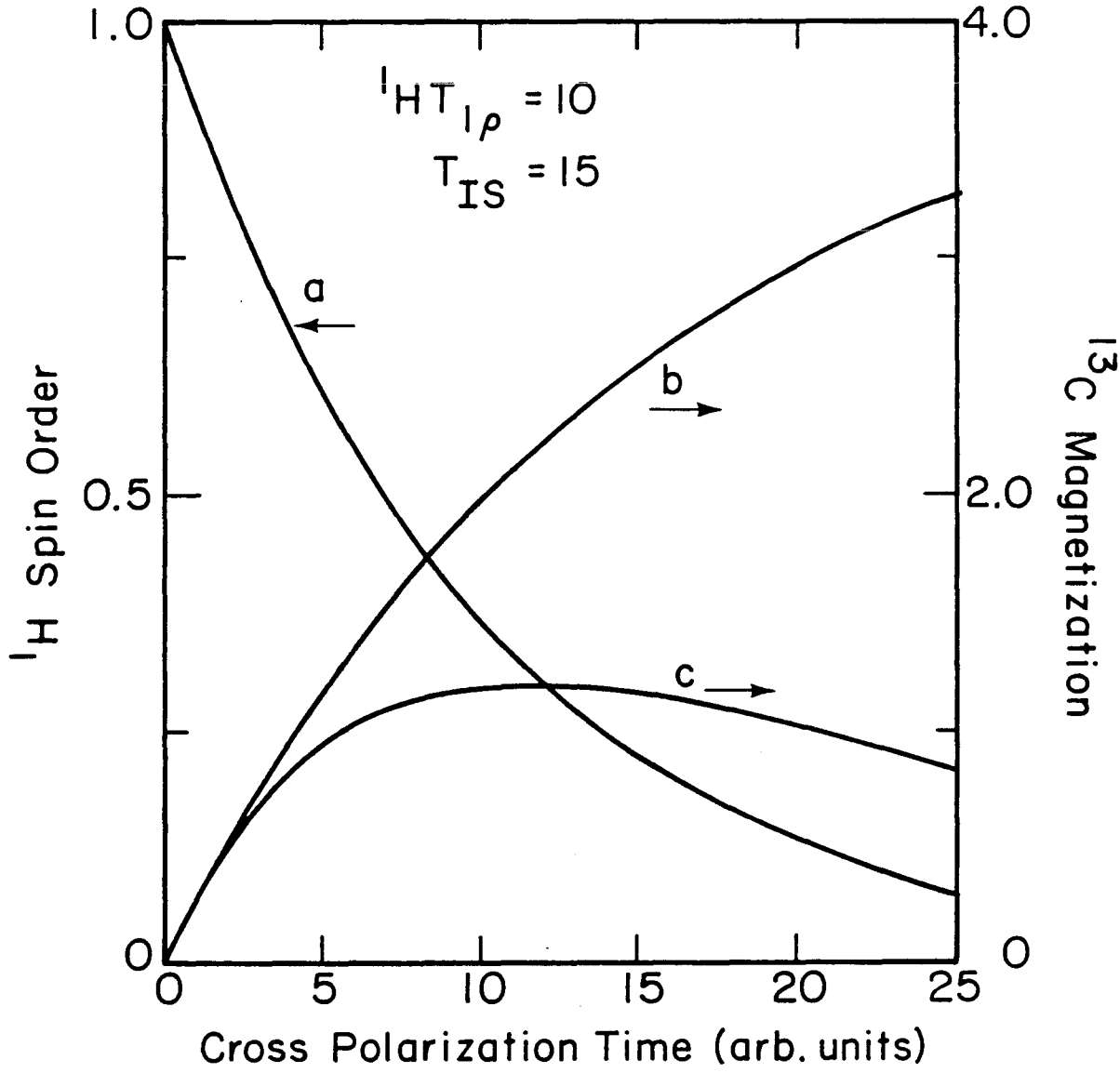

XBL 787-9788

Figure 2

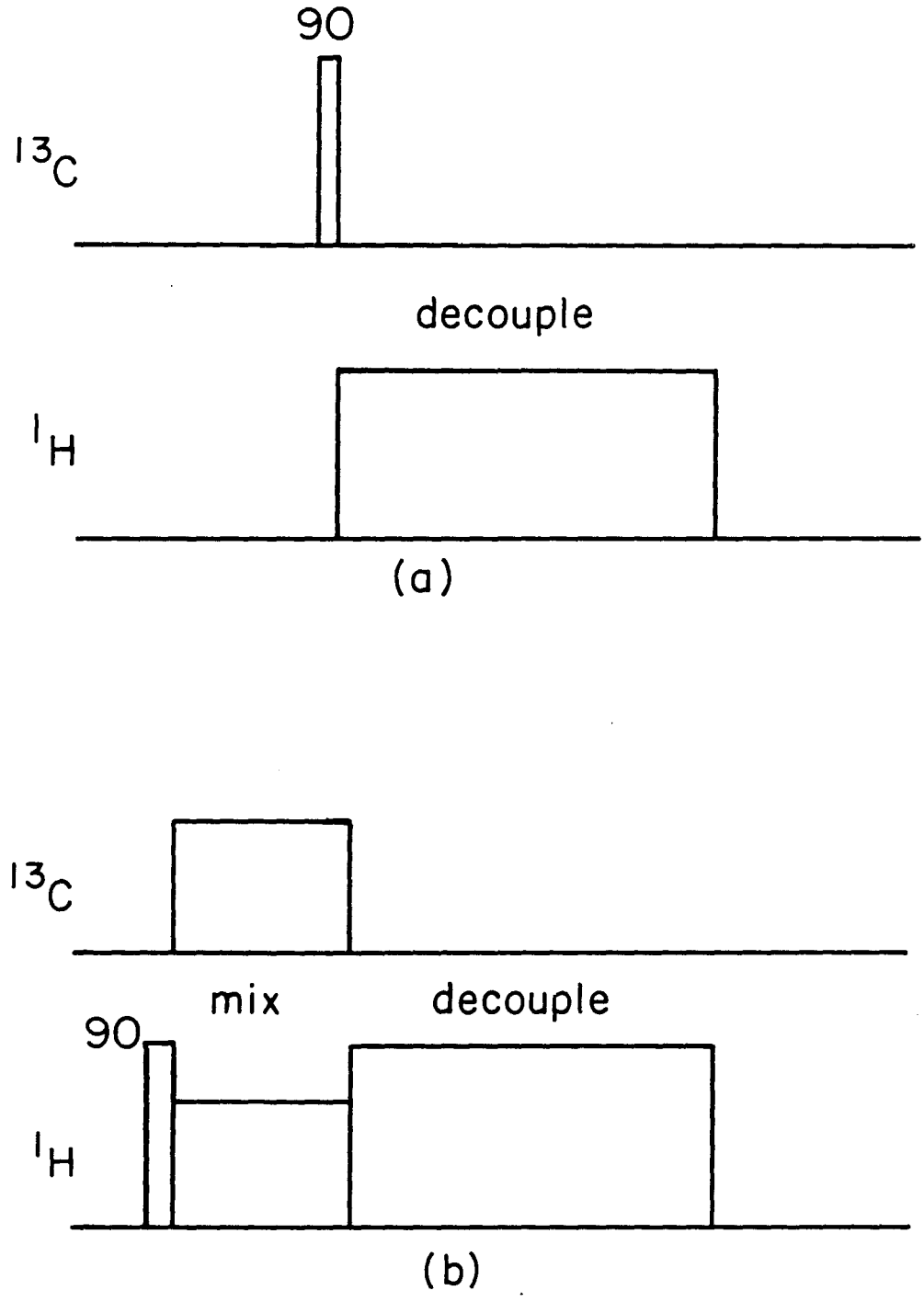

XBL 766-1987

Figure 3

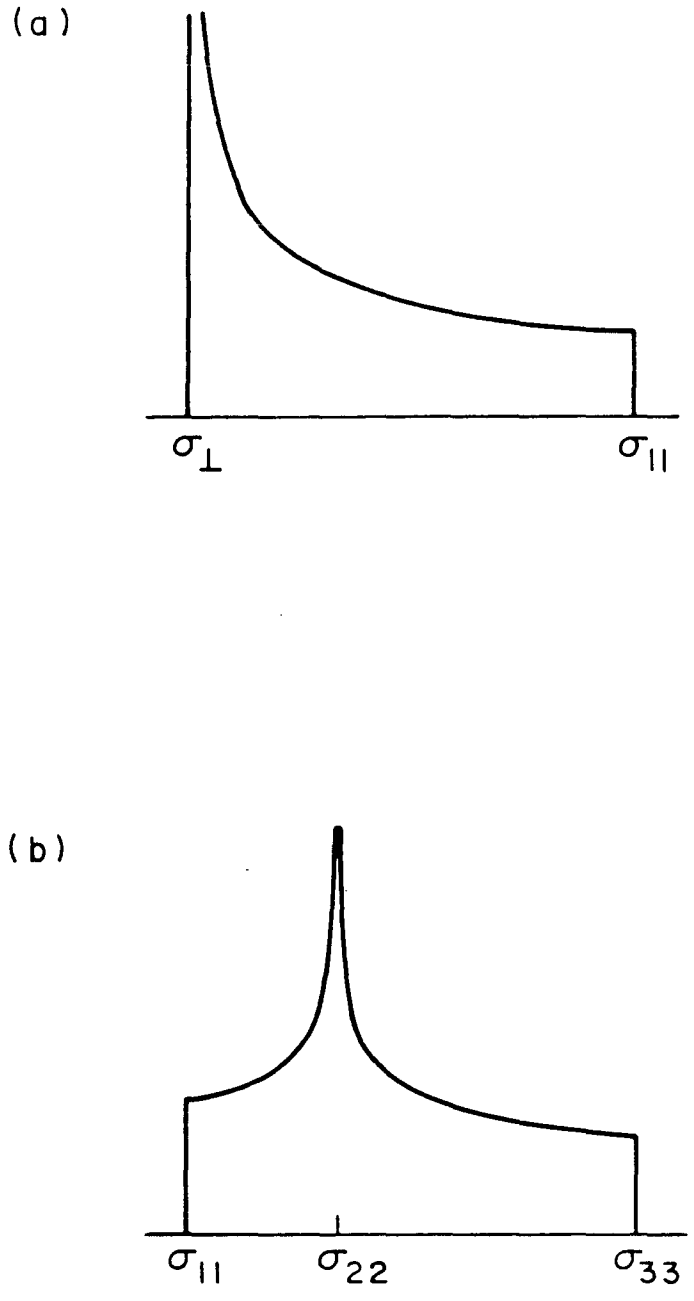

XBL 763-713

Figure 4

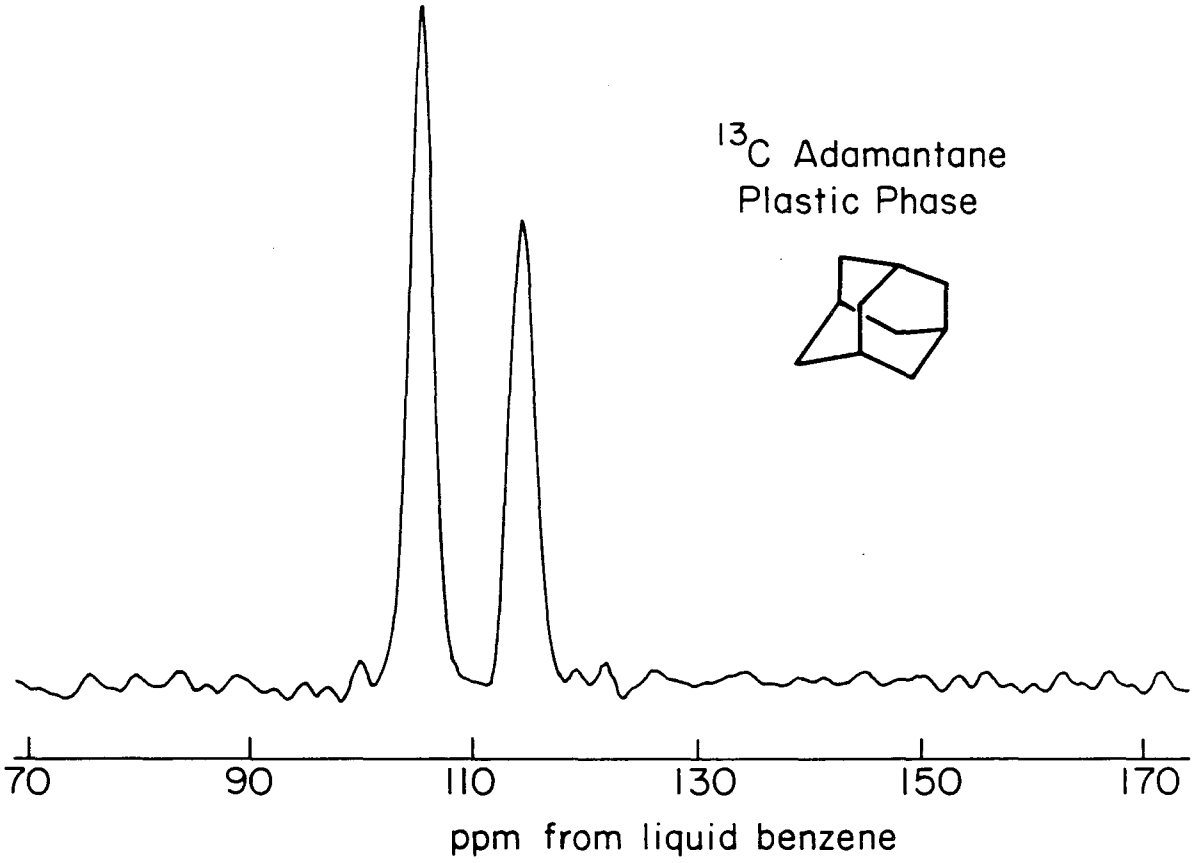

XBL 787-9786

Figure 5

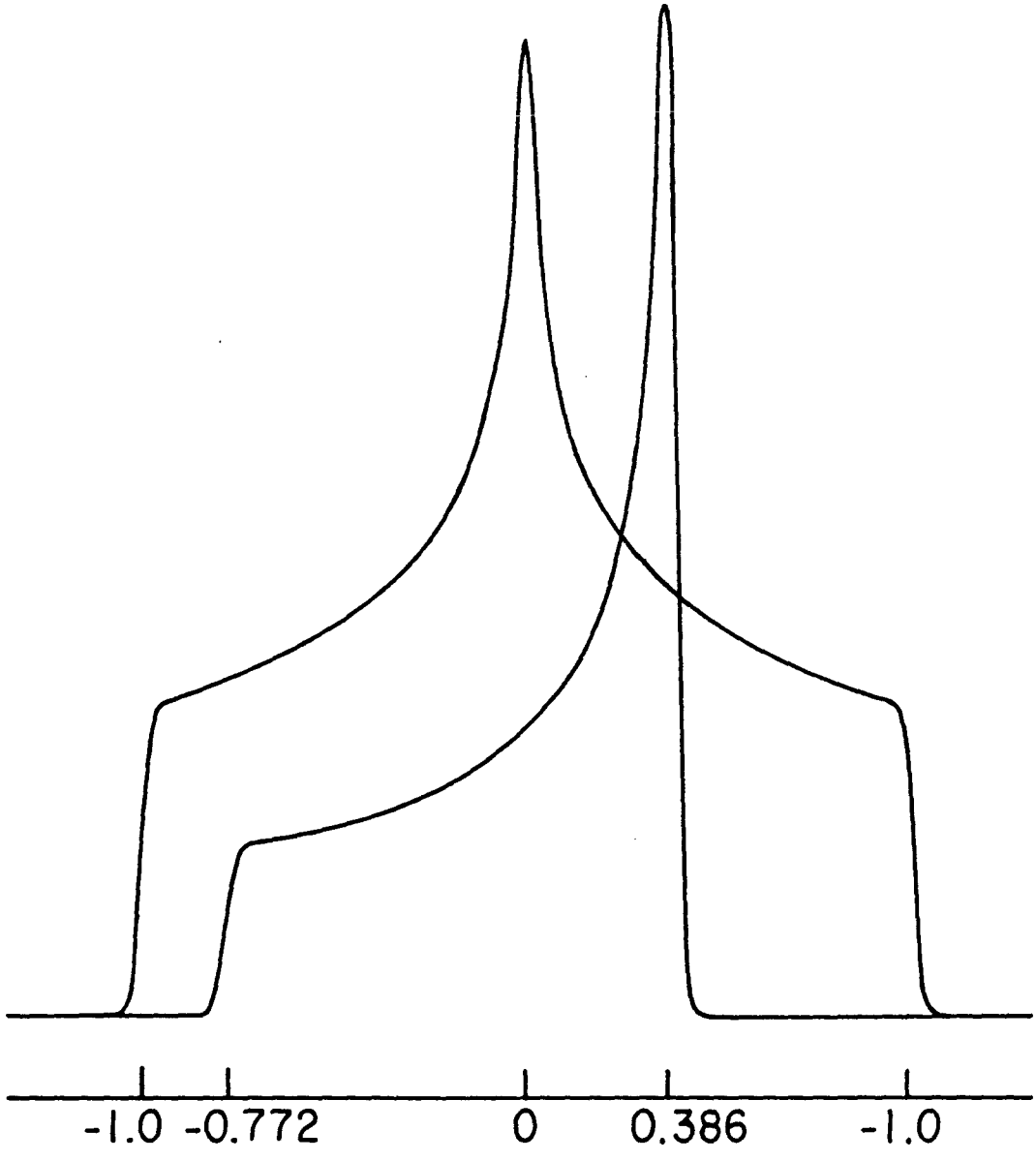

XBL 787-9785

Figure 6

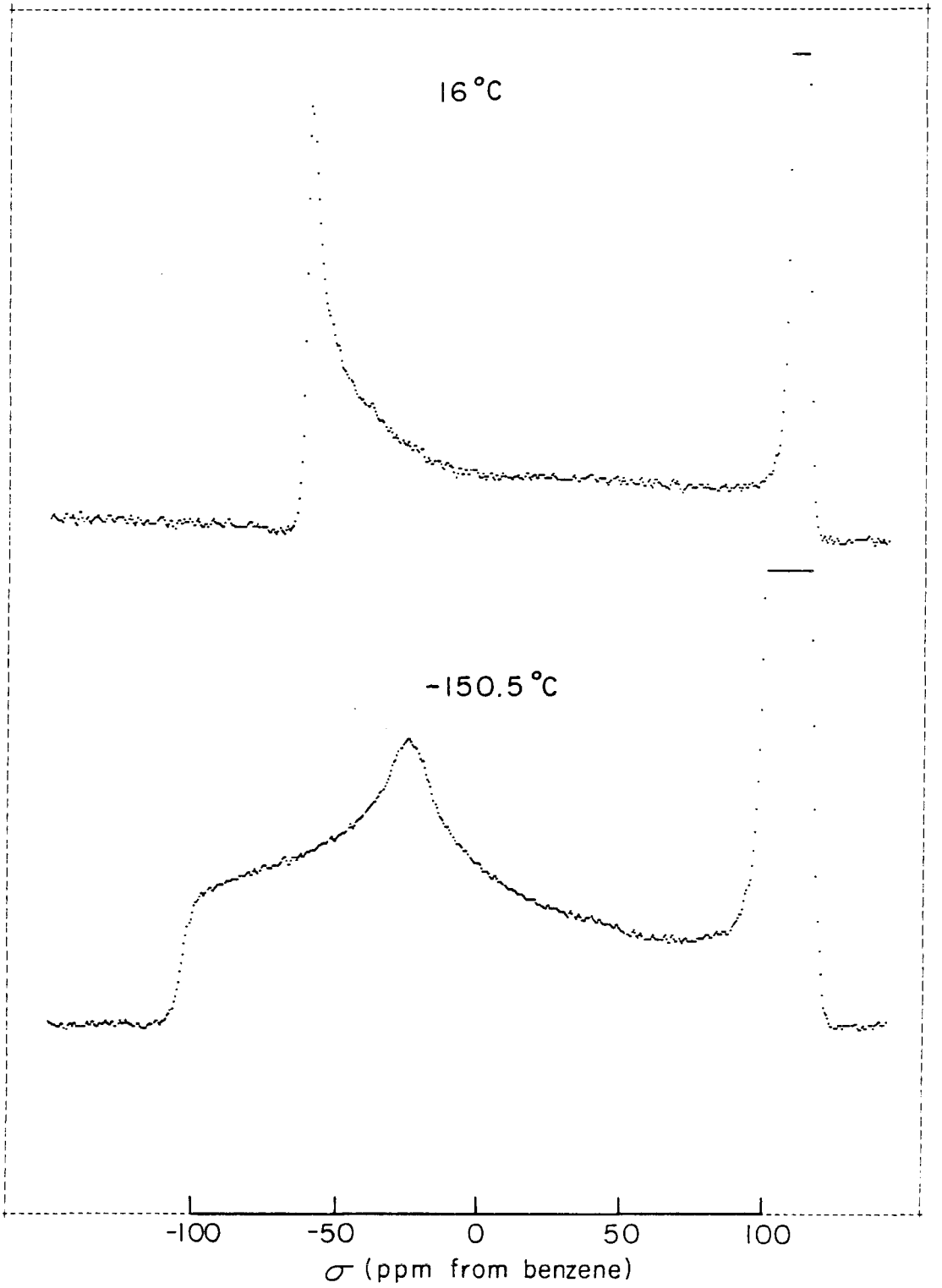

XBL 753-5946

Figure 7

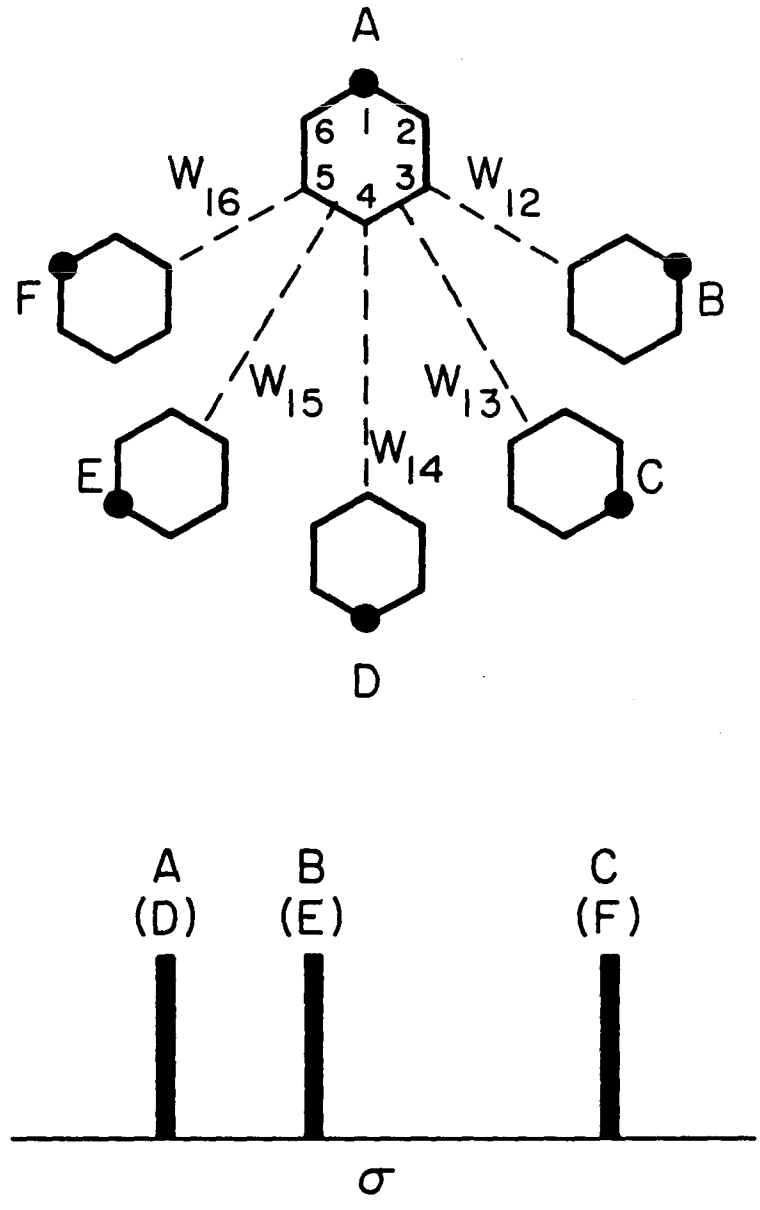

XBL 787-9790

Figure 8

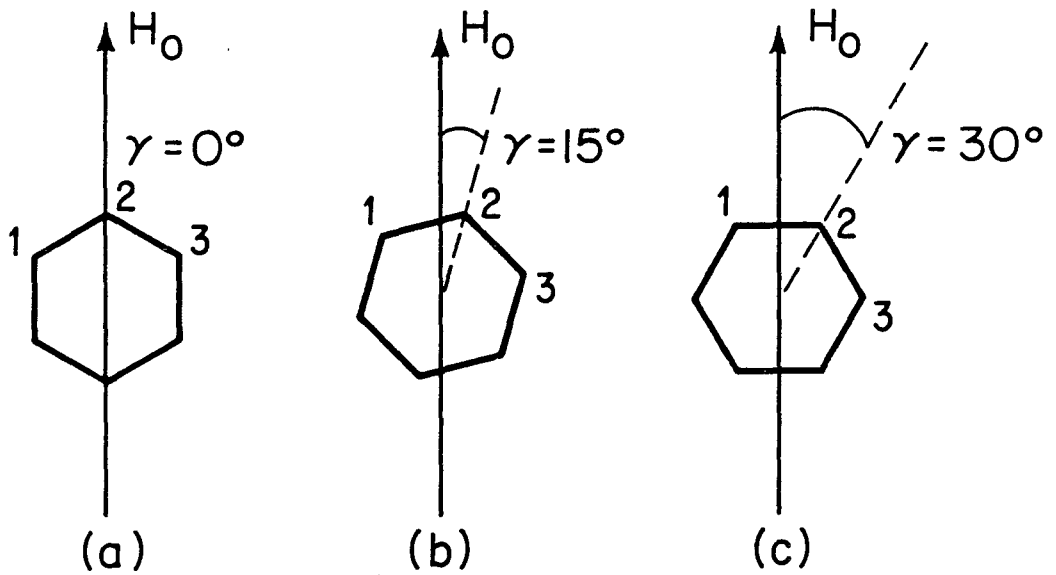

XBL 755-1348

Figure 9

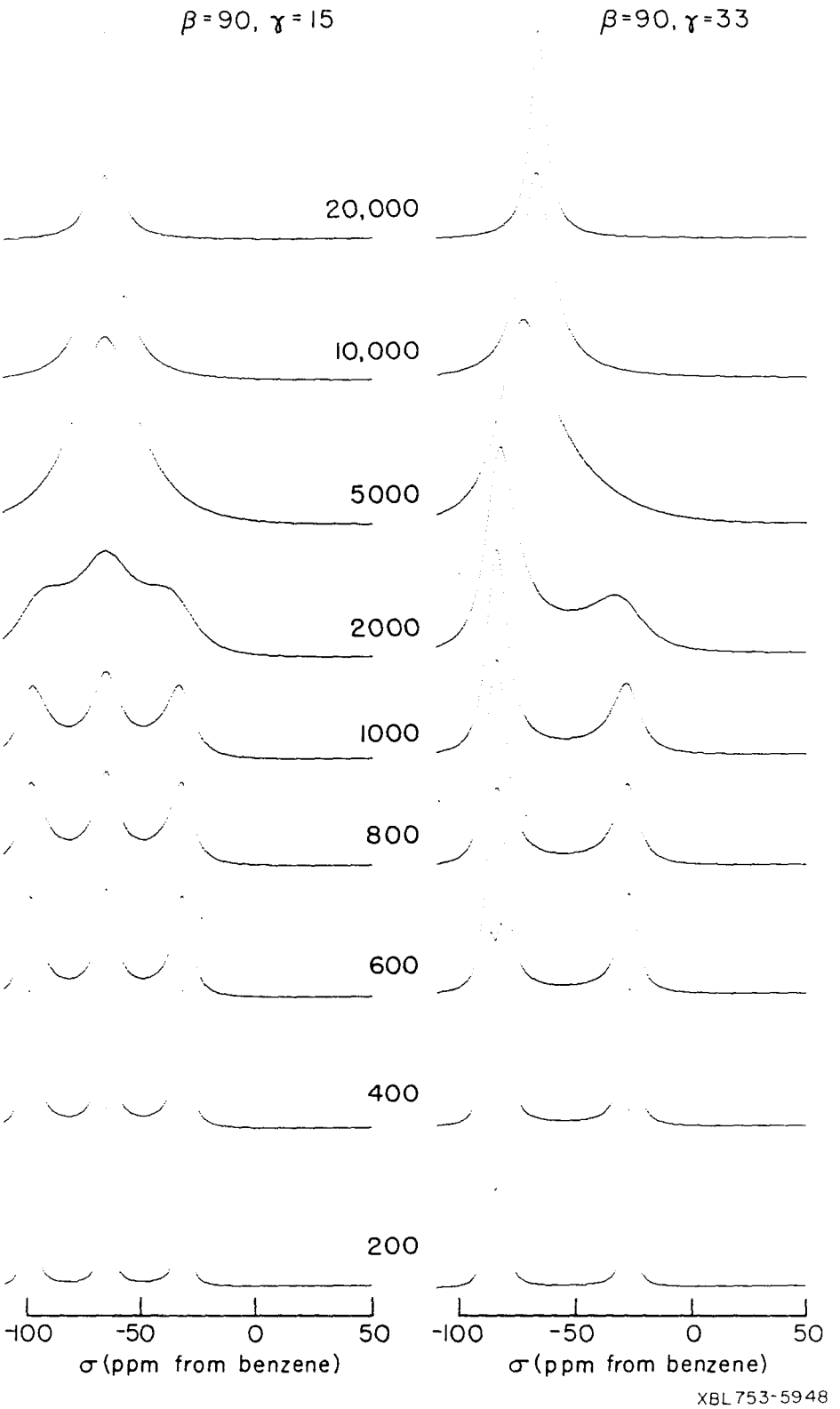
β = 90, γ = 15
β = 90, γ = 33
20,000
10,000
5000
2000
1000
800
600
400
200
-100
-50
0
50
σ (ppm from benzene)
-100
-50
0
50
σ (ppm from benzene)
XBL 753-5948

Figure 10

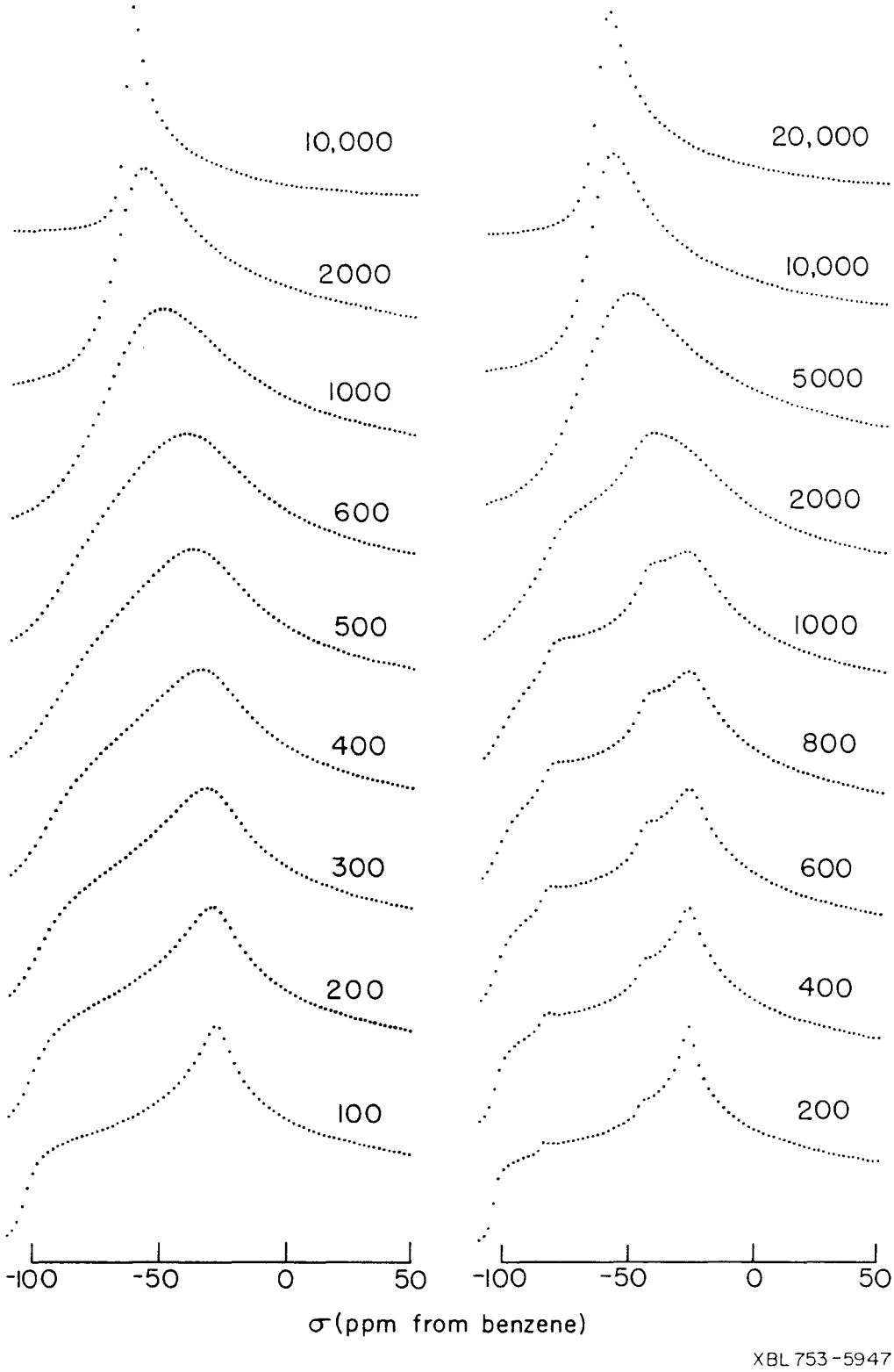
10,000
2000
1000
600
500
400
300
200
100
20,000
10,000
5000
2000
1000
800
600
400
200
-100
-50
0
50
-100
-50
0
50
σ (ppm from benzene)
XBL 753-5947

Figure 11

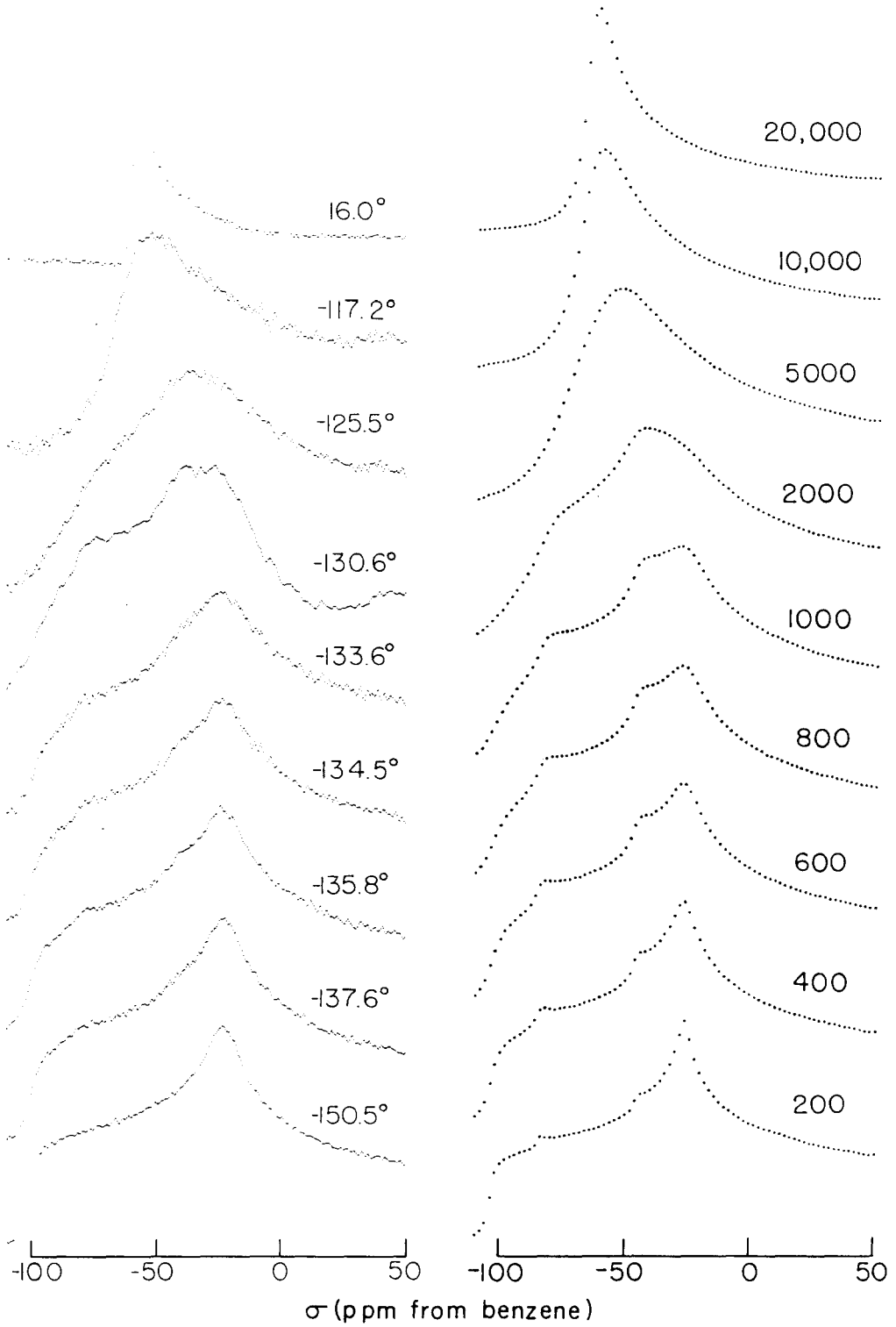

XBL 753-5947A

Figure 12

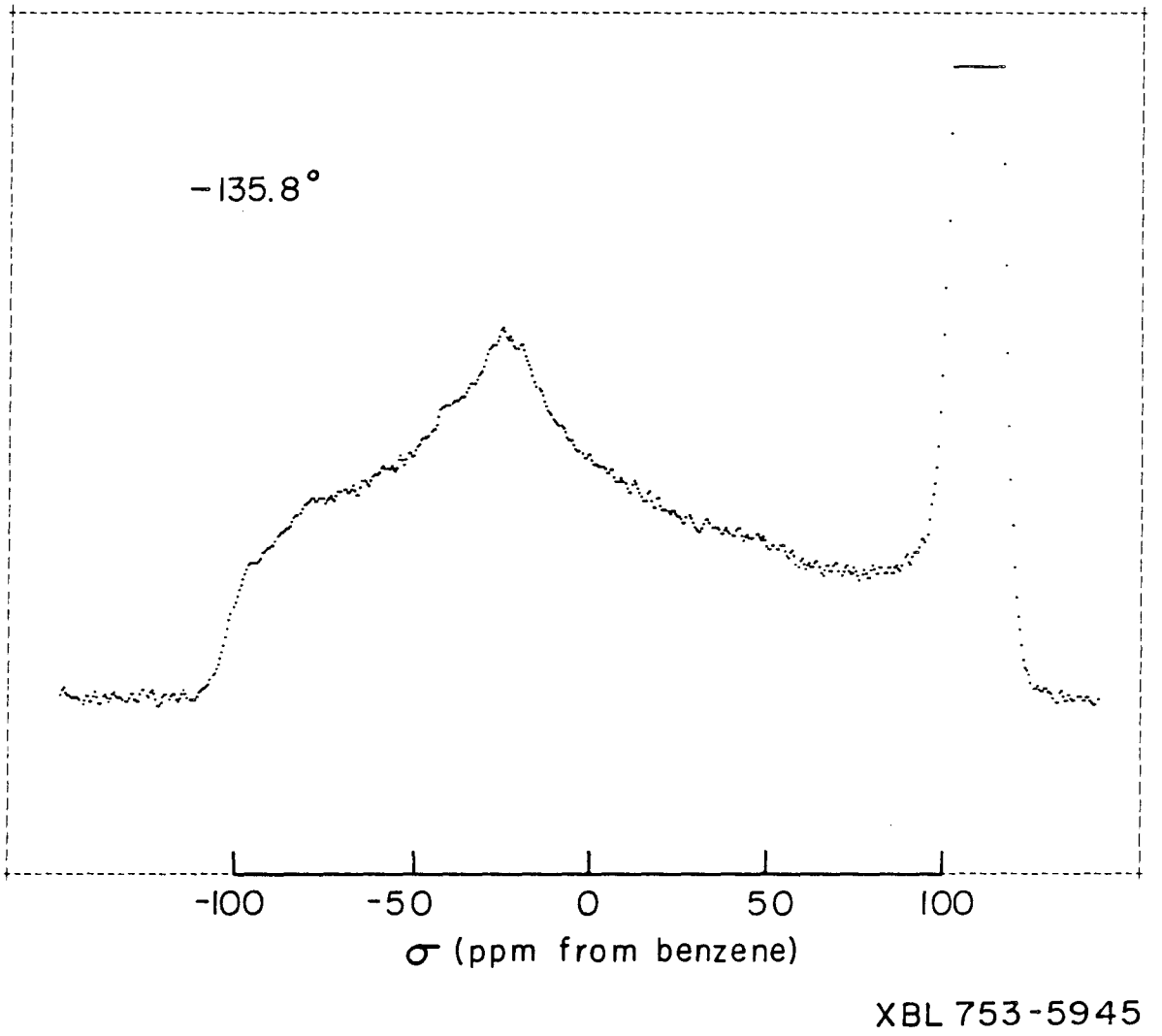

Figure 13

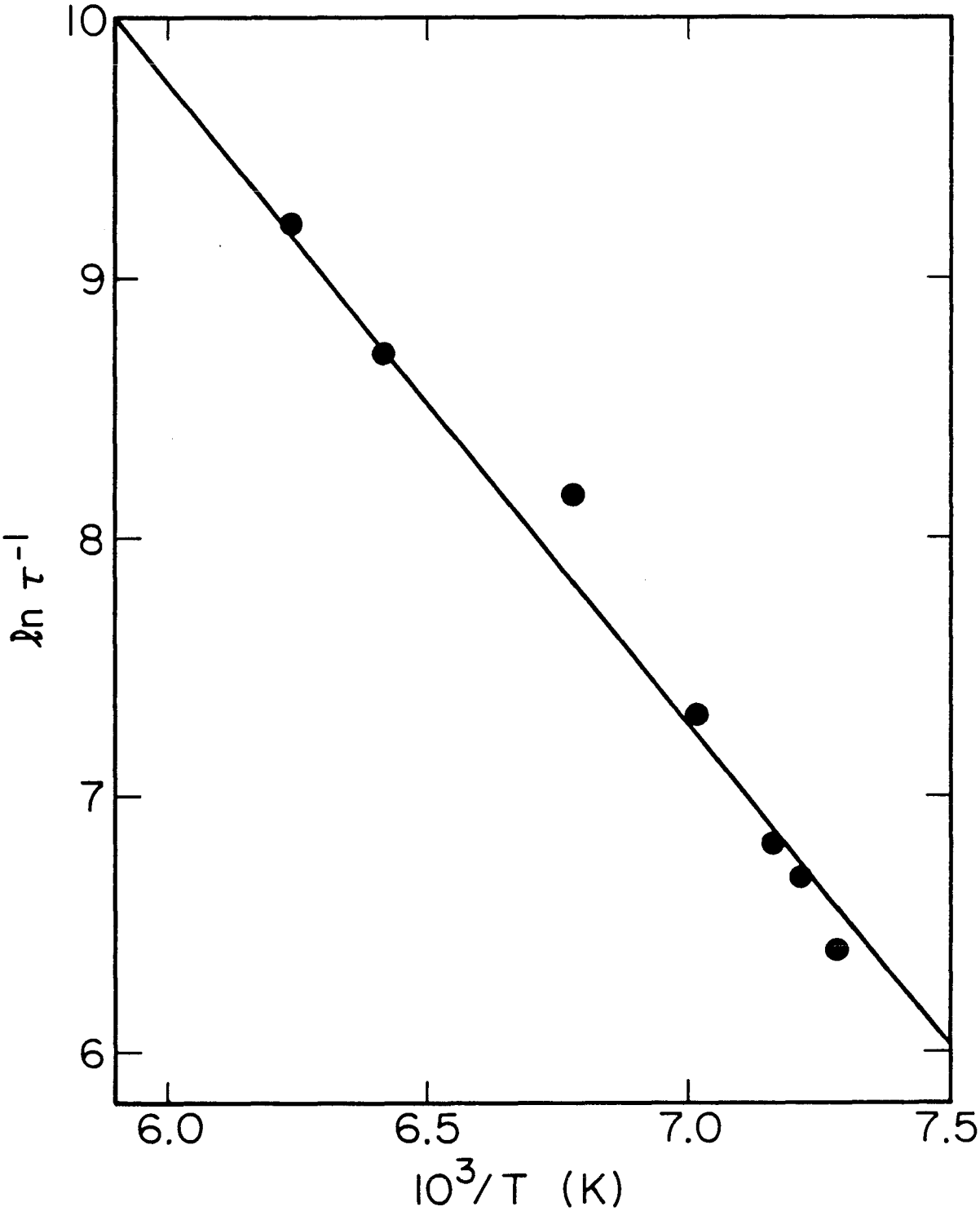

XBL 755-1370

Figure 14

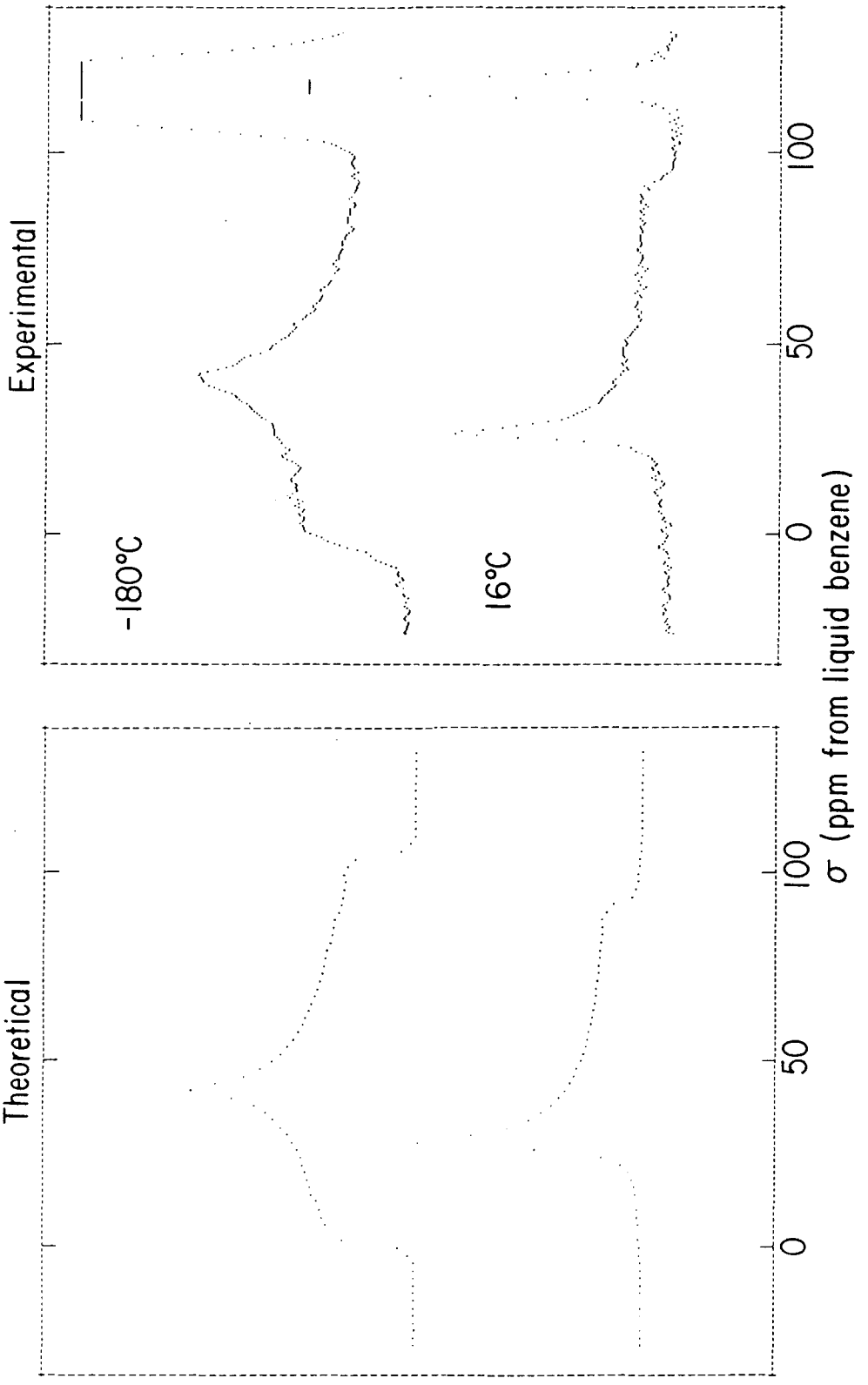

XBL 7511-9409

Figure 15

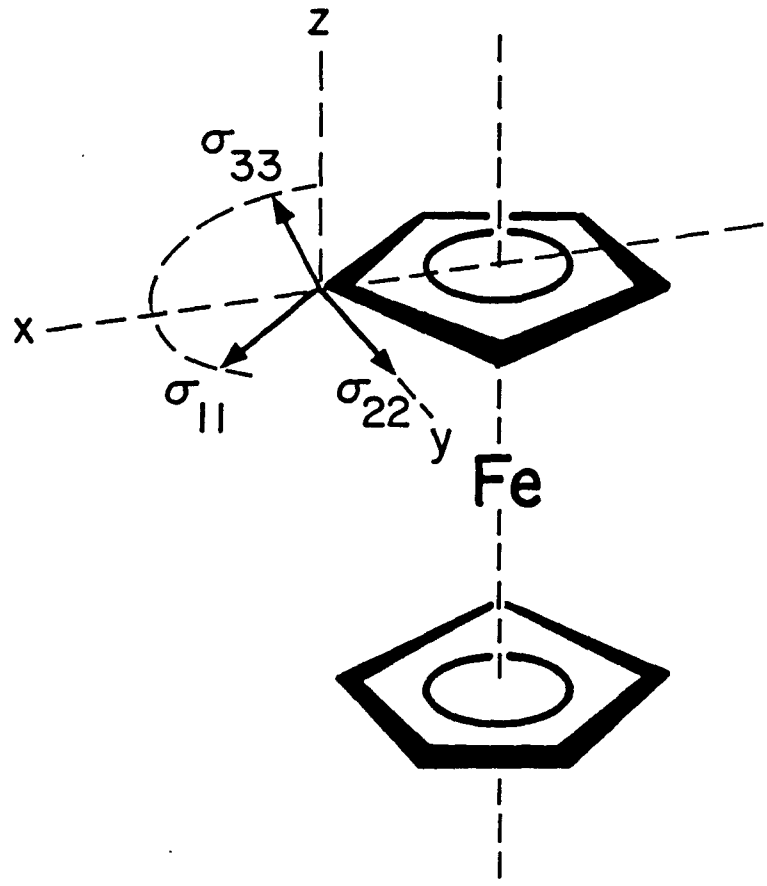

XBL 7512-9194

Figure 16

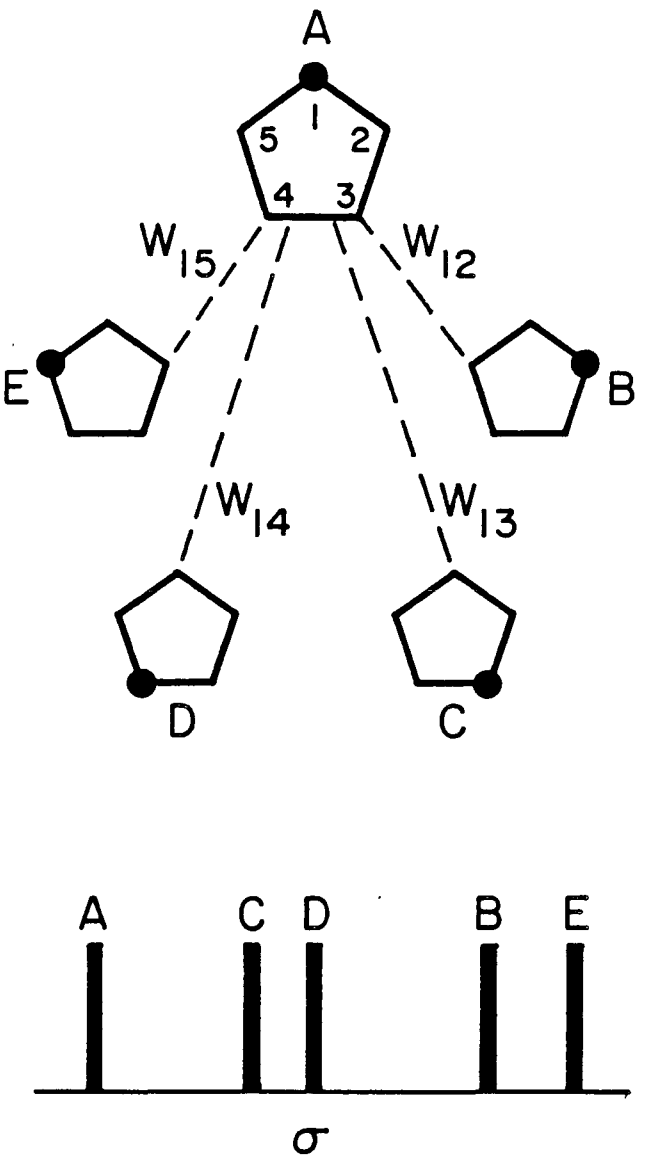

XBL 787-9791

Figure 17

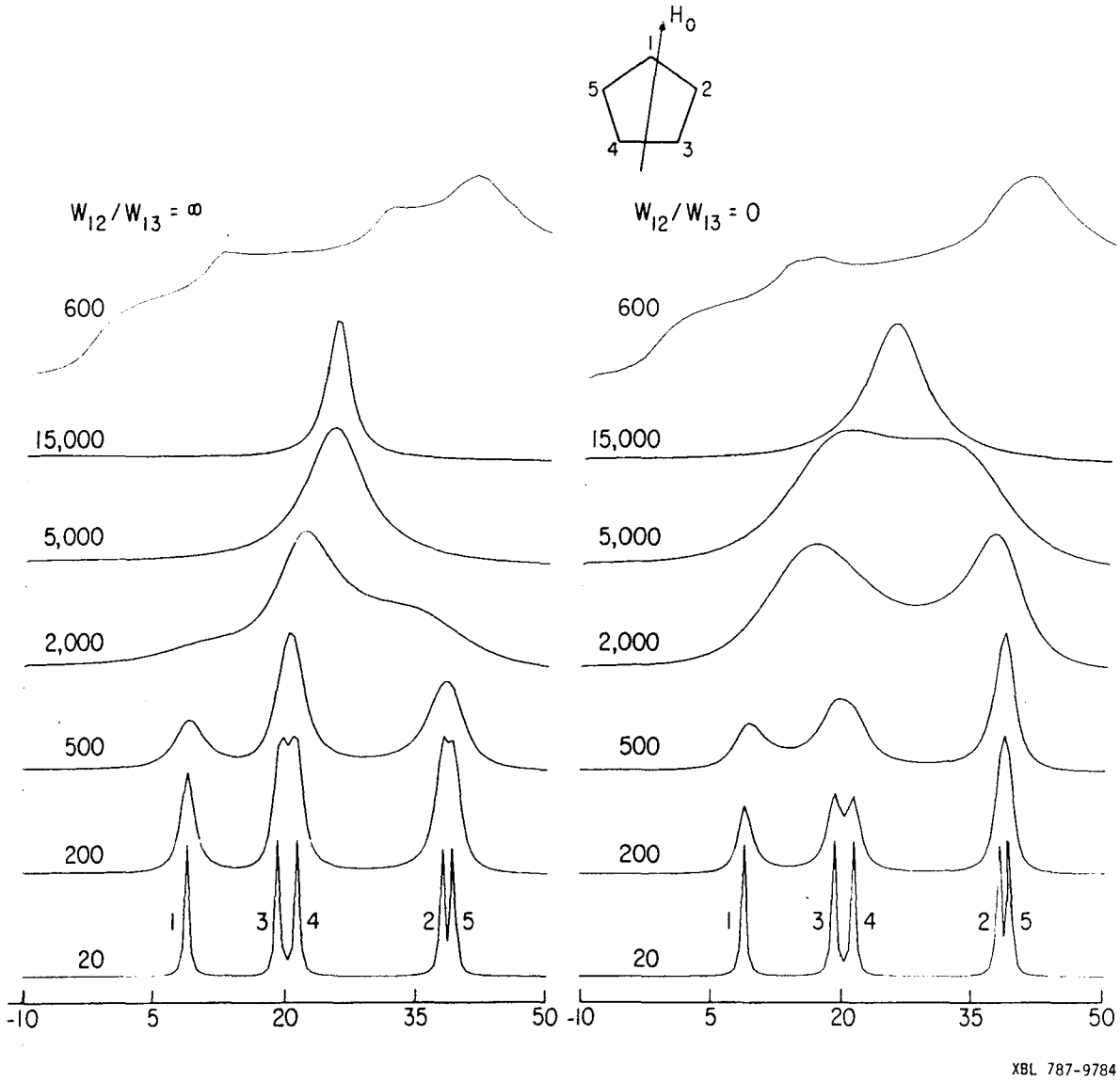
H0
1
2
3
4
5
W12/W13 = ∞
W12/W13 = 0
600
15,000
5,000
2,000
500
200
20
1
3
4
2
5
-10
5
20
35
50
XBL 787-9784

Figure 18

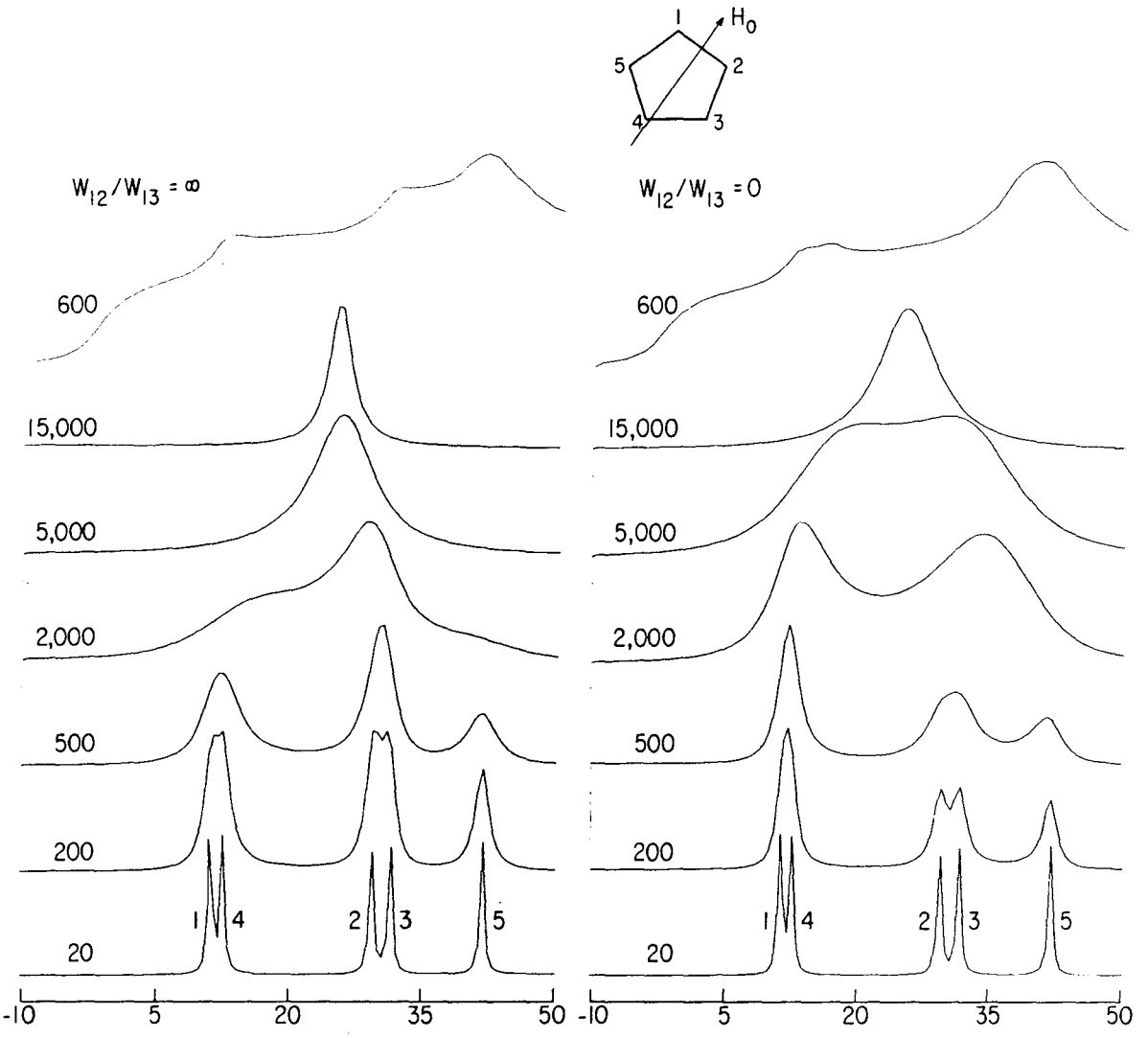

XBL 787-9783

Figure 19

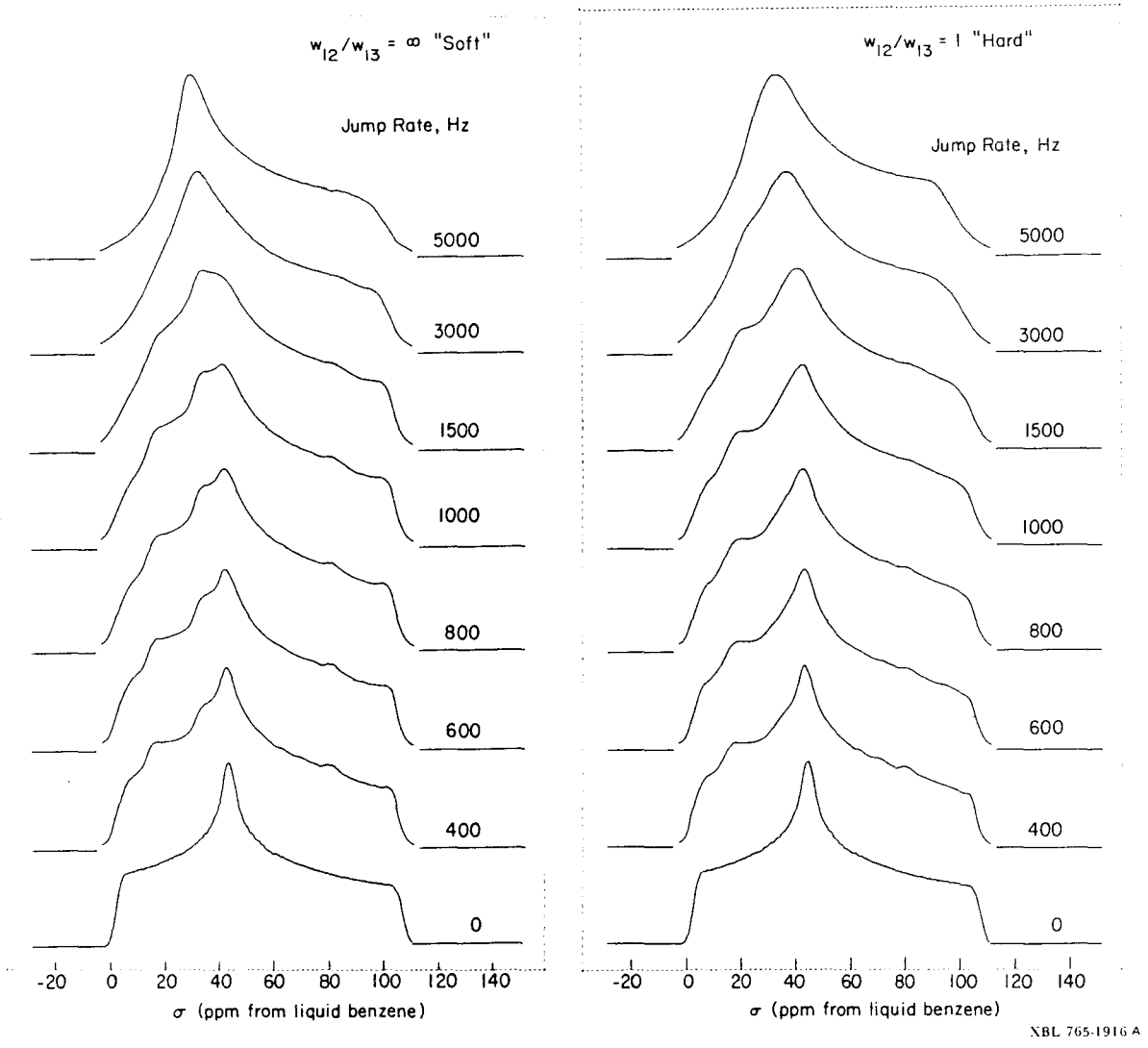
$w_{12}/w_{13} = \infty$ "Soft"
Jump Rate, Hz
5000
3000
1500
1000
800
600
400
0
-20 0 20 40 60 80 100 120 140
σ (ppm from liquid benzene)
$w_{12}/w_{13} = 1$ "Hard"
Jump Rate, Hz
5000
3000
1500
1000
800
600
400
0
-20 0 20 40 60 80 100 120 140
σ (ppm from liquid benzene)
XBL 765-1916 A

Figure 20

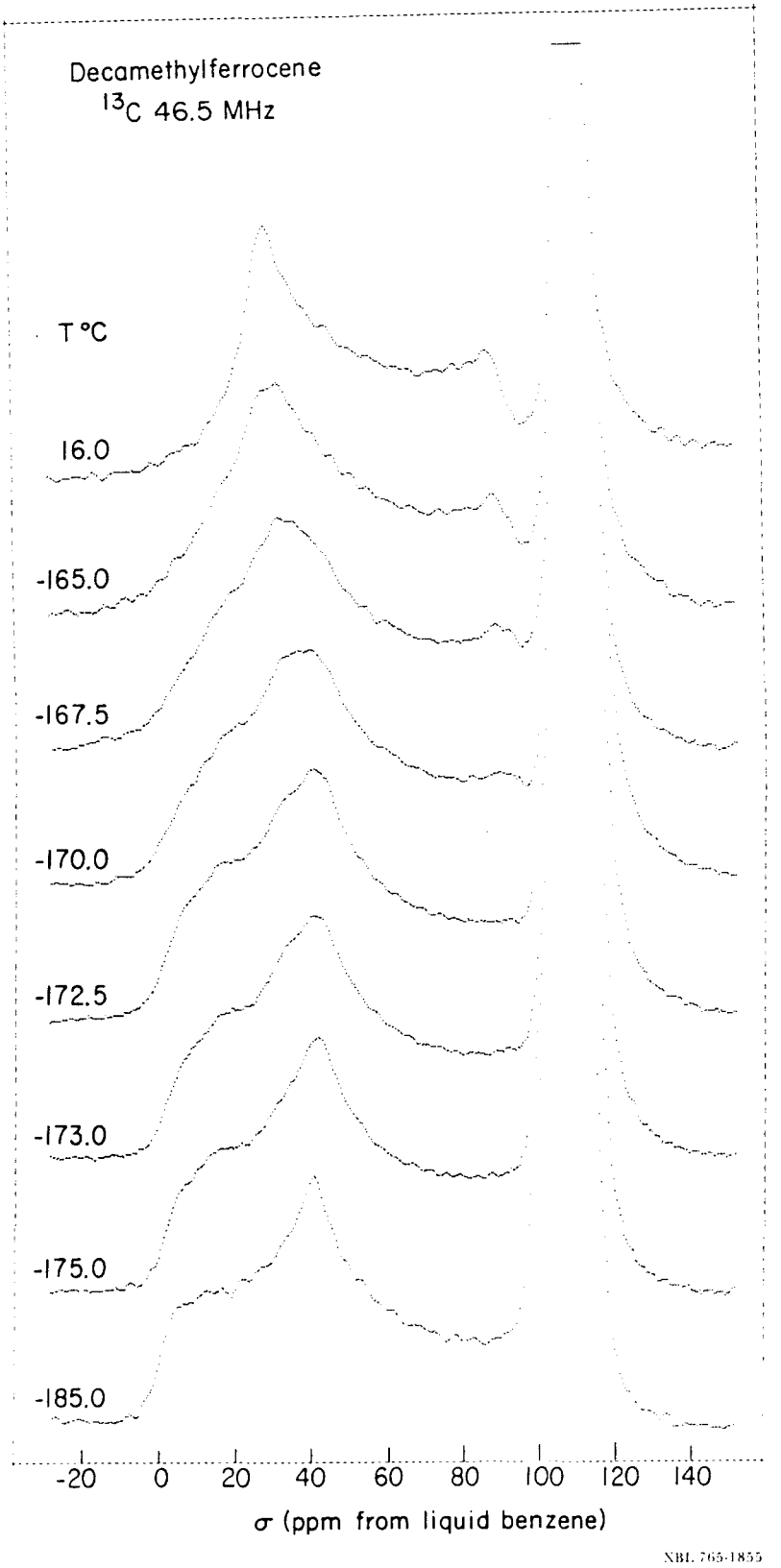
Decamethylferrocene
^{13}C 46.5 MHz
T °C
16.0
-165.0
-167.5
-170.0
-172.5
-173.0
-175.0
-185.0
-20
0
20
40
60
80
100
120
140
σ (ppm from liquid benzene)
XBL 765-1855

Figure 21

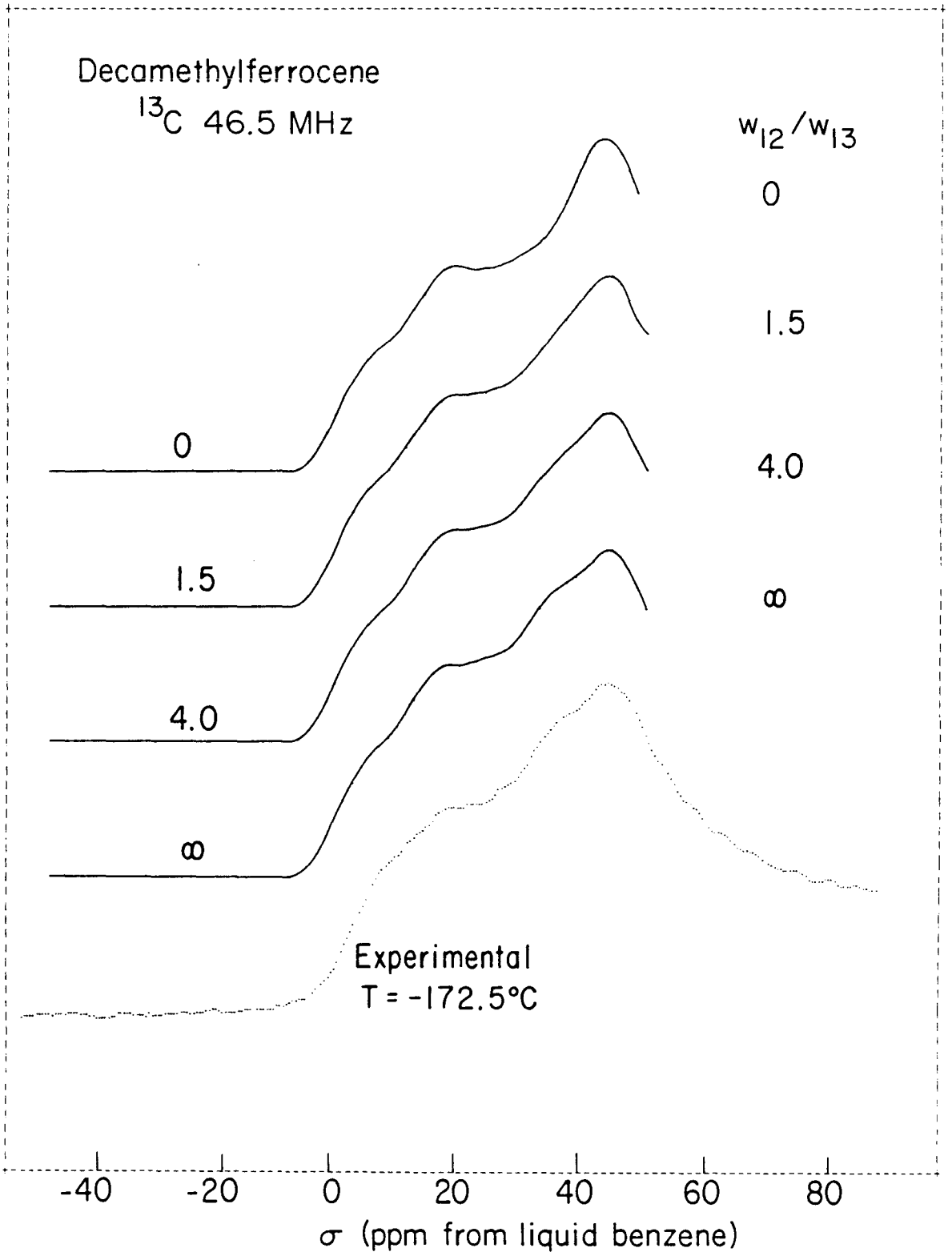

NBL 765-1854

Figure 22

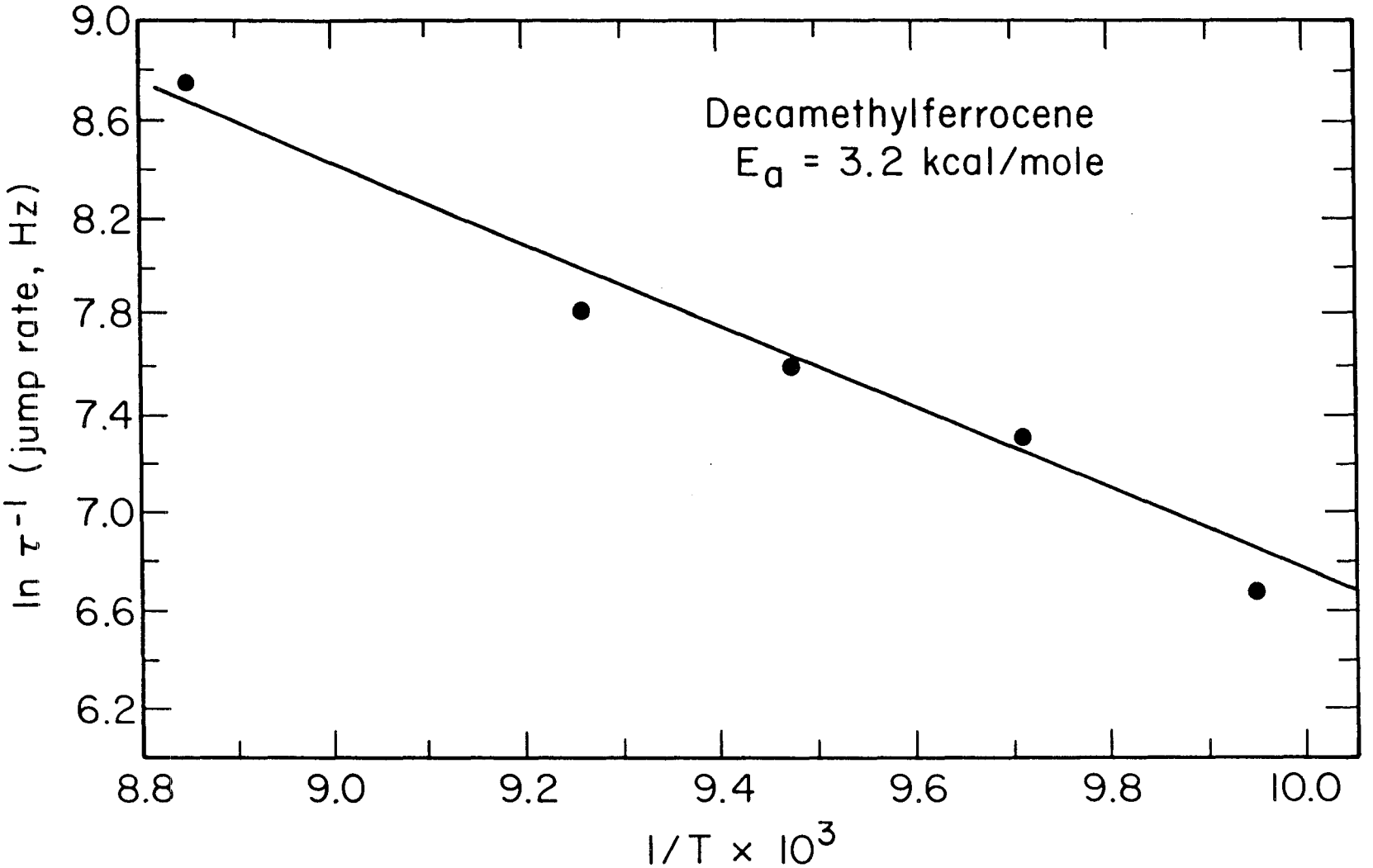

XBL 765-1857

Figure 23

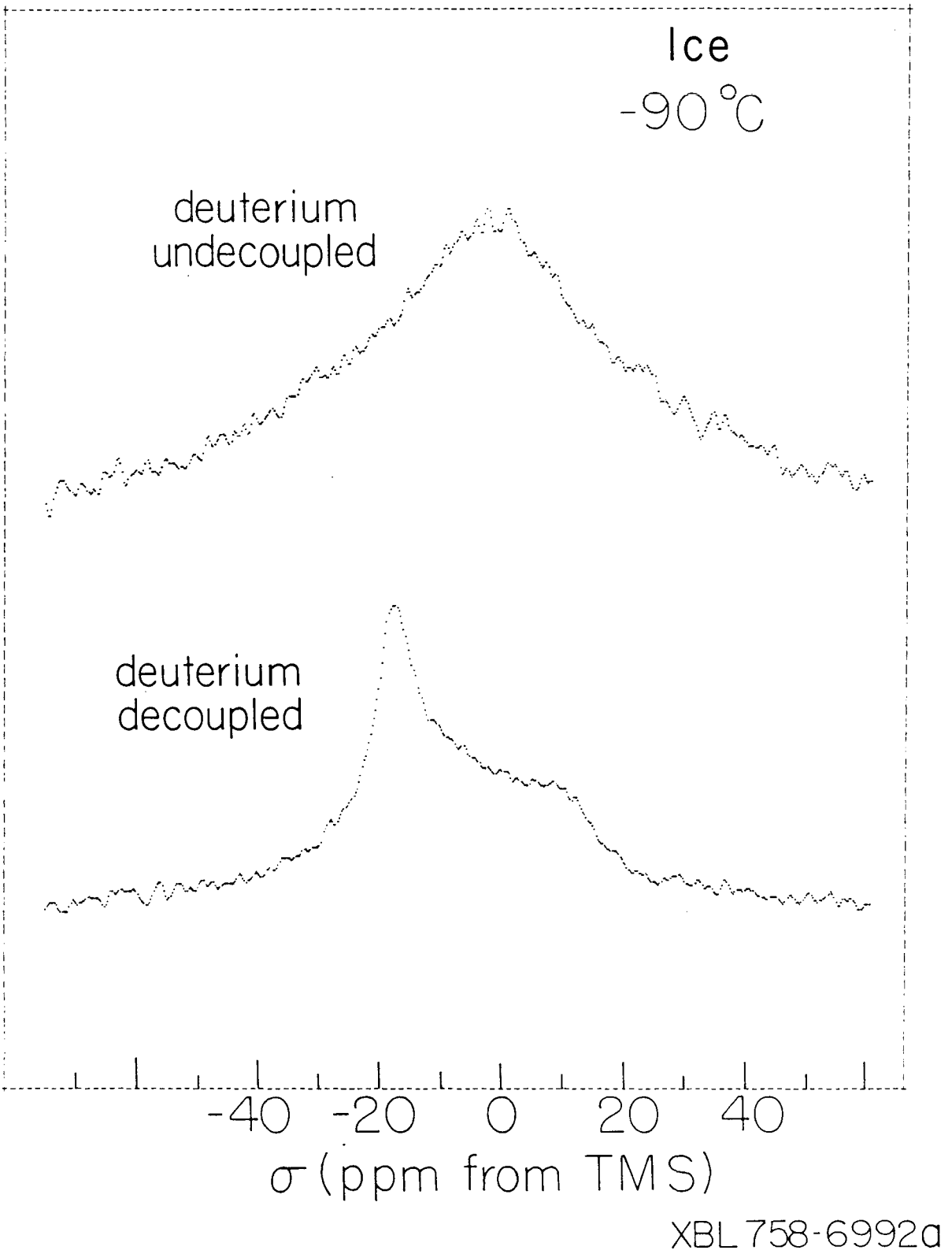
Ice
-90 °C
deuterium
undecoupled
deuterium
decoupled
-40
-20
0
20
40
σ (ppm from TMS)
XBL 758-6992a

Figure 24

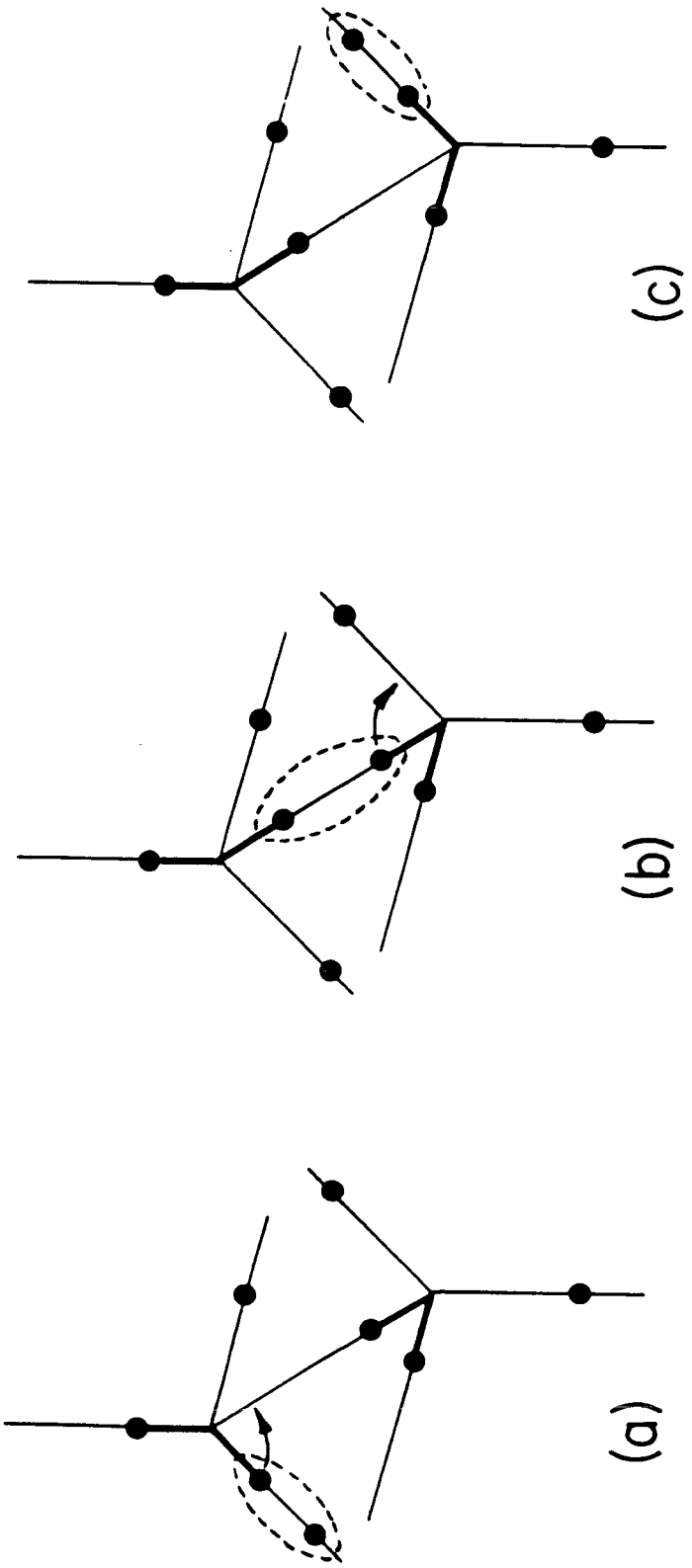

XBL 759-8287

Figure 25

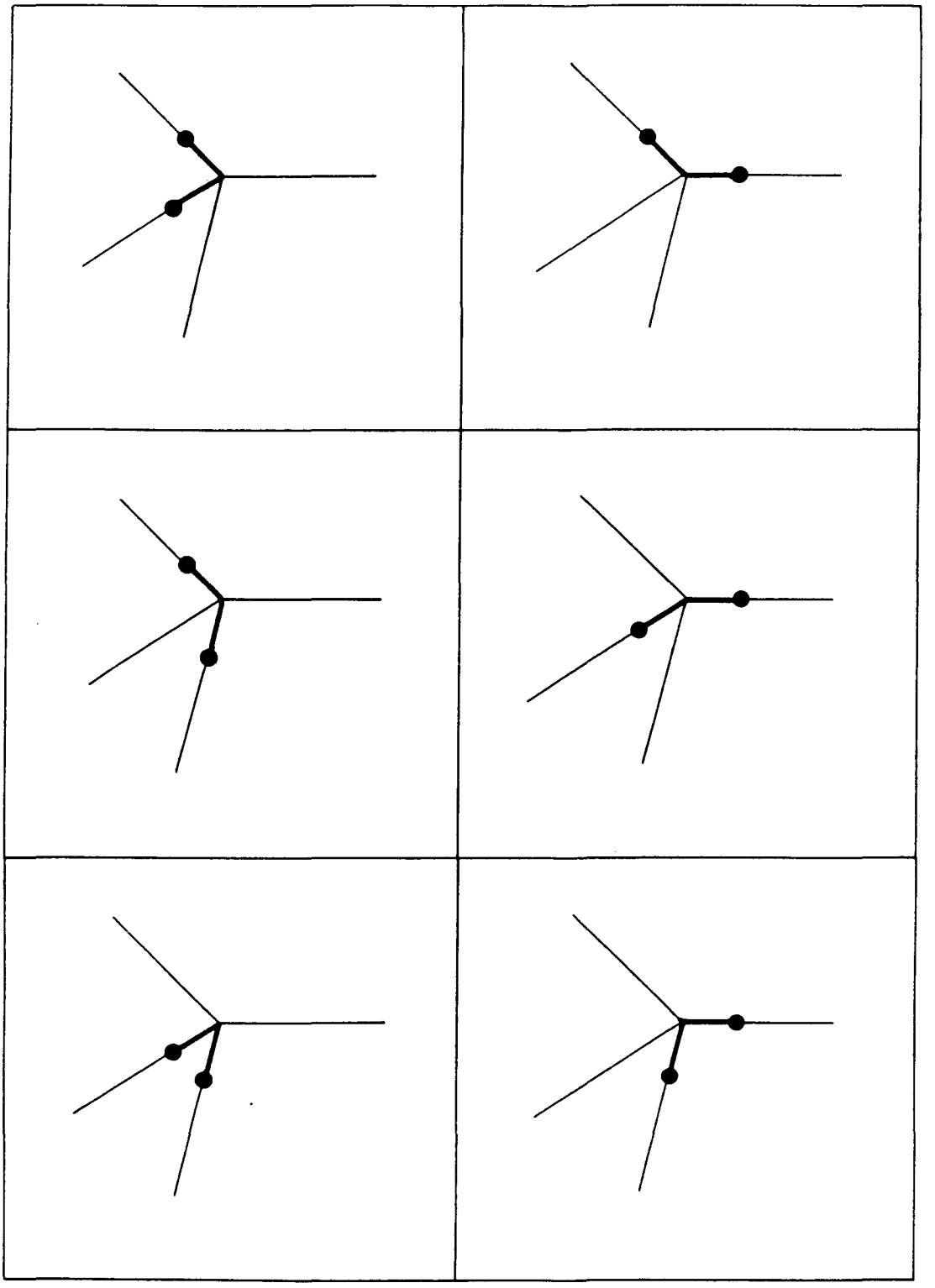

XBL 759-8288

Figure 26

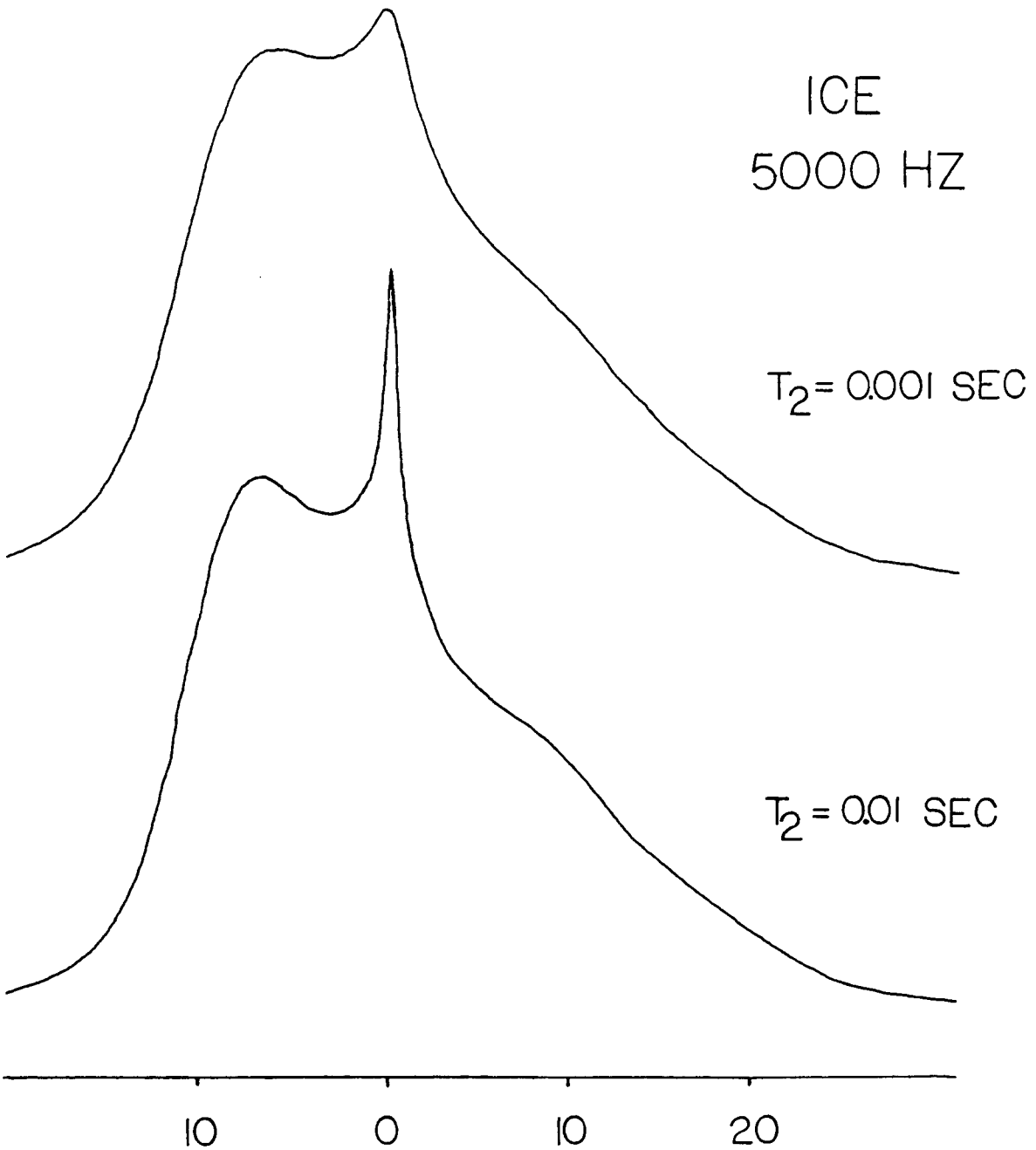

XBL 788-10123

Figure 27

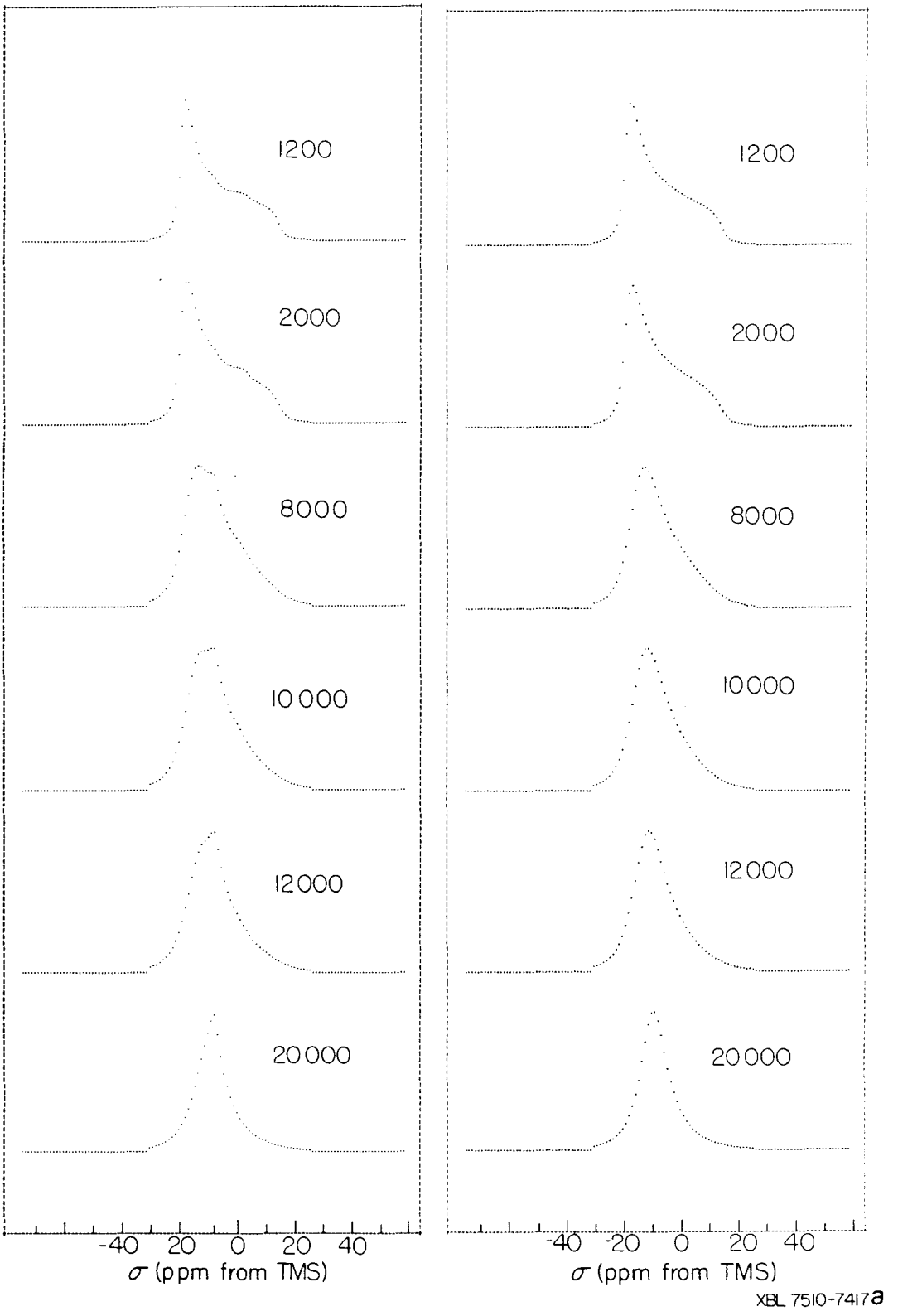
1200
2000
8000
10 000
12000
20000
-40 20 0 20 40
σ (ppm from TMS)
1200
2000
8000
10000
12000
20000
-40 -20 0 20 40
σ (ppm from TMS)
XBL 7510-7417a

Figure 28

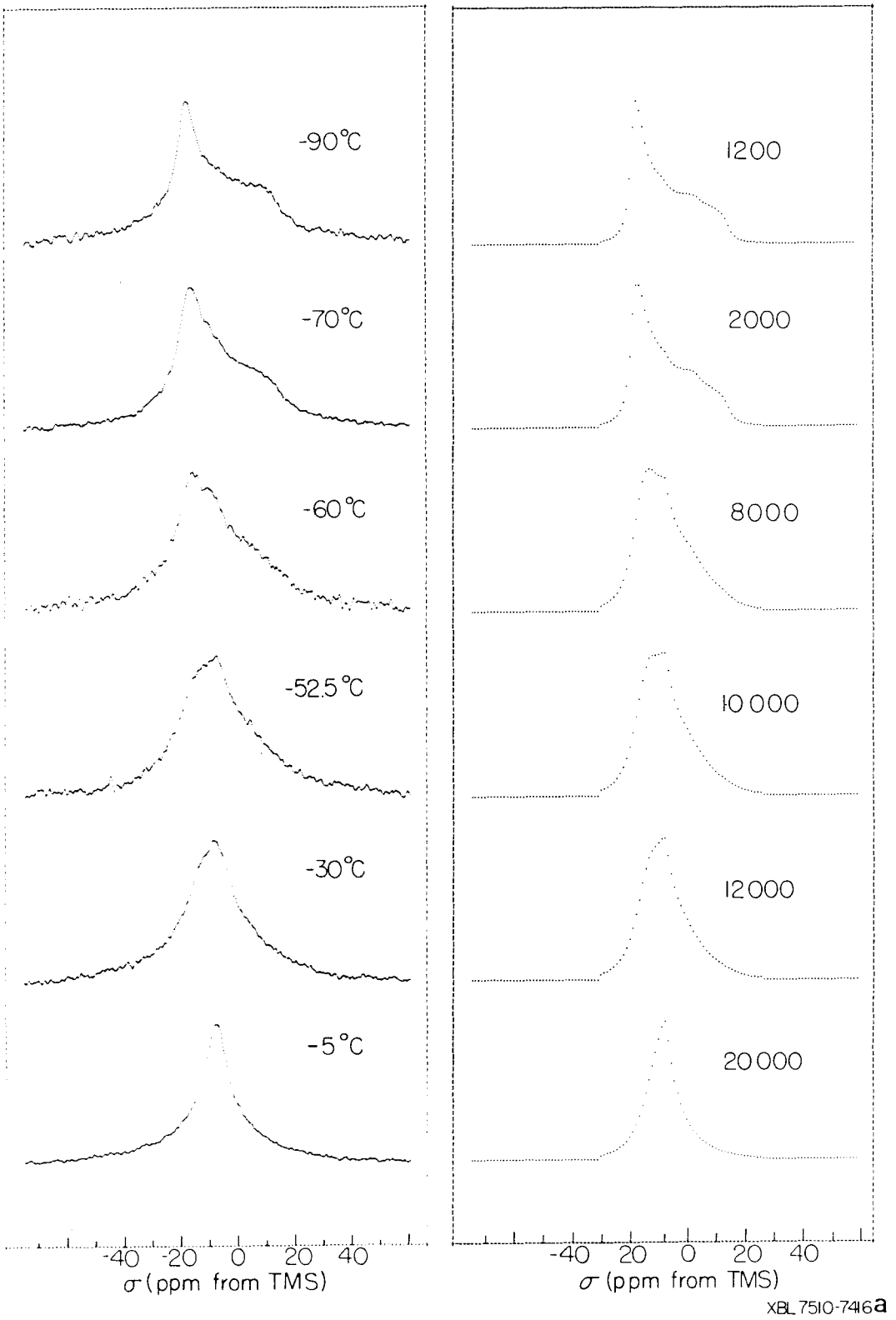
-90°C
-70°C
-60°C
-52.5°C
-30°C
-5°C
-40 -20 0 20 40
σ (ppm from TMS)
1200
2000
8000
10 000
12000
20000
-40 20 0 20 40
σ (ppm from TMS)
XBL 7510-7416a

Figure 29

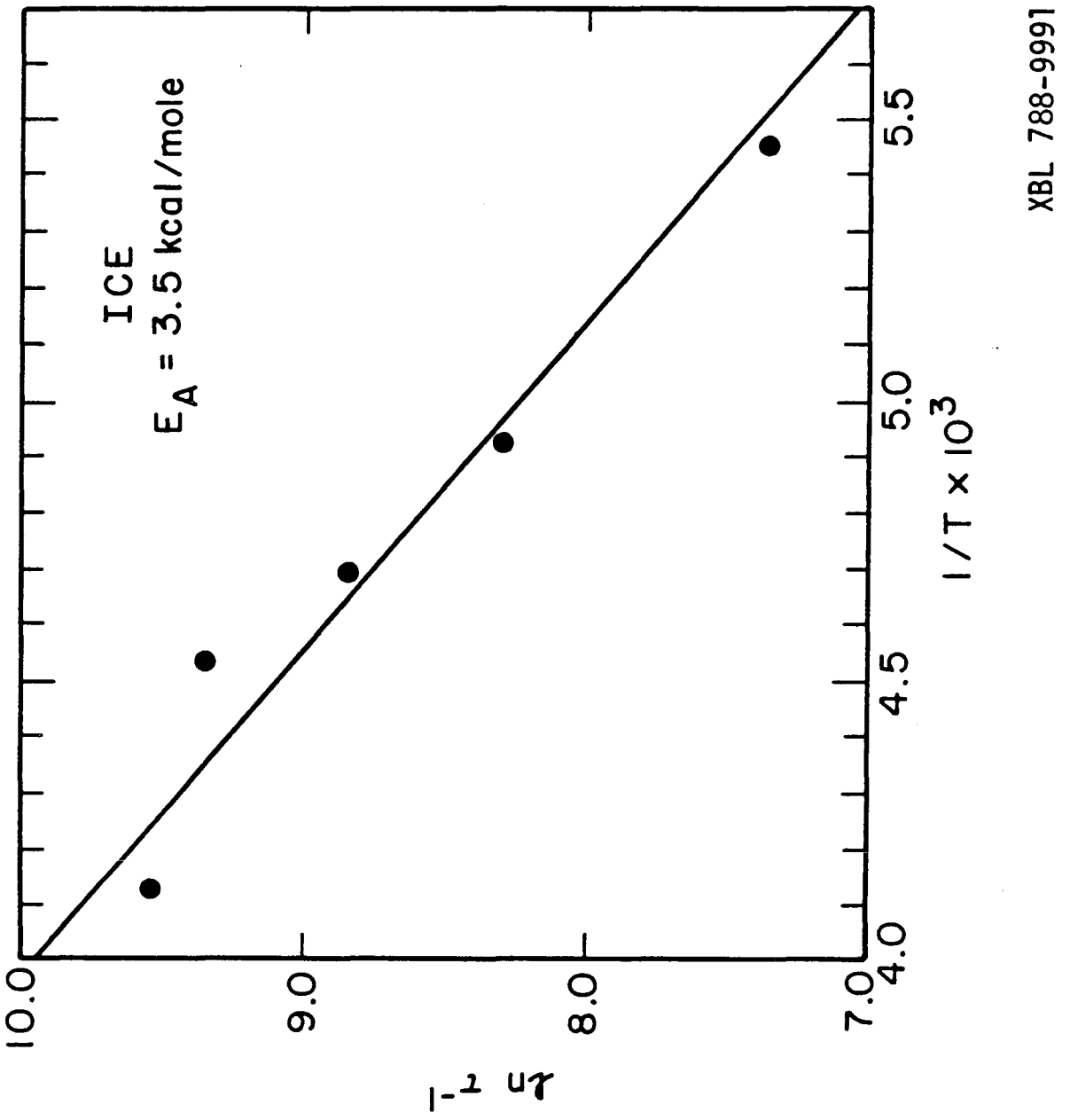
ICE
E_A = 3.5 kcal/mole
10.0
9.0
8.0
7.0
ln τ^{-1}
4.0
4.5
5.0
5.5
1/T × 10^3
XBL 788-9991

Figure 30

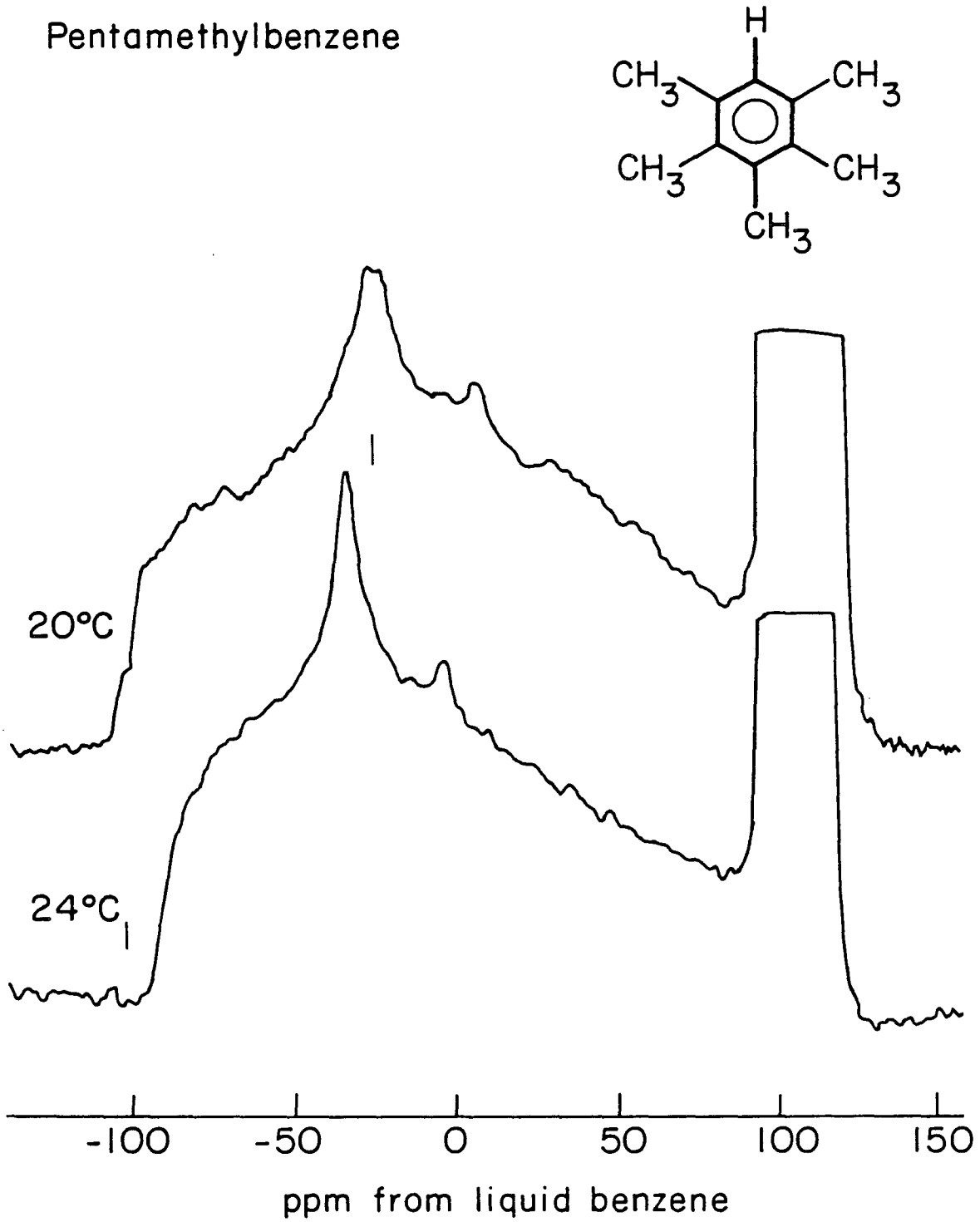

XBL 787-9789

Figure 30a

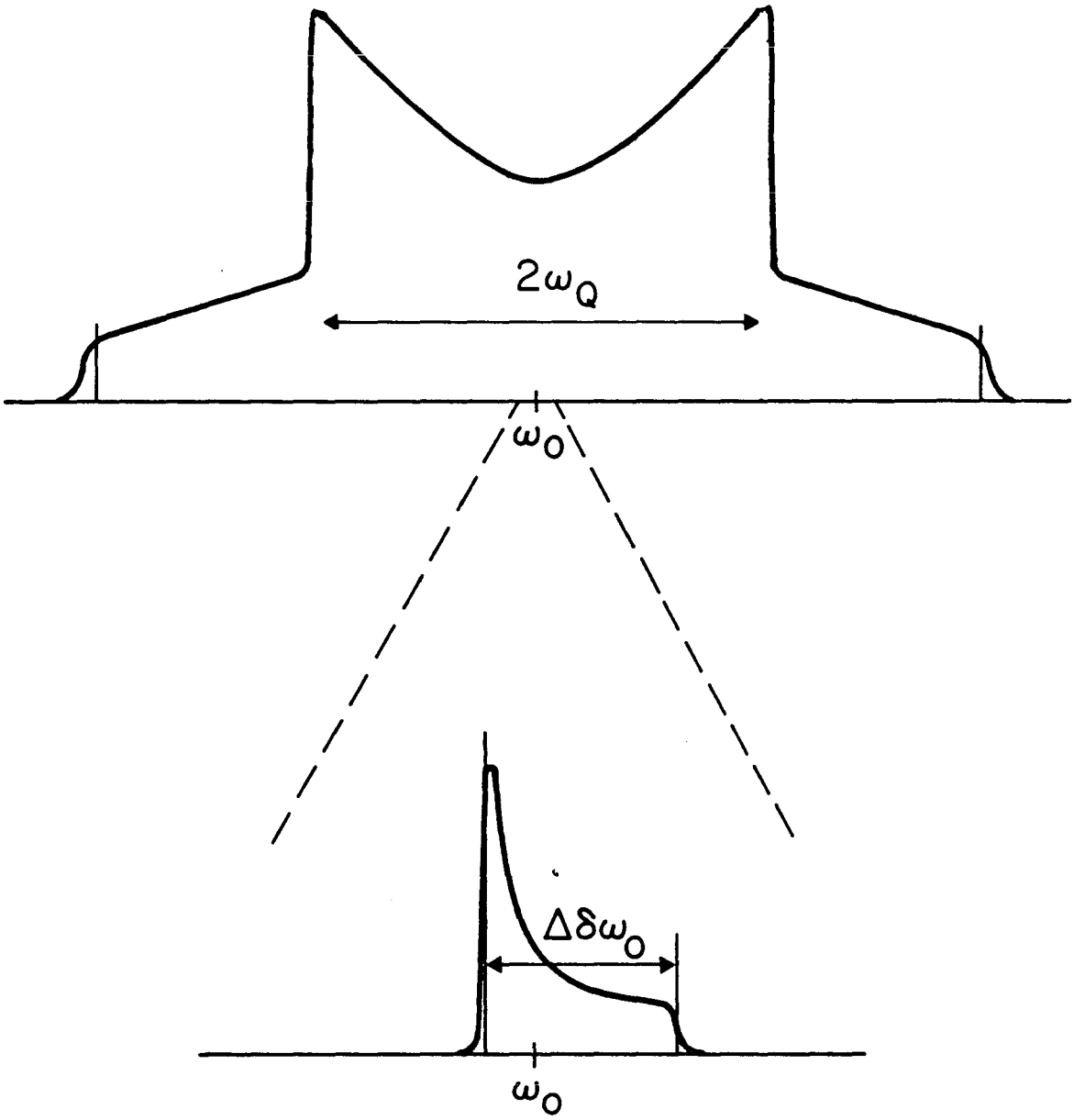

XBL 768-10182

Figure 31

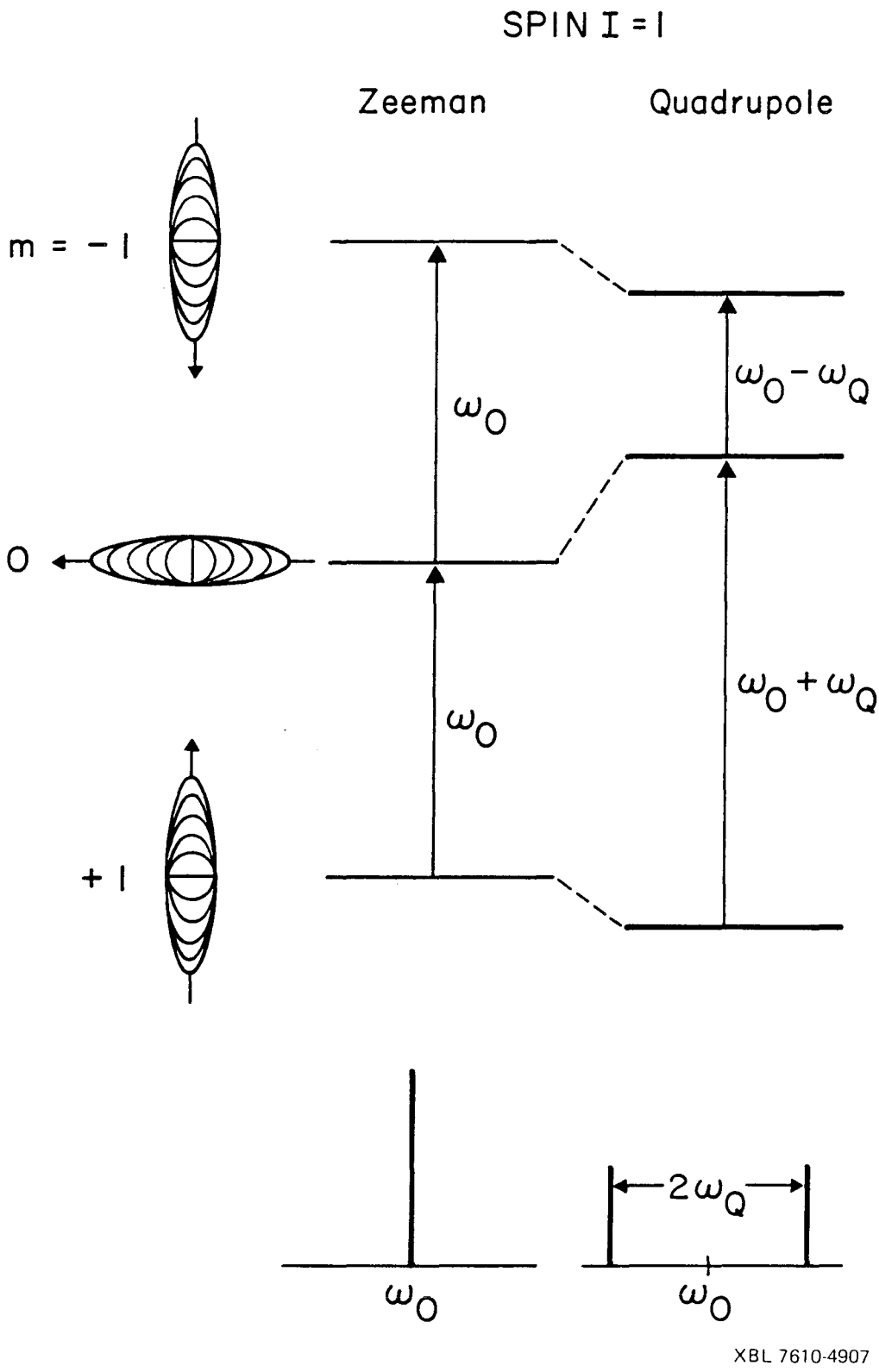
SPIN I = 1
Zeeman
Quadrupole
m = −1
0
+1
ω_0
ω_0
$\omega_0 - \omega_Q$
$\omega_0 + \omega_Q$
$2\omega_Q$
ω_0
ω_0
XBL 7610-4907

Figure 32

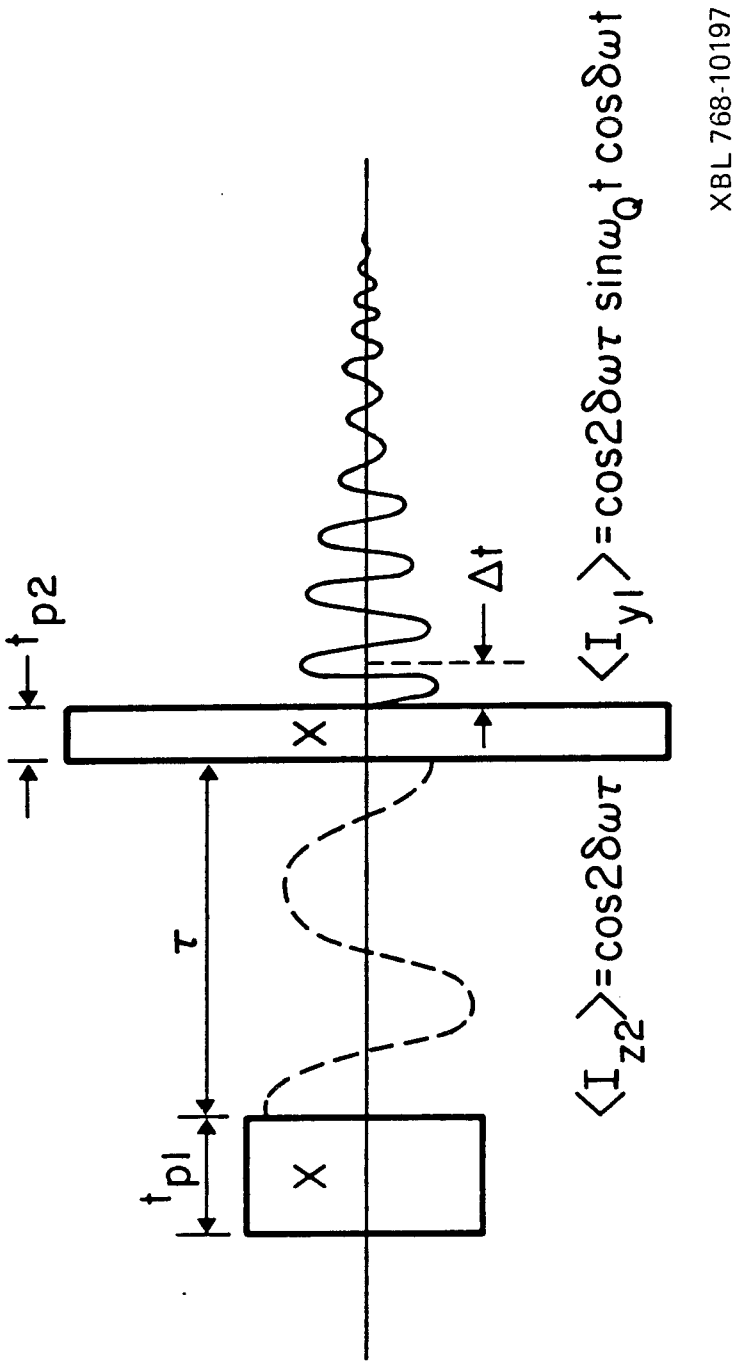
t_{p2}
t_{p1}
τ
Δt
$\langle I_{z2} \rangle = \cos 2\delta\omega\tau$
$\langle I_{y1} \rangle = \cos 2\delta\omega\tau \sin\omega_Q t \cos\delta\omega t$
XBL 768-10197

Figure 33

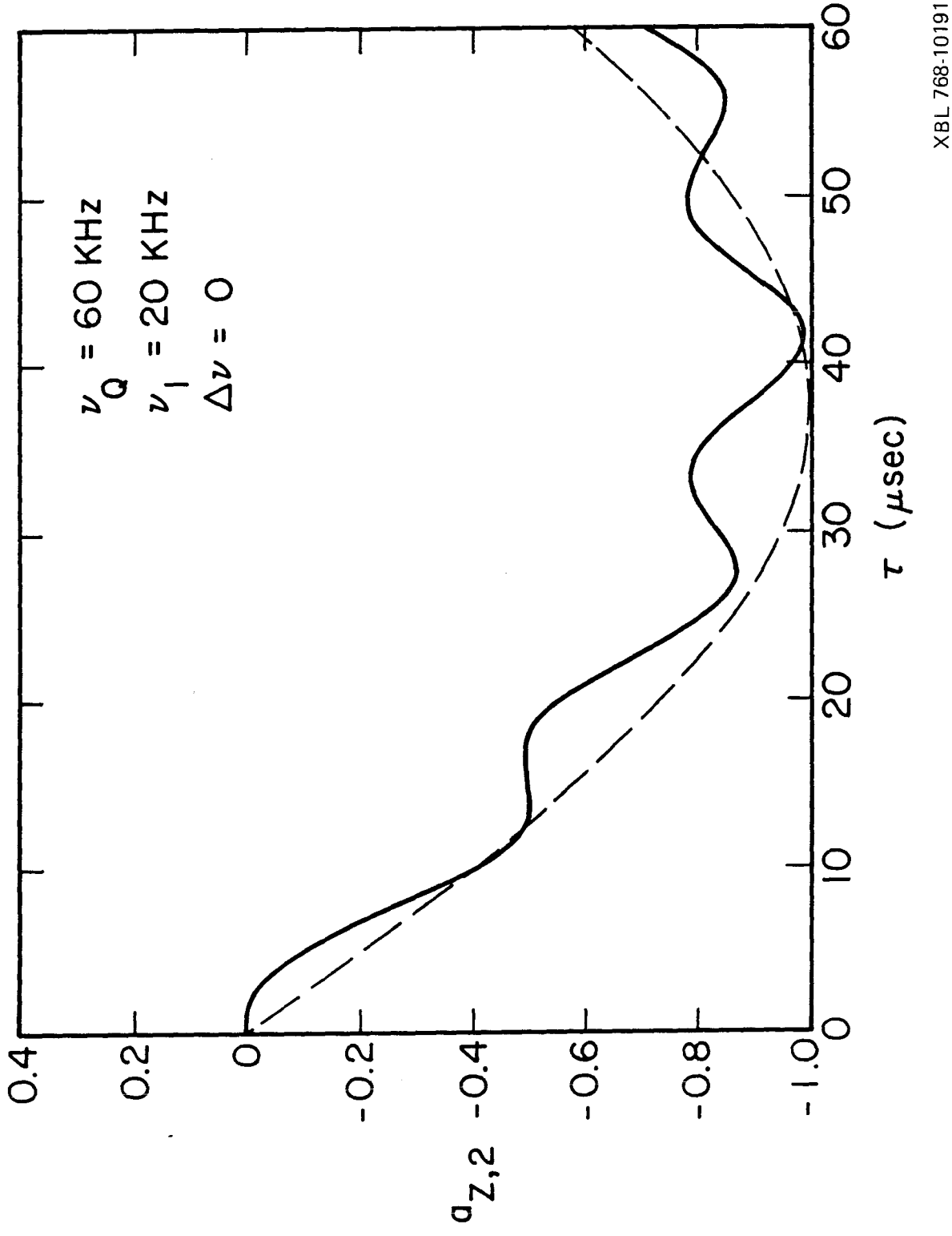

XBL 768-10191

Figure 34

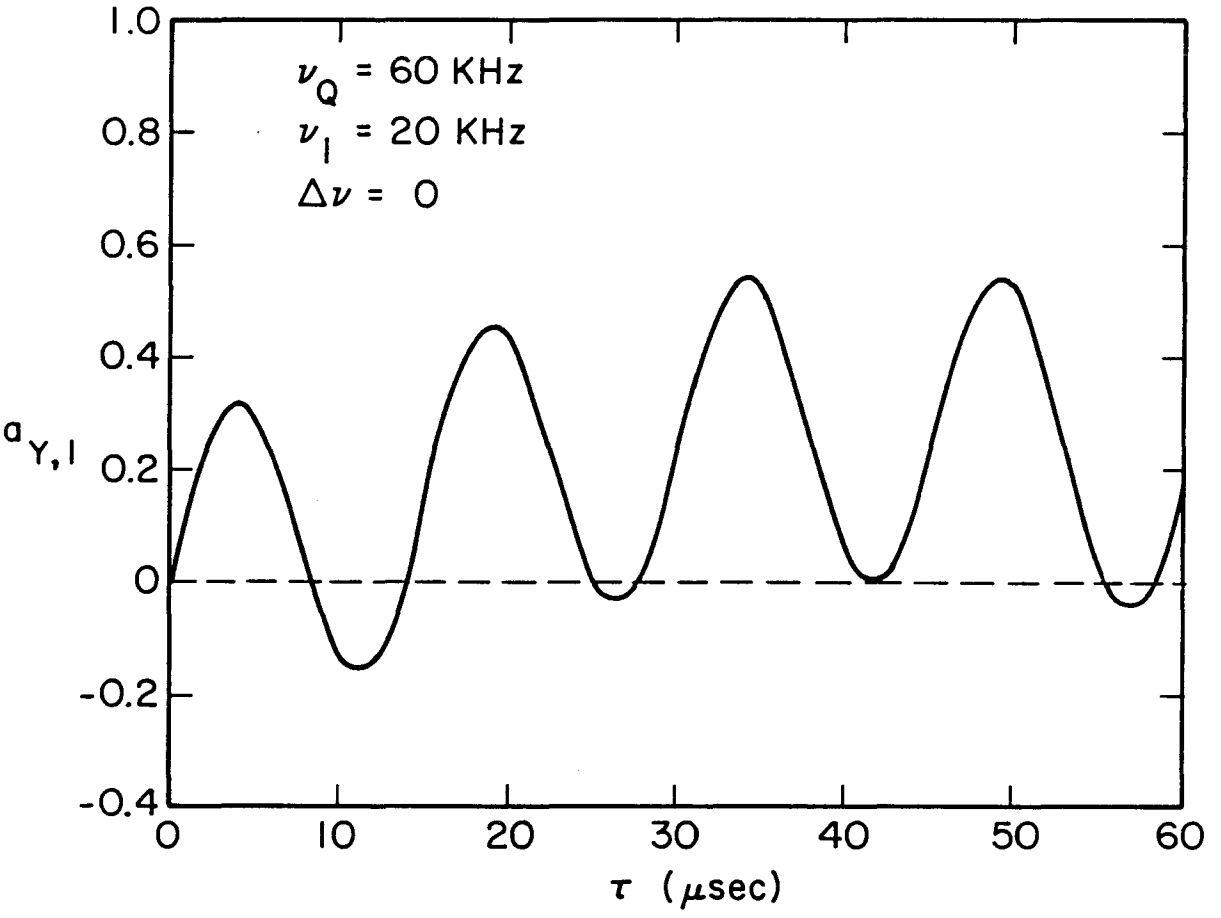

XBL 768-10213

Figure 35

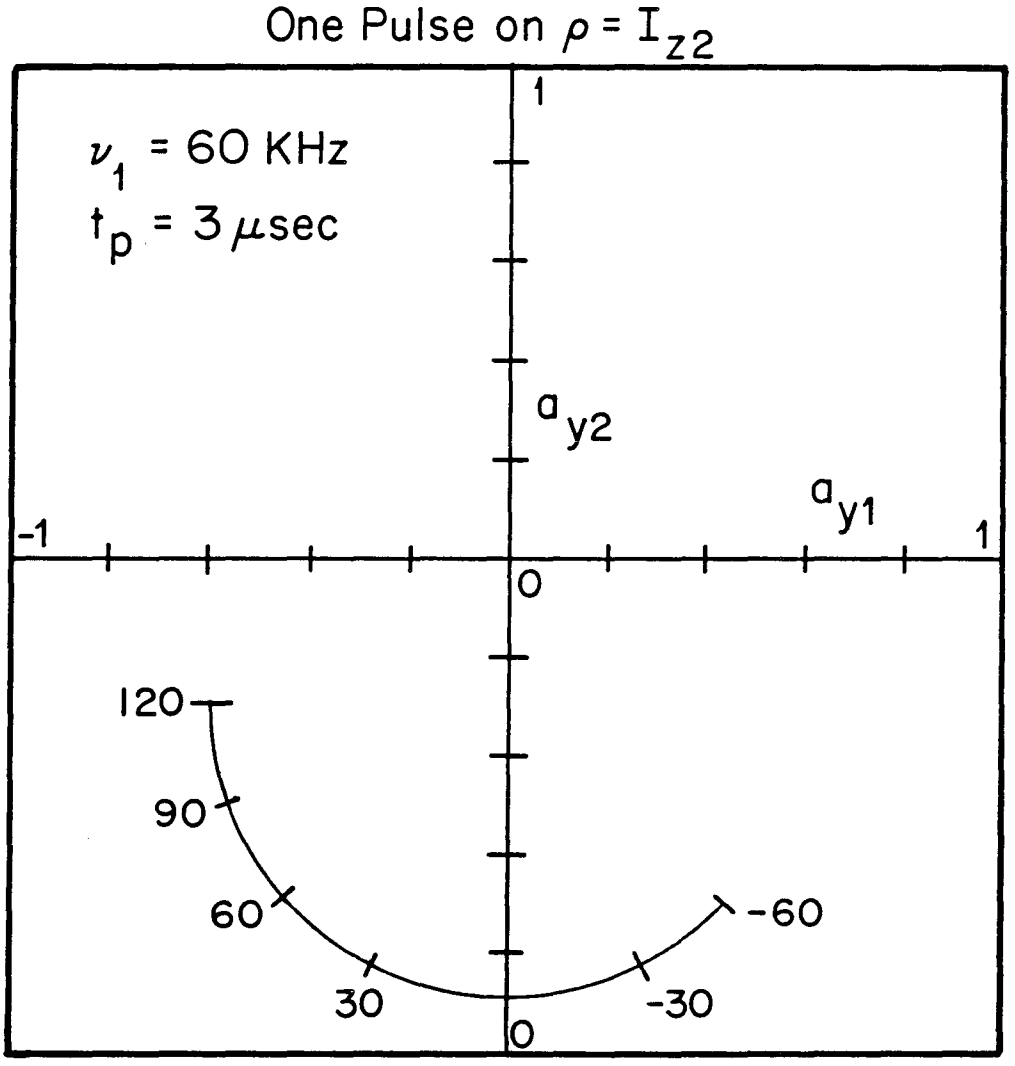

XBL 768-10212

Figure 36

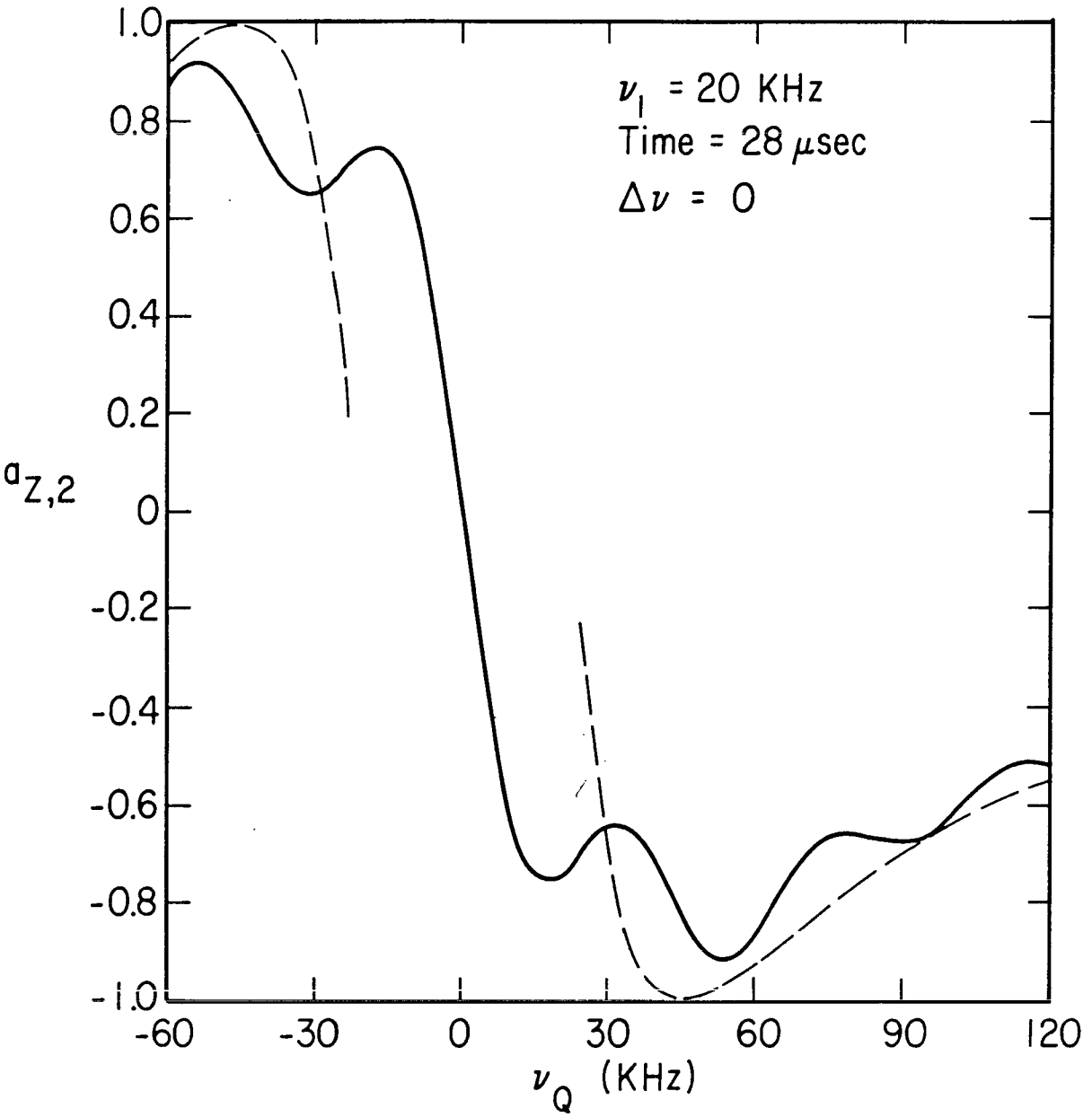

XBL 768-10189

Figure 37

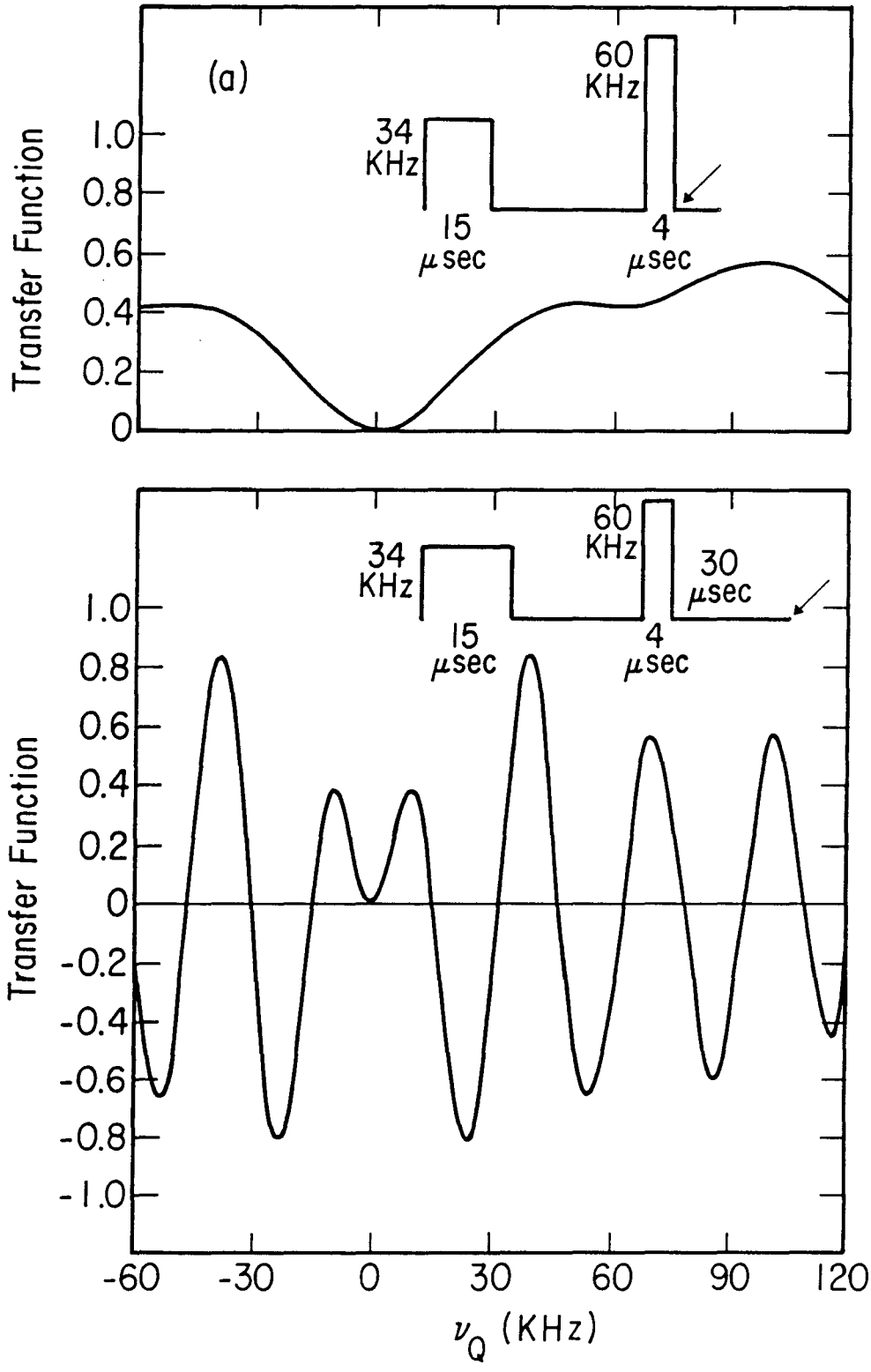

XBL 768-10184

Figure 38, 39

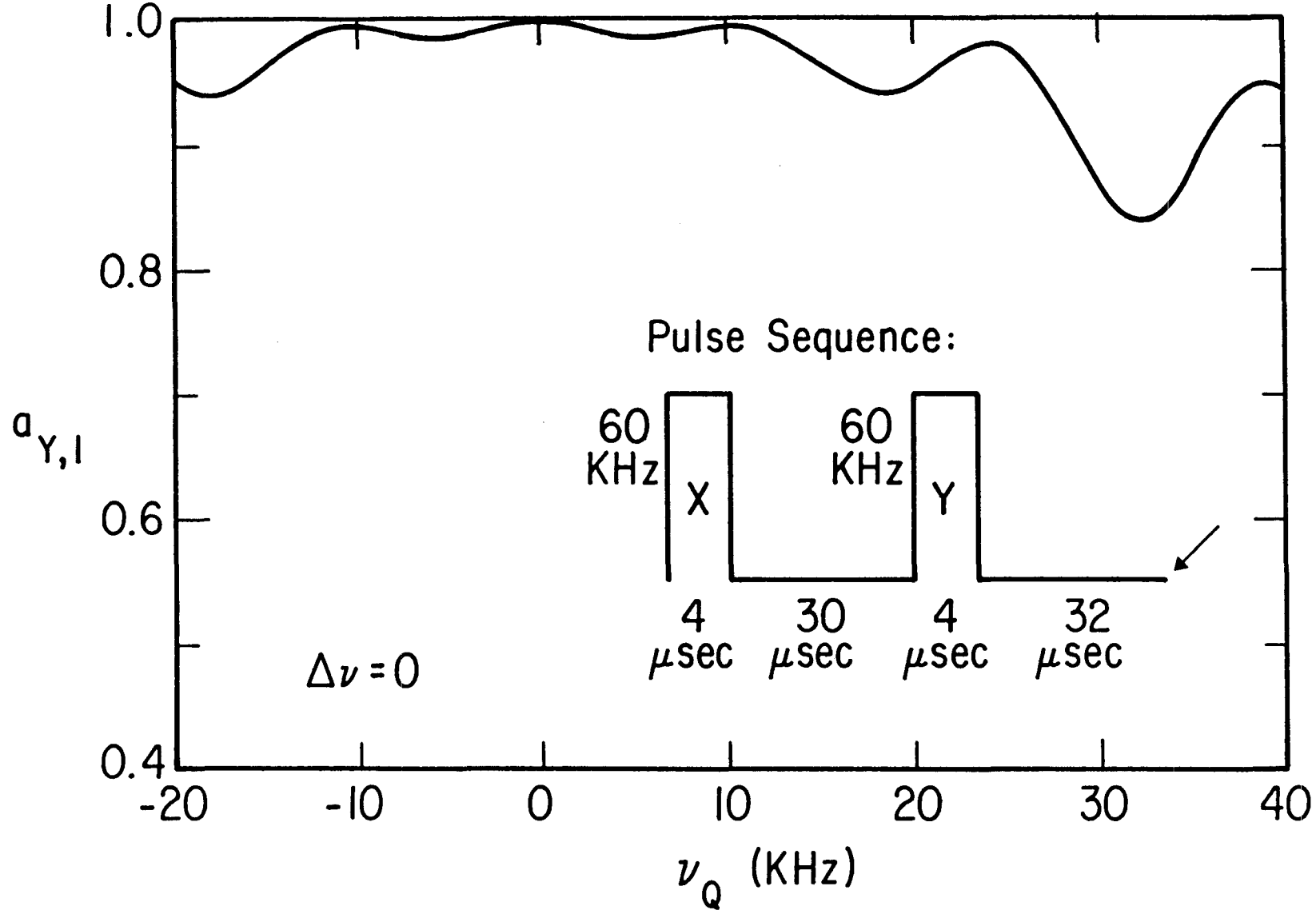

XBL 768-10186

Figure 40

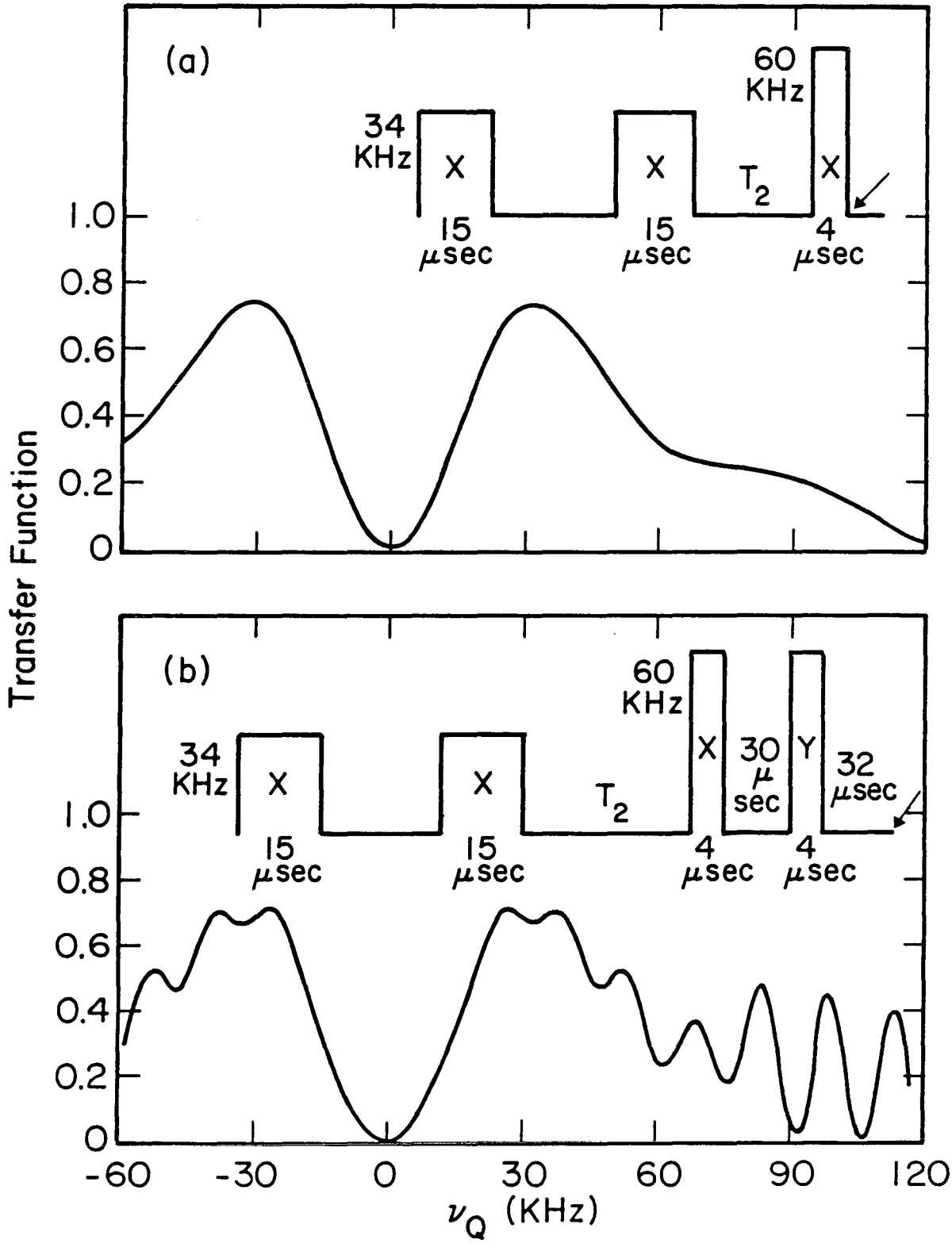

XBL 768-10208

Figure 41

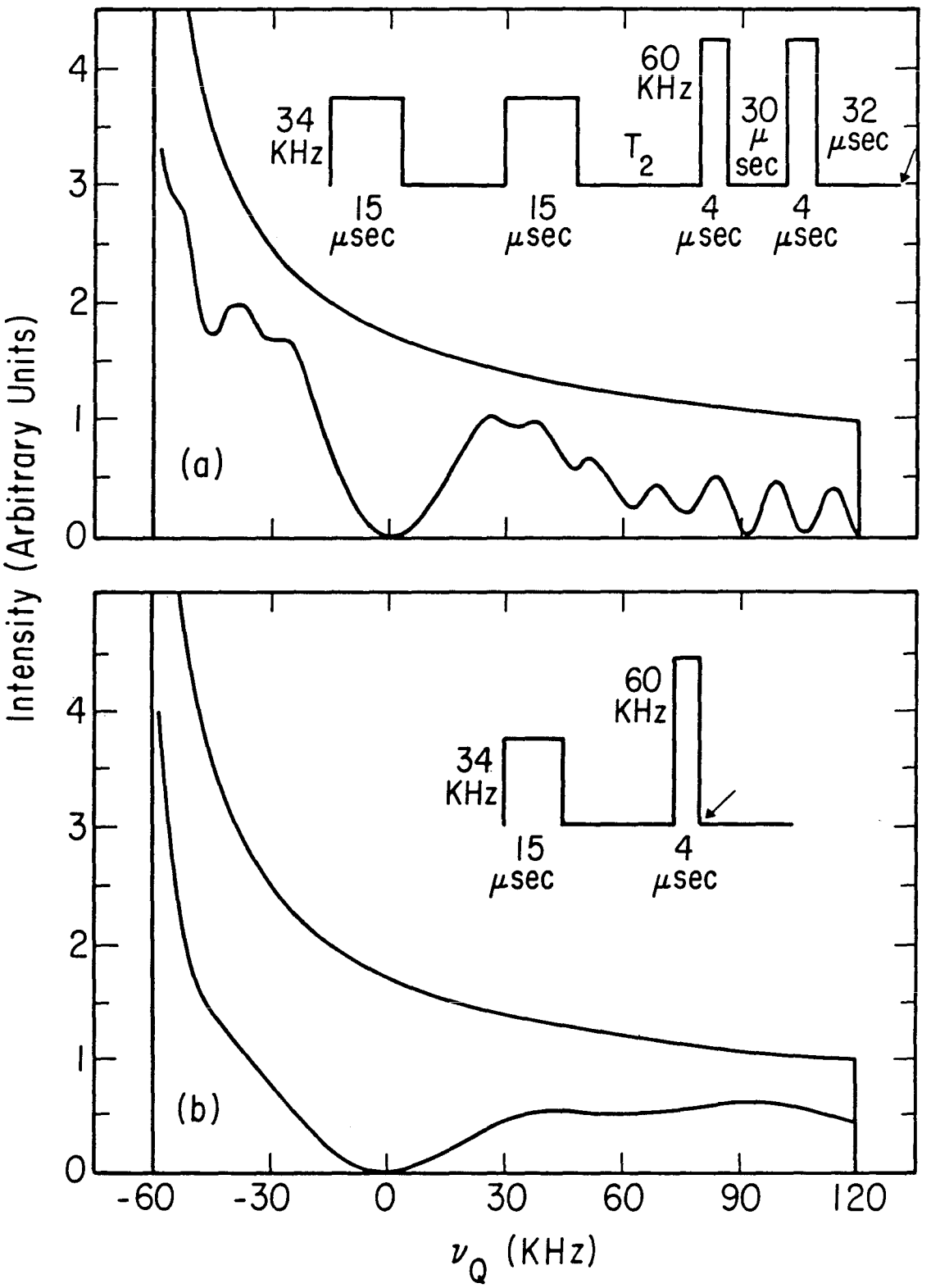

XBL 768-10209

Figure 42

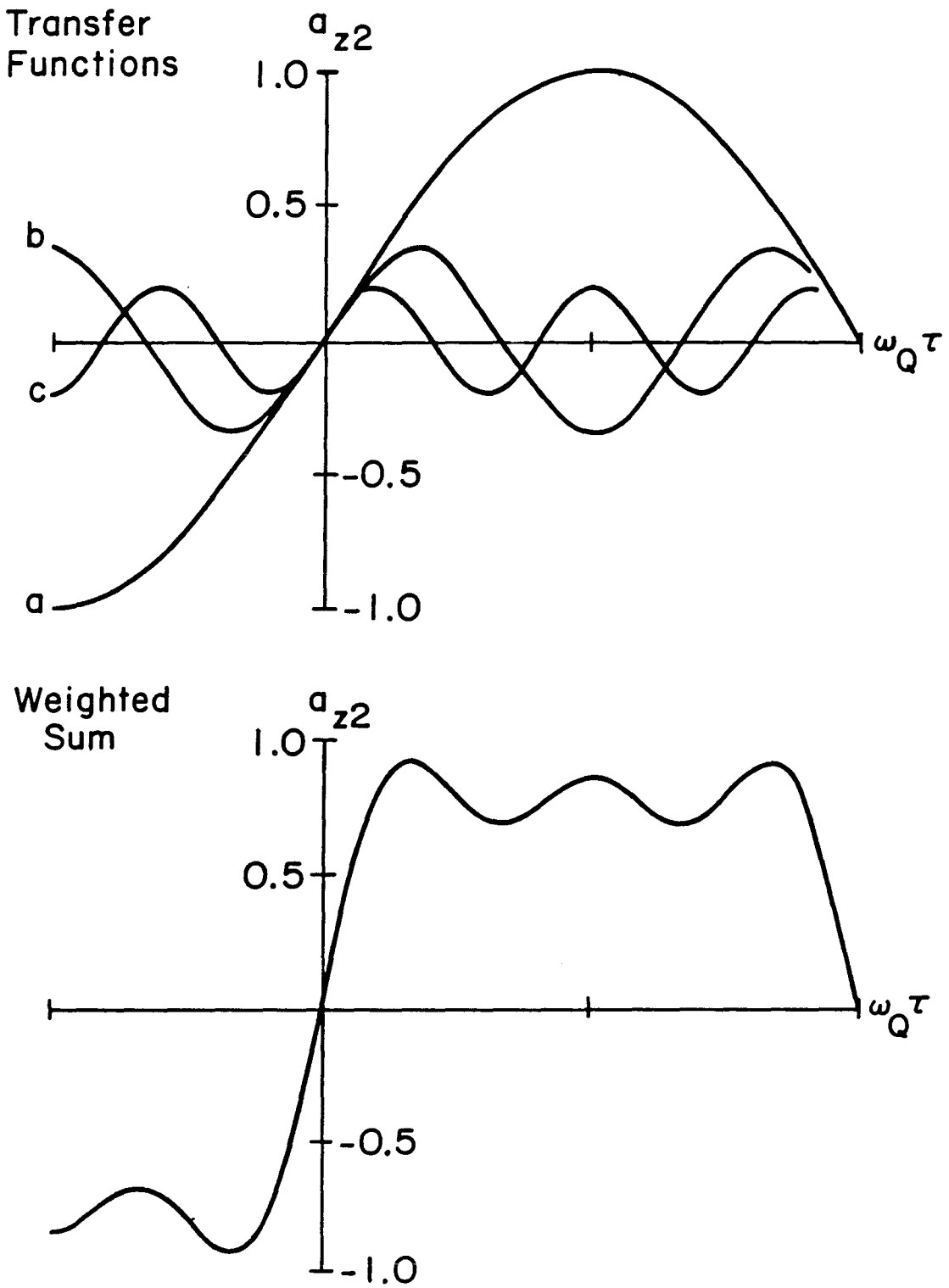
Transfer Functions
a_{z2}
1.0
0.5
-0.5
-1.0
b
c
a
$\omega_Q \tau$
Weighted Sum
a_{z2}
1.0
0.5
-0.5
-1.0
$\omega_Q \tau$
XBL 788-9988

Figure 43

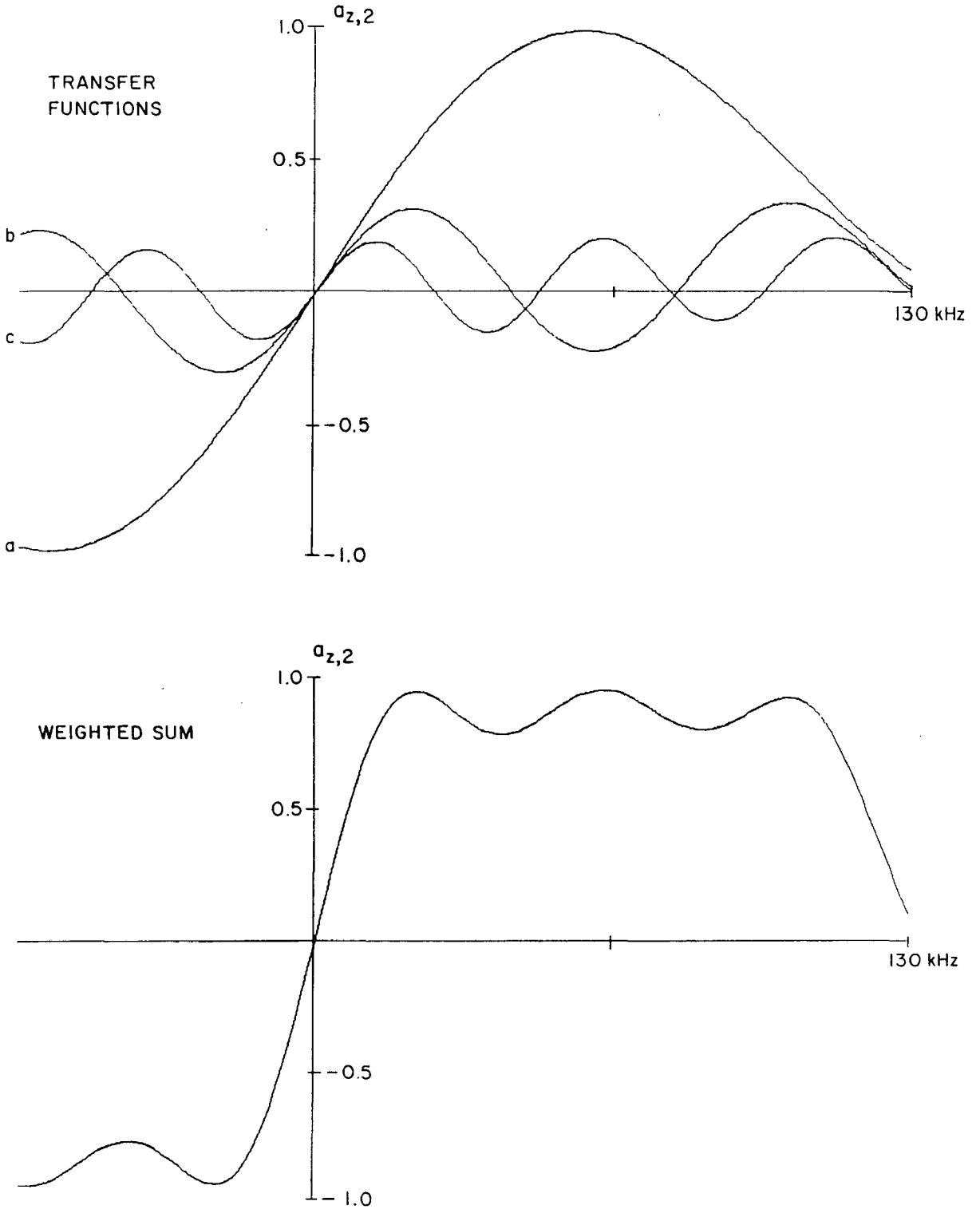

XBL 788-10111

Figure 44

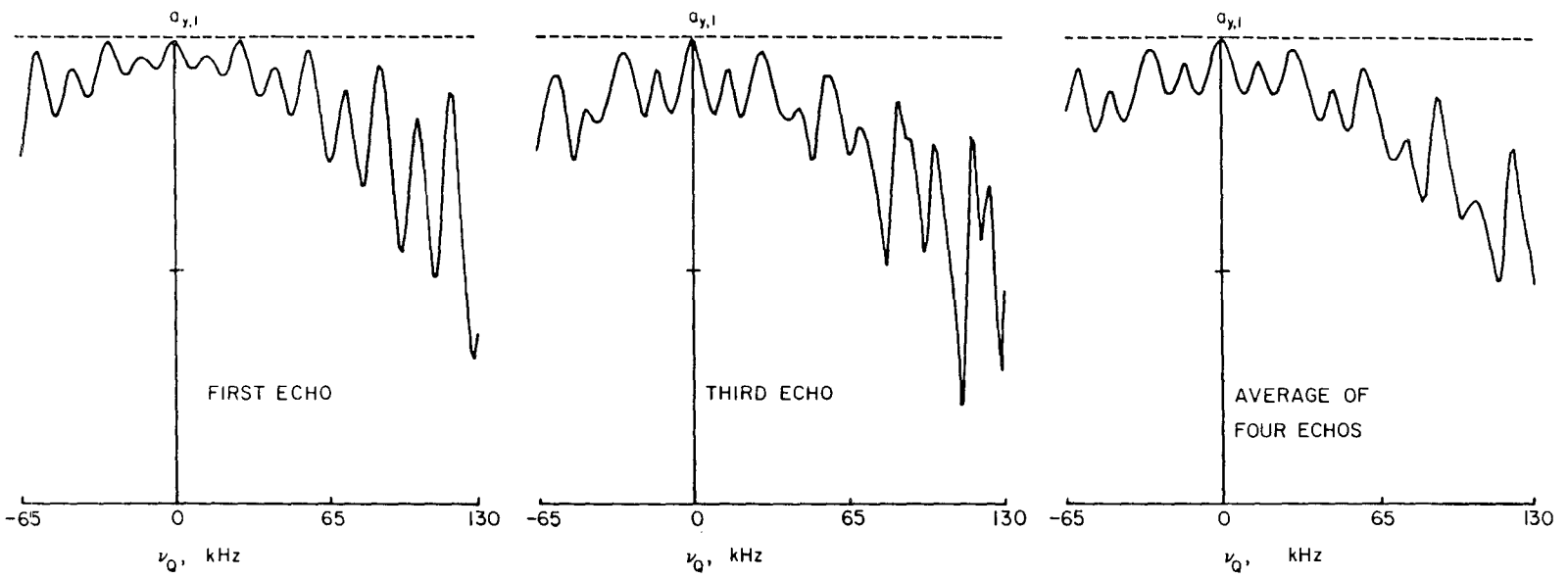

XBL 788-10116

Figure 45

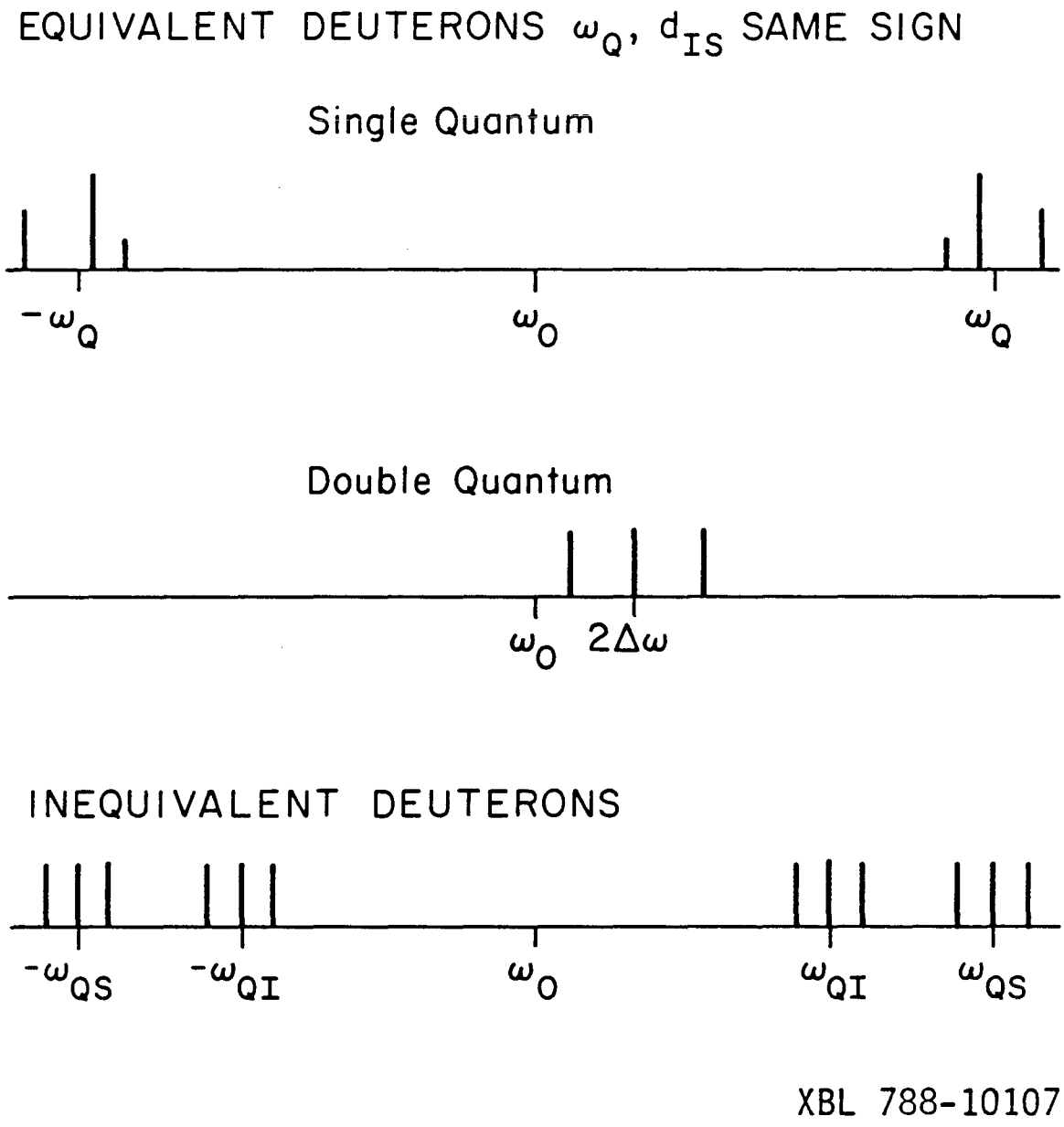

XBL 788-10107

Figure 46

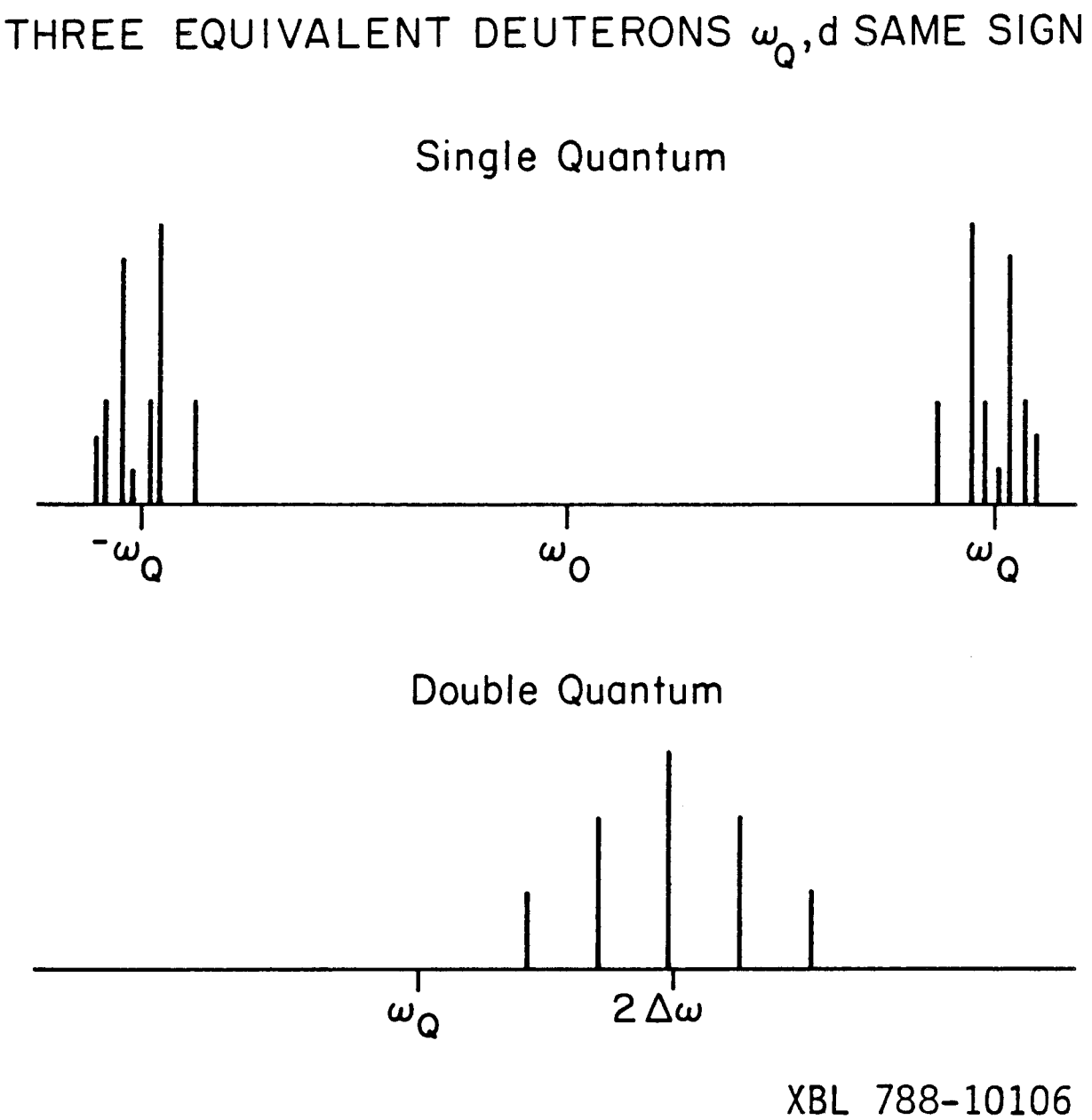
THREE EQUIVALENT DEUTERONS ω_Q, d SAME SIGN
Single Quantum
$-\omega_Q$
ω_0
ω_Q
Double Quantum
ω_Q
$2\Delta\omega$
XBL 788-10106

Figure 47

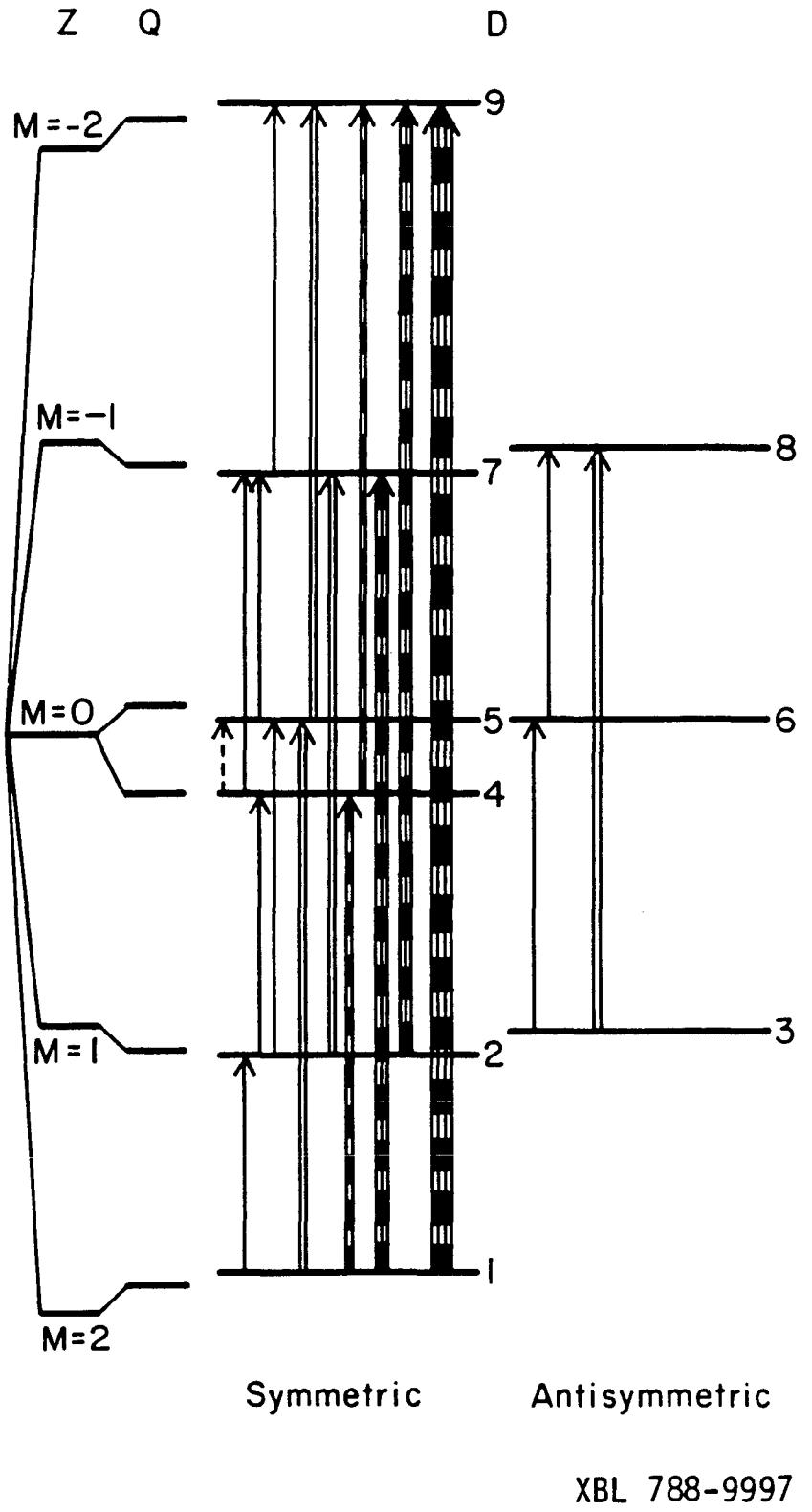
Z
Q
D
M=-2
M=-1
M=0
M=1
M=2
9
7
5
4
2
1
8
6
3
Symmetric
Antisymmetric
XBL 788-9997

Figure 48

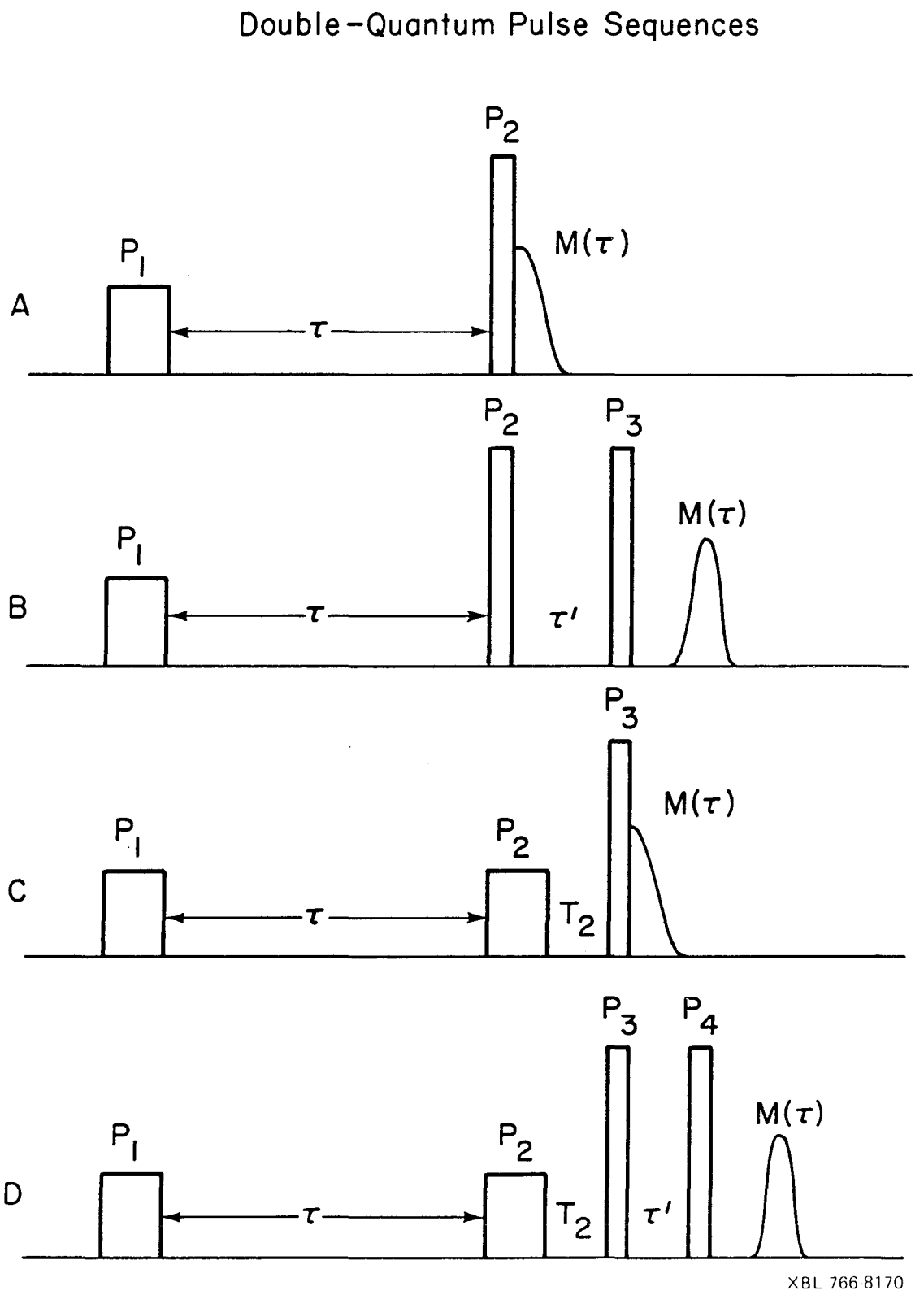
Double-Quantum Pulse Sequences
A
P1
P2
M(τ)
τ
B
P1
P2
P3
M(τ)
τ
τ'
C
P1
P2
P3
M(τ)
τ
T2
D
P1
P2
P3
P4
M(τ)
τ
T2
τ'
XBL 766-8170

Figure 49

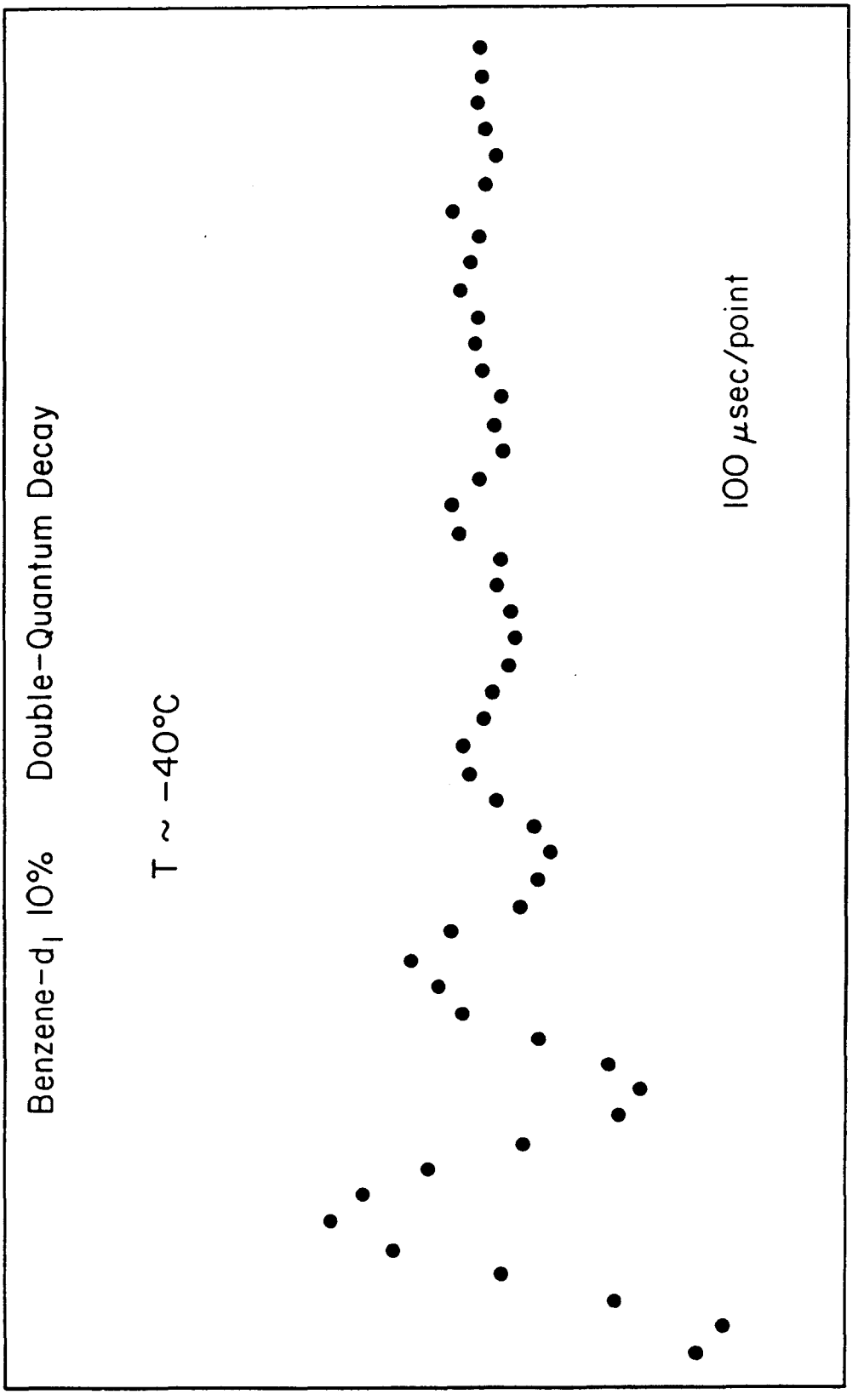

XBL 764-1090

Figure 50

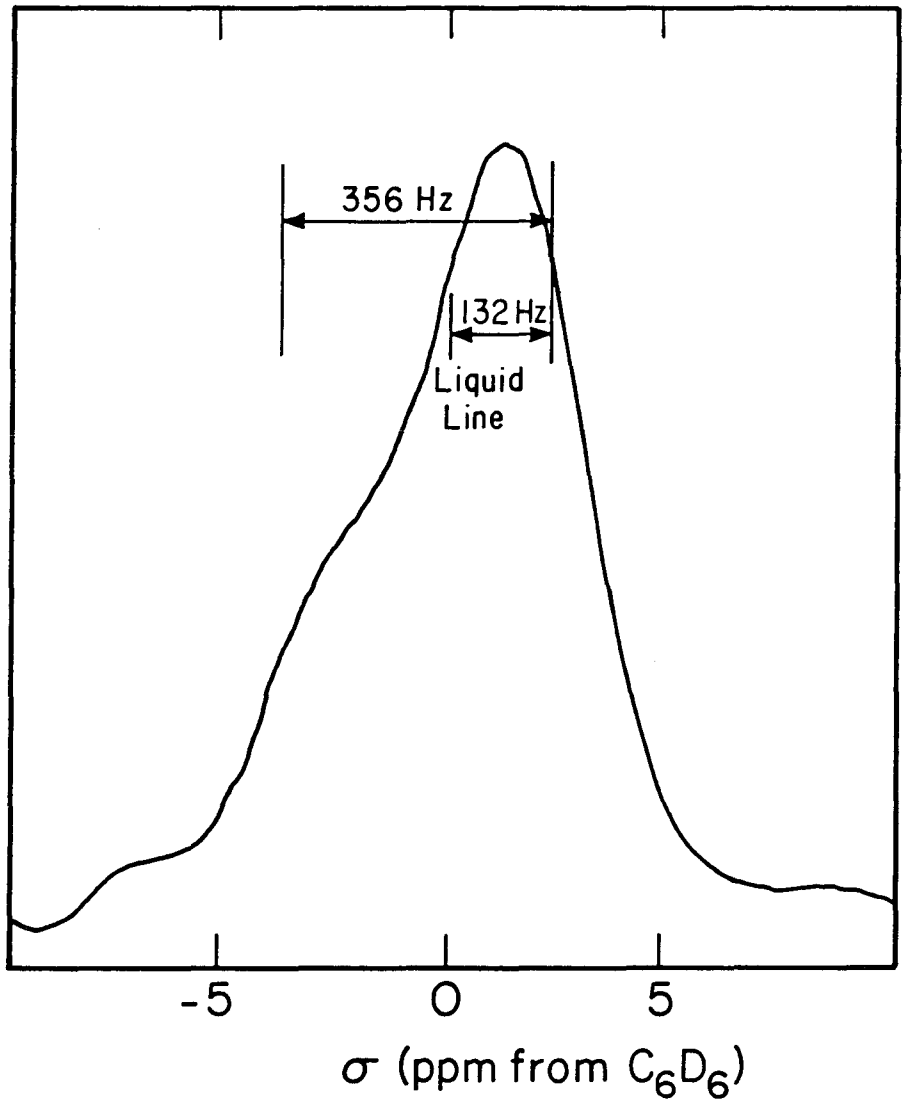

XBL 764-1092

Figure 51

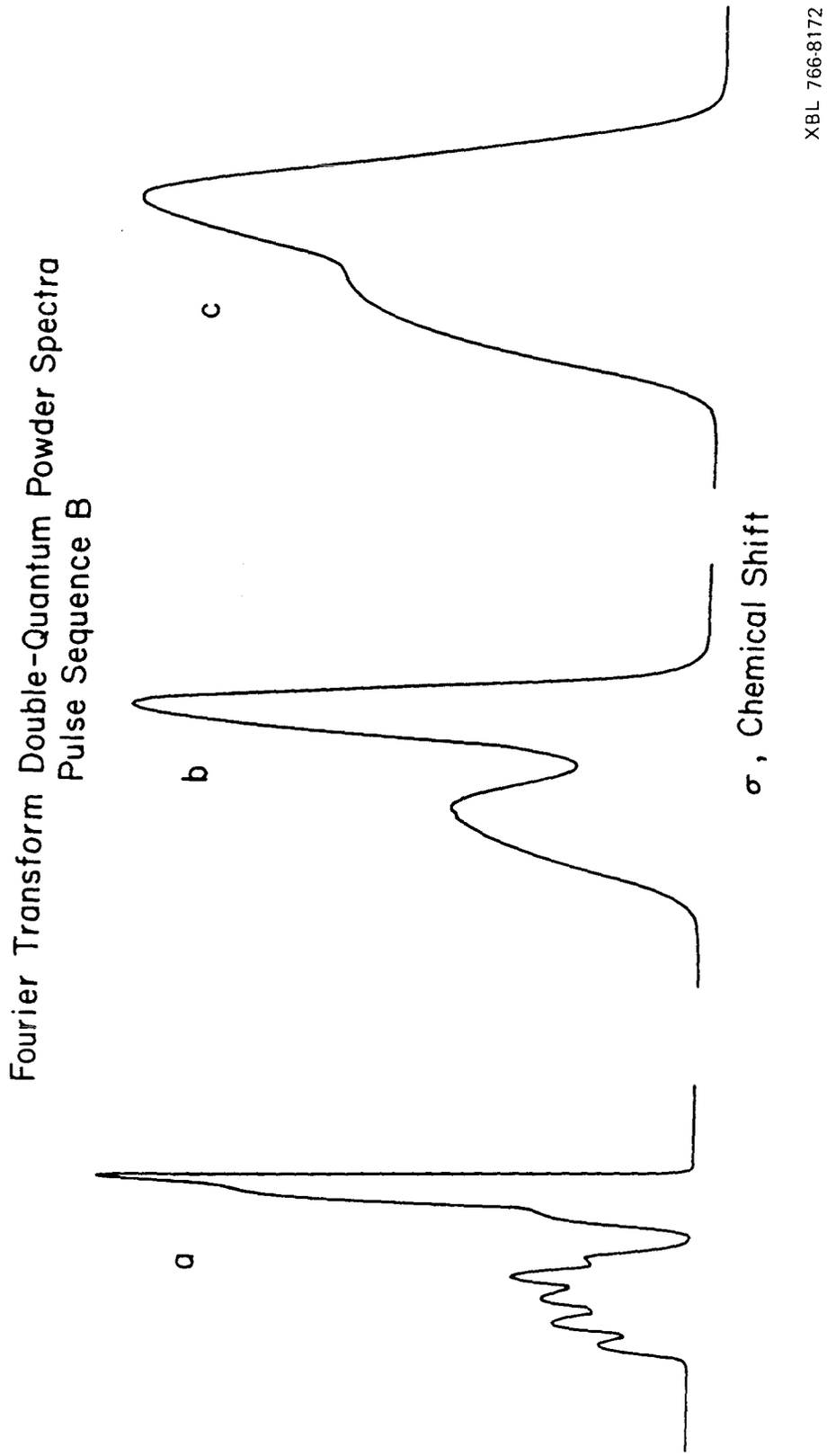
Fourier Transform Double-Quantum Powder Spectra
Pulse Sequence B
a
b
c
σ , Chemical Shift
XBL 766-8172

Figure 52

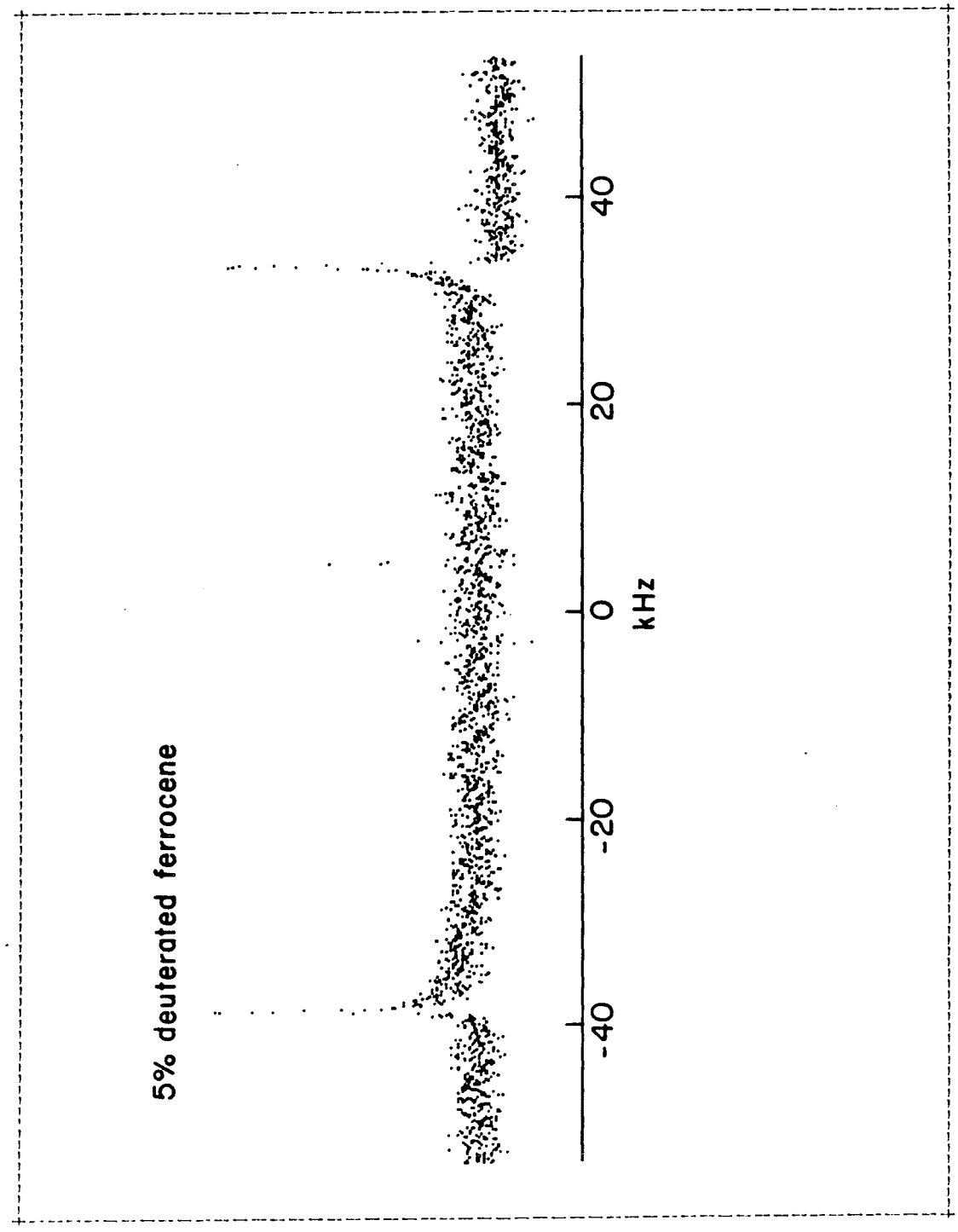

XBL 788-10000

Figure 53

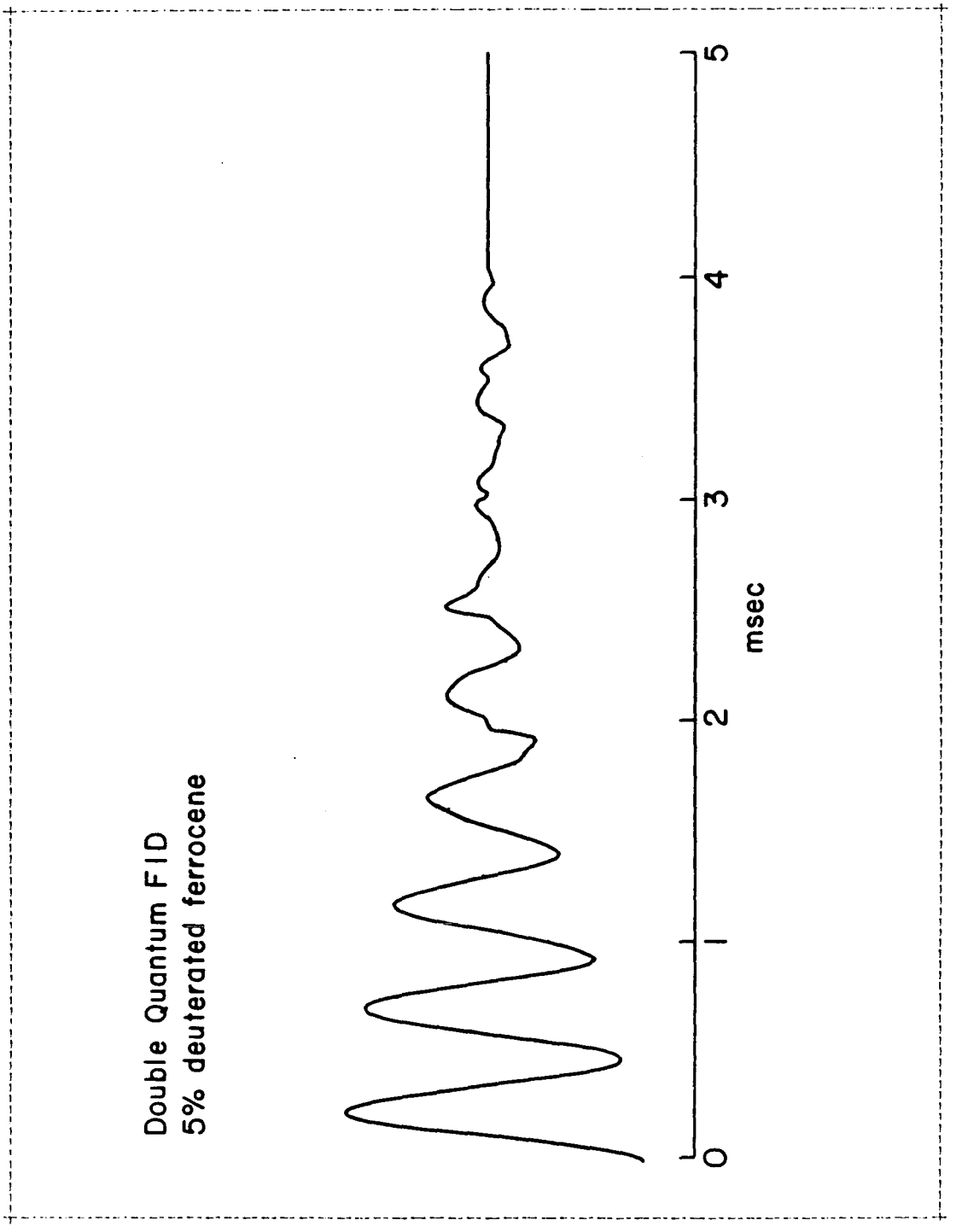

XBL 788-10001

Figure 54

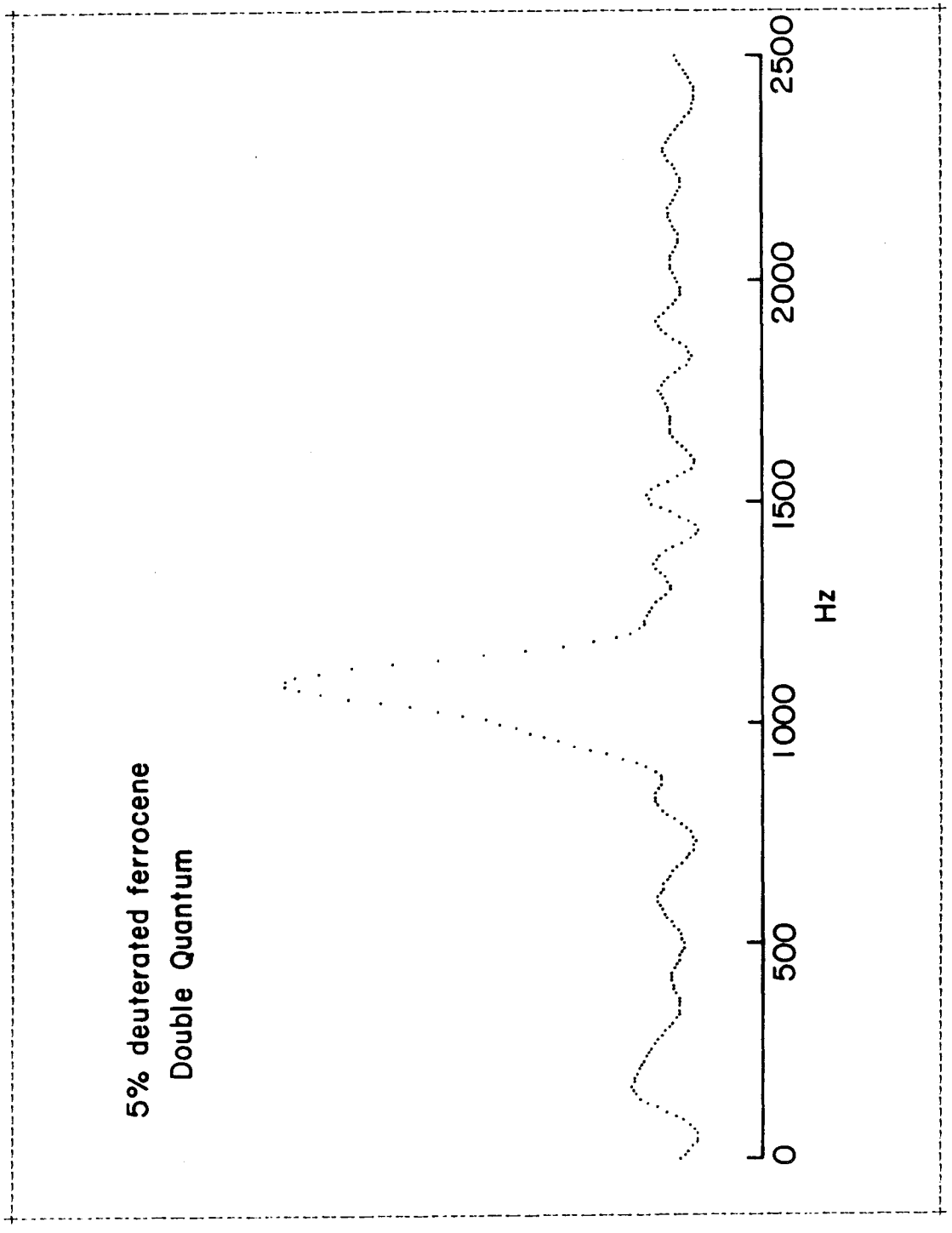

XBL 788-9987

Figure 55

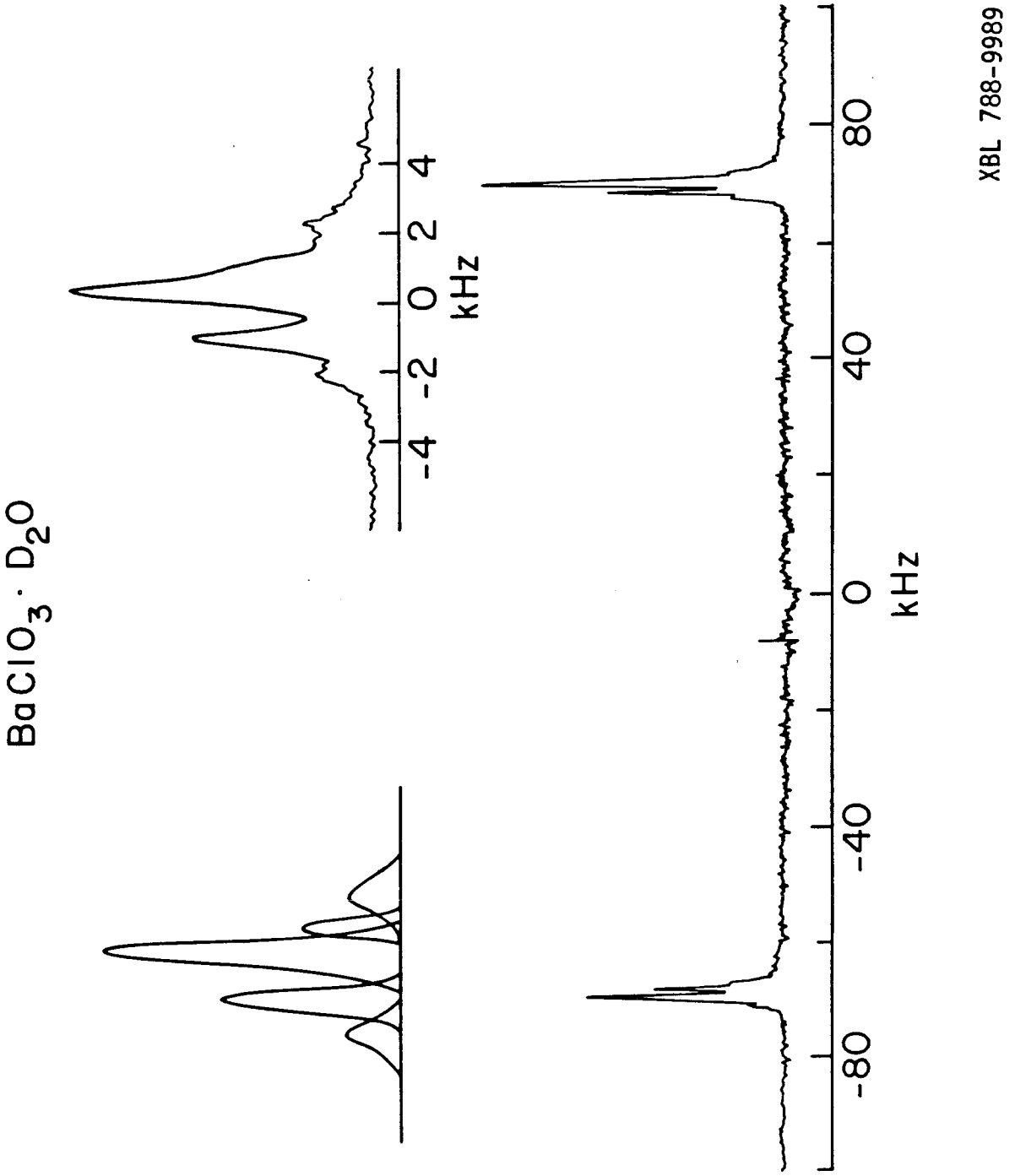

Figure 56

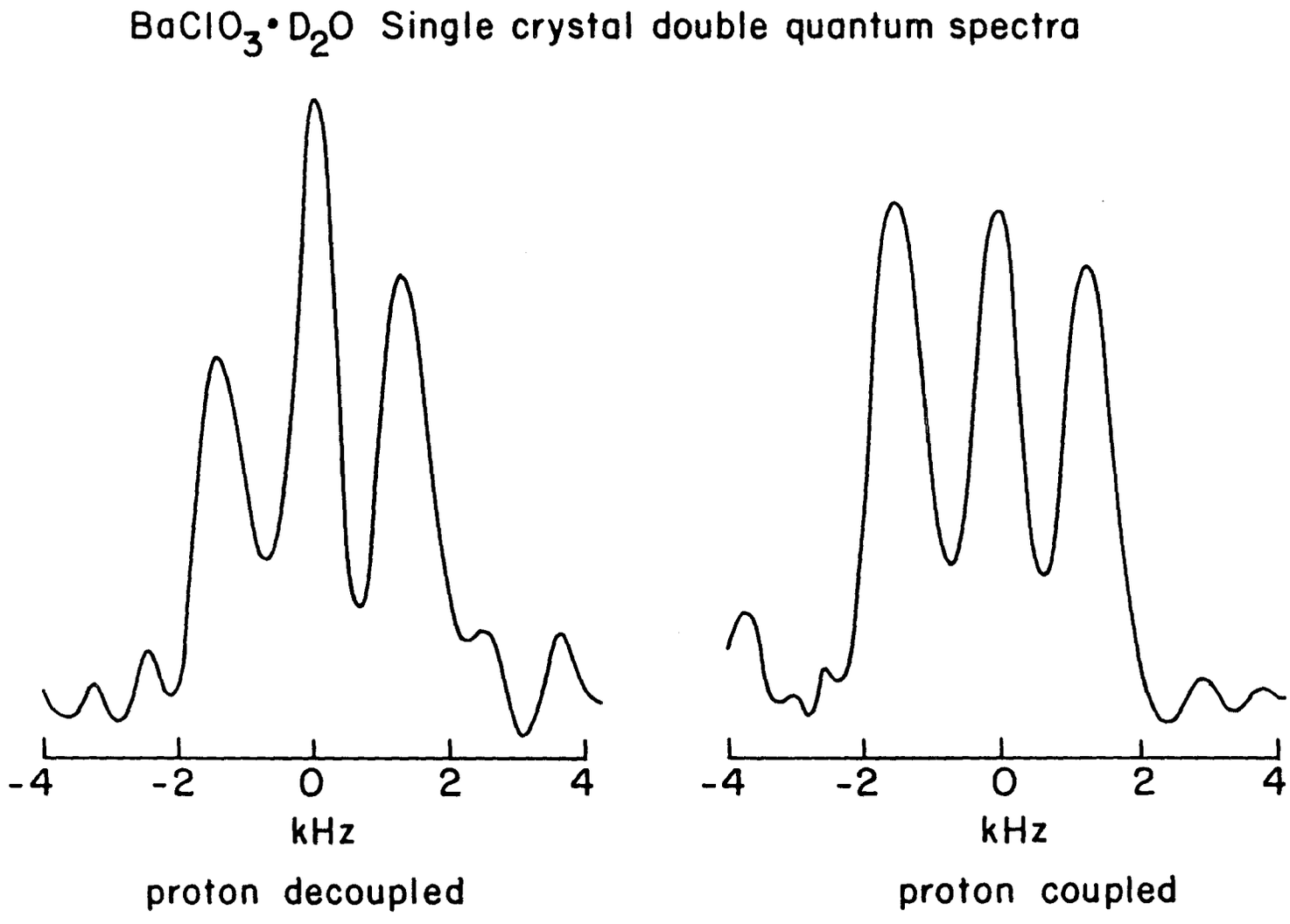
BaClO3•D2O Single crystal double quantum spectra
-4
-2
0
2
4
kHz
proton decoupled
-4
-2
0
2
4
kHz
proton coupled
XBL 788-9993

Figure 57

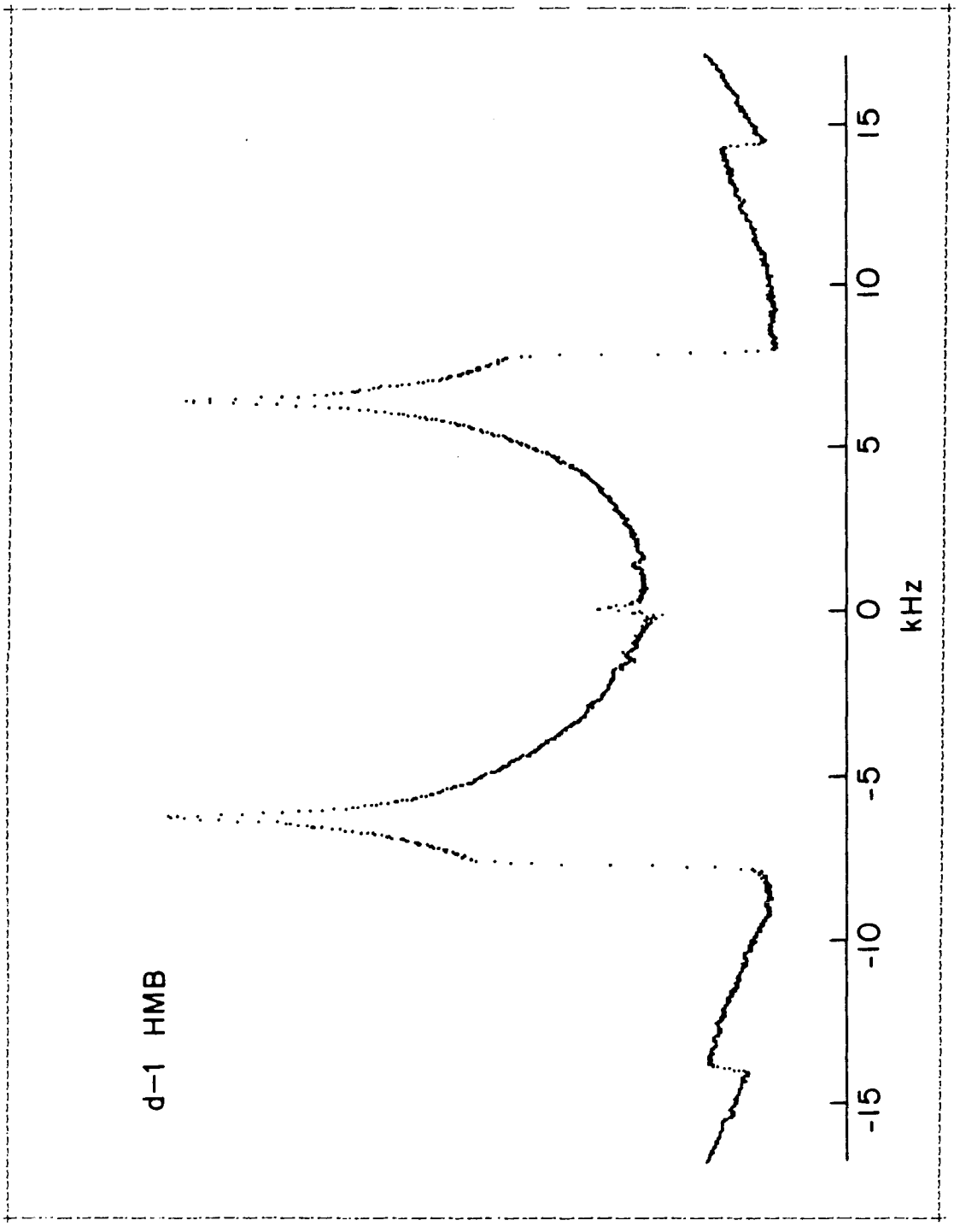

XBL 788-10002

Figure 58

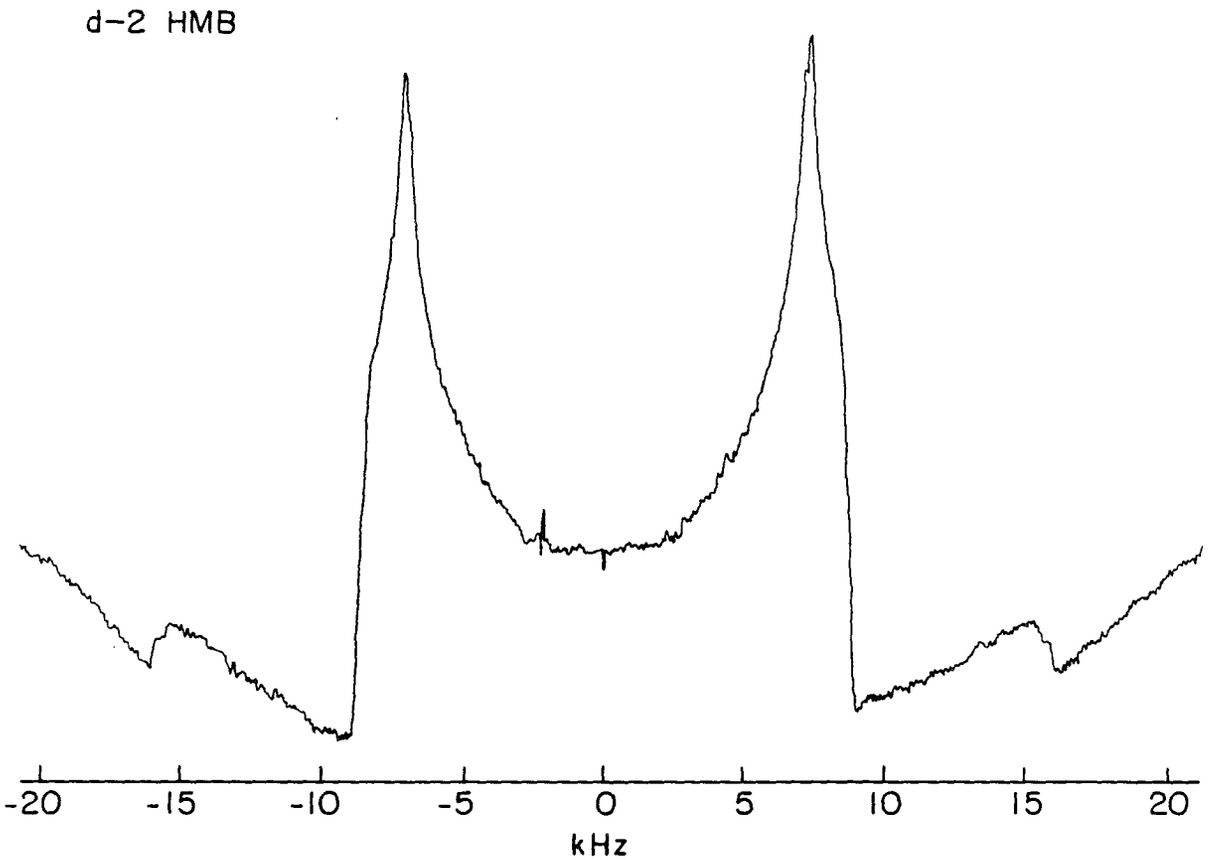

XBL 788-10121

Figure 59

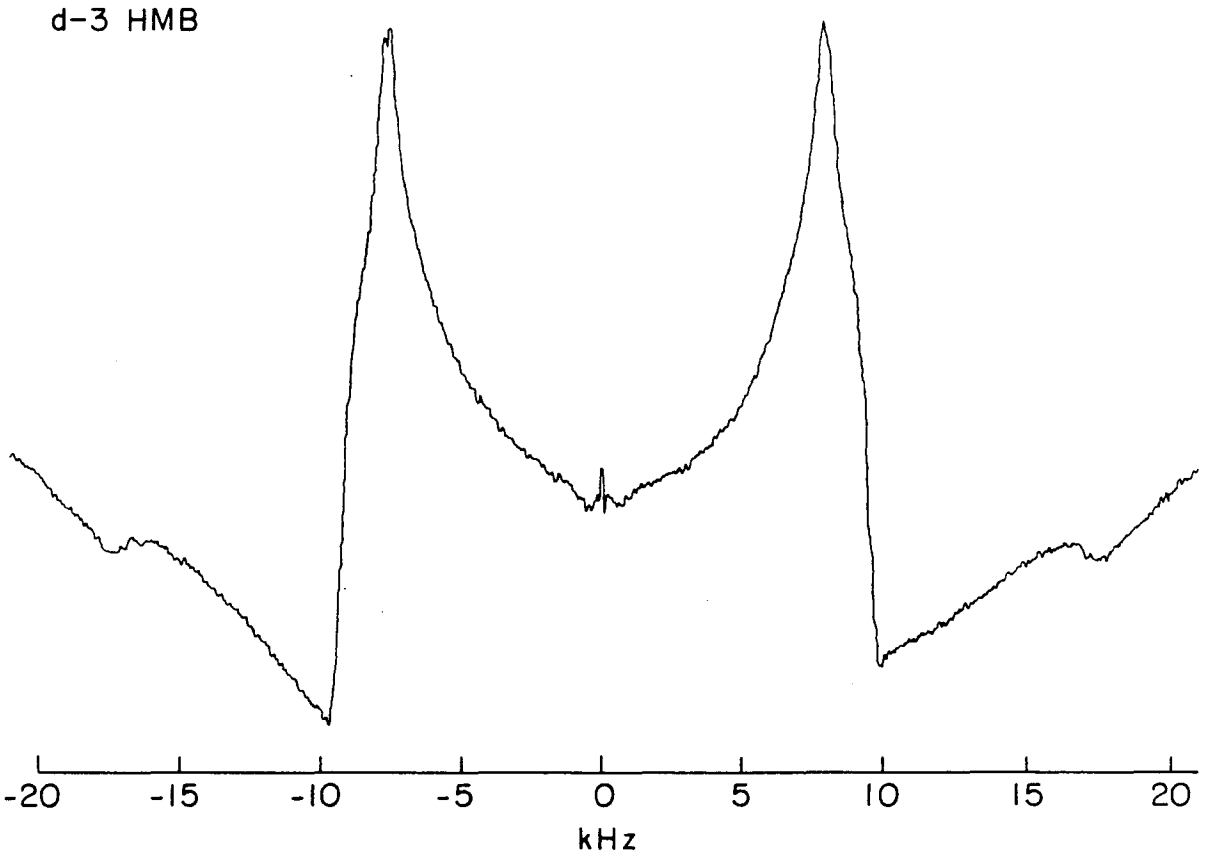

XBL 788-10119

Figure 60

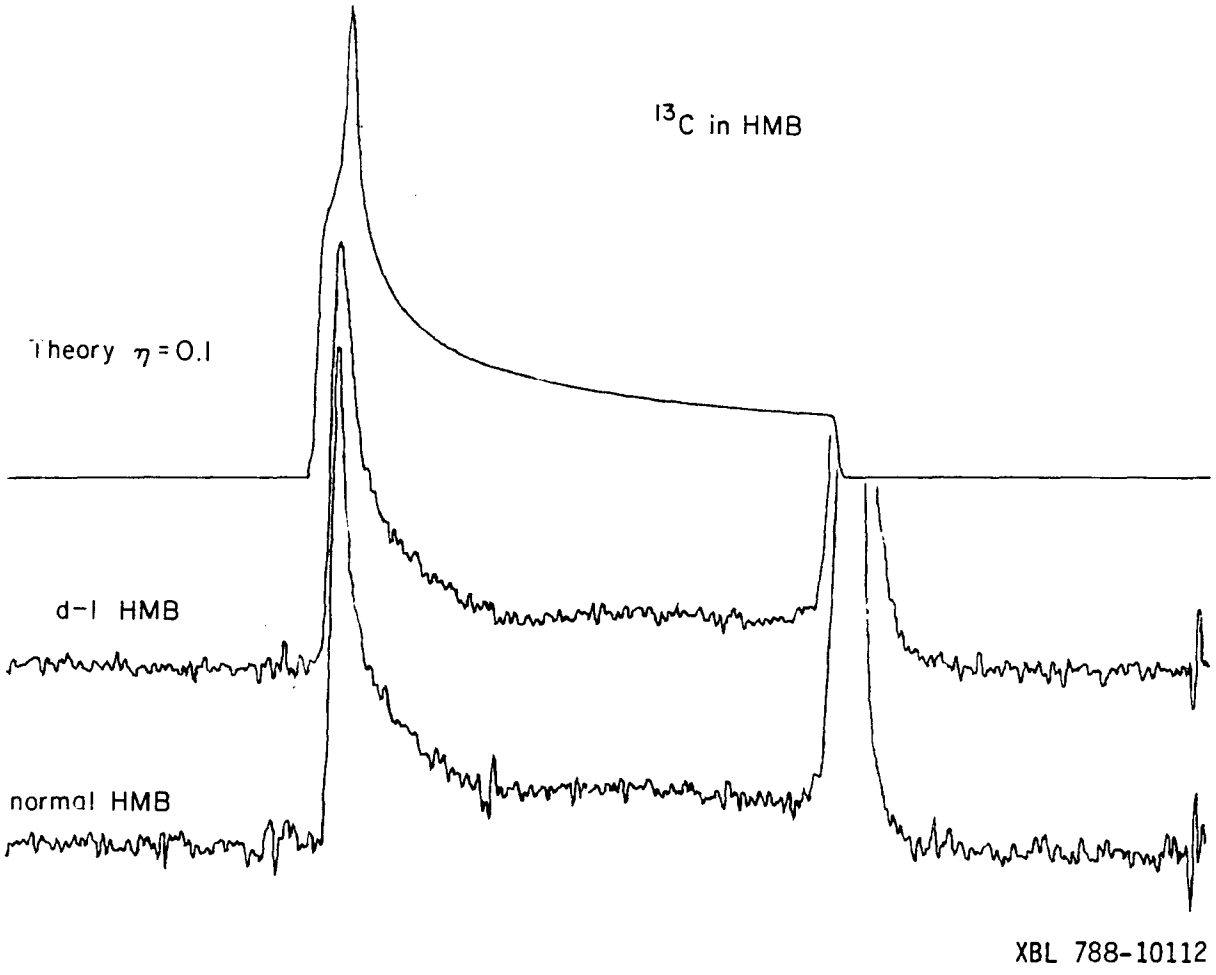

Figure 61

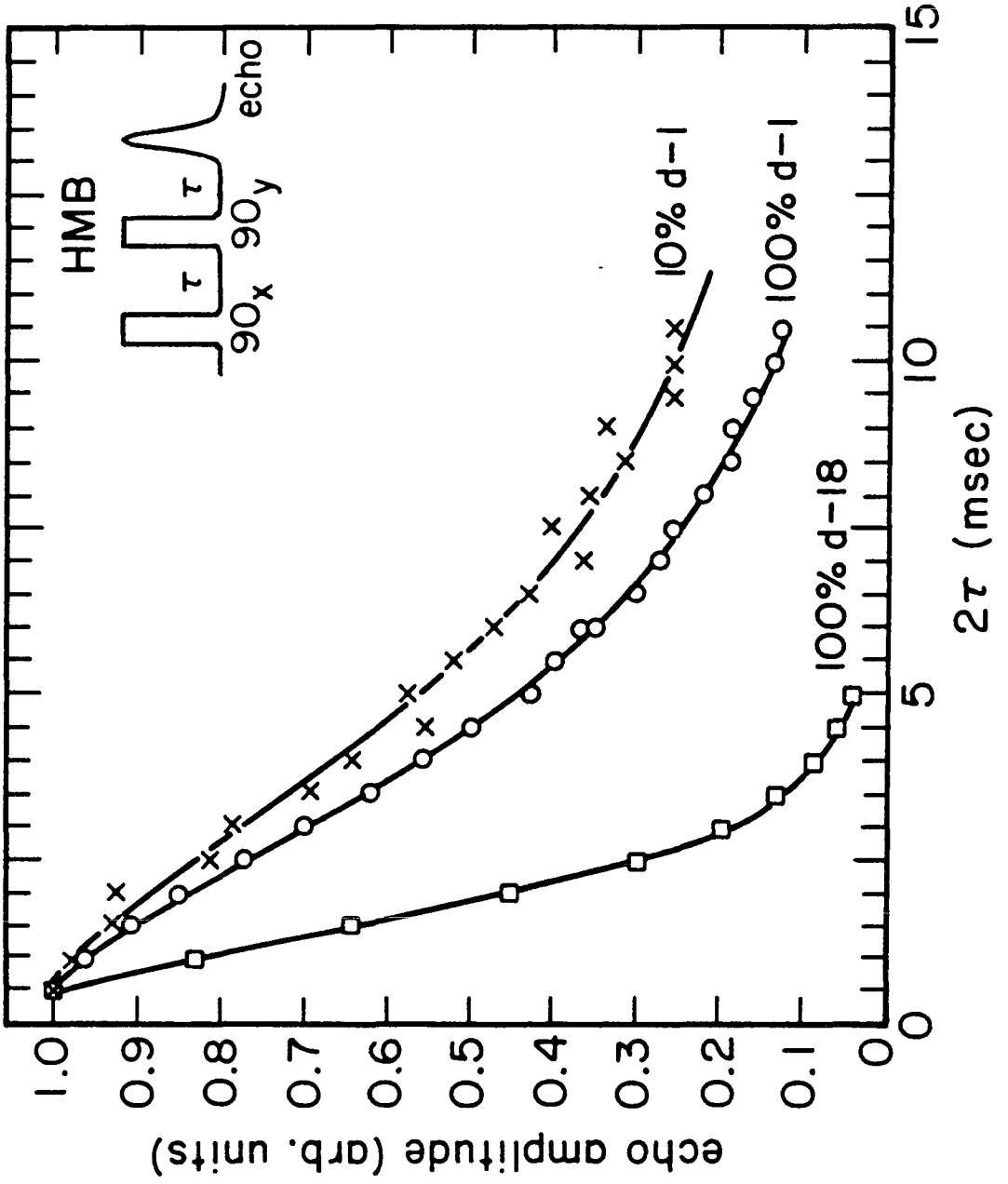

XBL 788-9992

Figure 62

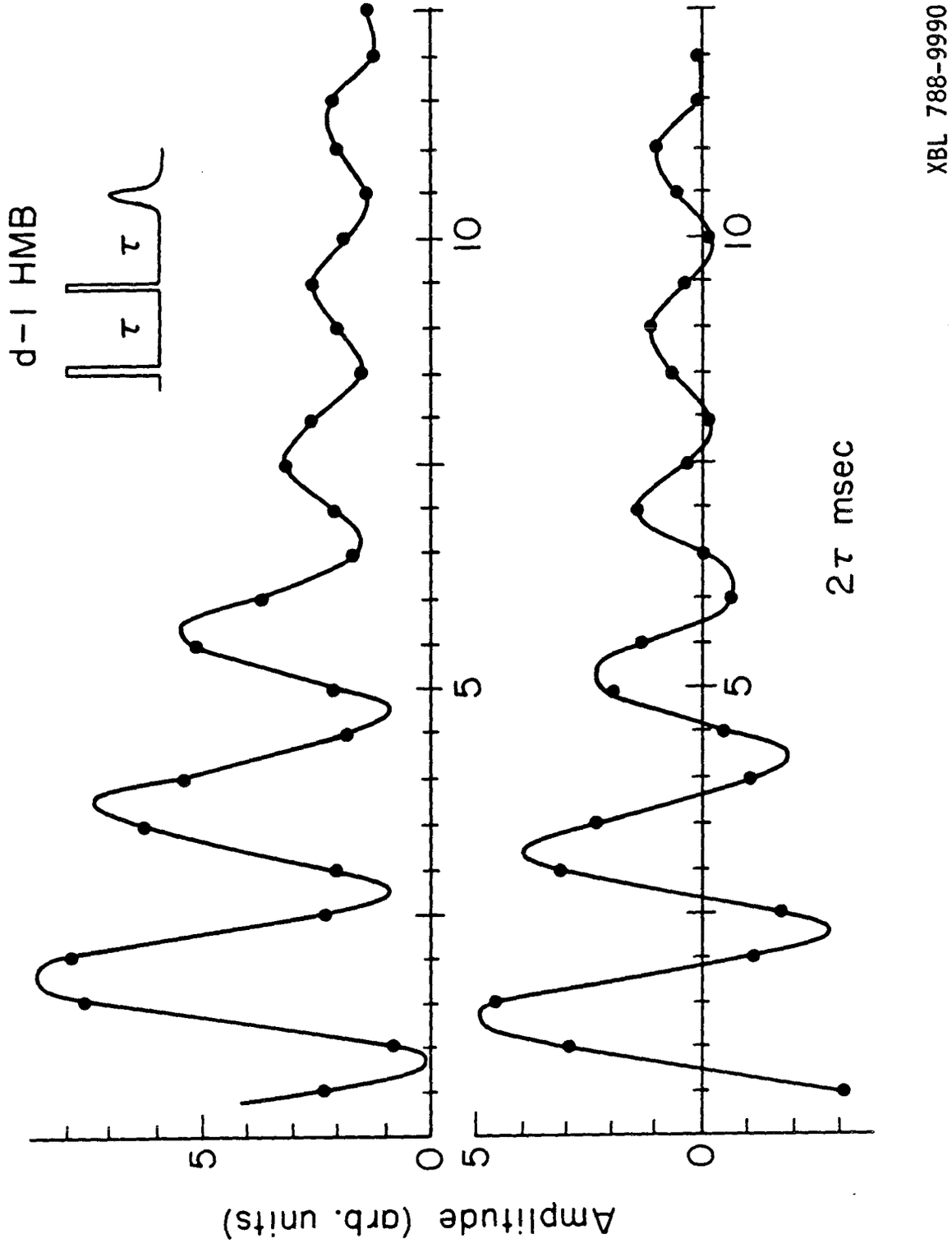
d-1 HMB
τ
τ
Amplitude (arb. units)
5
0
5
0
5
10
5
10
2τ msec
XBL 788-9990

Figure 63

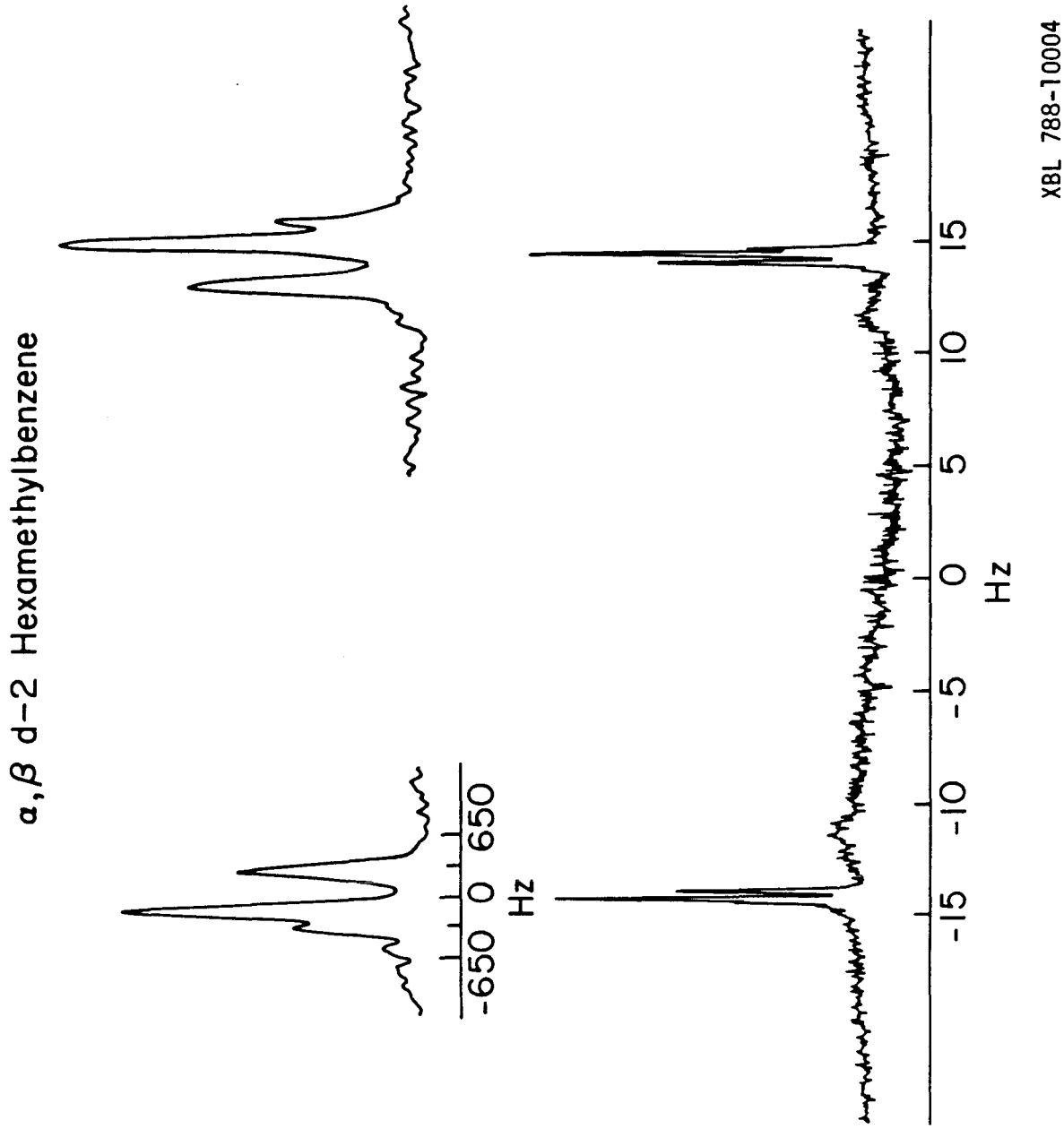
α,β d-2 Hexamethylbenzene
-650 0 650
Hz
-15 -10 -5 0 5 10 15
Hz
XBL 788-10004

Figure 64

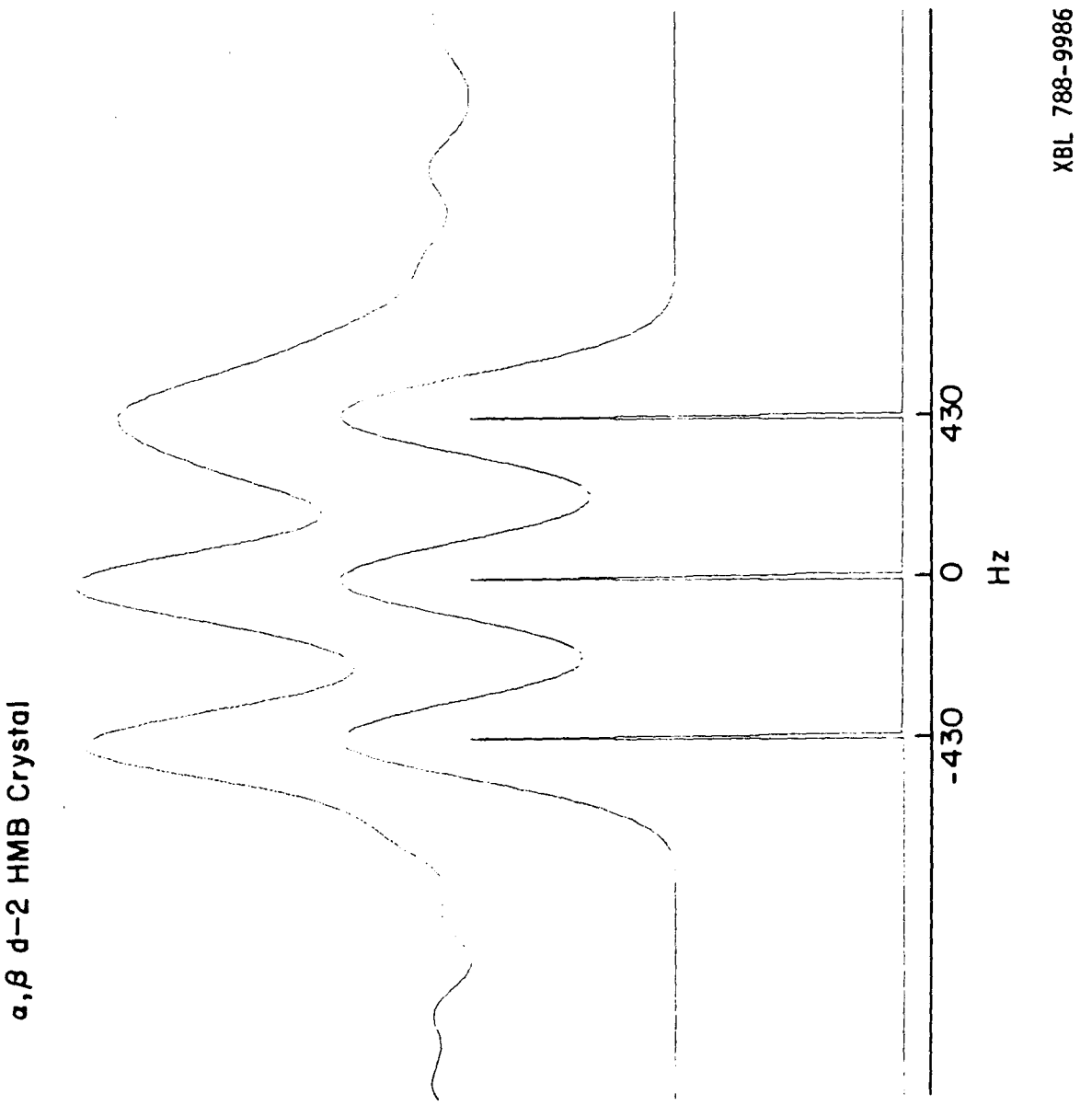

Figure 65

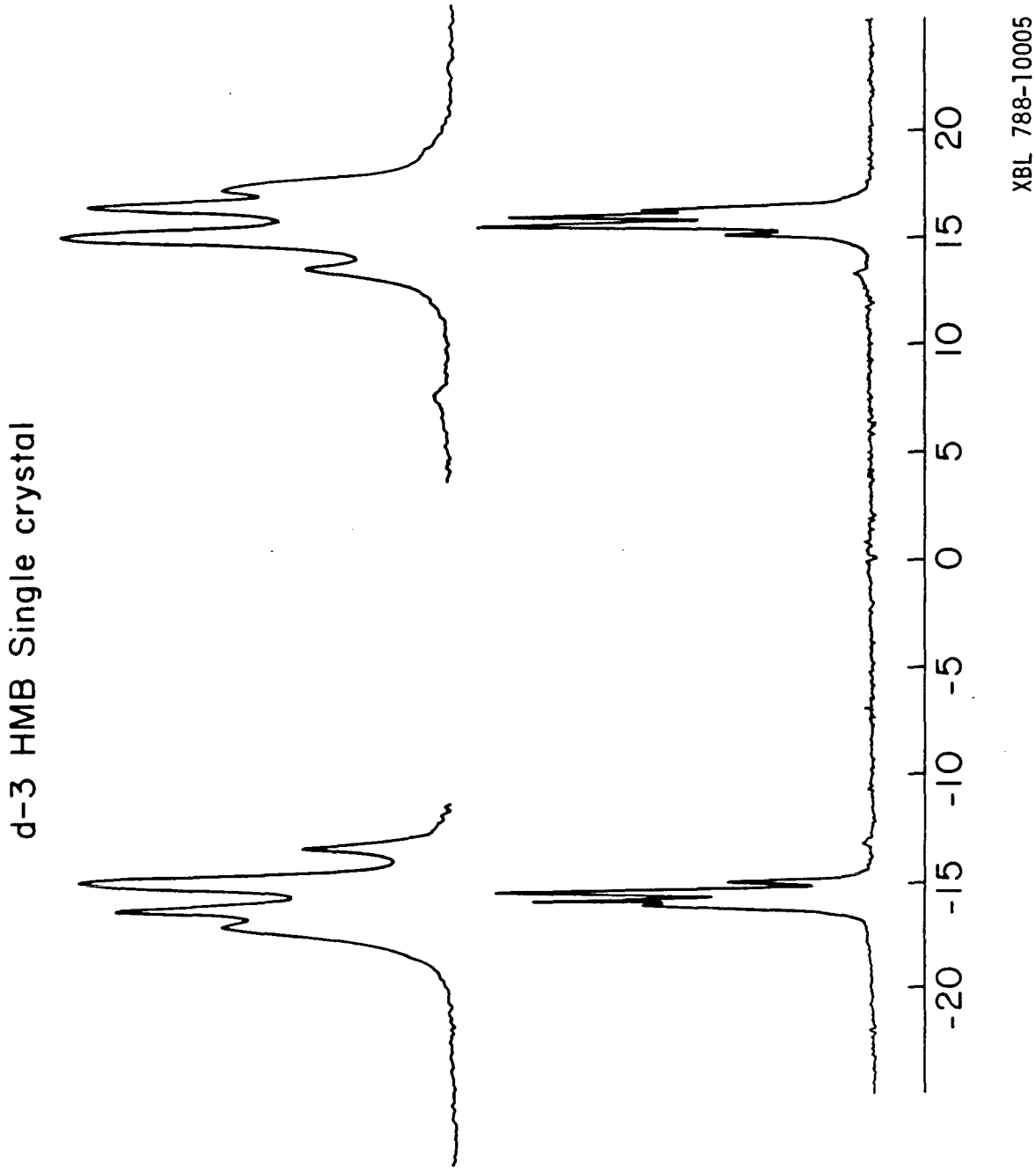

Figure 66

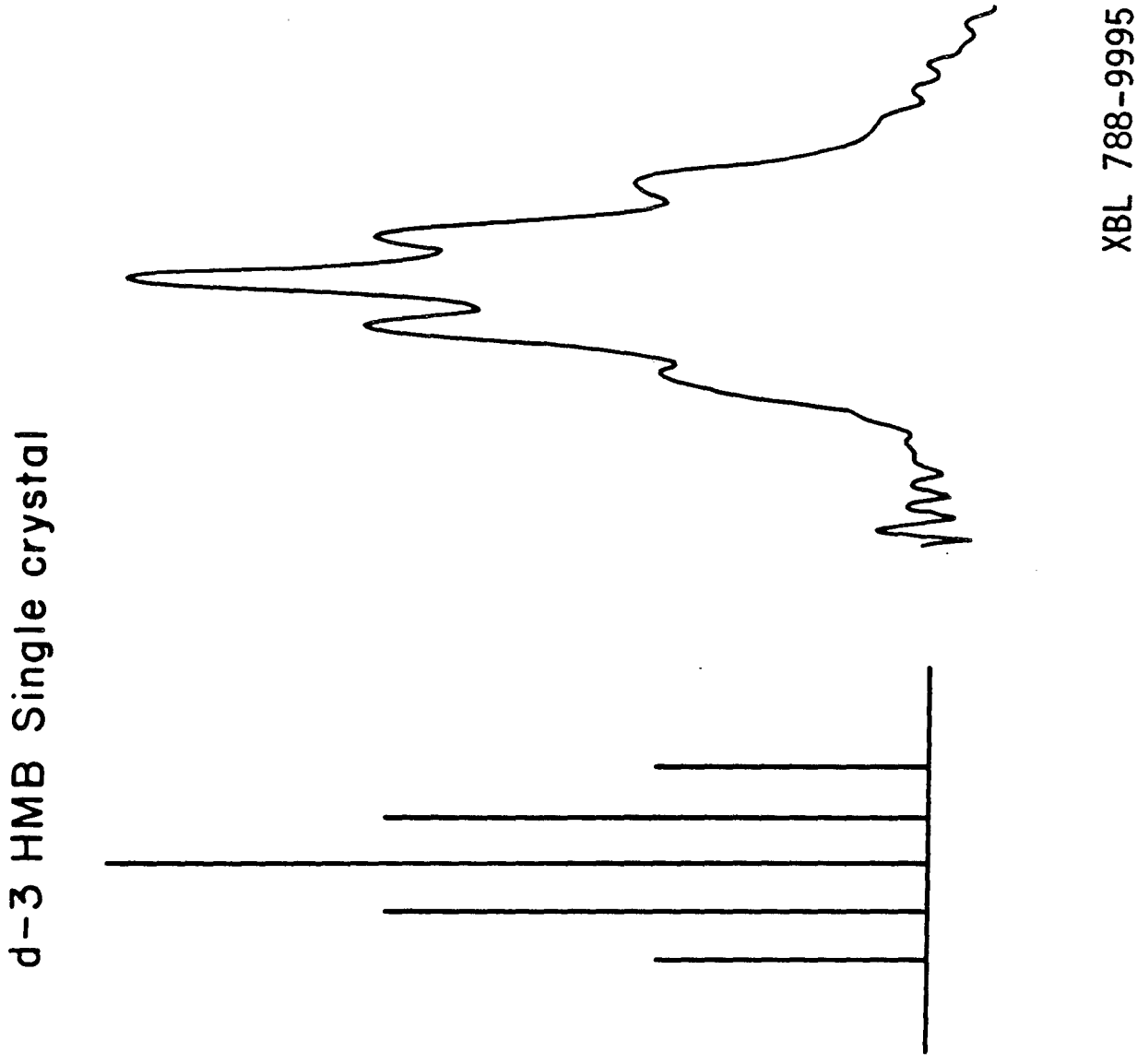

Figure 67

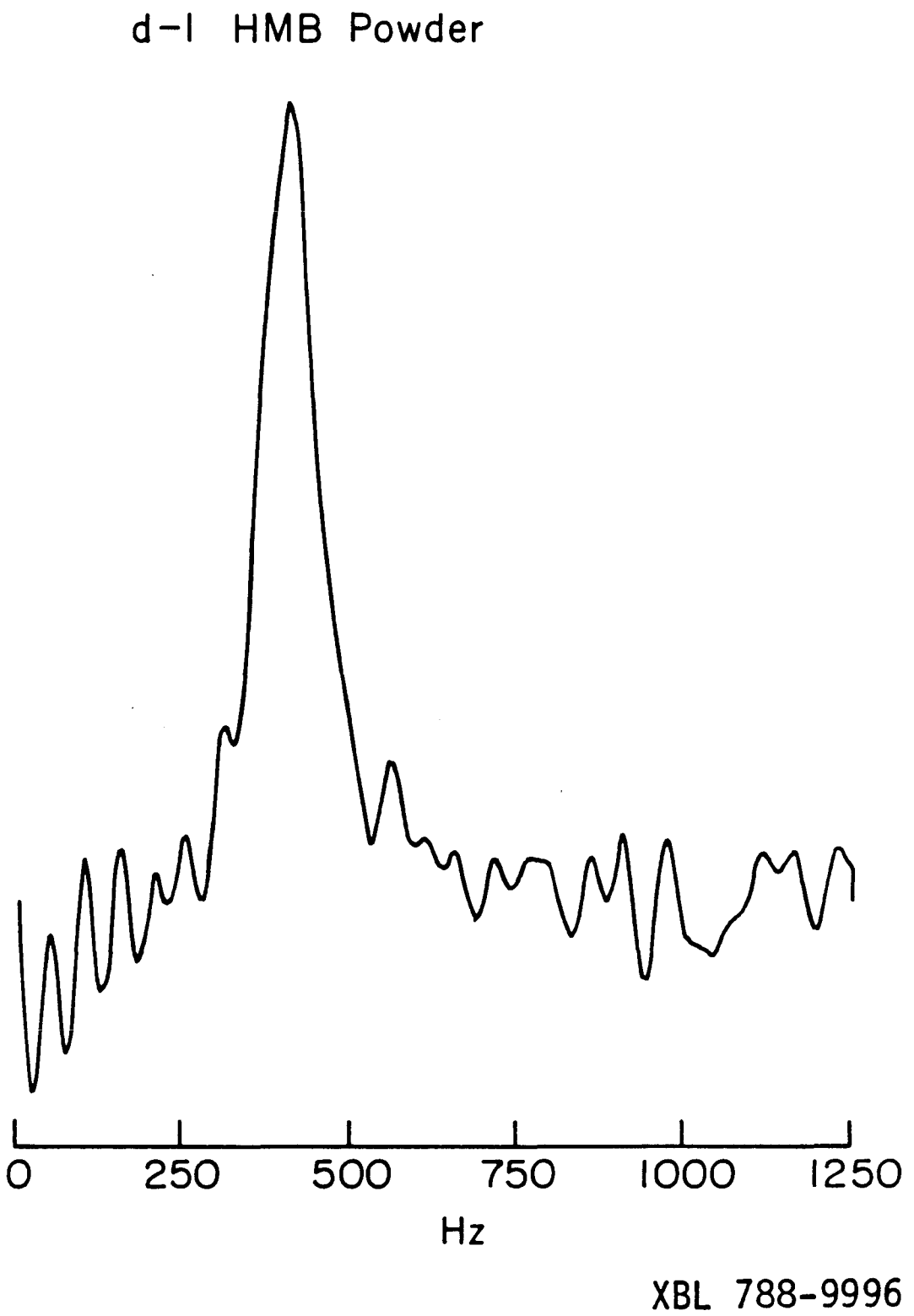

Figure 68

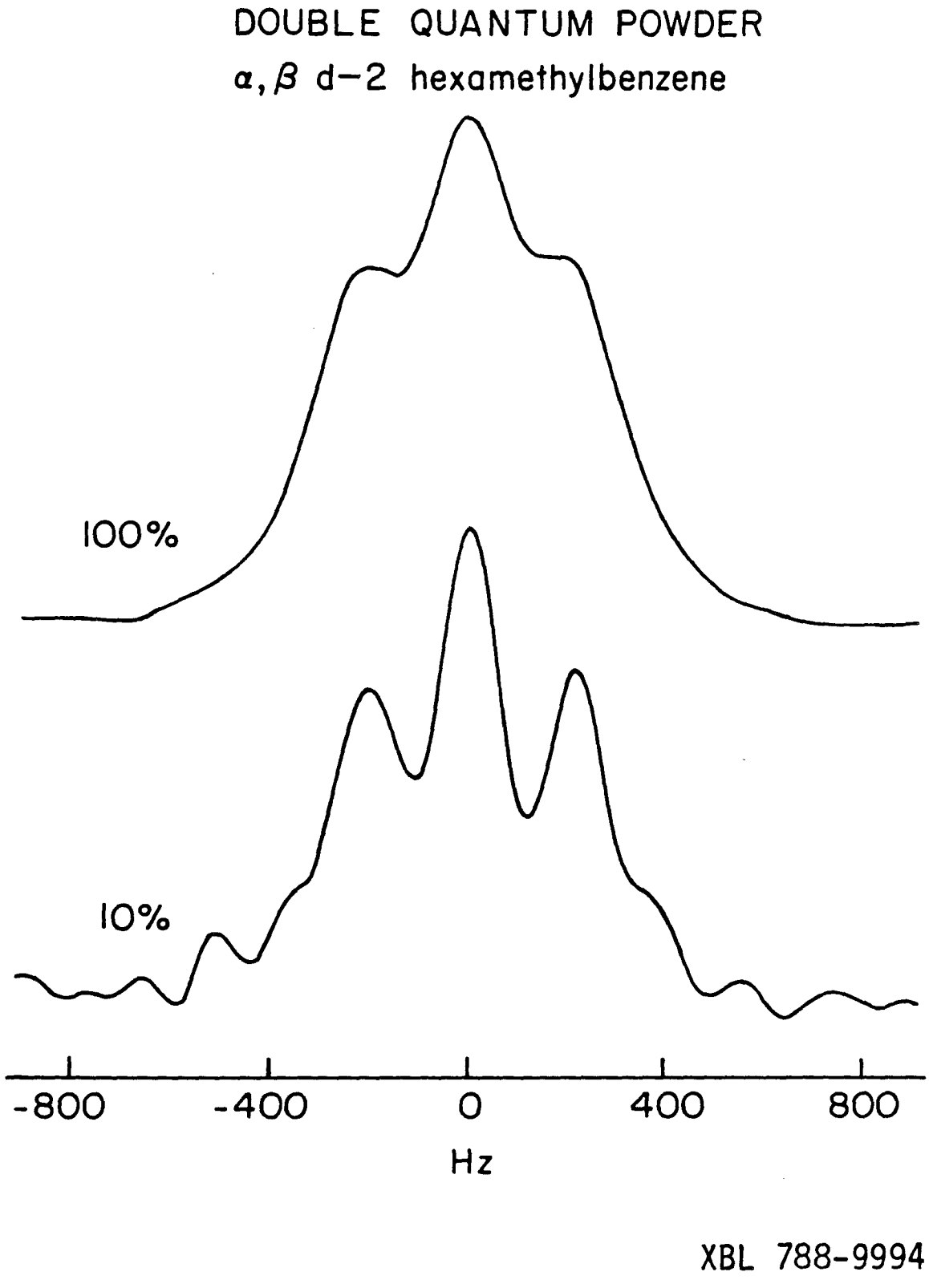
DOUBLE QUANTUM POWDER
α, β d−2 hexamethylbenzene
100%
10%
-800
-400
0
400
800
Hz
XBL 788-9994

Figure 69

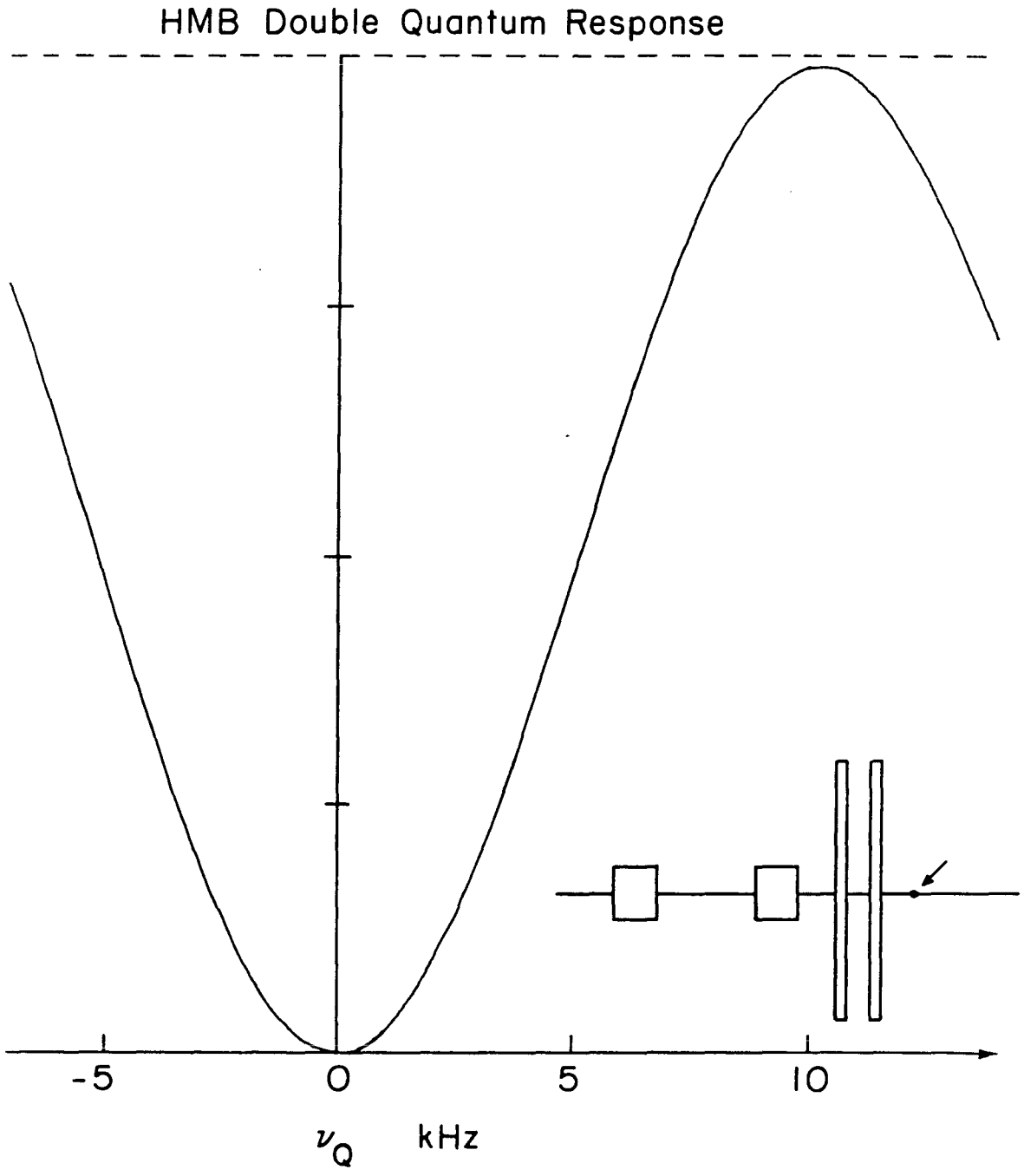

XBL 788-10115

Figure 70

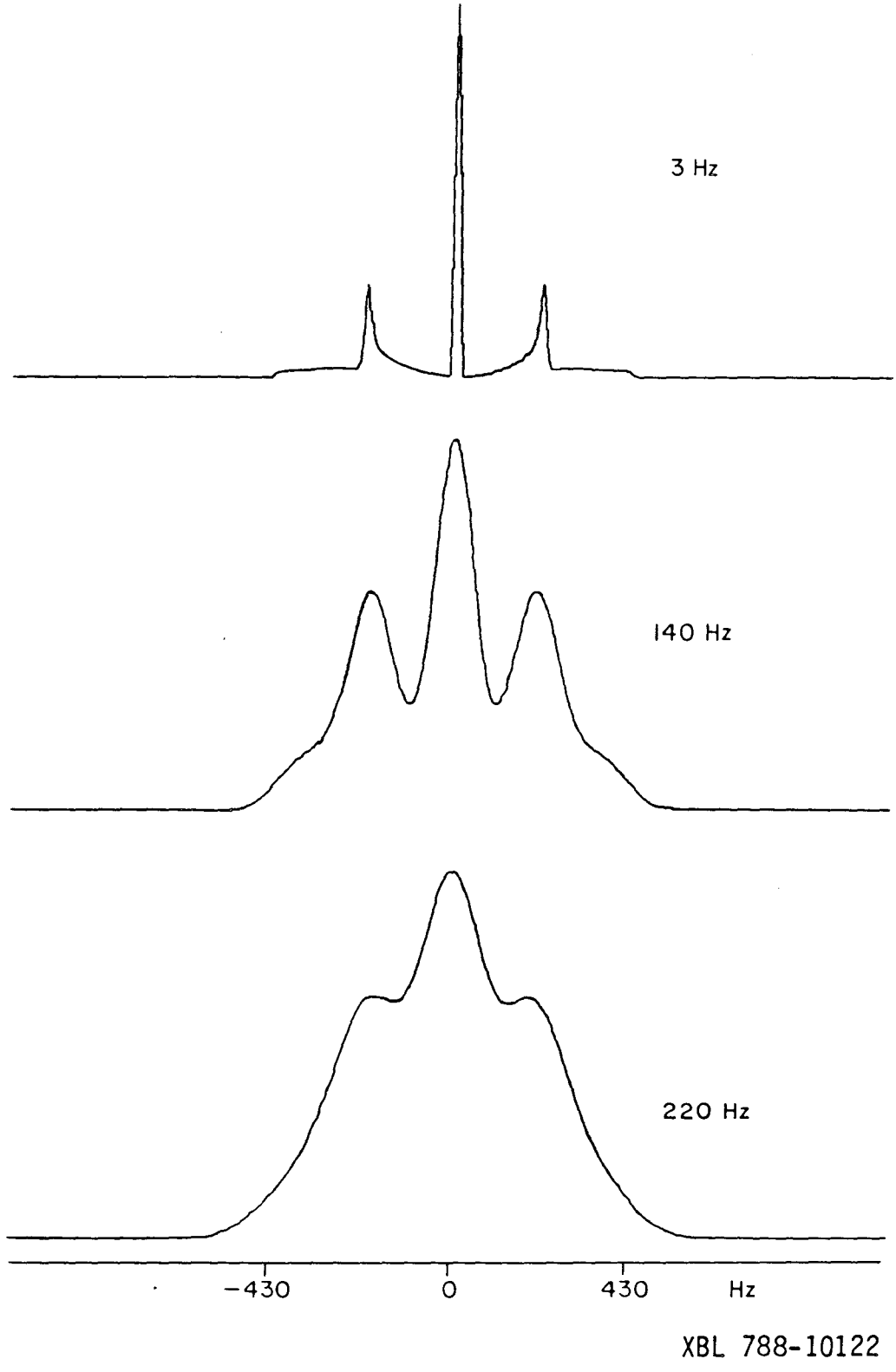

Figure 71

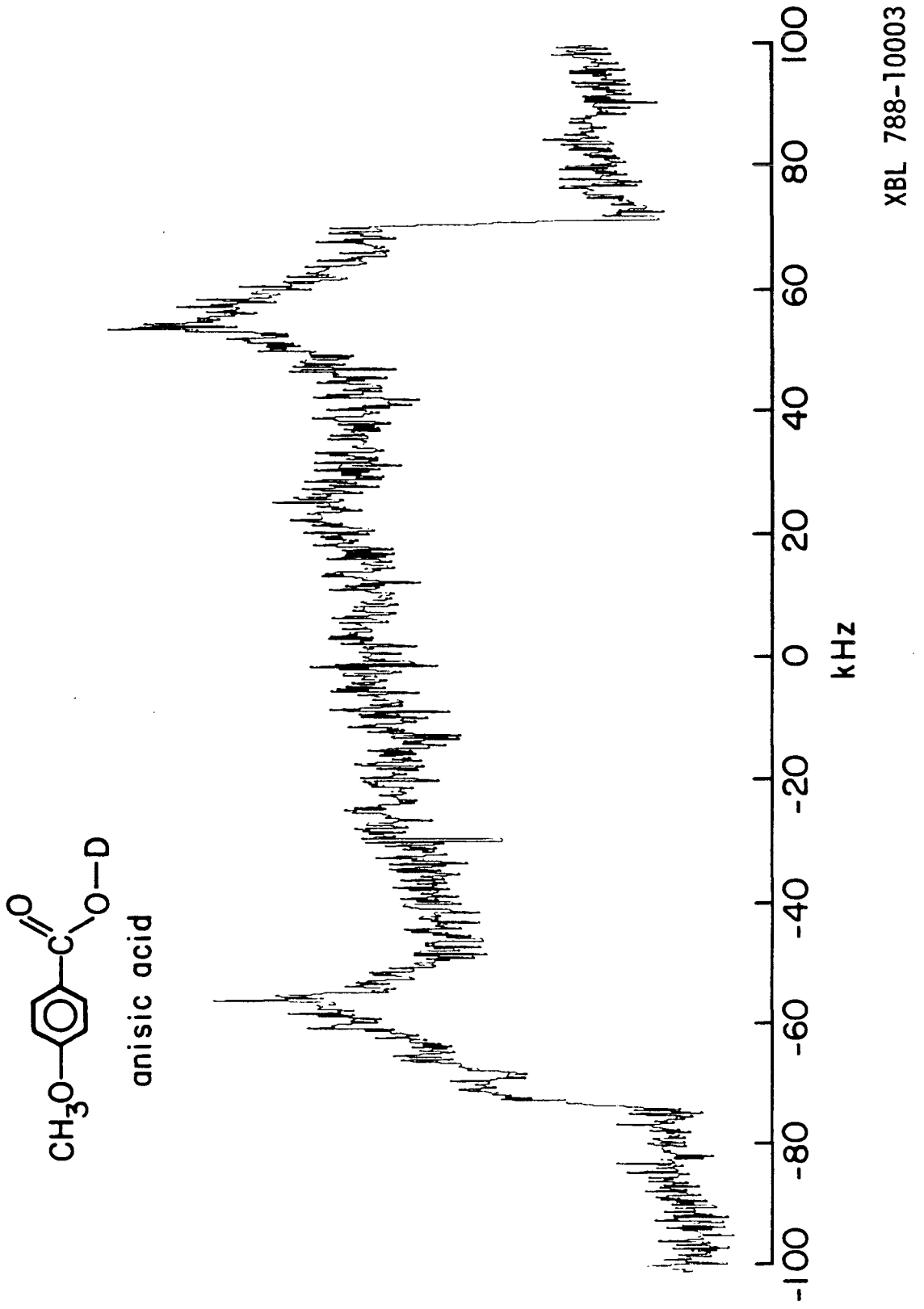
O
C
O—D
CH_3O
anisic acid
-100
-80
-60
-40
-20
0
20
40
60
80
100
kHz
XBL 788-10003

Figure 72

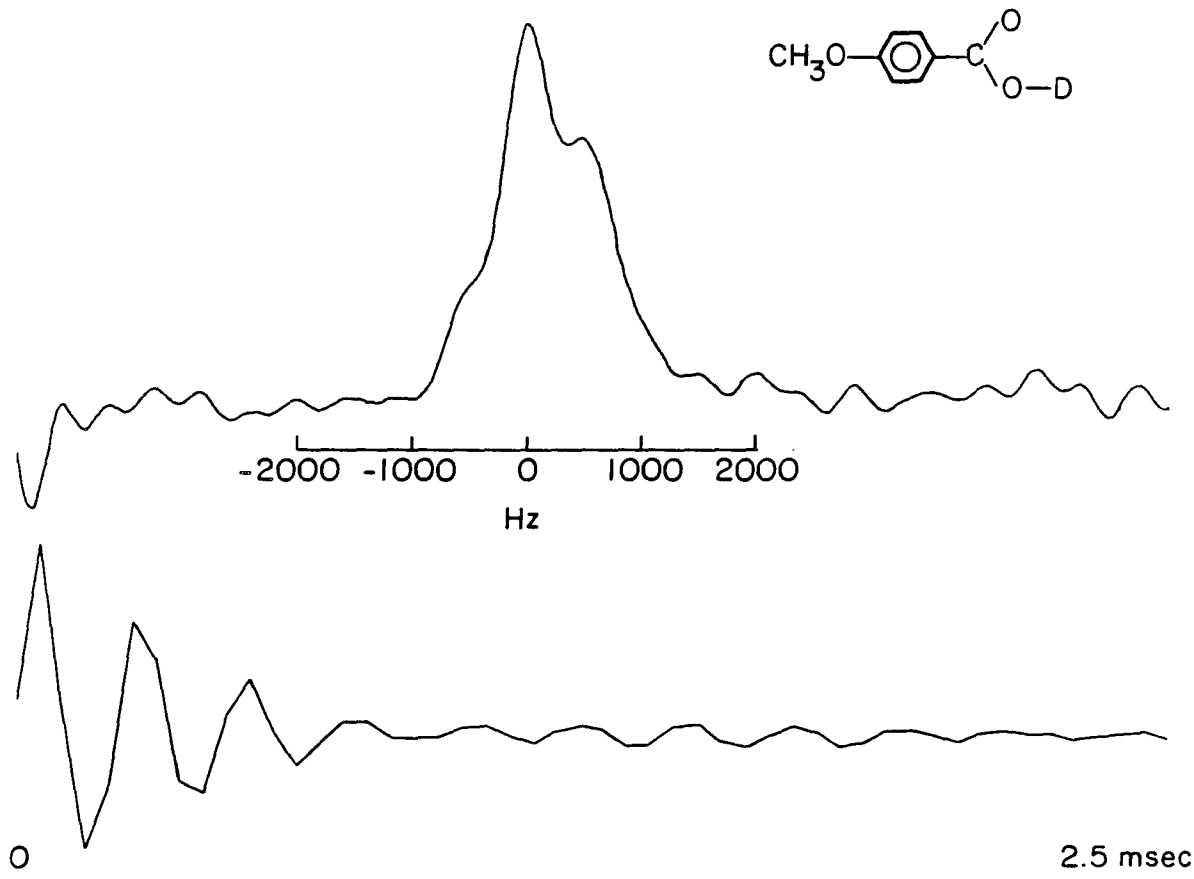

XBL 788-10120

Figure 73

MULTIPLE QUANTUM PULSE SEQUENCES

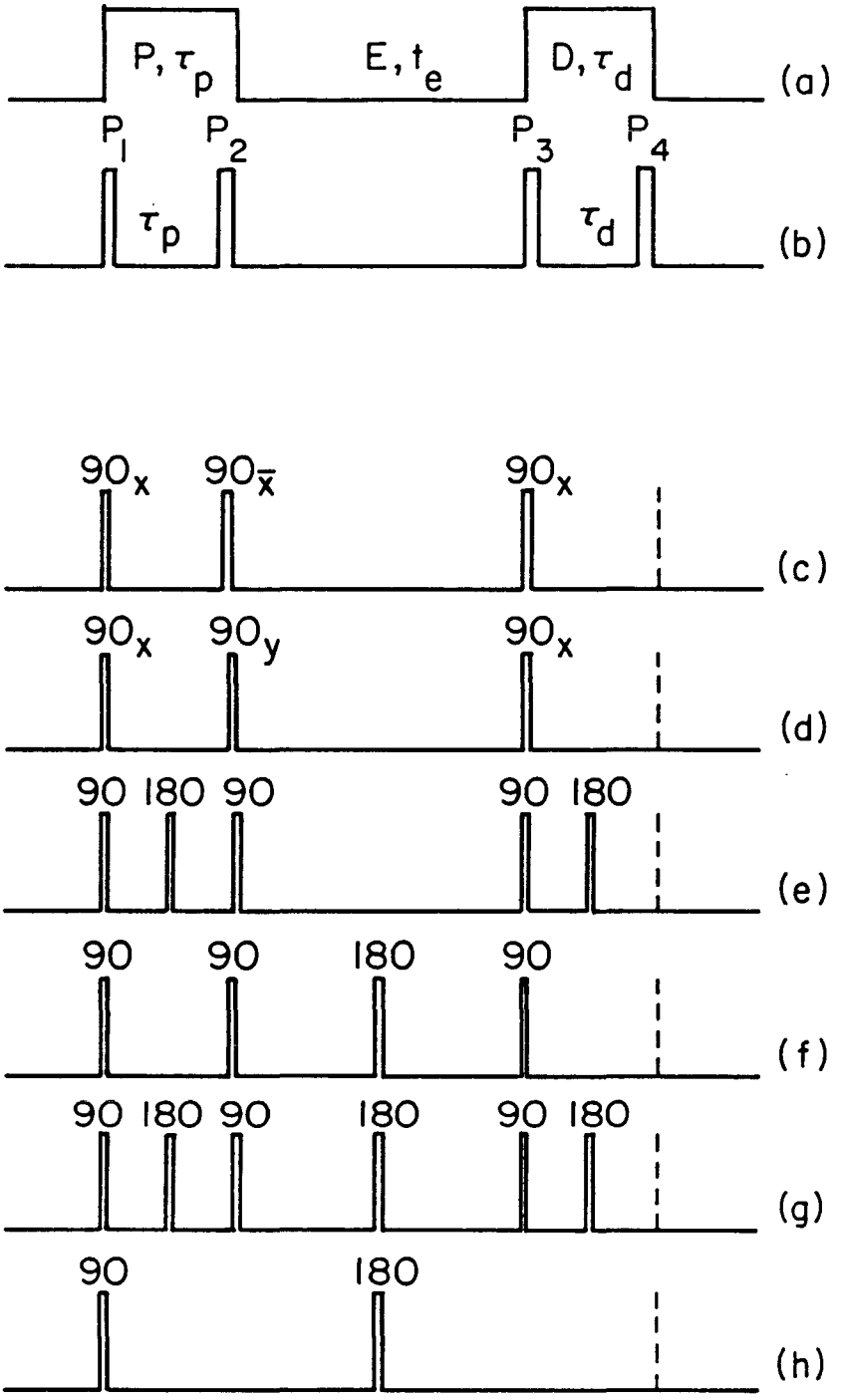

XBL 788-10105

Figure 74

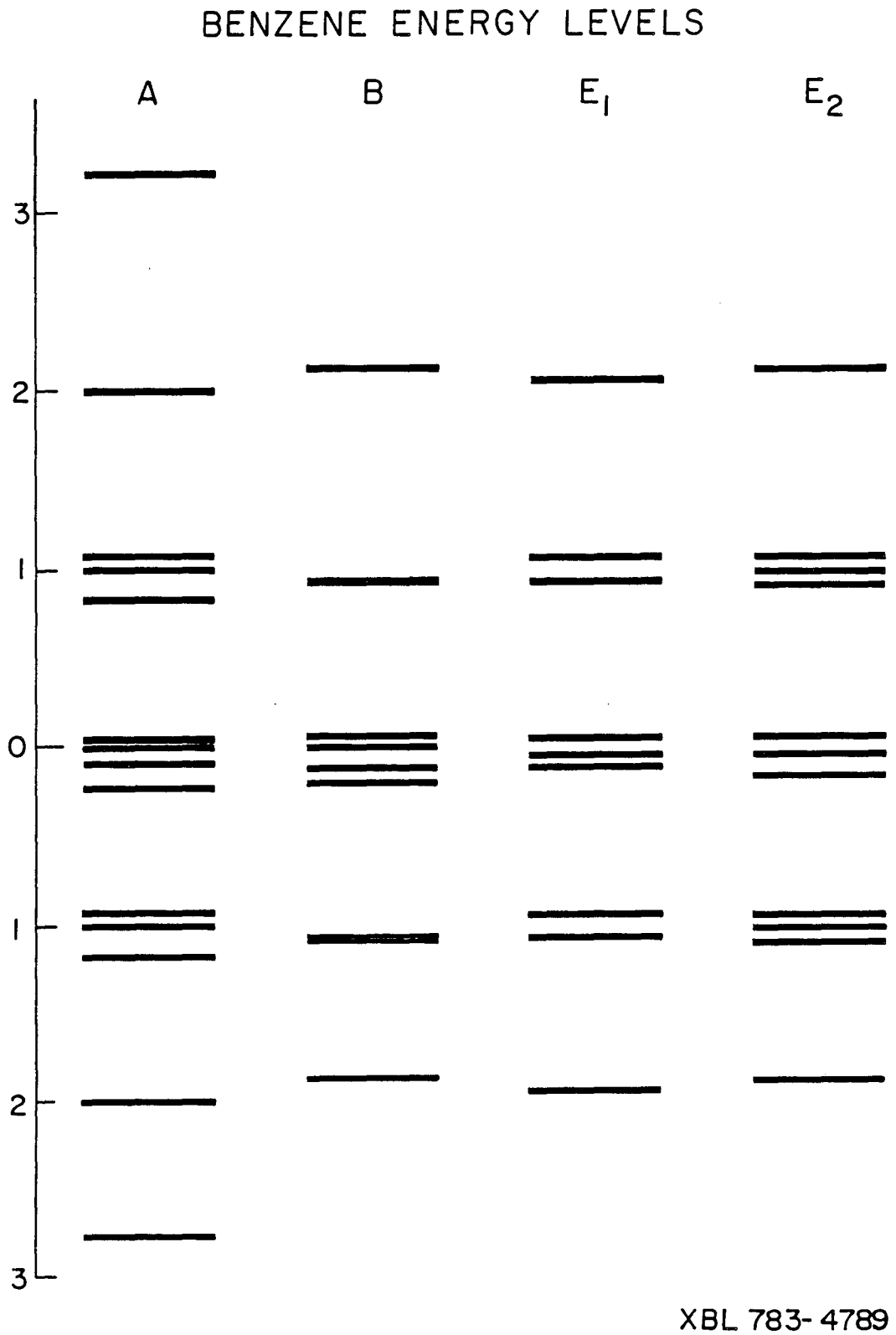

Figure 75

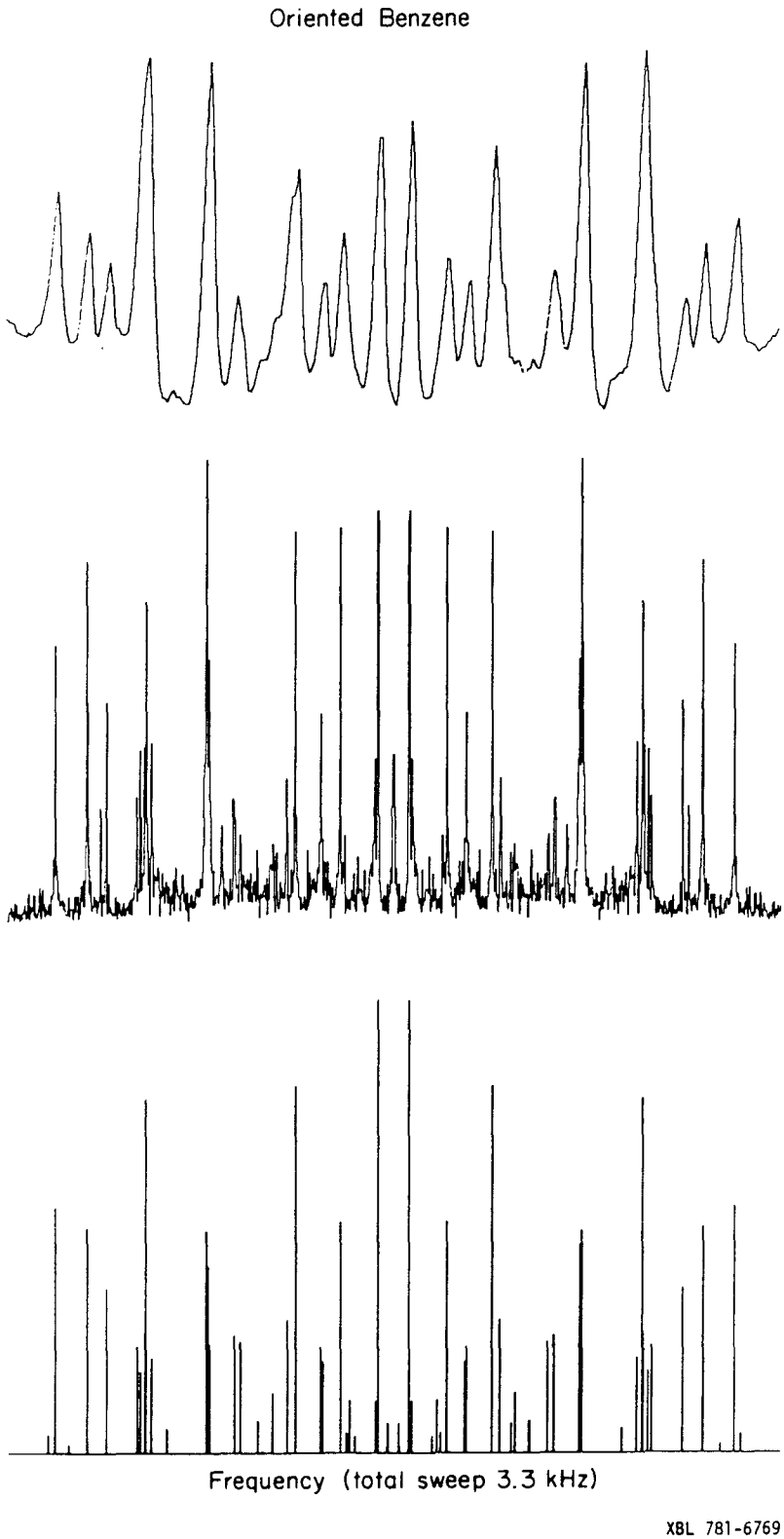

Figure 76

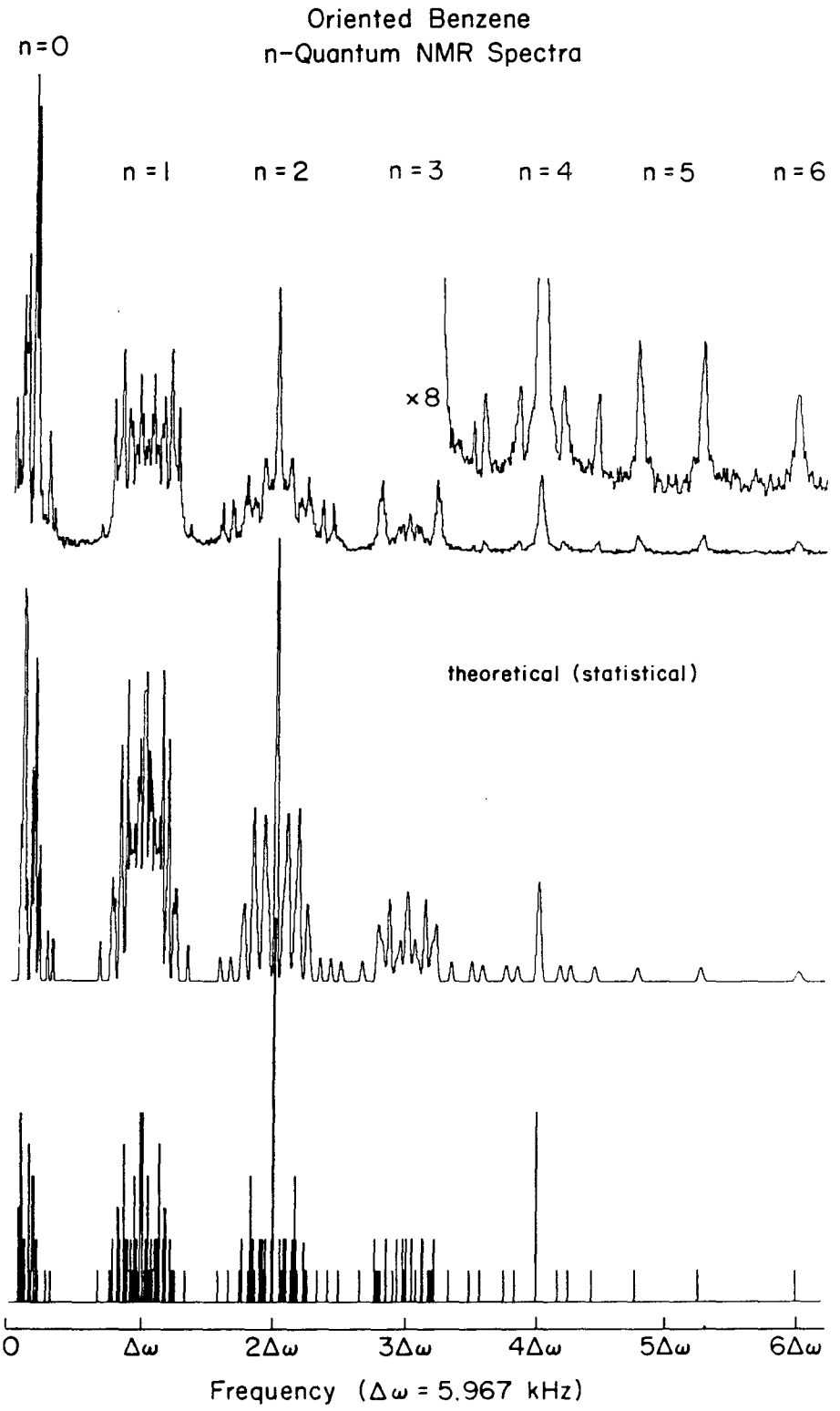
Oriented Benzene
n-Quantum NMR Spectra
n=0
n=1
n=2
n=3
n=4
n=5
n=6
×8
theoretical (statistical)
0
Δω
2Δω
3Δω
4Δω
5Δω
6Δω
Frequency (Δω = 5.967 kHz)
XBL 781-6770

Figure 77

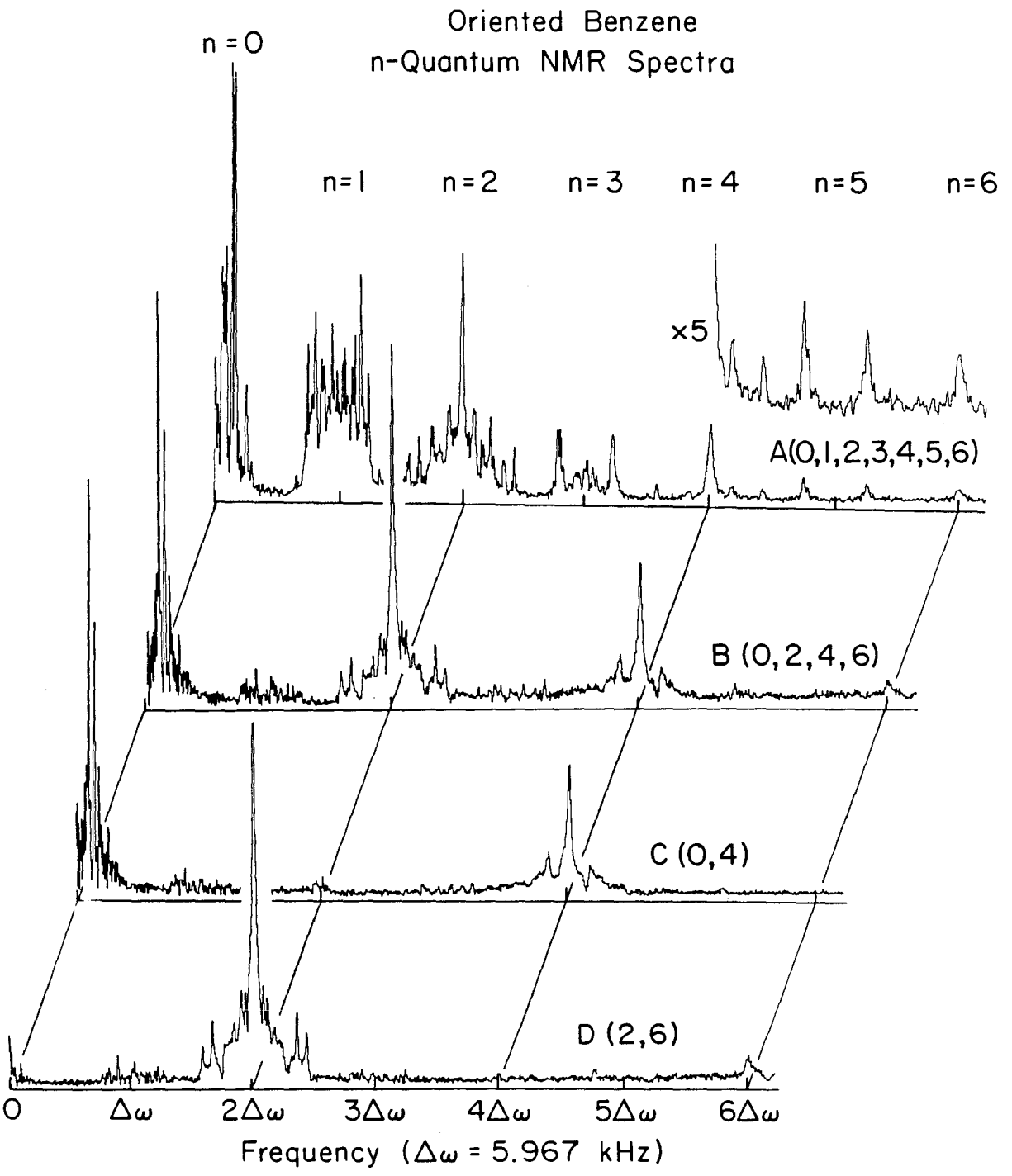

XBL 782-7143

Figure 78

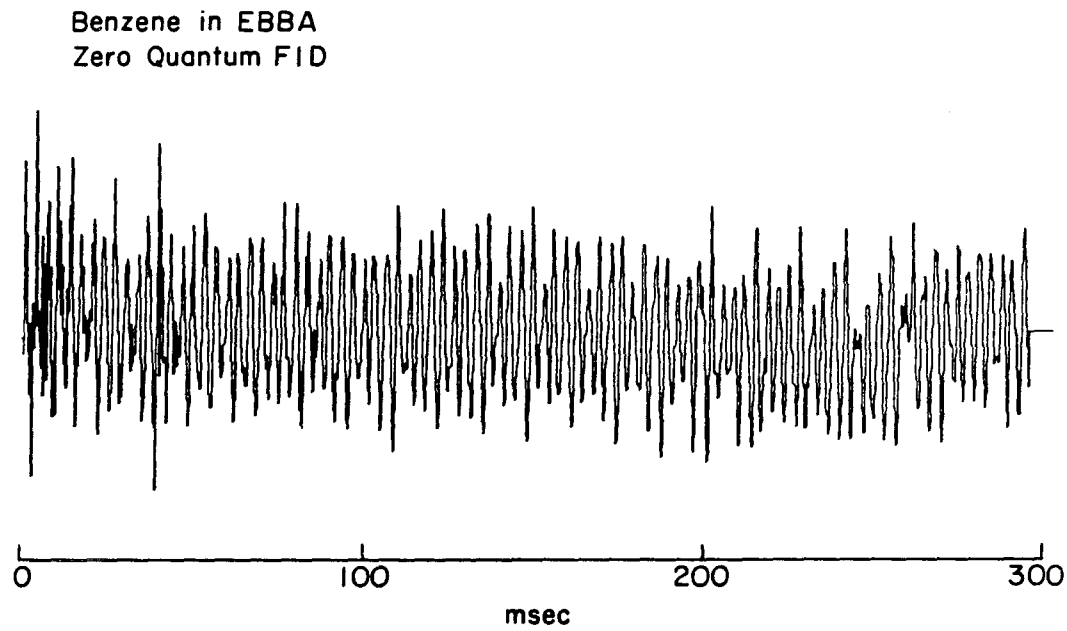

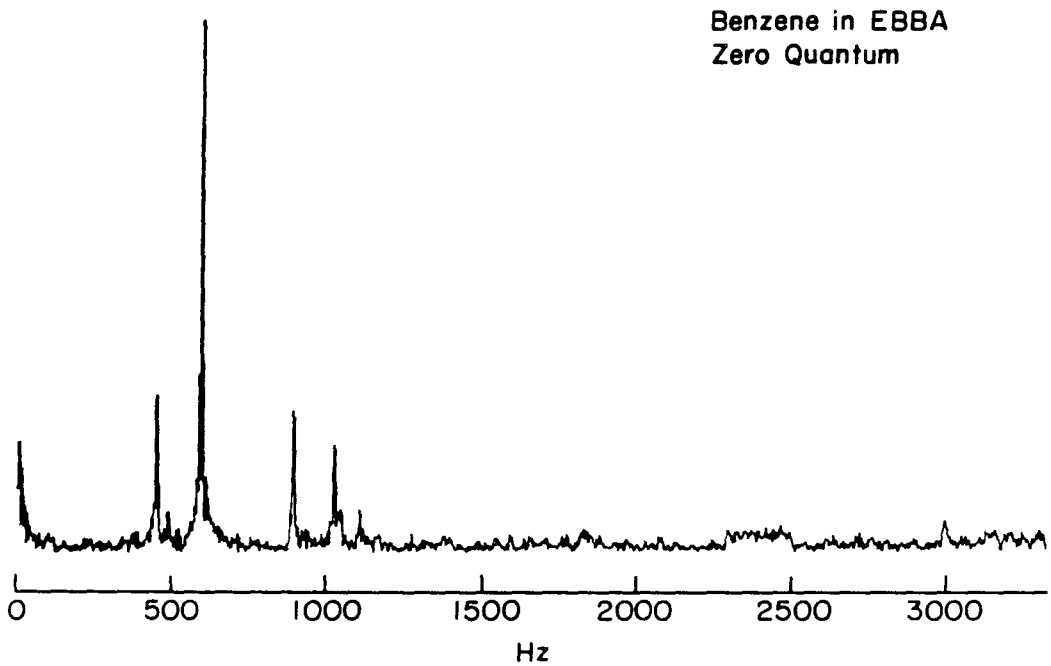

XBL 788-10006

Figure 79

ORIENTED BENZENE
FT MULTIPLE QUANTUM ECHOES

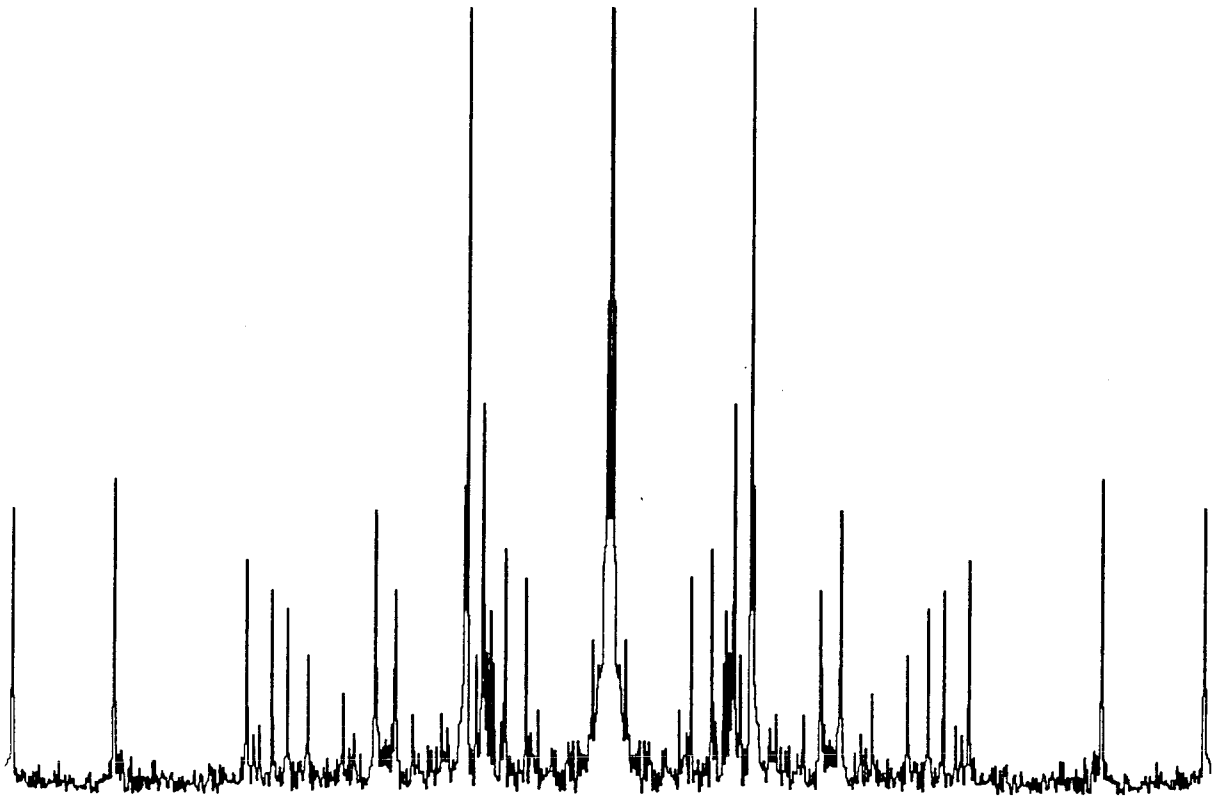

XBL 784 - 4827

Figure 80

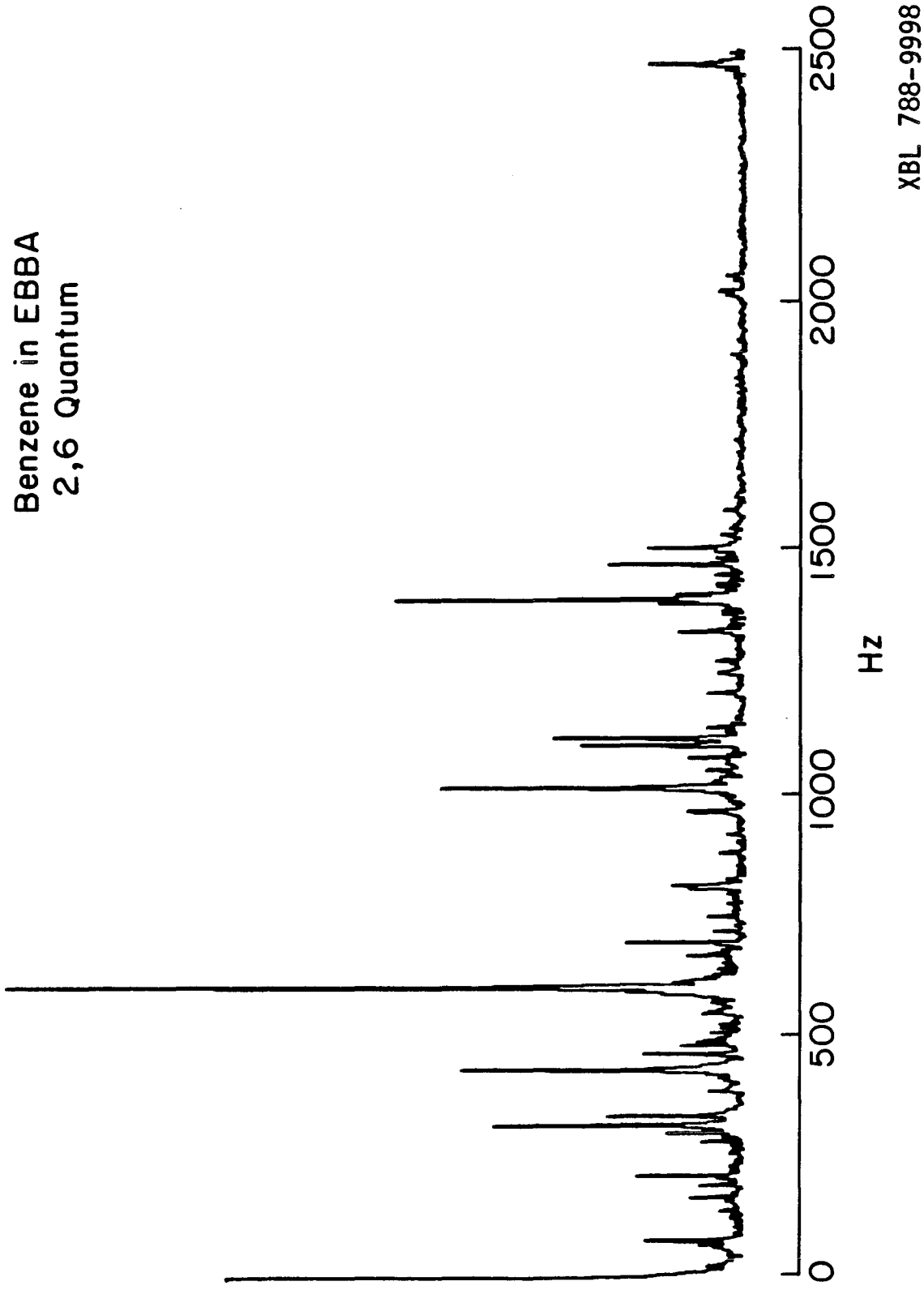
Benzene in EBBA
2,6 Quantum
0
500
1000
1500
2000
2500
Hz
XBL 788-9998

Figure 81

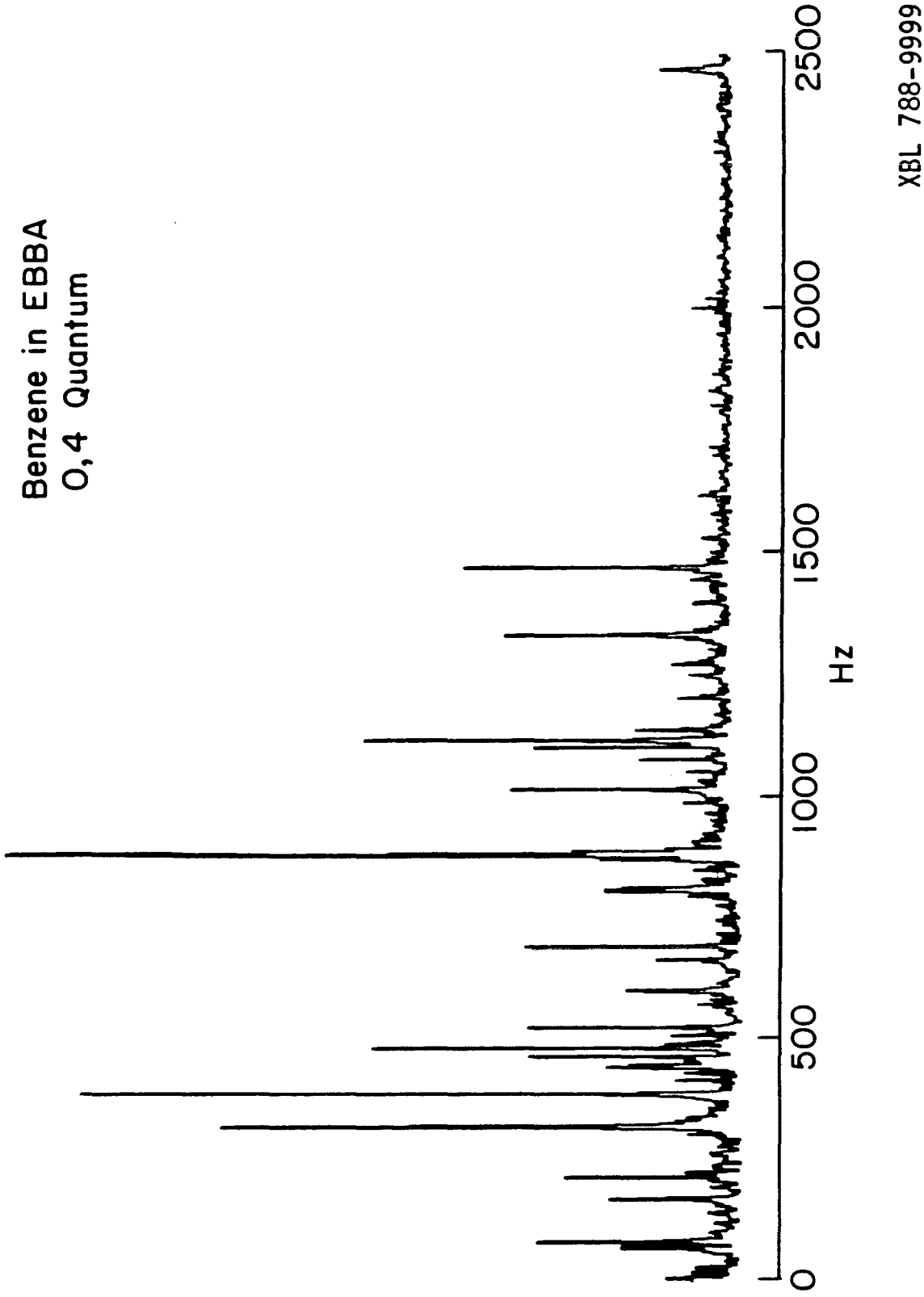
Benzene in EBBA
0,4 Quantum
0
500
1000
1500
2000
2500
Hz
XBL 788-9999

Figure 82

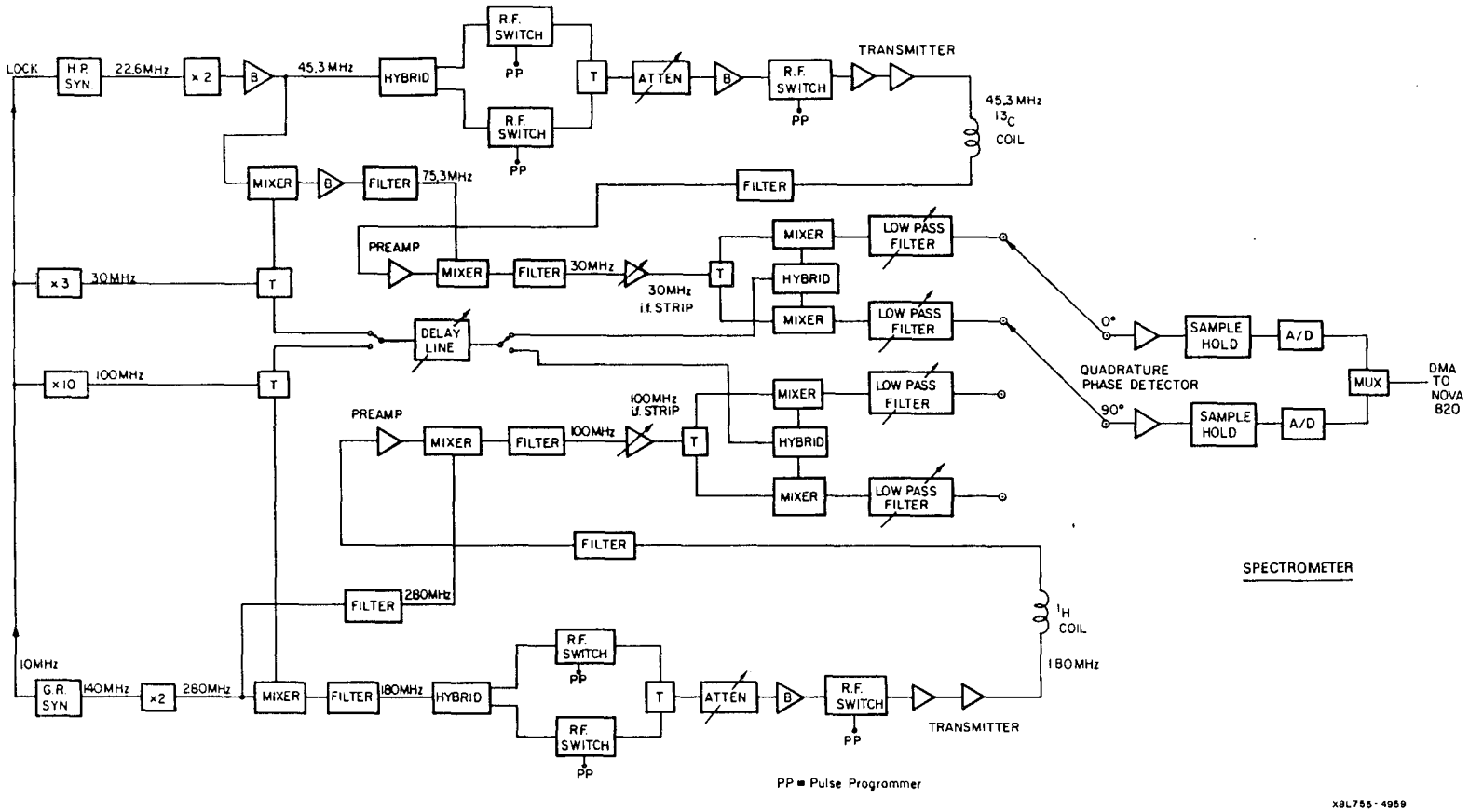
LOCK
H.P. SYN
22.6MHz
× 2
B
45.3MHz
HYBRID
R.F. SWITCH
PP
T
ATTEN
TRANSMITTER
45.3MHz
13C
COIL
MIXER
FILTER
75.3MHz
PREAMP
30MHz
30MHz i.f. STRIP
× 3
DELAY LINE
× 10
100MHz
100MHz i.f. STRIP
LOW PASS FILTER
0°
90°
QUADRATURE PHASE DETECTOR
SAMPLE HOLD
A/D
MUX
DMA TO NOVA 820
SPECTROMETER
1H
COIL
180MHz
280MHz
10MHz
G.R. SYN
140MHz
PP = Pulse Programmer
XBL755-4959

Figure 83

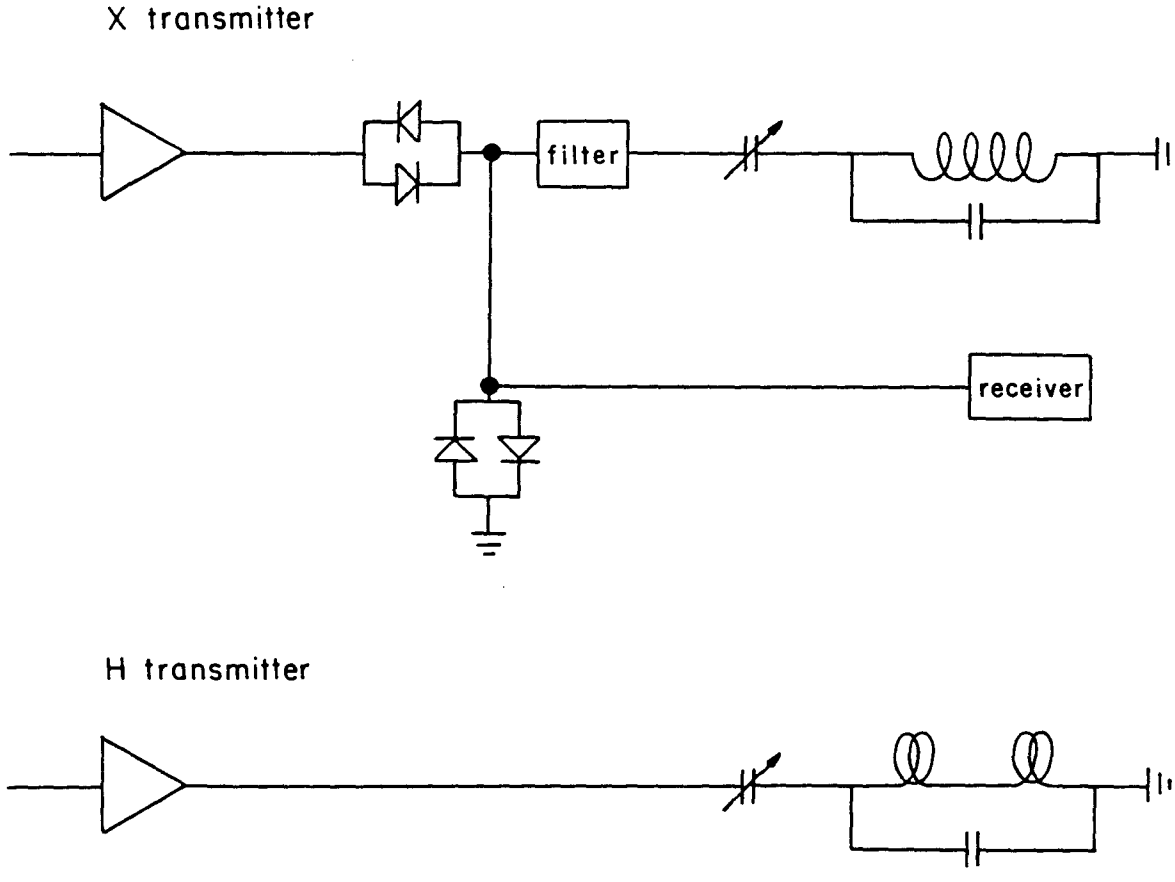

XBL 788-10110

Figure 84